Lecture Notes in Electrical Engineering 820

Chandan Kumar Chanda ·
Jerzy R. Szymanski · Afzal Sikander ·
Pranab Kumar Mondal ·
Dulal Acharjee *Editors*

# Advanced Energy and Control Systems

Select Proceedings of 3rd International Conference, ESDA 2020

Springer

# Lecture Notes in Electrical Engineering

## Volume 820

The book series *Lecture Notes in Electrical Engineering* (LNEE) publishes the latest developments in Electrical Engineering - quickly, informally and in high quality. While original research reported in proceedings and monographs has traditionally formed the core of LNEE, we also encourage authors to submit books devoted to supporting student education and professional training in the various fields and applications areas of electrical engineering. The series cover classical and emerging topics concerning:

- Communication Engineering, Information Theory and Networks
- Electronics Engineering and Microelectronics
- Signal, Image and Speech Processing
- Wireless and Mobile Communication
- Circuits and Systems
- Energy Systems, Power Electronics and Electrical Machines
- Electro-optical Engineering
- Instrumentation Engineering
- Avionics Engineering
- Control Systems
- Internet-of-Things and Cybersecurity
- Biomedical Devices, MEMS and NEMS

For general information about this book series, comments or suggestions, please contact leontina.dicecco@springer.com.

To submit a proposal or request further information, please contact the Publishing Editor in your country:

**China**

Jasmine Dou, Editor (jasmine.dou@springer.com)

**India, Japan, Rest of Asia**

Swati Meherishi, Editorial Director (Swati.Meherishi@springer.com)

**Southeast Asia, Australia, New Zealand**

Ramesh Nath Premnath, Editor (ramesh.premnath@springernature.com)

**USA, Canada:**

Michael Luby, Senior Editor (michael.luby@springer.com)

**All other Countries:**

Leontina Di Cecco, Senior Editor (leontina.dicecco@springer.com)

**** This series is indexed by EI Compendex and Scopus databases. ****

More information about this series at https://link.springer.com/bookseries/7818

Chandan Kumar Chanda · Jerzy R. Szymanski ·
Afzal Sikander · Pranab Kumar Mondal ·
Dulal Acharjee
Editors

# Advanced Energy and Control Systems

## Select Proceedings of 3rd International Conference, ESDA 2020

Springer

*Editors*
Chandan Kumar Chanda
Department of Electrical Engineering
Indian Institute of Engineering Science and Technology
Shibpur, West Bengal, India

Afzal Sikander
Instrumentation and Control Engineering
Dr. B. R. Ambedkar National Institute of Technology
Jalandhar, Punjab, India

Dulal Acharjee
Computer Science
Applied Computer Technology
Kolkata, West Bengal, India

Jerzy R. Szymanski
Department of Electrical Drives
Kazimierz Pułaski University of Technology and Humanity
Radom, Poland

Pranab Kumar Mondal
Mechanical Engineering
Indian Institute of Technology Guwahati
Guwahati, India

ISSN 1876-1100 ISSN 1876-1119 (electronic)
Lecture Notes in Electrical Engineering
ISBN 978-981-16-7273-6 ISBN 978-981-16-7274-3 (eBook)
https://doi.org/10.1007/978-981-16-7274-3



This Springer imprint is published by the registered company Springer Nature Singapore Pte Ltd.
The registered company address is: 152 Beach Road, #21-01/04 Gateway East, Singapore 189721, Singapore

# Preface

This proceeding book is composed with some of the revised good papers of "3rd International Conference on Energy Systems, Drives and Automations", ESDA2020, held during 30th and 31st of December 2020 as Online mode and managed from Kolkata, West Bengal, India. Most of the papers are from Electrical, Mechanical, Electronics and Instrumentations research and applications.

Some senior Professors, Scientists and Research Scholars who have contributed different chapters for this book are—Prof. Jerzy Szymanski (Kazmierz Pulaski University of Technology and Humanities, Radom, Poland), Prof. Chandan Kumar Chanda (IIEST, Howrah, India), Prof. Pradip Kumar Sadhu (IIT-ISM, Dhanbad, India), Prof. Kamrul Alam Khan (Jagannath University, Dhaka, Bangladesh), Prof. Madan Mohan Tripathi (Delhi Technological University, India), Pranab K Mandal (IIT, Guwahati, Assam, India.), Prof. Koushik Guha ( NIT, Silchar, Assam), Prof. Aminul Islam (BIT, Mesra, Jharkhand), Prof. Dip Prakash Samajdar (IIIT, Jabalpur, M.P.), Dr. Afzal Sikander (NIT, Jalandhar, Punjab), Dr. Neelu Nagpal (MAIT, Delhi) and many more.

About this edition, total 26 chapters are included as research papers, tutorials, survey papers and report of science-engineering projects. There are three sections in this book as (i) Sustainable Energy, Environment and Applications (ii) Embedded Control Systems and Sensors and (iii) Engineering Computing. Most of the topics covered in all three sections are—renewable energy, green bio energy, solar cells and its applications, charging of batteries, electrical appliances, household electronics, electrical drives, automation and control system using Artificial Intelligence, power transmission through grids, network design for load balancing, operational amplifier design, etc. are the main theme of maximum papers. Another group of papers having details of computing aspects of energy in wireless, traffic flow and algorithms in control system are included in section (iii).

Most of the papers are outcome of the study and research work of Ph. D students and their supervisors. Papers are composed within limited size of 8-12 pages having abstract, introduction, survey of existing works, mathematical model, methodology, machine setup, experiments and results. There are some tutorial papers having no results but would be worthy enough to the academicians. There are many

papers on low-powered circuits and devices as memresistor, sensors, silicon gate, FET, MOSFET, high electron mobility-based transistors, etc. Rather than energy and control systems, many papers are under microelectronics, nanotechnology, nanomaterials and its characteristics at different compositions.

All editors have written chapters for this book or have given their valuable feedback and comments to improve the quality of this book. Editors are thankful to all authors and especially to research scholars like Mr. Suman Kr. Ghosh, Mr. Dipanjan Bose, Ms. Silpee Talukdar, Mr. Suneet Kr. Agnihotri and many more who have given much effort to write and edit papers for this book. We offer thanks to all editors, authors, experts, reviewers of this edition of this book.

Many professors like Prof. Pierluigi Siano from Italy and Prof. Dr. Vanja Ambrozic from Slovenia as Keynote Speakers; Prof. Celia Shahnaz from Bangladesh, Prof. Kamrul Alam Khan from Bangladesh, Dr. Jerzy Szymanski from Poland, Dr. Olga Jaksic from Serbia Europe as Invited Speakers contributed in this conference ESDA2020 and advised to compose this book; we offer congratulations and gratitude to them. Lastly, we offer our thanks to all co-authors, HODs, management people of all institutes and Universities who allowed to present and publish papers in these proceedings.

Shibpur, India — Chandan Kumar Chanda
Radom, Poland — Jerzy R. Szymanski
Jalandhar, India — Afzal Sikander
Guwahati, India — Pranab Kumar Mondal
Kolkata, India — Dulal Acharjee

# Contents

# About the Editors

**Chandan Kumar Chanda** is working as a Professor with the Department of Electrical Engineering, IIEST, Shibpur, India. He has earned a Ph.D. degree from the Department of Electrical Engineering, B.E. College (DU), Shibpur, India. Dr. C. K. Chanda has over 30 years of teaching and research experience in the diverse field of Power Systems Engineering. His areas of interest include smart grid, resiliency, stability, and renewable energy. He is actively involved in various research projects funded by Centrally Funded Organizations like DST and UGC. He has published 135 research articles in journals and conferences of national and international repute.

**Jerzy R. Szymanski** is working as a Professor in the Faculty of Transport, Electrical Engineering, and Computer Science at the University of Technology and Humanities in Radom (UTH Radom), Poland. He has graduated Doctor of Philosophy (Ph.D.) in Electrical Engineering from Warsaw University of Technology. His research areas include power electronics converters in drive applications, application of power converters in renewable sources and battery electric vehicles, EMC compatibility in power converters systems, hybrid power systems in electric industry drives, energy storages for BEV, and active power filters, etc. He has about 75 scientific publications, and 03 patents to his credit. He has also supervised 05 doctoral students.

**Afzal Sikander** is an Assistant Professor in the Instrumentation and Control Engineering department at the Dr. B. R. Ambedkar National Institute of Technology, Jalandhar, India. He has earned a Ph.D. degree from the Department of Electrical Engineering, Indian Institute of Technology Roorkee, India. Dr. Afzal has over 10 years of teaching and research experience. His areas of interest include control theory and applications, model order reduction, machine learning, optimization, robotics, and renewable energy. He is actively involved in various research projects funded by CSIR, ISRO, TEQIP, etc. He has published 48 research articles in reputed national/international journals and conferences.

**Pranab Kumar Mondal** is an Associate Professor in the Department of Mechanical Engineering at the Indian Institute of Technology Guwahati since May 2015.

He received his undergraduate and postgraduate degrees from Jadavpur University, Kolkata, and completed his Ph.D. from the Indian Institute of Technology Kharagpur in 2015. His principal research interest, encompassing the broad area of microfluidics, covers various facets of micro-scale multiphase transport, electro-kinetics, and micro-scale transport of heat. He is currently working on stability analysis of flows with free surfaces, capillary filling of bio-fluids. He has co-authored more than 100 refereed journals conference publications.

**Dulal Acharjee** is working as Director in Applied Computer Technology, Kolkata, India. Before, he worked as a Professor in the Department of CSE & IT of Purushottam Institute of Engineering and Technology, Rourkela, Odisha. He also worked as Visiting Faculty in Maulana Abul Kalam Azad University of Technology, Kolkata. He received M.Tech. degree in Information Technology from Tezpur University. Before, he did M.Sc. in Applied Physics and Electronics from Dhaka University. He has vast experience of working in the software training and development industry with research interest in automated activity recognition systems, sensor-based applications, microprocessor- and microcontroller-based embedded systems, etc. Dr. Acharjee has over 80 research publications in international journals/conferences and 04 book chapters to his credit.

# Sustainable Energy, Environment and Applications

# Industrial Scenario of Renewable Energy-Based Electromobility


**Jerzy Szymanski and Marta Zurek-Mortka**

## 1 Introduction

Electromobility is a key factor in the development of sustainable industrial development, due to its high growth potential, which may also positively affect other sectors of the economy. Moreover, electromobility has a positive effect on air quality and reduces smog in many cities. Cars and light commercial vehicles are responsible, respectively, for around 12 and 2.5% of the total emissions of carbon dioxide ($CO_2$) [1]. Pursuant to Regulation (EU) 2019/631 of the European Parliament and the Council has an intermediate target of a 55% net reduction in greenhouse gas emissions by 2030 [1]. It is estimated that by 2050, exhaust emissions will be reduced by 90% and, thus, drastically reduce the emission of carbon dioxide into the atmosphere [2]. Figure 1 shows the extent to which the carbon footprint of the electric vehicle will be reduced compared to the internal combustion car (petrol and diesel engine) at the operational stage. For some models of electric vehicles, with an annual average mileage of 15,000 km, charging with energy from renewable sources reduces $CO_2$ emissions by over 3.5 tons. Data were obtained from [3]. Figure 1 shows that in vehicles the low efficiency of internal combustion engines (for spark-ignition engines; $\eta = 0.3–0.36$ injection engines; $\eta = 0.4–0.45$) results in over two times higher $CO_2$ emissions than in vehicles with electric engines (cage engines; $\eta = 0.89–0.95$ or permanent magnets engines; PMSM, BLDCM; $\eta = 0.95–0.98$). It also indicates the

J. Szymanski (✉)
Faculty of Transport, Electrical Engineering and Computer Science, Kazimierz Pulaski University of Technology and Humanities, Radom, Poland
e-mail: j.szymanski@uthrad.pl

M. Zurek-Mortka (✉)
Department of Control Systems, Lukasiewicz Research Network, Institute for Sustainable Technology, Radom, Poland
e-mail: marta.zurek-mortka@itee.lukasiewicz.gov.pl



C. K. Chanda et al. (eds.), *Advanced Energy and Control Systems*, Lecture Notes in Electrical Engineering 820, https://doi.org/10.1007/978-981-16-7274-3_1

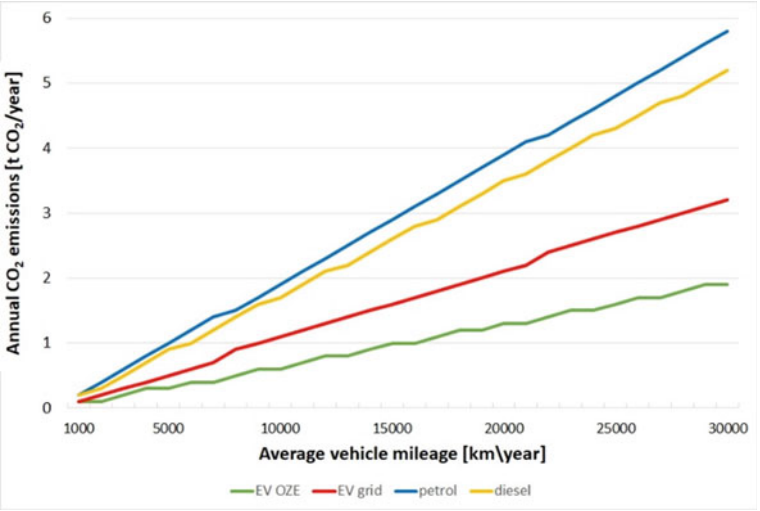


**Fig. 1** Scenario of $CO_2$ transport emissions in comparison of EV, petrol, and diesel vehicles average mileage per year [3]

share of $CO_2$ in the production of electricity (EV powered from RES and EV powered from the traditional power grid).

Considering the environmental effects of the development of electromobility in this context, there are doubts as to whether the change of the method of supplying vehicle propulsion from fossil fuels to electricity, produced, e.g., in Poland mainly thanks to coal combustion, will reduce $CO_2$ and other harmful substances emissions. In addition, the way of electricity is changing. Renewable energy sources have an increasing share, including distributed energy, the development of which brings many benefits to both investors and the energy transmission system. Therefore, with the use of ever cleaner electricity, the development of electromobility on a global scale brings evident environmental benefits [4].

This paper is organized as follows: the first part presents the perspectives for the development of electromobility in industrial companies. The next part is about the studies on fast charging stations for a company's EVs. In the final part of this paper, a novel type of DC/AC/DC converter was presented as an EV battery charger, in which the drive voltage frequency converter with an inbuilt output rectifier unit was used.

## 2 Perspectives for the Development of Electromobility in the Industry

The functionality of electric vehicles is often assessed by potential buyers in terms of range and speed of refueling compared to vehicles with internal combustion engines. Does the range and speed of charging of modern electric cars make them a practical and fully competitive means of transport in comparison to vehicles with internal combustion engines? The answer is affirmative assuming that the user of such a vehicle is provided with suitable fast charging infrastructure so that the driving time and charging time are similar to those of an internal combustion vehicle [5]. The existing and extensive infrastructure for internal combustion vehicles is taken as obvious and it is often forgotten that it was built successively with the development of the automotive industry. A car's driving range of 400–500 km is now considered the standard for a passenger car with an internal combustion engine, and some car models have a driving range of more than 700 km [6]. While the offer of electric passenger cars with a range of 400 km is constantly expanding, fast charging is a problem due to the lack of a properly developed network of high-power charging stations, and not all electric cars can be charged with high power. However, this situation is changing rapidly. Currently, usually manufacturers of lithium-ion batteries provide the possibility of charging the battery with an hourly current of 1C or 3C, which significantly reduces the battery charging time to about 20 min [7].

The use of electric energy to power vehicles has developed to such an extent that it is justified to raise the question about electric vehicles in the industry.

The industry uses many specialized vehicles, ranging from transporting people to heavy-duty vehicles for off-road and underground work. A good example of working machines with electric drives is surface mining machines, where cage induction motors have been used for many years and powered by drive frequency converters, e.g., lignite coal excavators, stackers, or conveyors with adjustable belt speed [8, 9]. Here, the next step in the development of electromobility is only to provide electricity from renewable energy sources. The distance covered by the mining machines is limited to the mine area; therefore, they supply MV cable lines installed on an ad hoc basis using cable cars. A cable car is a caterpillar machine with an electric drive system, which transports a MV cable with a length of approx. 3 km. These vehicles are so unique that they are usually custom-made and generate high purchase or modification costs. With hybrid and electric work vehicles attracting more attention, power train configurations, energy management strategies, and energy storage devices have also been increasingly reported in the literature [10–12]. The electric vehicle market has not been interested in this industry so far due to the lack of available technology and the high production costs of a small number of these vehicles.

In addition, the undoubted advantage of the usage of electric machines in the mines is that there is no need for expensive exhaust gas discharge and fuel transport. For the service sectors using electric vehicles, e.g., Border Guard, State Forests, or National Parks, the environmental pollution and noise in protected areas are reduced. Examples of wheel electric machines are presented in Fig. 2. An EV material haulage

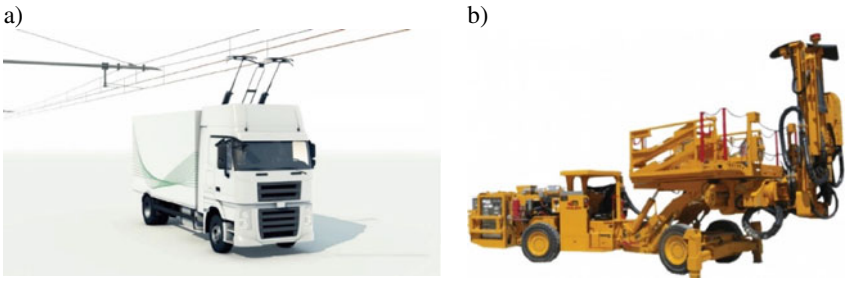


**Fig. 2** Electric wheel industrial vehicles: **a** electrified road freight traffic developed by Siemens Mobility [13], **b** electric machine in underground mines [14]

unit like a boom truck needs to be able to carry up cargo across rough road beds. So the question of how long it will last underground work is always going to be one of the first asked by mining companies evaluating the total cost of ownership for EV fleets. In the world of transport (especially in EU), electric drives of vehicles are to be an alternative to cars equipped with internal combustion engines. This is undoubtedly a good direction, but it must be well thought out in terms of infrastructure, including charging networks and vehicle production, which should be at least as burdensome for the natural environment as possible. The situation is more complicated in the case of heavy transport. Although electric vehicles are beginning to appear on the market, their capabilities (mainly ranges) are still low, between 200 and 300 km.

At the present, it is unlikely that trucks with large and heavy batteries will become a common solution for heavy-duty transport. Moreover, the issue of power requirements for these prototype solutions is so problematic that so far no country in the world has been able to meet these requirements if they are widely implemented. It seems that it is more realistic to use fuel cells in trucks and solutions with "external" power, e.g., from a pantograph (as presented in Fig. 2b) or other solutions that are being researched.

Figure 3 shows caterpillar surface mining machines powered by electric motors, to which electricity is supplied by cables laid on the ground. As the drive motors of the caterpillar drive control system are supplied from drive voltage frequency converters (VFCs), it is possible here to support the power supply of electric motors from renewable energy sources (Fig. 4).

Therefore, it can be said that infrastructure is the main brake to electromobility in the heavy transport sector. Electric buses, due to their popularity, have forced the development and implementation of chargers adapted to them [15]. In the case of heavy transport, the places where chargers should be built are also a problem. It would be logical to create large parking lots with an adequate number of chargers that could supply two vehicles simultaneously. Multi-station charging stations will reduce the costs of their implementation and operating costs. It is worth noting that, for example, high-power city chargers reduce the need for large batteries in the e-bus. From an economic point of view,if the higher is the charging power, the lower is the price of the charging station per 1 kW, but the higher is the price of

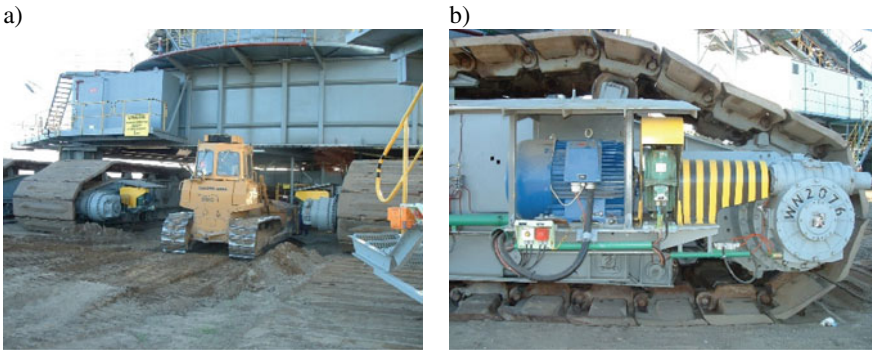


**Fig. 3** Example of caterpillar electric drive in open pit mining excavators or spreaders: **a** caterpillar electric drive system, where drive motors are supplied here with AC MV from dedicated the ground placed cables, **b** induction motor powered from drive frequency converter in caterpillar drive system [9]

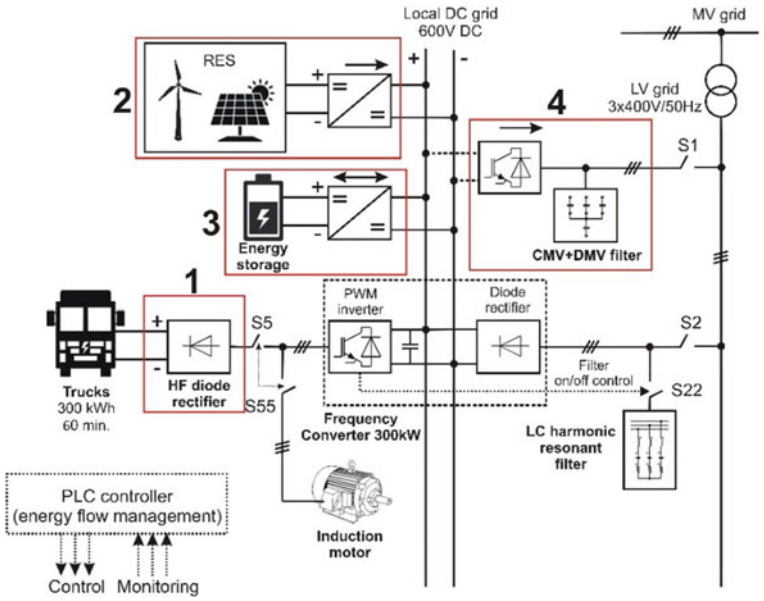


**Fig. 4** The model of hybrid EV fast charging station with DC microgrid

connection to the power grid. Charging can be performed with the use of a low-voltage network, a medium-voltage network with an LV/MV transformer, or from an overhead line, e.g., a tram line. In UE, currently, smart transformer stations are being implemented into the power system, which are powered by RES and are equipped with energy storage and high-power charging points for EV, e.g., 300 kW [16, 17].

The common occurrence of such smart transformer stations can significantly enrich the EV charging infrastructure.

For the purposes of fast charging of working machine batteries, it is necessary to take into account, in addition to the preparation of high-power charging stations, also ensuring the availability of these stations near the place of production tasks by these electric machines. Basic surface mining machines (excavators, stackers), in which electric caterpillar drives are equipped with voltage drive inverters, are due to their dimensions adapted to the use of local DC microgrid (Fig. 4). The use of energy storage located in machines and suppling from renewable energy sources will significantly increase their efficiency and improve energy quality indicators in the industrial AC network of the mining plant.

## 3 Fast Charging Stations for Enterprise's Electric Vehicles

Due to the lack of a uniform concept of the energy market model for EV charging, there are both free charging stations (e.g., the business model used by Tesla) and points selling the charging service. The diversity of standards has resulted in the creation of stations dedicated to specific vehicles as well as stations managed by operators enabling the charging of any vehicle.

The concepts of multi-station EV charging stations, creating an intelligent microgrid with renewable energy sources (RES), are investigated [18, 19]. A microgrid is an autonomous energy microsystem covering a limited area of the building, housing estate, commune, and enterprise, in which there are sources of energy production (electricity and heat), energy storage devices, controllers as well as controllable and non-controllable energy receivers connected by means of a grid. These structures can work synchronously with the rest of the power system or create independent islands.

The unique concept of a fast charging station for a company's EVs is presented in [20]. Usually, a low-voltage AC grid is used to charge the EV batteries. The paper analyzes the possibility of using a low-voltage DC microgrid, as it can be connected directly to the power supply of intermediate circuits of frequency converters, e.g., as adjustable frequency drives of electric motors, which are commonly used in industry. The DC line is used to exchange energy between the drive frequency converter, which eliminates the need to use power resistors to discharge excess energy in the intermediate circuits of the drive frequency converters during the motor operation as generators. These motors transmit energy to the DC grid. The use of a drive PWM (Pulse Width Modulation) inverter for charging EV battery in the configuration as shown in Fig. 4 is a new innovative solution.

The EV charging microgrid can include the following elements:

- RES units: e.g., PV modules and wind turbines,
- power connection with security (connection to the power system, ensuring intelligent measurement of energy and its flow as well as supervision of electricity quality parameters),

– energy storage (ES) (e.g., Li-ion batteries, supercapacitors) reduce the impact of non-controllable loads on the power system and create the possibility of connecting microgrids to the power system through a lower power connection (without the need to modernize the network),
– charging terminals with an interface that allows the user to connect and settle costs,
– AC/DC and DC/AC converters,
– harmonics filters,
– management module (control, diagnostics, etc.).

To integrate the EV charging station with the power system in the enterprise, there should be provided a suitable selection of the topology of the local system, supplying infrastructure of the station and taking into account its stages of expansion to ensure the charging of EV batteries with renewable energy. The annual balance sheet demand for renewable energy may be used here. The topology includes a local DC voltage renewable energy plant, e.g., PV power plant, and energy storage as a Li-ion battery. This type of battery is often used and characterized by the ability to fast deliver high-power energy to the local DC microgrid. Low-voltage drive VFC equipped with 6-pulse diode rectifier unit is used as a charging converter. Depending on the production specificity of the industrial plant, drive VFCs may have power up to approximately 2 MW. Their usage to charge EV batteries does not require the expansion of the company's power supply network and does not increase the maximum power demand of enterprises.

The equipment of hybrid EV fast charging station power supply system can be developed in steps as presented in Fig. 4:

1. Adaptation of the drive voltage frequency converter to the battery charging function through the use of a rectifier unit (1).
2. Construction of a solar power plant with the annual production capacity of renewable energy for charging EV batteries (2).
3. Equipping the charging station power supply system with energy storage for supporting the supply of industrial drives during short interruptions in energy supply from the industrial power system (3). If the local grid is able to fully use RES energy for the production processes, then in balance terms it is natural energy storage for EVs.
4. The use of an Active Front End (AFE) recuperative inverter for transmitting renewable energy from the DC line to the AC voltage side to introduce it to the power system (4), when there is a need to improve the energy quality indicators of AC line in the peak load hours.

Figure 5 shows the conceptual model of a grid-connected RES and ES system. This combination can produce a daily amount of dispatchable energy $E_{PV+ES}$, e.g., for the needs of charging stations of battery machines in the enterprise.

In a 24-h day cycle, the PV unit is generating an $E_{PV}$ amount of energy. A portion of this energy is delivered to the grid. The redundant energy of the PV unit is used to charge the ES unit $E_{ES}^{CH}$, rather than curtailing it when the PV output is high during

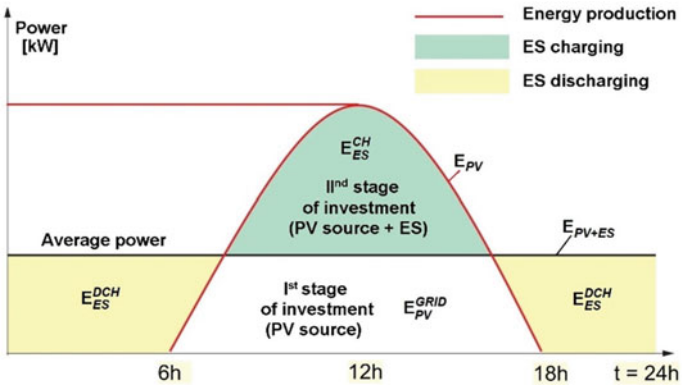


**Fig. 5** Renewable energy (e.g., PV) demand coverage of the EV charging station

the day. This stored energy is then discharged to the grid $E_{\mathrm{ES}}^{\mathrm{DCH}}$, when the PV output is small or zero during the night. The PV and ES units are placed in the same location to avoid grid energy losses when charging the ES unit. Generalizing, the total output power balance equation of the main components can be described as a power model. This expression presents RES capacity in a period, e.g., 1 year.

$$\int_0^T p_{\mathrm{PV}}(t)dt = \sum_{i=1}^{n} \int_0^T p_{l_i}(t)dt + \int_0^T p_{\mathrm{ES}}(t)dt \tag{1}$$

where

$T = 1$ year,

$I$—number of battery charging points for EVs,

$p_{PV}(t)$—power of PV plant,

$p_{li}(t)$—power of EV charging station, and

$p_{ES}(t)$—power of energy storage.

Figure 6 shows the quarterly energy production of a rooftop PV plant with power $6\mathrm{kW_p}$ on sunny days in middle Europe, where the maximum insolation in summer is about 1 kW/m$^2$ with 16 h per day and 0.1 kW/m$^2$ with 8 sunny hours per day taking into account storing energy and delivering it to loads connected to the DC microgrid or to the AC grid. The annual energy production of a PV power plant is about 6MWh. Thanks to this small PV plant, over the indicated period (since the 2018 year), it was possible to reduce over 17,7 tons of carbon dioxide, which is also reflected in the planting of approx. 210 trees. Assuming that, for example, a small enterprise has 1 electric car, which consumes max. 20kWh/100 km (e.g., Ford E-Transit), and has the annual mileage max. 30,000 km, the solar power plant is able to meet the energy demand for charging this vehicle. Similar assumptions can be

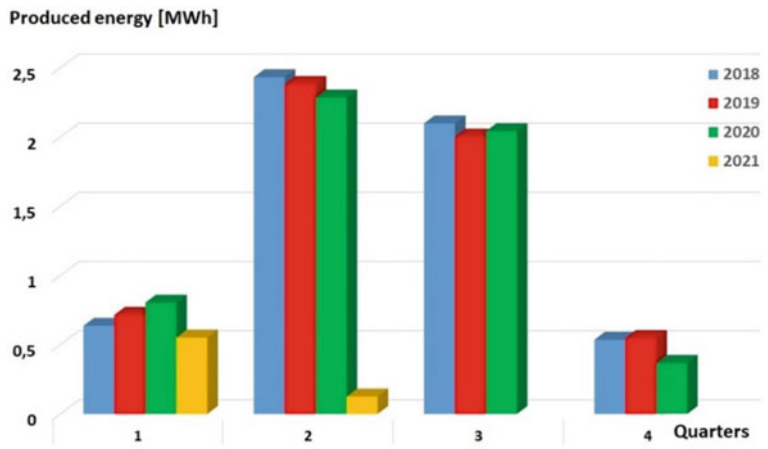


**Fig. 6** Energy production from PV power plant 6 $kW_p$

adopted and scaled depending on the fleet of electric vehicles in the enterprise, the electricity consumption profile, or the type of enterprise activity (service, production, etc.).

The minimum energy $E_{\text{minPV}r}$ should be provided by RES during the year for charging EV batteries and it should be not less than the energy required for EV charging stations $E_{l_r}$, which is shown in the following expression (2):

$$E_{\text{minPV}_r} \geq E_{l_r} \tag{2}$$

EVs are an integral part of such a microgrid, in which they can act as both receivers and energy sources. The operation of the system is controlled by a management system that performs the functions of monitoring, diagnostics, and controlling the operation of the microgrid. The function of the target may be to minimize costs, and thanks to the possibility of storage, it is possible to optimize in the long term. With forecasting, the microgrid operator can manage electricity flow, maximizing profits.

## 4 Research of Using Low-Voltage Drive Frequency Converters in EV Charging Stations

The widespread occurrence of drive VFCs prompted the authors to modify them for the needs of fast and ultra-fast charging stations for EV batteries. To check the possibility of using the components of the drive VFC to create a DC/AC/DC converter supplying an EV battery by DC voltage, the model of the integrated circuit with a rectifier unit was built. This experiment is described in [20].

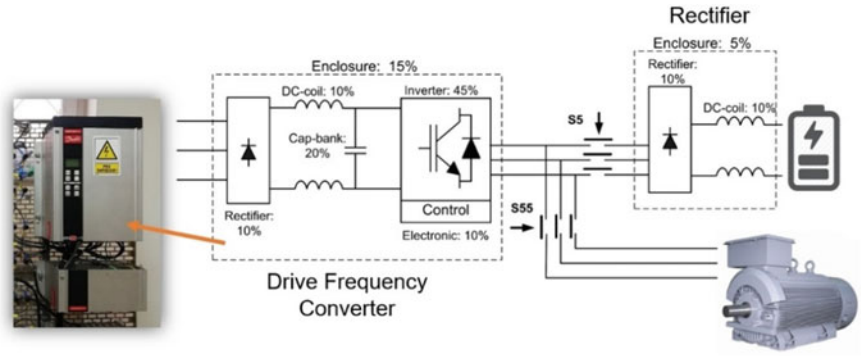


**Fig. 7** Approximate component costs in percent's of the drive VFC (100%) powered by the 600 V DC microgrid

When a PWM inverter is supplied to a 600 V DC microgrid, a DC voltage source with adjustable value was obtained in such a way that a constant current of battery charging was ensured. The use of rectifier and inverter implemented in one power integrated circuit eliminates the negative side effects of the inverter common-mode voltage.

When the drive frequency converter is powered from the AC network, it is necessary to use an additional fast diode rectifier module and connect it to the VFC inverter. Then the motor is disconnected because the inverter voltage needs to be shaped according to the needs of ensuring a constant charging current of the battery connected to the rectifier [20].

Figure 7 shows the percentage share of costs in a drive system with a voltage frequency converter. The cost of the rectifier is small, so it is justified to build a battery charging point from low-voltage and low-cost modules.

The mathematical model of the PWM inverter of the drive VFC, which is connected to a 6-pulse diode rectifier, was built using ANSYS Simplorer and it is shown in Fig. 8. The bipolar PWM voltage inverter is supplied by a 600 V DC microgrid and its control is shown as state graphs above the model. The modulating sinusoidal frequency wave of 300 Hz is used for rectifying process (to mitigate AC components of rectifier DC output voltage). Figure 9 presents the simulation results of this model. Figure 9a shows the near linear dependence of the battery DC voltage value on the modulation factor M. The voltage value at the rectifier output is controlled by setting the appropriate value of the modulation factor M from 0 to 1, where M is defined as follows (3):

$$\mathrm{M} = \frac{\text{amplitude of sine modulating voltage (SINE1)}}{\text{amplitude of carrier wave (TRIANG1)}} \tag{3}$$

Figure 9b shows that regardless of the current value, the output voltage of the battery is constant. Only the voltage value is variable depending on the modulation

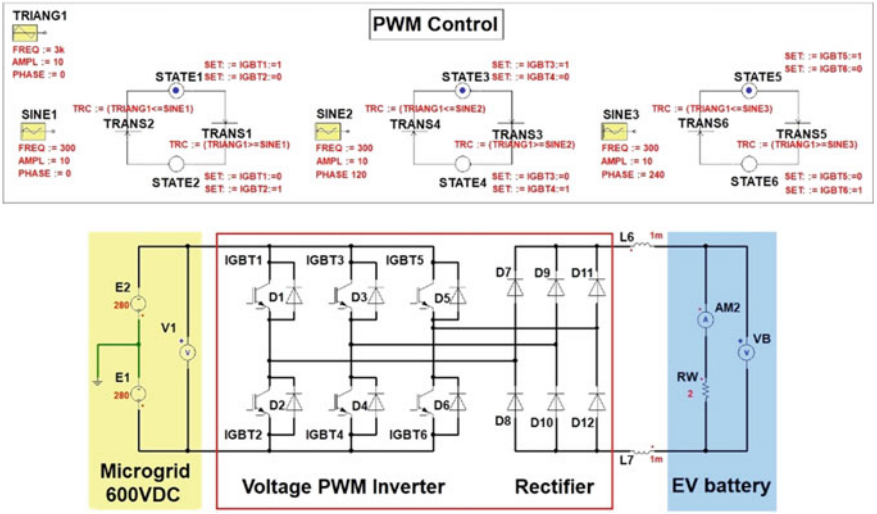


**Fig. 8** The model of the integrated circuit with a rectifier unit for fast charging of EV batteries

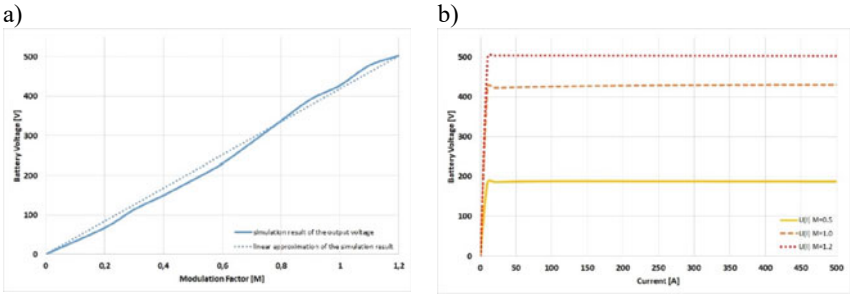


**Fig. 9** Simulation results: **a** battery DC voltage as a function of the modulation factor M, **b** constant battery charging current for the set rectifier constant voltage value (for a given M factor value)

factor M, but in this case, it can be treated as different types of batteries. The obtained results of the simulation tests of the presented model confirm that it is possible to control the DC voltage and current value of the diode rectifier charging the EV battery.

## 5 Conclusion

In industrial enterprises, the rapid development of the infrastructure for EV charging with high power with minimal financial outlays is possible by adapting the existing on-site power grid to use renewable energy both for production purposes and for

charging EV batteries. The possibility of adapting drive VFCs for the needs of EV battery charging has been demonstrated. The existing power supply network of drive VFCs is used to power the proposed EV battery charging system. The structure of power electronic modules is similar in the inverters and bidirectional DC/DC converters. The simulation tests confirm the assumed hypothesis of using drive VFCs as unidirectional EV battery chargers. It is to be expected that soon there will be multifaceted converters on the market that use the PWM inverter of the drive VFC as a unidirectional or bidirectional DC/DC converter, which allows charging the EV battery or drawing energy from the battery to the DC line. Additionally, only favorable legal and economic regulations are needed for the rapid development of enterprise electric transport and local delivery of goods in urban areas.

## References


1. Regulation (EU) 2019/631 setting $CO_2$ emission performance standards for new passenger cars and for new light commercial vehicles, https://ec.europa.eu/clima/policies/transport/vehicles/regulation_en (accessed on 6th April 2021), (accessed on 21 April 2021)
2. International Energy Agency (2021), Electric Vehicles, IEA, Paris, https://www.iea.org/reports/electric-vehicles (accessed on 21 April 2021)
3. K. Masanobu, Reductions in $CO_2$ emissions from passenger cars under demography and technology scenarios in Japan by 2050. Sustainability **12**, 6919 (2020). https://doi.org/10.3390/su12176919
4. J.M. Grutter, K.J. Kim, E-mobility Options for ADB Developing Member Countries, ADB Sustainable Development Working Paper Series, No. 60, Asian Development Bank (2019). https://doi.org/10.22617/WPS190075-2
5. C. Capasso, et al., Charging architectures integrated with distributed energy resources for sustainable mobility. *Energy Procedia* **105** (2017)https://doi.org/10.1016/j.egypro.2017.03.666
6. R. Garcia-Valle, J.A. Pecas Lopes, Electric vehicle integration into modern power networks, in *Chapter II: Electric Vehicle Battery Technologies*. Springer (2013). ISBN 978-4614-0134-6
7. Battery Cell Technical Specification, Winston LFP200AHA Cell, www.gwl.eu, 2020, (accessed on 21 April 2021)
8. Z. Kasztelewicz, J.R. Szymański, Energy saving control method of electrical drives in conveyor belts with regulated speed in surface brown coal mine. Arch. Min. Sci. Pol. Acad. Sci. (7–8) (2008)
9. Z. Kasztelewicz, J.R. Szymański, Digital control method of caterpillar electric drives in surface mine machines. Arch. Min. Sci. (2) (2009)
10. D. Wang, et al., Performance analysis of hydraulic excavator powertrain hybridization. Autom. Constr. **18**(3) (2008). https://doi.org/10.1016/j.autcon.2008.10.001
11. A. Soma, et al., Simulation of dynamic performances of electric-hybrid heavy working vehicles, in *Eleventh International Conference on Ecological Vehicles and Renewable Energies (EVER)* (IEEE, 2016). https://doi.org/10.1109/EVER.2016.7476371
12. A. Soma, Trends and hybridization factor for heavy-duty working vehicles, in: *Hybrid Electric Vehicles, red. Donatao T, InTech Croatia* (2017). ISBN 978-953-51-3297-4, https://doi.org/10.5772/intechopen.68296
13. https://press.siemens.com/global/en/feature/ehighway-solutions-electrified-road-freight-transport (accessed on 21 April 2021)
14. https://macleanengineering.com/products/mining/electric-vehicle-series (accessed on 21 April 2021)

15. G.N. Jordbakke, et al., Technological maturity level and market introduction timeline of zero-emission heavy-duty vehicles, Institute of Transport Economics, Norwegian Centre for Transport Research (2018). ISSN 2535-5104
16. J. Rodrigues, C. Moreira, J.P. Lopes, Smart transformers as active interfaces enabling the provision of power-frequency regulation services from distributed resources in Hybrid AC/DC grids. Appl. Sci. **10**(4), 1434 (2020). https://doi.org/10.3390/app10041434
17. H.C. Hesse, M. Schimpe, D. Kucevic, A. Jossen, Lithium-ion battery storage for the grid—a review of stationary battery storage system design tailored for applications in modern power grids. Energies **10**(12) (2017). https://doi.org/10.3390/en10122107
18. Y. Chen, et al., Design of PV Hybrid DC/AC microgrid for electric vehicle charging station, in *IEEE Transportation Electrification Conference and Expo, Asia-Pacific (ITEC Asia-Pacific)* (2017).https://doi.org/10.1109/ITEC-AP.2017.8081027
19. E. Ancillotti, et al., Experimental set-up of DC PEV charging station supported by open and interoperable communication technologies, in *IEEE International Symposium on Power Electronics, Electrical Drives (SPEEDAM)* (2016). https://doi.org/10.1109/SPEEDAM.2016.7526036
20. J.R. Szymanski, Unidirectional DC/DC converter with voltage inverter for fast charging of electric vehicle batteries. *Energies* **13**(18), 4791. https://doi.org/10.3390/en13184791

# COVID-19: Impact Analysis on Power Sector (A Comprehensive Review on Demand Change)


**Chandan Kumar Chanda, Emily Vanlalnunsangi, Soumya Adabala, and Dipanjan Bose**

## 1 Introduction

The first case of Coronavirus was detected in December 2019. The virus is found to be highly infectious and easily spread through contact. To date, a whopping 120 million individuals have been recorded to be infected by this virus leaving us with a new normal to ensure social distancing. The pandemic affects the economy, educational institutions, hospitals, and any other professions and industries. Among this, the electricity sector seems to be the most affected and the one industry which is at the most risk [1–4]. Most of the electrical consumers like factories are made to run at a lower operating level [5]. Social distancing and work from home policy have increased the residential load at hours which before the pandemic were considered a non-peak hour, which led to the shift in the Residential Load composition throughout the week confusing the operator [6]. The lockdown that has to be imposed due to the Pandemic has brought about a lot of daily lifestyle changes which in turn interrupts the supply chain and thus disrupts the maintenance of the assets. The reduction in electricity price and emissions from power electricity generation was immediately observed after the lockdown imposition, which was because of the decrease in electricity demand and the increased use of renewable generation [7, 8]. The biggest worry of most of the electrical sector has been the infection of the workers leaving the utility industry with a few to no individual operators which could lead to blackouts or shortage of power supply. In such conditions, the most affected are Hospitals that need uninterrupted power supply for ventilators, electrocardiograms, etc.

This paper will try to provide a detailed review and close insights into the different load compositions of the three big power consumers, India, Italy, and the USA, further

C. K. Chanda (✉) · E. Vanlalnunsangi · S. Adabala · D. Bose
Department of Electrical Engineering, IIEST, Shibpur, Howrah, India



C. K. Chanda et al. (eds.), *Advanced Energy and Control Systems*, Lecture Notes in Electrical Engineering 820, https://doi.org/10.1007/978-981-16-7274-3_2

detailing us how the pandemic has changed the power demand and how this change has posed a threat to the Utility industry, thus increasing the probability of blackout and Cyber attacks as well [9, 10]. A detailed graph is also provided to help us analyze and compare them better.

## 2 Change in Global Energy Demand

The world since its existence has undergone worldwide unrest caused by deadly diseases like the bubonic plague, influenza, etc. which occur approximately thrice every century. The wave of events that hit the world may be in the form of a highly infectious disease (such as COVID-19 and Spanish flu) or a war of unrest such as World War II or even the stock market crash which led to the Great Depression. History has taught us that those mentioned have shifted the Energy Demand in one way or the other (Fig. 1).

The graph explains how such different events have impacted the power demand. Spanish Flu (1918) was reported to be contracted by 50 million leaving almost 20 million dead; the Great Depression (1930) has been the peak of Unemployment and a series of economic breakdowns which had the second sharpest decline in energy demand; World War II (1939–1945) was fought between 30 countries leaving almost 70 million dead; the two Oil Shocks (1973–1974, 1979) caused the price of oil to skyrocket.

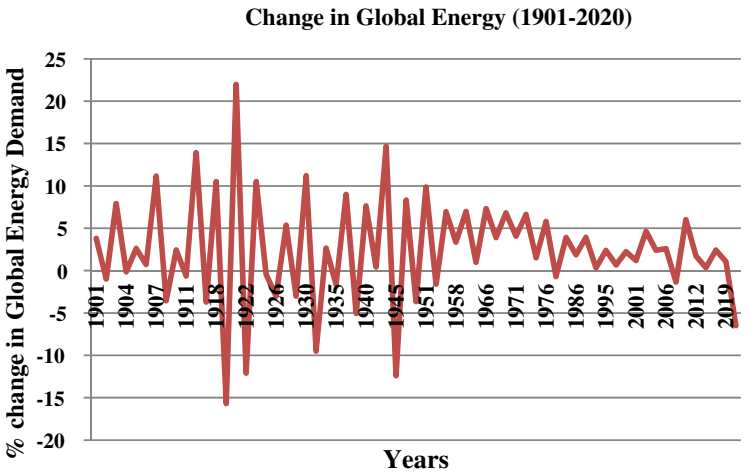


**Fig. 1** Global energy change graph [7]

## 3 Pandemic and Utility Sector

Direct impact implies changes that occur in the grid owing to the pandemic. The changes could include various implications like Power Demand Variations. Let's study in detail the load variation in countries whose utility industry is known to be affected the most by the Lockdown imposed due to the Pandemic and certain restrictions because of which the Industry and business have slowed down their work and the global stock market stocks reduced by over 25% in March 2020 [1]. The strict lockdown imposed all over the country has halted the industrial operation. However, on the other hand, the above-mentioned inactivity in all the sector reduces the emission of carbon dioxide and nitrogen dioxide levels in the lower atmosphere. A detailed analysis of Power Demand change, challenges, and threats faced and measures taken to overcome such challenges for countries like India, Italy, and the USA has been given below.

### *3.1 India*

India's power sector is most diversified and complex, with an installed capacity of 373,548 GW as of October 31, 2020 [2]. It is the third-largest producer and consumer of electricity. The COVID-19 pandemic adversely affected the socio-economic growth of the country. Because of the high infection rate of the virus, Government of India imposed a nationwide lockdown from 25 March which resulted in a stagnation of vital industrial and commercial operations. The variations in the load pattern caused an economic strain on the power sector. According to Power System Operation Corporation Limited (POSOCO), the country's power demand decreased by 28% up to the end of March 2020. To meet the new energy demand, POSOCO needed to change the generation pattern [3].

It minimized coal, diesel, and natural gas-based generation plants but maintained the power generation from renewable energy sources (RES) and nuclear generation units. It is also observed that COVID-19 has impacted the duck curve pattern within the power network of the accessibility of huge penetration of solar rooftop in urban areas. Due to this type of situation, the utilities during the lockdown became prosumers and utilized maximum power at households as "stay at home" policies were imposed all over the region. So, therefore, the selling capacity to the grid is lower which shifted the duck curve a little bit upward. Utilities must cope with the new shape of the curve and schedule the generators accordingly for the economic dispatch program.

Electricity demand and solar production don't always align throughout the day and the phenomenon of power generation can be plotted as a curve which is called Duck Curve. When the sun is out, PV installations capture this sunlight and send it to the energy grid. However, this energy influx drops off after sunset right as home

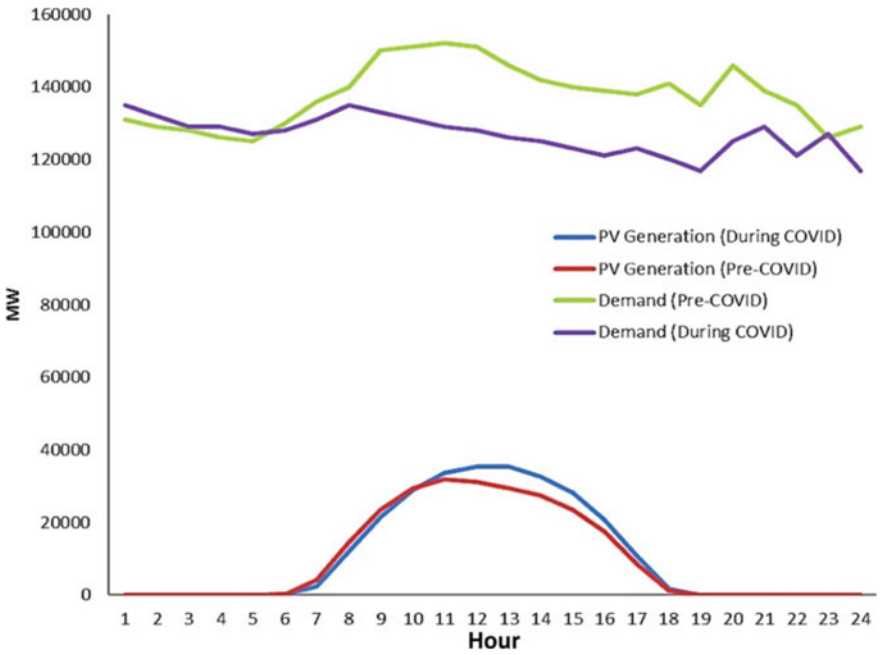


**Fig. 2** Duck curve pre- and during COVID-19 period [4]

electricity begins to peak. As a result, utilities must rapidly ramp up other sources of electricity, which is very inefficient [4] (Fig. 2).

When viewed at a 24-h snapshot, the empty space between the two lines plotting the difference between supply and demand on a graph resembles a duck, providing the name for this phenomenon. The duck curve typically occurs only during Spring when it's sunny but not yet too hot. But in the COVID-19 situation due to the above-said reasons, it resulted in a noticeable change in the duck curve pattern and raised the Under Frequency-based Load Shedding (UFLS) problem [4] (Fig. 3).

To tackle this, POSOCO adapted df/dt and UFLS and relay schemes and maintained the stability of the grid [4]. Government of India lifted the lockdown in a phased manner. This supported the gradual restoration of feeders to the normal operating condition. Lockdown crippled the financial status of a large section of people, and they could not pay their electricity bills in time. This directly affected the revenue of the power sector [5]. Illness among the workforce, insufficient stock of necessary equipment, and unavailability of proper transportation made the restoration process challenging.

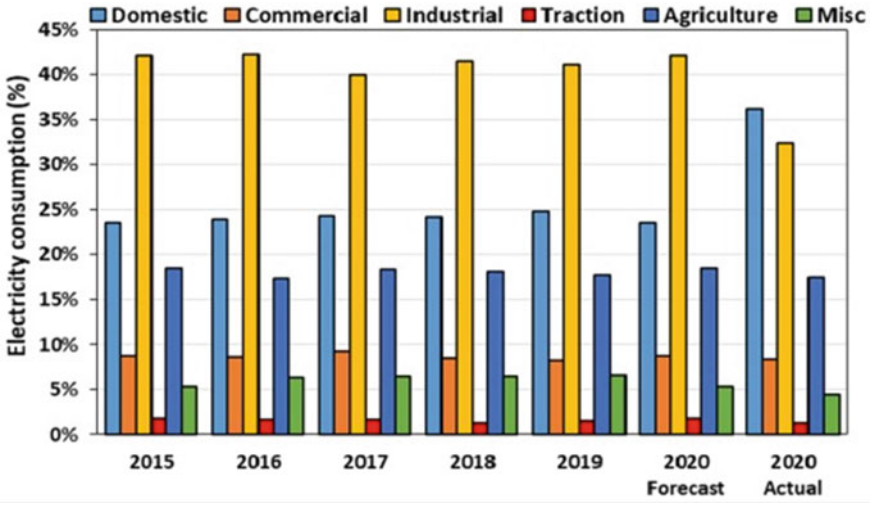


**Fig. 3** Consumption of electric energy in different sectors of India [2]

## *3.2 USA*

We will be analyzing the COVID-19 impact on the US electricity market due to two major reasons. First, the accurate data for change in the load profile of the US electricity market is available readily and is easily accessible. Second, the US has one of the eight hardest hit Electricity sectors globally. Primarily, we can categorize the influence factors of COVID-19 on the electricity sector into three—1. The number of recorded COVID-19 patients and overall public health. 2. The number of people under Lockdown. 3. Rate of Shutdown of commercial and industrial activities [6] (Fig. 4).

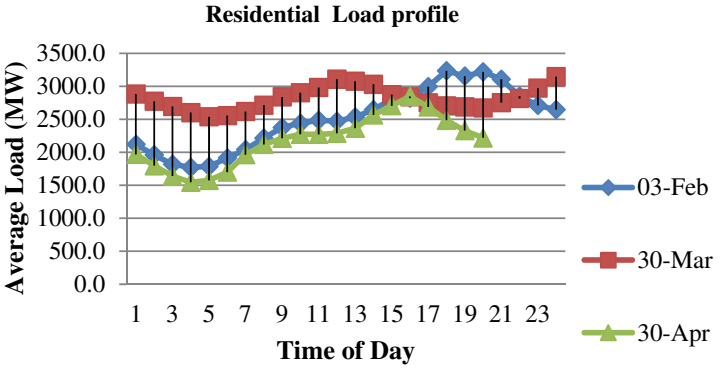


**Fig. 4** Load profile for residential load from February 3–April 30, 2020, for Illinois [6]

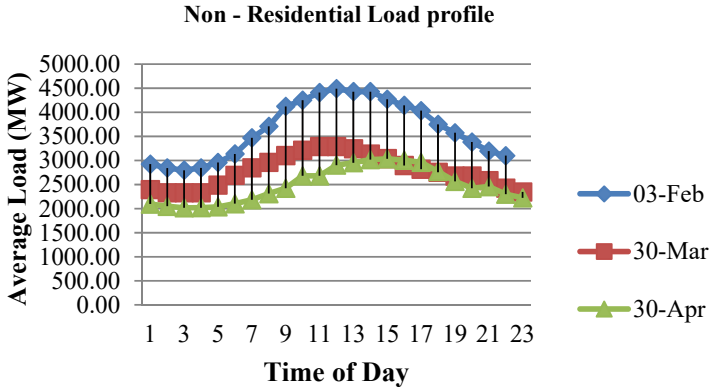


**Fig. 5** Load profile for non-residential load from February 3–April 30, 2020, for Illinois [6]

All these factors directly determine how the load profile for Residential and Non-Residential Loads has changed since the imposition of the stay-at-home policy (Fig. 5).

Moreover, all the factors listed above appear to be having an interconnected relationship between them as well. According to Energy Information Administration (EIA), the residential load has increased by 12% and the non-residential load decreased by 16% during April 2020 compared to April 2019. Residential and non-residential load demand has been seen differently [7]. The non-residential load remains to be consistent throughout the pandemic although the residential load has seen a dramatic change in its shape. It has higher working hour (9 am–5 pm) peaks than usual and lower demand toward the end of the day. The load profile for Energy Consumption of the USA for the 2019 and 2020 comparison has been made for the first 6 months of the year which shows the daily consumption for combined residential and non-residential loads [1]. The change in demand for residential and non-residential load for Illinois has been shown from March 3–April 30, 2020 [8] (Fig. 6).

## *3.3 Italy*

The COVID-19 pandemic had an unpredictable global impact on the energy sector. Italy is one of the most adversely affected countries in the world. The country's demand for electricity supply fell by 7.4% between January and April 2020 relative to its 2019 demand for electricity. Government of Italy enforced lockdown sequentially. The first phase started on March 6, 2020, by closing all the schools, training centers, and universities.

The second phase started on March 12, 2020, where companies and public buildings, and non-essential factories were closed (partial shutdown), and in the ultimate

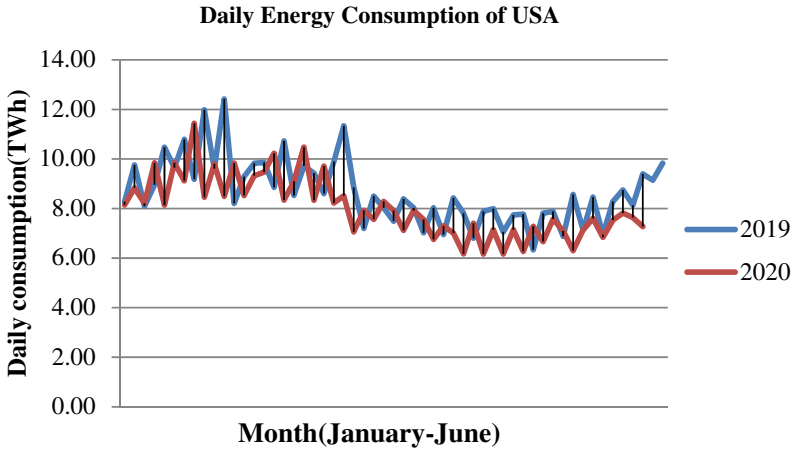


**Fig. 6** Daily electricity consumption of the USA [6]

phase, airports and seaports were closed to passenger traffic (shutdown) [9]. The lockdown led to a variation of the typical daily consumption curve pattern. Electricity usage went more steadily during the morning hours and peaks in the evening remained persisted (Fig. 7).

The study of the electricity mix fed into the national grid from January–April 2020 reveals that non-renewable energy generation meets 51% of national energy needs, with a decrease of −15.7% relative to 2019. Electricity generation from renewable energy exceeded a quota equal to 36% of energy needs, with a rise of 3% in the first 4 months of 2020 relative to the previous year [10]. Renewables were the only energy sources that saw a positive rise during the pandemic. Still, the consequences of the

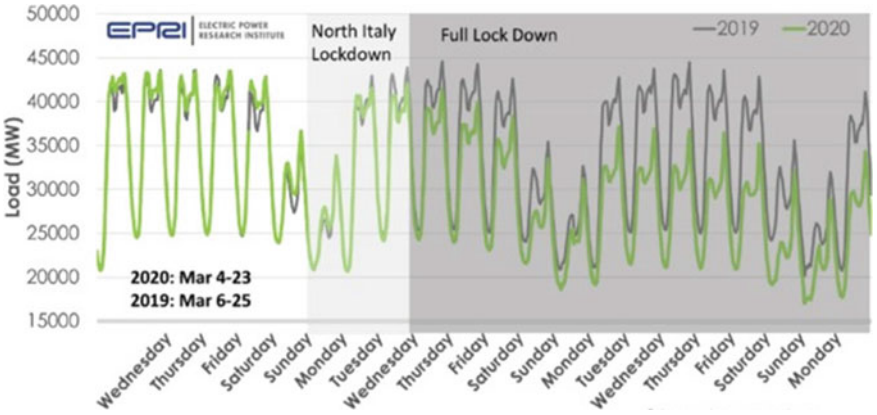


**Fig. 7** Load profile variations during the COVID-19 lockdown period in 2020 compared to the same in 2019 of Italy [5]

pandemic have also affected the clean energy market. As the lockdown prevailed, the cessation of manufacturing operations and technical disruptions in the supply chain drastically slowed down the development and start-up of new renewable energy projects. The lockdown has led to an intensive decrease in the development and start of new power plants, resulting in the cessation of manufacturing operations and logistical disruptions in the supply chain.

The Italian government included multiple incentive initiatives, mostly related to taxation, intended to promote and support energy conservation in buildings and electric cars to contain a decline in energy productions, in the latest Emergency Decree No. 34 dated May 19, 2020 (Decreto Rilancio). The decree law deducts 110% of expenditures for particular measures on energy-efficient structures, on the removal of seismic threats, and for relevant activities on the construction of photovoltaic systems and pillars to charge electric vehicles between July 1, 2020, and December 31, 2021 [11].

## 4 Impacts of COVID-19 on the Power Sector

The pandemic or COVID-19 has no direct effect on the Utility Industry. However, the changing of the lifestyle of the people during this pandemic changed the dynamics of the power generation-demand scenario. It has caused a huge shift in load demand and peak load hours. The reliability of the power system increased up to a certain extent, but the resiliency of the system is reduced in this situation. As various generating stations are put the generation of power is on hold, but the demand of the customer is increased throughout a very large region.

### *4.1 Voltage Regulation Issues*

In India, transmission lines are maintained at a varied range of voltage from 11 to 1200 kV. During this pandemic, the loads associated with large industrial sectors are declined significantly, whereas the loads associated with households has increased, which put the power grids at risk. Some of these are indirect or direct effects on any operation relating to the Power commercial and industrial operations have come to a halt and power demand has decreased significantly. To tackle this, many power transformers and transmission lines are made to run under loading conditions. This, however, has a direct consequence, especially for high-voltage lines. Regional Load Dispatch Center (RLDC) has issued certain measures to overcome this challenge: incorporating reactors while disconnecting the capacitor bank to prevent overvoltage at a consumer level, using STATCOM and Static VAR Compensator in Voltage mode. Additionally, Thermal generators were used to absorb extra reactive power during high voltage. Due to the precautionary measures taken, Voltage Deviation Index of major substations in India has shown a reduced operating level [12].

### 4.2 Frequency Profile

Due to the dynamic shift in the Power Demand, maintaining grid frequency within an acceptable band is a challenge. The huge difference in the load demand and supply has caused frequency instability and the grid frequency to deviate from standard 50 Hz. This phenomenon could cause generators to be out of synchronism and eventually the power system to collapse and black out [12]. In India, to tackle the frequency deviation issue, all the Region grids (Northern, Southern, Eastern, Western, and North-Eastern) ensured that their under frequency and df/dt load shedding are functional to prevent the cascading tripping of the power system due to any contingency [13]. Regular Inspection of the Under Frequency Relay (UFR) is done as well [14].

### 4.3 Reduction in Electricity Price

As a result of the reduced electricity demand and the decreasing prices of natural gas, oil, and coal, most electricity markets have observed a dramatic decline in the electricity bill, which lead to the Revenue disaster of the distribution companies [15]. The European and US electricity markets are seen to experience the most severe price drop in the world, with monthly average prices falling to their lowest.

### 4.4 Rise in Renewable Energy Uses

Power demand decrease has urged the Plant Operators to look for a cheaper and cleaner Power Source (Fig. 8).

Thus, in less than 10 weeks, the USA increased its renewable energy consumption by about 40% and India by 45%, Italy and other European countries by about 15%, and China by about 22% as given in the graph above [14]. The intermittent Renewables (Solar, Wind) posed a challenge in balancing the demand and supply; the non-intermittent Renewables (hydro, biomass, and geothermal) are much easier to deal with [16].

### 4.5 Cyber Security

The Covid-19 enforced worldwide lockdown. At that time, the operators of several organizations are working from their own places. This puts the utility industry vulnerable to cyber-attack. The attackers could hack the system from their remote places and may cause huge damage to the utility sector. To ensure safety from cyber attacks,

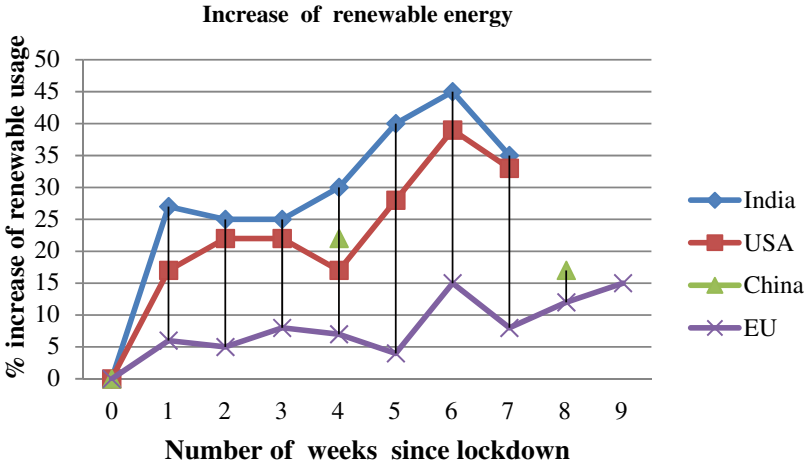


**Fig. 8** Percentage increase in renewable energy in different countries [14]

Utility Industry should possess a Defense Mechanism by changing its cyber security architecture [4].

### *4.6 Financial and Economic Losses*

Since the beginning of the lockdown to date, the stay-at-home policy has impacted the load profile immensely. The Domestic load has increased from 23.53 to 36.15% while the Industrial load has declined from 42.1% to 32.34%. Despite the increase in residential load, the Utility and Power Companies make their major profit from Industrial and Commercial load [4]. In India, this has caused the Revenue Loss of most Distribution Companies of almost INR 25,000–INR 30,000 crores.

## 5 Conclusion

The power system is the backbone of the industrial as well as financial sectors of any country. During the Covid-19 pandemic, the power sector witnessed an anarchy situation worldwide. This reason directly affects the GDP of all the countries in this situation. We expect the resilient power system to survive with low probability, and high-risk extreme cases including unusual natural disasters and man-made attacks. The COVID-19 pandemic sparked significant global market erosion, leading to a drastic drop in oil prices due to the lack of lockout demand. The pandemic sped up the demise of coal and other non-renewable resources and proved clearly that Renewable energy is robust in this market. A combination of past policies, legislation,

and technologies rooted in the power sectors of various forward-thinking countries handles the steady rise of renewable energy in the Grid.

This study is about how the outbreak of the novel Coronavirus affected the utility sector. It provides an insight into the demand variations and their impact on the stability of the power grid. Worldwide the power sectors have faced huge financial losses throughout the pandemic situation. Although the pandemic is incidental and unforeseen, the current result for the power sector isn't. A faster significant change for the power sector is triggered by the inter-related technology growth, regulations, and market conditions during COVID-19. The continuous expansion in sustainable power into the grid results from a combination of past policies, guidelines innovations, motivating forces, incentives, and developments embedded in the power sector of a much forward-thinking nation. By definition, the future is unpredictable, but there is a certain need for resilience.

## References


1. H. Zhong, Z. Tan, Y. He, L. Xie, C. Kang, Implications of COVID-19 for the electricity industry: a comprehensive review. CSEE J. Power Energy Syst. **6**(3), 489–495 (2020). https://doi.org/10.17775/CSEEJPES.2020.02500
2. Growth of Electricity sector in India from 1947–2019-by Central Electricity Authority, Minsirty of power, Government of India, http://cea.nic.in/dailygeneration.html. Accessed 17 Apr 2020
3. National Power Portal, India, https://npp.gov.in/publishedReports. Accessed 13 Dec 2020
4. R.M. Elavarasan, G.M. Shafiullah, K. Raju, V. Mudgal, M. T. Arif, T Jamal, S. Subramanian, V.S. Sriraja Balaguru, K S. Reddy, U Subramaniam, COVID-19: Impact analysis and recommendations for power sector operation. Appl Energy **279**, 115739 (2020), https://doi.org/10.1016/j.apenergy.2020.115739
5. E. Ghiani, M. Galici, M. Mureddu, F. Pilo, Impact on electricity consumption and market pricing of energy and ancillary services during pandemic of COVID-19 in Italy. Energies **13**(13), 3357 (2020), https://doi.org/10.3390/en13133357
6. G. Ruan, D. Wu, X. Zheng, H. Zhong, C. Kang, M.A. Dahleh, S. Sivaranjani, L. Xie, A cross-domain approach to analyzing the short-run impact of COVID-19 on the US Electricity sector. Joule **4**(11), 2322–2337 (2020). https://doi.org/10.1016/j.joule.2020.08.017
7. IEA, Global Energy Review 2020: The impact of the Covid-19 crisis on global energy demand and CO2 emissions (Apr 2020), https://www.iea.org/reports/global-energy-review-2020.
8. C. Burleyson, A.D. Smith, J.S. Rice, N. Voisin, A. Rahman, Changes in electricity load profiles under COVID-19: implications of "the new normal" for electricity demand (2020), https://doi.org/10.31224/osf.io/trs57
9. Power and people: How utilities can adapt to the next normal, https://www.mckinsey.com/industries/electric-power-and-natural-gas/our-insights/power-and-people-how-utilities-can-adapt-to-the-next-normal
10. The ratification of Law Decree No. 34/2020 ("Decreto rilancio") and Law Decree No. 104/2020 ("Decreto agosto"): measures in matter of employment, https://www.lexology.com/library/detail.aspx?g=4e526ccc-bc05-4925-9fdc-15a2f77c7d53
11. Impact of Corona Virus in India: An Economic Shock, https://fairgaze.com/fgnews/impact-of-corona-virus-in-india-an-economic-shock.html
12. Report of Expert Group to review and suggest measures for bringing power system operation closer to National Reference Frequency (vol. 1), Central Electricity Regulatory Commision ,November 2017, http://www.cercind.gov.in/2018/Reports/50%20Hz_Committee1.pdf

13. C.P. Reddy, S. Chakrabarti, S.C. Srivastava, A sensitivity-based method for under-frequency load-shedding. IEEE Trans. Power Syst. **29**(2), 984–985 (2013), https://doi.org/10.1109/TPWRS.2013.2288005
14. COVID-19 is a Game-Changer for Renewable Energy; Nelson Mojarro; World Economics Forum (2020), https://www.weforum.org/agenda/2020/06/covid-19-is-a-game-changer-for-renewable-energy
15. Discoms to suffer Rs 30K cr revenue loss, face Rs 50K cr liquidity crunch due to lockdown: CII, https://energy.economictimes.indiatimes.com/news/power/discoms-to-suffer-rs-30k-cr-revenue-loss-face-rs-50k-cr-liquidity-crunch-due-to-lockdown-cii/75197169
16. A. Werth, P. Gravino, G. Prevedello, Impact analysis of COVID-19 responses on energy grid dynamics in Europe. Appl Energy **281**, 116045 (2020), https://doi.org/10.1016/j.apenergy.2020.116045

# Electricity Price Forecasting Using LSTM Network and K-Means Clustering by Considering the Effect of Wind Power Generation


**Jyothi Varanasi and M. M. Tripathi**

## 1 Introduction

Global warming is a major concern to the world as power generation from conventional sources causes 30% environmental pollution [1]. Thus, renewable energy (RE) generation is gaining attention in the power sector, which is transforming the existing electricity market to an RE-enabled electricity market. The development of smart grids all over the world encourages large penetrations of wind and solar power generations [2]. In 2019, the total cumulative installed electricity generation capacity from wind power and solar power amounted to 600 GW and 300 GW, respectively [3]. Deregulation of the electricity market across the globe has enabled competition in generation, transmission and distribution due to which electricity market price suffers from high volatility [4]. This makes both suppliers and consumers more interested in devising future electricity price strategies as electricity price forecasting assists the suppliers in trading and bidding of electricity and consumers can systematically manage their utilization of electricity [5].

Electricity price is strongly related to physical characteristics of a power system such as loads, meteorological conditions, fuel price, unit operating characteristics, emission allowances and transmission capacity, and power generation. Electricity price is highly volatile, and the electricity market experiences price dynamics due to its unique features such as non-storability and the need for power system stability. The major causes of the volatility of the modern electricity market include load uncertainty, fuel prices and its availability, intermittent nature of wind power and solar power generations, irregularity in hydro-electric production, unplanned outages, transmission constraints, etc. [6]. Further, the price forecasting in today's electricity market, amid wind and solar power penetrations, is a highly challenging one [7–10].

Many methods are used for short-term price forecasting by implementing various statistical, learning and hybrid models. Wavelet neural network with data filtering is

J. Varanasi (✉) · M. M. Tripathi
Electrical Engineering Department, Delhi Technological University, Delhi, India



C. K. Chanda et al. (eds.), *Advanced Energy and Control Systems*, Lecture Notes in Electrical Engineering 820, https://doi.org/10.1007/978-981-16-7274-3_3

proposed for price forecasting in the deregulated electricity market. Wavelet decomposition is used to partition loads at different frequencies. For decomposed loads at different frequencies, separate neural networks are applied and results are combined finally to get the complete error [11]. A hybrid approach of relevance vector machine and extreme gradient boost is proposed and proved to be the best one among various models like multilayer perceptron (MLP), recurrent neural network (RNN), relevance vector machine (RVM), random forest, support vector machine (SVM) and LASSO with the computation of confidence interval [12]. The extreme learning machine-bootstrap method is employed for probabilistic forecasting of electricity price. Reliability and sharpness are considered in the evaluation of the hybrid approach. The forecasting uncertainty is evaluated with model uncertainty and the data noise [13]. The input–output hidden Markov model (IOHMM) is proposed to forecast electricity prices with good accuracy and to provide dynamic information of the market [14]. A rigorous analysis on electricity price forecasting is carried out with the RNN–Elman network and various models like ARIMA, wavelet ARIMA, fuzzy neural network, radial basis function neural network, adaptive wavelet neural network and hybrid intelligent system [15].

This paper proposes a hybrid approach using the LSTM network and k-means clustering for short-term electricity price forecasting to investigate the effect of wind power penetration on electricity price forecasting. The historical electricity price, load, wind power generation and solar wind power generation data of the year 2016 of the Austrian electricity market has been used in this work. The accuracy of the proposed model is compared with FNN-PSO and SVR models. The simulation results show that the proposed model is superior to the other two models in forecasting the price, and the accuracy improves further with consideration of wind power generation.

The rest of the paper is organized into five sections. Section 2 describes the techniques used in price forecasting. Section 3 presents the methodology of the proposed model. Section 4 presents simulation and results, and Sect. 5 concludes the paper.

## 2 Techniques Used in Price Forecasting

The various techniques such as k-means clustering, recurrent neural network and LSTM network used in this paper are described below.

### *2.1 K-Means Clustering*

The aim of any clustering technique is to achieve the intrinsic grouping of a set of data with large variations. K-means is one of the simplest unsupervised learning algorithms. This algorithm resolves clustering problems. Being a method of vector

quantization, it gained wide popularity for cluster analysis in data mining [16]. The crucial steps involved in the algorithm are as follows:

I. Partition of the data into K number of non-empty subsets.
II. Identifying the cluster centroids (mean points) of the current partition.
III. Allotting each individual to a specific cluster.
IV. Computing the distance from each individual to its own cluster mean and other clusters.
V. Allotting the individuals to a cluster based on minimum distance from the centroid.
VI. After re-allotting the individuals, find the centroid of new clusters framed.
VII. Repeat steps 4, 5 and 6 until no more relocations occur.

The algorithm can be presented mathematically as follows.
Consider D is a set of n vectors

$$\text{i.e.} \qquad D = \{X_1, X_2, X_3, .....X_i....X_n\} \tag{1}$$

where $X_i$ represents each record as an m-dimensional vector.

$$X_i = \{X_{i1}, X_{i2}, X_{i3}, .....X_{im}\} \tag{2}$$

$$C_j = cluster(X_i) = \arg_j \min \left\| X_i - \mu_j \right\|^2$$

'arg min' indicates the argument of the minimum and $\mu$ indicates the mean point of a specific cluster.

$$Distortion = \sum_{i=1}^{n} (X_i - C_i)^2 \tag{3}$$

The distortion is minimized by partially differentiating Distortion with respect to each cluster center and is equated to zero.

In this work, to handle the high volatility of electricity prices and to forecast them with higher accuracy, clustering has been performed in two ways. Conventionally, the electricity price is much dependent on the load demand of the region. Considering the RE-enabled electricity market, wind power generation is one more feature chosen for clustering. Firstly, the days of the year are clustered into three groups based on similar wind power pattern. To achieve this, a data set of maximum wind power, minimum wind power and average (mean) wind power of the day for all days of the year is prepared as per Eq. 4 and then k-means is applied to partition the data. Secondly, the days of the year are clustered into three groups based on similar load patterns. In order to partition the data into three groups, a data set of maximum load, minimum load and average (mean) load of the day is prepared as per Eq. 5, for which, k-means is applied to finally split the whole year data into three groups [17, 18].

$$D_1 = [WP_{\max}, WP_{\min}, WP_{mean}] \tag{4}$$

$$D_2 = [L_{\max}, L_{\min}, L_{mean}] \tag{5}$$

where $WP_{\max}$, $WP_{\min}$, $WP_{mean}$ represent the day's maximum, minimum and average values of wind power generation, respectively. Similarly, $L_{\max}$, $L_{\min}$, $L_{mean}$ represent maximum, minimum and average values of the load for the day.

## 2.2 Recurrent Neural Networks

Conventional neural networks presume all the inputs and outputs are independent of each other. However, RNNs take the advantage of sequential information. RNNs retain the information in each state and are used for the next state. As shown in Fig. 1, RNN has a unique structure with a chain of repeating modules [13, 15].

A rolled RNN and an unrolled RNN are shown in Fig. 1 [19]. Accordingly,

I. $u$, $v$ and $w$ represent weights of input, output and neuron connections, respectively, in the neural network.
II. At time step t,$x_t$ is the input.
III. Also at time step t, $s_t$ indicates the hidden state. It replicates the memory of the network. Considering the current step input and previous hidden state, $s_t$ is calculated as $s_t = f(ux_t + ws_{(t-1)})$
IV. In general, the function f represents a non-linear function Ex. tan h.
V. The first hidden state is computed from $s_{-1}$ which is initialized to all zeroes.
VI. $o_t$ is the output at step t: $o_t = soft\max(vs_t)$, where *softmax* is the activation function.
VII. Here, $s_t$ captures information from all previous time steps.

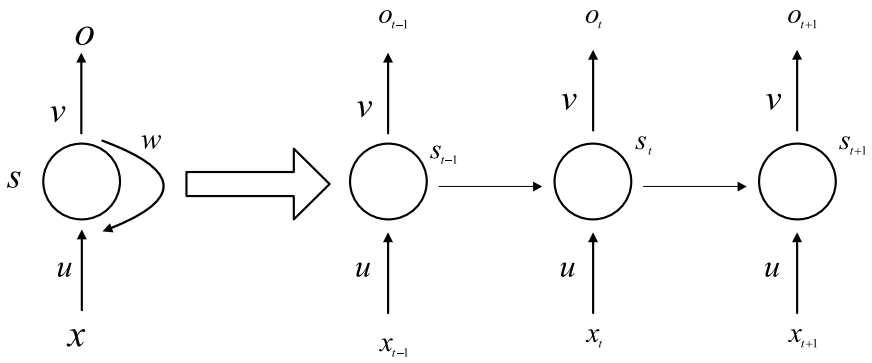


**Fig. 1** An unrolled RNN

VIII. The output is computed as per the memory at time t.
IX. An RNN implements the same $u$, $v$ and $w$ for all steps, hence reducing the number of network parameters.
X. The important feature of an RNN is its hidden state that retains the information of a sequence.

Due to some limitations of RNNs in handling long-term dependencies, LSTMs grab the attention to address the issue.

## 2.3 LSTM Networks

LSTM networks are considered to be special ones among RNNs, which can learn long-term dependencies. The networks have the capability to remember information for a long time. LSTMs have a similar structure to RNN with the difference in the internal structure of repeating modules as shown in Fig. 2. The repeating module has four layers unlike standard RNNs, which have a single layer.

As shown in Fig. 2, the internal module performs four important tasks.

Task 1: It decides on retaining the old information. The output is obtained as per Eq. 6 for each number in the cell state and varies from 0 to 1.

$$f_t = \sigma(w_f.[h_{(t-1)}, x_t] + b_f) \tag{6}$$

where $\sigma$ represents the *sigmoid* function.

Task 2: It stores new information in the cell state.

It has two parts.

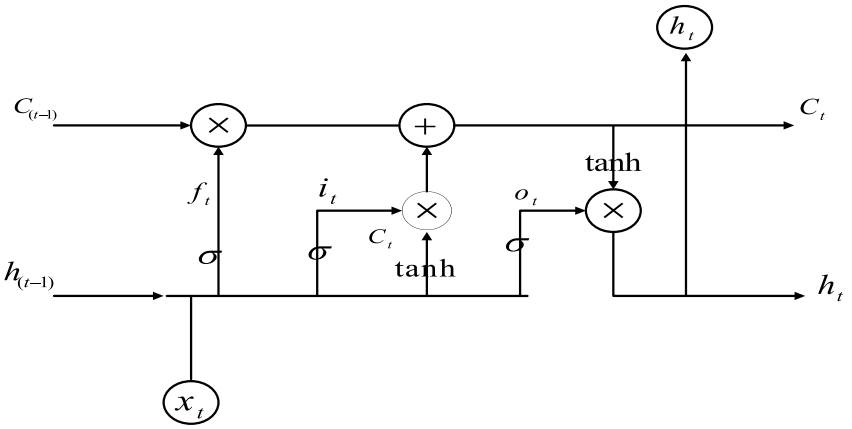


**Fig. 2** Internal structure of LSTM network

I. A sigmoid layer decides the values to be updated. The output $i_t$ is presented in Eq. 7.

$$i_t = \sigma(w_i.[h_{(t-1)}, x_t] + b_i) \tag{7}$$

II. The layer computes a vector of new values, i.e. $\tilde{C}_t$ as per Eq. 8.

$$\tilde{C}_t = \tanh(w_c.[h_{(t-1)}, x_t] + b_c) \tag{8}$$

Task 3: It combines $i_t$ and $\tilde{C}_t$.

Task 4: New cell state $C_t$ is computed by updating the old cell state $C_{(t-1)}$ as per Eq. 9.

$$C_t = f_t * C_{(t-1)} + i_t * \tilde{C}_t \tag{9}$$

Finally, the output is obtained as per Eqs. 10 and 11.

$$o_t = \sigma(w_o.[h_{(t-1)}, x_t] + b_o) \tag{10}$$

$$h_t = o_t * \tanh(C_t) \tag{11}$$

## 3 Methodology

### *3.1 The Proposed Model*

The proposed model is presented in Fig. 3 through a flow chart. The data of the Austrian electricity market is collected and normalized after pre-processing it. The data consists of hourly data of historical electricity price, load, wind power generation and solar wind power generation of the year 2016. A data set of the days of similar load patterns is clustered into three groups by using the k-means clustering technique. This clustering is performed by considering three parameters such as maximum load, minimum load and average (mean) load of the day. A data set of 30 similar days to forecasted days are fed to the LSTM network where it is used for training the network. Various parameters of the LSTM network such as the number of neurons of the network layers and epochs as mentioned in Table 1 and are optimized with the grid search method. After the training is complete, a separate data set is used for testing and forecasting electricity prices. In this paper, electricity price a day ahead is forecasted.

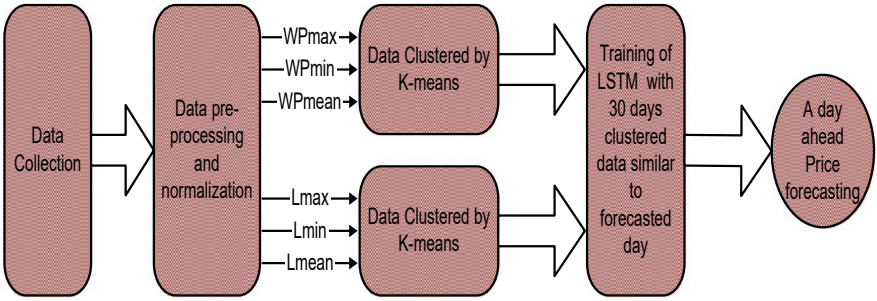


**Fig.3** A proposed hybrid approach

**Table 1** Parameters of LSTM model

| Parameters | Values |
|---|---|
| Layers of LSTM | 2 |
| Number of neurons in layer 1 | 10 |
| Number of neurons in layer 2 | 50 |
| Optimizer | Adam |
| Loss function | Mean squared error |
| Epochs | 180 |

## *3.2 SVR and FNN-PSO Models*

To emphasize the performance of the proposed model in short-term price forecasting, SVR and FNN-PSO models are compared to the proposed model. The SVR and FNN-PSO models are designed by tuning their various parameters [20]–[26]. The optimized values of the parameters are depicted in Tables 2 and 3. The parameters listed in Table 2 are optimized by applying the grid search method.

**Table 2** Parameters of SVR model

| Parameters | Values |
|---|---|
| Kernel | Rbf |
| Regularization parameter © | 1 |
| Gamma | 0.1 |
| Tolerance | 0.00001 |

**Table 3** Parameters of FNN-PSO model

| Parameters | Values |
|---|---|
| Network layers | 3 |
| Hidden layer neurons | 5 |
| Population in PSO | 10 |
| Number of iterations | 1000 |
| Tolerance | $10^{-15}$ |

## 4 Simulations and Results

The historical data of the Austrian electricity market for the year 2016 is used in the work carried. The data is pre-processed for the set of data that contains hourly data of load, wind power generation, solar power generation and electricity price. As the data consists of different features of different ranges, hence, it is normalized to values less than or equal to 1. With the computation of correlation factors, it is analyzed that wind power is a highly correlated parameter to price than solar power after the load demand. The contribution of solar power generation to the grid is also very marginal. Thus, this work only focuses on the impact of wind power on electricity prices. Then similar days of the year are clustered as per wind power generation into three clusters. Later, similar days of the year as per load demand are clustered into three clusters. Then 30 days of clustered data based on wind power similar to forecasted day is considered for proper training of the LSTM network to forecast a day-ahead electricity price of September 6, 2016. The clustered data based on load is also used for training to compare the accuracy of forecasting. Without applying clustering also, the same day's price is forecasted by training LSTM with previous 30 days data. Similarly, using the SVR model and the FNN-PSO model, the same day price is forecasted after training the models with previous 30 days' data. To analyze the impact of wind power generation on electricity price forecasting, by only considering load as input, the model is trained and tested for the prediction of electricity price of the same day, and the forecasting accuracy is compared to the accuracy of price forecasting, when both load and wind power are considered as input.

To evaluate the performance of forecasting models, three important evaluation factors are used. They are mean absolute percentage error (MAPE), mean absolute error (MAE) and root mean squared error (RMSE).

$$MAE = \frac{1}{N}\sum_{i=1}^{N} |A_i - F_i| \tag{12}$$

$$MAPE = \frac{1}{N}\sum_{i=1}^{N} \left| \frac{A_i - F_i}{A_i} \right| \tag{13}$$

**Table 4** MAPE, MAE and RMSE values of a day-ahead price forecasting

| Approach | Input parameters | MAPE | MAE | RMSE |
|---|---|---|---|---|
| LSTM-K-means (based on load) | Load and wind power | 8.29 | 2.90 | 4.01 |
| LSTM-K-means (based on load) | Load | 10.37 | 3.63 | 4.72 |
| LSTM-K-means (based on wind power) | Load and wind power | 12.16 | 4.26 | 5.67 |
| LSTM-K-means (based on wind power) | Load | 12.51 | 4.38 | 6.07 |
| LSTM model | Load and wind power | 12.71 | 4.46 | 6.05 |
| SVR | Load and wind power | 13.75 | 4.82 | 6.61 |
| FNN-PSO | Load and wind power | 16.18 | 5.67 | 7.65 |
| FNN-PSO | Load | 18.17 | 6.37 | 7.63 |

$$RMSE = \sqrt{\frac{1}{N}\sum_{i=1}^{N}(A_i - F_i)^2} \tag{14}$$

In Eqs. 12, 13 and 14, $A_i \, and \, F_i$ represent actual and forecasted values, and N indicates the total number of samples of the forecasting period. As per Eq. 13, MAPE is widely used to evaluate the performance of any forecasting method. In price forecasting, the same may not work properly sometimes as the actual value is zero; MAPE would be infinity. Even large actual values also make improper MAPE computation. Thus, as per the modified equation in Eq. 15, MAPE is computed in the present work. The results are depicted in Table 4.

$$MAPE = \frac{1}{N}\sum_{i=1}^{N}\left|\frac{A_i - F_i}{\overline{A}}\right| \tag{15}$$

where $A_i \, and \, F_i$ are the actual and forecasted values and $\overline{A}$ represents the average value of N number of actual values.

The plot in Fig. 4 compares actual prices to predicted prices of the proposed model and the LSTM network on the day of prediction. It is clearly evident that the predicted price curve of the proposed model is closer to the actual price curve. The second plot in Fig. 5 compares the predicted price curve of the proposed model (LSTM and k-means) to the predicted price curve of other models such as the SVR model and the FNN-PSO model and depicts the best accuracy by the proposed model. The best performance of the proposed model is also depicted by errors computed and presented in Table 4. In this work, clustering of data is performed in two cases using the k-means clustering technique. Based on wind power variations also, the whole data is clustered and based on load variations also the data is clustered into three groups. The implementation of clustered data based on load has reported better forecasting

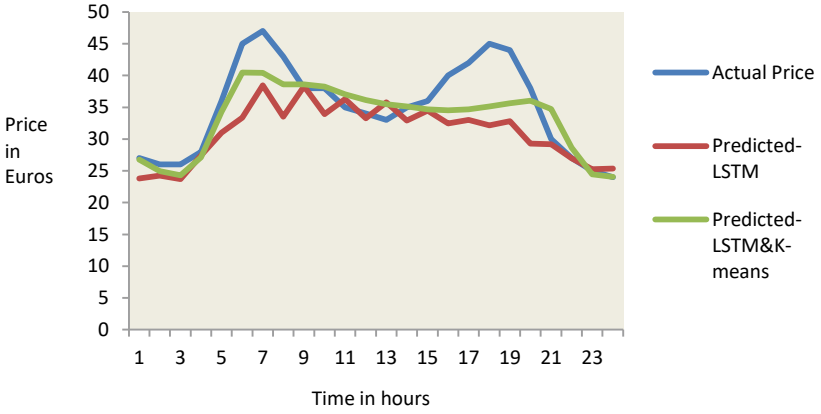


**Fig.4** Predicted price versus actual price on September 6, 2016

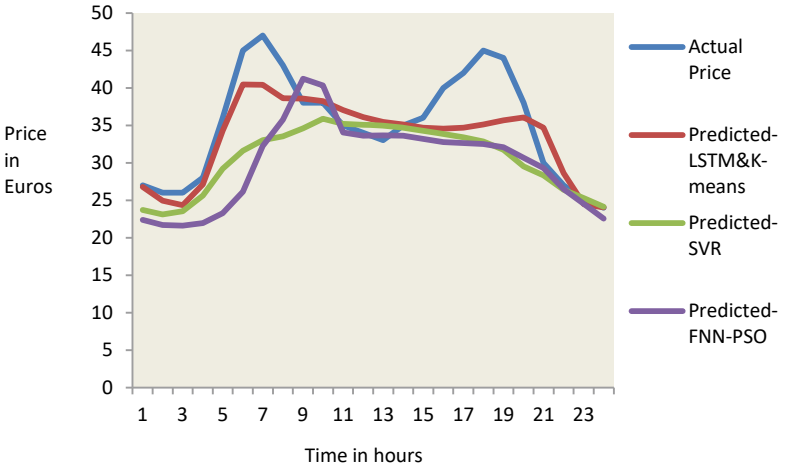


**Fig.5** Predicted price versus actual price on September 6, 2016

performance with higher accuracy as presented in Table 4. There is a significant error reduction in terms of MAPE, MAE and RMSE in price forecasting using the proposed model when the model performs clustering according to load variations. The errors are lowest for the proposed model among all the models with minimum MAPE, i.e. 8.29%. The proficiency of the proposed model is further illustrated with the computation RMSE, which is the lowest among all models. The proficiency of the SVR model is superior to the FNN-PSO model and inferior to the proposed model. The plots in Figs. 6 and 7 clearly indicate the improvement in forecasting accuracy with the consideration of wind power as input, which is a right indication of the impact of wind power generation on electricity price forecasting for the renewable

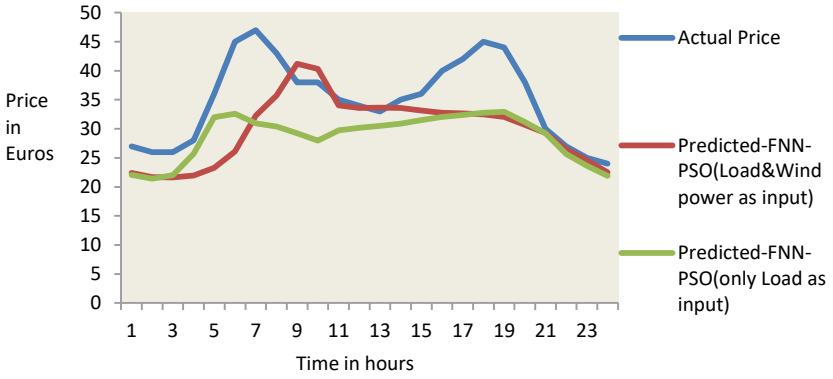


**Fig.6** Predicted price versus actual price on September 6, 2016

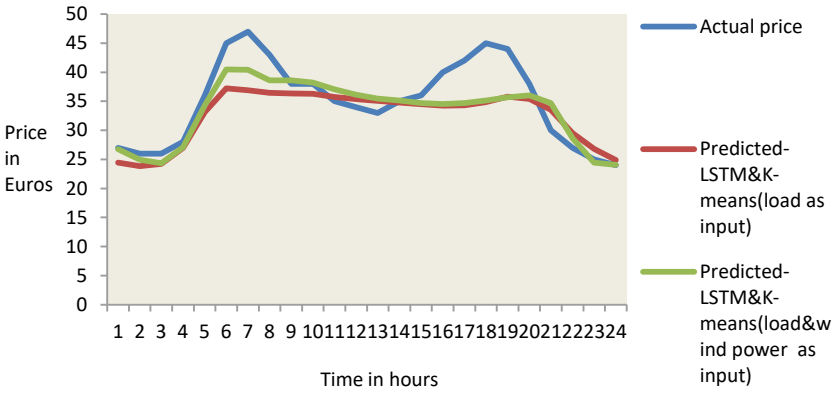


**Fig.7** Predicted price versus actual price on September 6, 2016

energy-enabled electricity market. The improvement in forecasting accuracy also depends on the contribution of wind power generation to the power grid on the respective day of price forecasting.

## 5 Conclusion

Electricity price is a special commodity unlike any other commodity in the market. Its storage is not an easy task. It is influenced by many factors like load demand, power generations, time factor, industrial requirements, weather conditions, fuel prices, transmission constraints, etc. Thus, the electricity market experiences a lot of fluctuations making prices highly volatile. One of the recent concerns for the volatility is power generation from renewable energy sources. The work carried in

this paper has suggested a suitable hybrid approach using k-means clustering and the LSTM network for short-term electricity price forecasting showing its proficiency in accurate price forecasting amid wind power penetration. The impact of wind power generation on price forecasting has been analyzed and results depicted that the impact of wind power generation on the accuracy of price forecasting is significant with the considerable reduction in errors. However, it is also noticed that the contribution of wind power generation to the grid also matters in the forecasting period. Further, the scope is left for implementing any other clustering technique other than k-means for future research and to analyze the impact of solar power generation also on price forecasting.

## References

1. J. Varanasi, M.M. Tripathi, A comparative study of wind power forecasting techniques–a review article, in *Proceedings of the 10th INDIACom; INDIACom-2016* (March 2016), pp. 16–18
2. M. Rambabu, G.V. Nagesh Kumar, S. Sivanagaraju, Optimal power flow of integrated renewable energy system using a thyristor controlled series compensator and a grey-wolf algorithm. Energies **12**(11), 2215 (2019)
3. A.S. Anees, Grid integration of renewable energy sources: challenges, issues and possible solutions, in *IEEE 5th India International Conference on Power Electronics (IICPE)*, (6–8 Dec. 2012)
4. M.M. Tripathi, A.K. Pandey, D. Chandra, Power system restructuring models in the Indian context. Electr. J. **29**, 22–27 (2016)
5. M. Shahidehpour, M. Alomoush, Restructured electrical power systems operation, trading and volatility (Marcel Dkker,Inc., New York.Base, 2001)
6. A Mishra, G.V. Nagesh. Kumar, S.K. Bali, Optimized utilization of interline power flow controller in an integrated power system. World J. Eng. **17**(2), 261–266 (2020)
7. X. Li, L. Gao, G. Wang, F. Gao, Q. Wu, Investing and pricing with supply uncertainty in electricity market: a general view combining wholesale and retail market. Smart Grid Communications, China Communications (2015)
8. J. Lin, W. Yu, X. Yang, Towards multistep electricity prices in smart grid electricity markets. IEEE Trans. Parallel Distrib. Syst. **27**(1) (2016)
9. J.J. Sánchez, D.W. Bunn, E. Centeno, J. Barquín, Dynamics in forward and spot electricity markets. IEEE Trans. Power Syst. **24**(2) (2009)
10. M.M. Tripathi, S.N. Singh, K.G. Upadhyay, Price forecasting in competitive electricity markets: an analysis, in *IEEE International Conference on Energy Engineering (ICEE-2009), Pondicherry, India* (2009)
11. A.K. Pandey, D. Chandra, M.M. Tripathi, Short-term price forecasting using new wavelet-neural network with data pre filtering in ISO New England market, in *International Conference on Emerging Trends in Electrical, Electronics and Sustainable Energy Systems (ICETEESES–16)*, (11–12 Mar. 2016)
12. R.K. Agrawal, F. Muchahary, M.M. Tripathi, Ensemble of relevance vector machines and boosted trees for electricity price forecasting. Appl. Energy **250**, 540–548 (2019)
13. C. Wan, Z. Xu, Y. Wang, Z.Y. Dong, K.P. Wong, A hybrid approach for probabilistic forecasting of electricity price. IEEE Trans. Smart Grid **5**(1) (2014)
14. A.M. González, A.M.S. Roque, J. García-González, Modeling and forecasting electricity prices with input/ output hidden markov models. IEEE Trans. Power Syst. **20**(1) (2005)
15. S. Anbazhagan, N. Kumarappan, Day-ahead deregulated electricity market price forecasting using recurrent neural network. IEEE Syst. J. **7**(4) (2013)

16. W. Wu, M. Peng, A data mining approach combining *K*-means clustering with bagging neural network for short-term wind power forecasting. IEEE Internet of Things J. **4**(4) (2017)
17. C.-M. Huang, S.-J. Chen, S.-P. Yang, C.-J. Kuo, One-day-ahead hourly forecasting for photovoltaic power generation using an intelligent method with weather-based forecasting models. IET Gener. Transm Distrib. **9**(14), 1874–1882 (2015)
18. J. Varanasi, M.M. Tripathi, K-means clustering based photo voltaic power forecasting using artificial neural network, particle swarm optimization and support vector regression J. Inf. Opt. Sci. **40**(2) 309–328 (2019)
19. P. Liu, X. Qiu, X. Huang, Recurrent neural network for text classification with multi-task learning, in *Proceedings of the Twenty-Fifth International Joint Conference on Artificial Intelligence (IJCAI-16)* (9–15 July 2016)
20. J. Shi, W.J. Lee, Y. Liu, Y. Yang, P. Wang, Forecasting power output of photovoltaic systems based on weather classification and support vector machines. IEEE Trans. Ind. Appl. **48**(3) (2012)
21. J. Varanasi, M.M. Tripathi, Performance comparison of generalized regression network, radial basis function network and support vector regression for wind power forecasting. Int. Rev. Model. Simul. (I.R.E.MO.S.) **12**(1) (2019)
22. J. Varanasi, M.M. Tripathi, Artificial Neural Network based wind speed & power forecasting in US wind energy farms, in *IEEE 1st International Conference on Power Electronics, Intelligent Control and Energy Systems (ICPEICES)*, (4–6 July 2016)
23. AK Choudhary, KG Upadhyay, MM Tripathi (2012) Soft computing applications in wind speed and power prediction for wind energy, in *IEEE Fifth Power India Conference*, (19–22 Dec. 2012)
24. D.K. Chaturvedi, M. Mohan, R.K. Singh, P.K. Kalra, Improved generalized neuron model for short-term load forecasting. Soft Comput. **8**, 10–18 (2003). (Springer)
25. A. Yona, T. Senjyu, T. Funabashi, C.-H. Kim, Determination method of insolation prediction with fuzzy and applying neural network for long-term ahead PV power output correction. IEEE Trans. Sustain. Energy **4**(2) (2013)
26. Y.K. Semero, J. Zhang, D. Zheng, PV power forecasting using an integrated GA-PSO-ANFIS approach and gaussian process regression based feature selection strategy. CSEE J. Power Energy Syst. **4**(2) (2018)

# Solid Waste Management Challenges in India


**Shraddha Sharma**

## 1 Introduction

In India, the problem of solid waste management is getting bigger and bigger especially in urban areas. India's economic growth has led to the establishment of new industries, and urbanization is increasing at a very rapid pace. This has significantly changed the lifestyle of Indian citizens. In comparison to the developed nation, the per capita solid waste generation in India is quite low but inefficiency in dealing with the collection, transportation and disposal has posed a high risk to the environment as well as the health of the people. The waste generation rate is rising at a horrible speed. Total waste generated by 2050 is expected to become 3.4 billion tonnes per year as compared to the current generation of nearly 2 billion tonnes per year [1]. Due to rapid growth in population and industrialization, yearly waste generation will increase by 70% as compared to 2016. Kuwait produces the maximum solid waste in the world amounting to 5.72 kg per day per capita but due to the policies of Kuwait, this value is expected to reduce to 4 kg per day per capita. In India, the amount of solid waste generated every year is about 960 million tonnes [2]. In India, the largest MSW producing city is Delhi while the least MSW producing city is Agra. It is observed that in general, the quantity of MSW produced depends on the population of the city but the population of Delhi is less as compared to that of Mumbai. Hence, there are some other factors that contribute towards solid waste generation. In this article, Sect. 2 is about the literature review while in Sect. 3, various methods of solid waste management used in India have been explained. In Sect. 4, the collection and transportation strategies have been discussed. Section 5 presents a detailed comparison among various countries about the disposal methods and waste management techniques. Section 6 discusses about the future of solid waste management in

S. Sharma (✉)
Department of Civil Engineering, IILM-College of Engineering and Technology, Greater Noida, India
e-mail: shraddha.sharma@iilm.edu



C. K. Chanda et al. (eds.), *Advanced Energy and Control Systems*, Lecture Notes in Electrical Engineering 820, https://doi.org/10.1007/978-981-16-7274-3_4

India and its progress towards efficient solid waste management. Suggestions and conclusions are presented in Sect. 6.

## 2 Literature Review

According to Nandan et al. [3], India cannot bear ineffective SWM because it is one of the fastest growing economies in the world. Although many effective policies are available for waste treatment but only on paper due to political and executive will. This is creating an alarming situation. The authors suggest the adequate implementation of the provisions mentioned in MSW Rules 2000. Inefficient waste management must be replaced by scientific methodologies. The role of public awareness is equally important in the maintenance of cleanliness in the city and solid waste management because public awareness helps a lot in maintaining rules and regulations about the SWM. Public awareness is also helpful in improving environmental conditions and human health. Although solid waste management methods are improving, their speed needs to be accelerated. New technologies can be highly supportive in improving the quality of SWM.

Pamnani and Sriniwasrao [2] provided an overview of MSW management in big cities, medium and small towns. Collection of solid waste is done by door-to-door collection while waste collection from slums and commercial complexes is done separately as per the MSW Management Rules 2000. The collection is done keeping in mind the minimization of the cost of transportation while maintaining the environmental constraints. Management of solid waste in metro cities poses one of the most challenging tasks because such cities are facing grave problems related to pollution due to a large amount of solid waste generation. In most of the cities, MSW from households is deposited at the local bins from where it is transferred to the community bins and then sent to the landfill sites. In India, rag pickers are a significant component of the Municipal Solid Waste Management system as they pick reusable and recyclable waste from the heap. Despite declared rules and regulations of depositing and collecting the waste in most of the parts, the waste is dumped on the roads due to inadequate solid waste storage capacity. According to the census of 2011, nearly 71% of the population resides in villages. In villages, most of the waste generated is biodegradable, and hence, disposable solid waste is quite less as compared to the small towns. Hence, for better management, the interface can be established between small towns and nearby villages.

According to the Waste Management Handbook [4], Municipal Solid Waste Rules 2000 made it mandatory for municipal authorities to establish facilities for disposal, processing and identification of sites for sanitary landfill and improvement in current dumpsites of solid waste. The Environment Protection Act 1986 deals with environment protection and helped in preparing a framework for managing hazardous solid waste. Biomedical waste management rules were formed in 1989 and then amended in 2000 and later in 2003. E-waste management was formed in 2011 to deal with electronic waste.

ICRIER in April 2018 [5] analysed the sustainability of SWM under financial and environmental aspects. The paper presented the assessment about the rapidly growing amount of MSW, its change in composition and the practice of mingling dry waste with biodegradable waste. The paper also described the emission of greenhouse gases from solid waste. SWM rules of 2016 provide an efficient framework for dealing with the MSWM in India. It is suggested that local authorities should be empowered to encourage citizens' participation to minimize the challenges of global warming and public health. In 2014–15, the annual MSW generation was 52 Million Tonnes while in 2017, it became 72 Million Tonnes. Only construction and demolition contribute to about 30% of the total waste. Among the six largest metropolitan cities in 2016, Delhi generates 9260 tonnes per day while Hyderabad generates 4000 tonnes per day, and together both the cities produce 21% MSW of all the cities in India while they contribute only 16% of the total population. Biodegradable waste is one of the major components of MSW and it is decomposed by using suitable bacteria. Aerobic decomposition is vital in breaking organic waste into water, carbon dioxide and compost as produced in this process which enhances the fertility of the soil.

Agrawal et al. [6] suggested that a number of private companies are providing brilliant solutions to manage MSW. Subhash Project and Marketing Limited (SPML) is involved in collecting, transporting and disposing of Hazardous as well as Municipal waste. This company is also involved in recycling and segregation of MSW as well as sanitary landfill management and construction. A US-based company is involved in sewer rehabilitation. HCL is working on the recycling of electronic waste. For this purpose, HCL has created an online registration form where individuals or corporations can make a request for the same, irrespective of their purchase place. Nokia India has launched an attractive take back scheme where people can drop their old electronic goods for recycling or scientific disposal and win gifts on behalf of the company. The main problem in dealing with various types of waste is segregation and collection at source, little awareness among people, etc. Developing countries, apart from the above problems, have to face a financial crisis because they cannot apply expensive technologies suggested by the developed nations.

## 3 Methods of Solid Waste Management in India

Although all types of wastes are harmful to humans as well as the environment, municipal solid waste can be managed suitably without creating any pollution or harm to the environment, animals or humans. A number of methods are used to deal with solid waste in making energy or compost.

### 3.1 Sorting

After the waste is generated through various sources, sorting is required to separate the materials which can be recycled and hazardous materials can be dealt with separately [7]. The sorting reduces the waste to be filled in landfills, and the separation of reusable materials prevents them to recombine with the waste stream [8]. Sorting can be done at our houses, bins placed by the municipal corporations, central sorting facility, at processing sites or at landfill sites. The sorting in India is usually carried out by either recycling middlemen (Kabadiwala), rag pickers, wholesale dealers or recycling factories. Sorting can be done manually or by semi or fully automatic machines.

### 3.2 Storage

Almost every commercial or non-commercial establishment produces waste and its safe storage is essential before collection. If a proper storage facility is not available, the waste will litter on the roads which will pose a problem for public health and pollute the environment. In lack of proper storage facility, in most parts of India, the waste is thrown on the roads or in municipal sewers or drains which blocks the flow of water. This causes extra cost in maintaining the cleanliness. In order to avoid such a situation, people must be educated to store the waste at the source according to the size and types of waste. They should learn the directions provided by the local municipal bodies for the disposal of various types of solid wastes. People should participate in clean drive activities not only on special occasions but on weekly basis to learn techniques and help educate other people. Local authorities can explain about how to separate recyclable, non-recyclable and biodegradable waste [9].

### 3.3 Collection of Waste

In India, waste is collected mostly daily in many parts from door to door. Biodegradable waste should be collected on a daily basis due to climatic conditions in India but recyclable waste may be collected at longer time intervals because they do not usually decay. Sometimes hazardous waste is also produced in households but in very less amount as compared to the industries; hence, they may also be collected at longer time intervals. But once collected, such wastes can be put in the central bins provided by the municipal corporation for the assigned purpose.

### 3.4 Recycling

Recycling is an important method to avoid waste production because a product causes 95% of the environmental impact before discarding [7, 10]. If the waste is not separated at the source level, it becomes very difficult to recycle with added cost and effort. Mixed waste is neither useful for recycling nor in the generation of energy, such waste is usually burnt instead of dumping into landfills. Hence, the separation of waste at the source level will play a significant role in solid waste management which will not only save cost but will also save time and will be fruitful in reuse and recycle.

### 3.5 Compost Formation by Aerobic Digestion

Aerobic digestion is a process in which organic materials are decomposed in presence of oxygen and suitable living organisms. In this process, compost is obtained which can be used as fertilizer for agricultural land. The main problem in this process is that sometimes the compost obtained by this process consists of heavy metals which are harmful to the environment, and hence, it has restricted use in agriculture [11].

### 3.6 Energy Generation

Energy generation is a process of producing chemical energy in MSW. Chemical energy stored in wastes is a fraction of input energy expanded in making those materials. There are a number of methods to convert MSW into electricity but the most common method is mass burning of solid waste in big incinerators. These are connected to the boilers which generate steam. The steam rotates turbine blades to produce electricity. Sometimes, the solid waste is converted to fuel pallets to be used in small-scale power plants. Electricity generation by the burning of solid waste includes steps which include (1) Dumping of MSW from garbage trucks into large pits, (2) This waste is dumped into the combustion chamber using a crane with giant claw, (3) The burning waste releases heat, (4) The heat produced turns boiler water into high-pressure steam, (5) The steam rotates turbine blades to produce electricity, (6) Pollutants are removed from the combustion gas before releasing through the chimney and (7) Ash produced in the boiler is removed before reloading it. The advantage of this process includes a reduction in the volume of the waste and fly as produced is used in the construction of roads and cement production [12]. Another waste-to-energy method is gasification which reduces the volume of waste by 95% and produces less emission as compared to the incineration process [13]. In addition to incineration and gasification technologies, microbial fuel cells

and microbial electrolysis cells can convert MSW into electricity and hydrogen gas (Figs. 1 and 2).

Organic as well as inorganic material is found in municipal solid waste. Organic material contains latent energy which can be extracted by suitable technologies for waste treatment. Energy can be extracted from the biodegradable as well as a non-biodegradable organic matter either by thermo-chemical conversion or by bio-chemical conversion. In thermo-chemical process, the organic compound is decomposed to release heat energy, oil or gas while in bio-chemical process, decomposition takes place with the help of microbes, and methane and alcohol are produced. Parameters that affect the recovery of energy from MSW are its quantity and the chemical

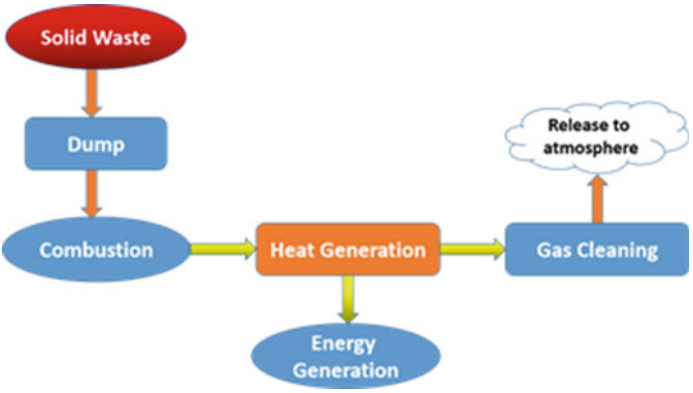


**Fig. 1** Schematic of the incineration process

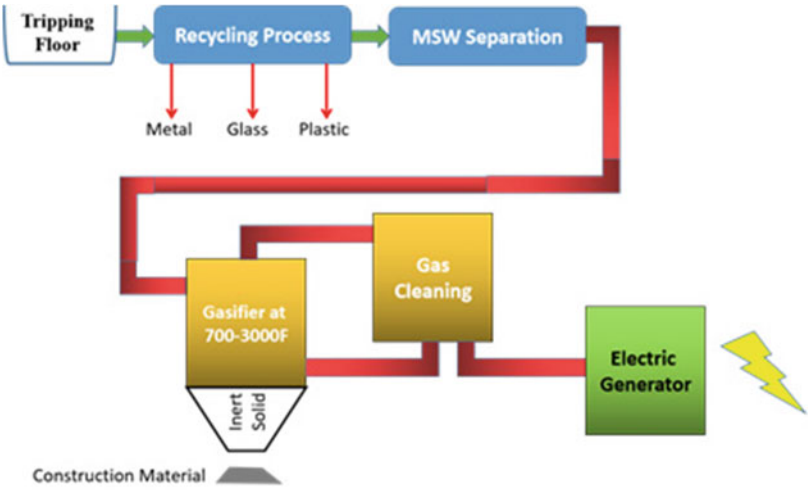


**Fig. 2** Schematic diagram of electricity generation by gasification

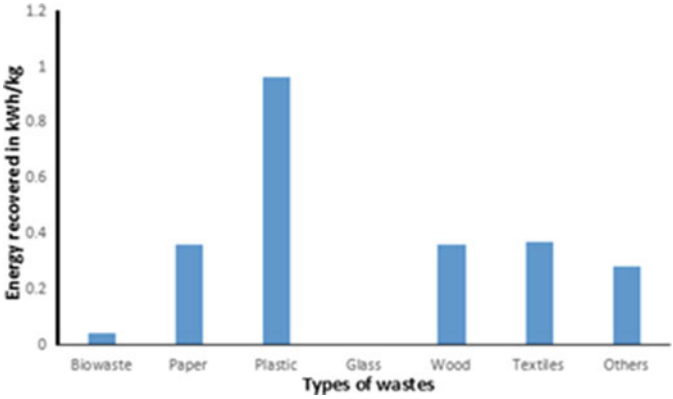


**Fig. 3** Waste incineration energy recovery

and physical characteristics of the MSW. The important physical parameters which are considered in the extraction of energy are constituent size, density and moisture content. The small size helps in faster decomposition while high-density waste provides a large amount of biodegradable organic material and low-density waste includes combustible materials like paper and plastic.

According to Pandyaswargo et al. [14], the maximum energy is recovered from the waste incineration of plastic (0.96 kWh/kg) while no energy is recovered from the glass by this process (Fig. 3).

Energy recovery potential assessment of biodegradable as well as non-biodegradable matter can be performed as follows:

Let the total waste quantity = W tonnes.

The net calorific value of the waste as calculated by the experiments = NCV kcal/kg

$$\begin{aligned}\text{Energy recovered from the waste (kWh)} &= \text{NCV} \times \text{W} \times 1000/860 \\ &= 1.16 \times \text{NCV} \times \text{W}.\end{aligned}$$

$$\text{Power generated by the waste (kW)} = 1.16 \times \text{NCV} \times \text{W}/24 = 0.48 \times \text{NCV} \times \text{W}.$$

If the conversion efficiency of the system is $\eta\%$, then actual power generation potential $= 0.0048 \times \text{NCV} \times \text{W} \times \eta$.

In bio-chemical conversion, the main contribution to the energy output is only by biodegradable organic matter. Let the total waste be W tonnes with the total volatile solid (VS) nearly 50%; experimentally, the organic biodegradable fraction is found to be 66% of VS, that is, 0.33 W. Typical efficiency of digestion is 60%.

$$\begin{aligned}\text{Biogas yield (B)} &= 0.80\text{m3/kg of VS} \\ &= 0.80 \times 0.60 \times 0.33 \times \text{W} \times 1000\end{aligned}$$

$$= 158.4 \times \text{W}.$$

Calorific value of biogas = 5000 kcal/m3.

Energy recovered (kWh) = B × 5000/860 = 921 × W.

Power generated (kW) = 921 × W/24 = 38.4 × W.

Bio-chemical conversion efficiency = 30%.

Hence, net power generated (kW) = 11.5 × W.

### *3.7 Land Filling*

According to Kumar et al. [15], in the past decade, the generation of waste in India has increased tremendously to 62 Million Tonnes every year. Out of this waste, only 42 Million Tonnes is collected per annum and only 28% of waste is treated while the remaining is transferred to the landfills. 1240 hectares of land is required annually as a sanitary landfill. According to an estimate by 2030, the annual waste generation will reach 165 Million Tonnes. The largest landfill area in India is in Bengaluru followed by Mumbai and Hyderabad. The problem of landfills can be minimized by considering the waste as a resource for energy extraction. Recyclable and reusable materials can also be extracted from the waste for judicious uses.

## 4 Comparison with Other Countries

Comparison of waste management in India and developed countries can be studied on various points like regulatory framework, waste composition and quantity and MSWM practices. In India, the despite control and command type regulations regarding waste management have not proved to be very fruitful in improving the waste situation, while in Japan, the regulations are harmonious and due to community participation proved to be very successful [16]. From British India to Post Independence, a number of regulations were passed for waste management but the concern for sanitation remained only on paper. Some of the rules notified by the Indian government for solid waste management include Hazardous waste and chemical rules, 1989, Municipal solid waste management rule 2000, Electronic waste rule 2011, etc. But these rules cannot be implemented successfully due to non-cooperation from households, lack of public awareness and paucity of equipment for the collection of segregated waste. While Japan was once considered to be one of the most polluted countries in the 1960s but in 1970, law related to waste disposal and cleansing was enacted. Subsequent amendments and public involvement changed the picture of Japan.

In India, more than 90% of municipal solid waste is dumped on land in an unsatisfactory manner which not only affects public health and the environment but also engages a lot of useful land. The three landfill sites in Delhi are located at Okhla, Ghazipur and Bhalsawa. In India, some of the municipal corporations have used the composting method for waste treatment but it lies between 10–12% [17]. The first large-scale composting plant was set up in 1992 in Mumbai. Later on, a number of composting sites were established in many metro cities but municipal corporations are reluctant for such cheaper and environment-friendly projects. For example, BMC rejected window composting-based project worth US $1.1 million, instead the project was given to United Phosphorous Limited for US $8.8 million.

The Bhabha Atomic Research Center (BARC) installed Nisarguna a biogas plant for disposal of Kitchen waste in an eco-friendly manner. By the end of 2014, around 146 locations biogas plants have been set up and 100 entrepreneurs are contributing to this technology. Bangalore Corporation has already planned to set up 12 Nisarguna plants to convert the biodegradable waste into methane and organic manure across the city. The Chennai Corporation and BMC have also started the discussion with BARC. As the mixed waste contains a lot of non-organic material, hence, in the Indian scenario, the success of these processes is difficult. When mixed waste is composted, the end product is of poor quality.

In Japan, organic waste is recycled according to Food Recycling Law. The law was amended in 2007 so as to promote the purchase of farm products that are grown using animal feed or food waste-derived compost. Kyoto and Hita like cities are using this biomass technology for producing bio-diesel fuel. Although Composting has limited potential, methods like the Bokashi and Takakura methods which are home-based composting are useful. Point-wise discussion can be presented as follows [18]:

(i) Source reduction: In India, it is rarely incorporated in an organized manner while in Japan, organized programs have been incorporated.
(ii) Collection: In India, the collection rate lies between 40–80% while in Japan, it is more than 90%.
(iii) Recycling: Informal sectors in India are not well regulated while in Japan, they are well regulated and technically advanced.
(iv) Composting: Large composting biogas plants are not common due to poor marketing while in Japan, some initiatives are being taken.
(v) Incineration: This process generally failed in India but in Japan, it is very common.
(vi) Landfilling: In India, it is done in an uncontrolled manner at open sites while in Japan, there are limited landfill sites.

## 5 Future of Solid Waste Management in India

The first priority is the political will and the governments will have to think about the future problems that may arise due to mismanagement of municipal waste. Instead of thinking about the political gains, only leaders must have a positive approach for strict

and effective implementation of the regulations regarding solid waste management. Although the government is working in the direction of improving waste collection and storage, a sense of cooperation is being developed among communities, and in near future, 100% collection and transportation will take place. The government is also working in the direction of applying modern technologies used in the developed countries with enhanced funding in dealing with various types of solid wastes. Research is being promoted for energy generation using MSW and recycling and reuse processes. Sewage water treatment plants are being developed so as to clean the sewage water primarily for irrigation purposes. Wastes like plastics and papers are separated from the storage as these can be recycled for judicious use. Techniques for segregation at source are being improved by intensive studies about the developed nations. New machines should be implemented to avoid manual rag picking to prevent health issues of the workers.

Currently, the Indian government has stressed on reduce, reuse and recycling of the MSW in an effective way [3]. Reducing is the most important aspect of solid waste management which includes the reduction in amount as well as the toxicity of the waste. Some of the wastes can be reused for the same types of application, for example, a plastic bag, tin container or cardboard boxes can be used in multiple ways in daily life applications. Some products can be disassembled and restored like new. The third important factor is recycling, in this process, waste can be used as raw materials for the manufacturing of other products [22]. The recyclable materials include paper, plastic, glass, aluminium heavy metals and construction debris.

The government is also paying attention towards the judicial use of MSW in electricity generation. It has been reported that by the use of municipal solid waste, $95m^3$ of methane/tonne is produced with a calorific value of 19.43 $MJ/m^3$. According to Kumar et al. [19], electricity of $12.98 \times 10^5$ kWh/Year can be produced if the generator efficiency is 80% and the conversion efficiency is 25%.

## 6 Conclusion

In conclusion, it can be said that a number of ways are available in India for improving solid waste management. The government has started the "Swachh Bharat Mission" to initiate awareness among people about cleanliness and its advantages. Proper management of solid waste can save a lot of money spent on human health and contribute towards the development of India. There are a few discrepancies but they can be removed or minimized by political will and community contribution. Government should increase financial support to the municipal corporation so as to strengthen them to effectively implement the rules and regulations to save the society from the hazards of waste.

## References


1. S. Kaza, L.C. Yao, P. Bhada-Tata, F. Van Woerden, *What a waste 2.0: A Global Snapshot of Solid Waste Management to 2050* (Urban Development, Washington, DC: World Bank. © World Bank). https://openknowledge.worldbank.org/handle/10986/30317. License: CC BY 3.0 IGO (2018)
2. U. Patel, Solid waste management in India, ICRIER, New Delhi January 4. http://icrier.org/pdf/4-Jan-2019/Utkarsh_Patel-SWM_%20in_India.pdf (2019)
3. A. Nandan, B.P. Yadav, S. Baksi, D. Bose, Recent scenario of solid waste management in India. World Sci. News **66**, 56–74 (2017)
4. A. Pamnani, M. Sriniwasrao, Municipal solid waste management in India: a review and some new results. Int. J. Civ. Eng. Technol. **8**, 1–8 (2014)
5. TERI Press (2014), Waste to resources: a waste management handbook. Energy Resour. Inst. 3–10
6. J.I. Ahluwalia, U. Patel, Solid waste management in India: an assesment of resource recovery and environmental impact, in *Working Paper No. 356, Indian Council for Research on Internationa Economic Relations* (2018)
7. R. Agarwal, M. Chodhary, J. Singh, Waste mangementinitiatives in India for human well being. Eur. Sci. J. SPECIAL, 105–127 (2015)
8. V. Bharti, J. Singh, A.P. Singh, A review on solid waste management methods and practices in India. Trends Biosci. **10**, 4065–4067 (2017)
9. P. Bhada, N. Themelis, *Feasibility Analysis of Wasteto-Energy as a Key Component of Integrated Solid Waste Management in Mumbai, India* (Earth Engineering Center, Waste-to-Energy Research and Technology Council, New York, 2008)
10. Hennepin Energy Recovery Center, HERC. More power than you know. In *Inspector America* (History Channel)
11. K. Sunil, Municipal solid waste management in India: present practices and future challenge. in *Clean Development Mechanism* (United Nations Framework Convention on Climate Change)
12. A. Kumar, S.R. Samadder, A review on technological options of waste to energy for effective managementof municipal solid waste. Waste Manag. **69**, 407–422 (2017)
13. H.A. Arafat, K. Jijakli, Modeling and comparative assessment of municipal solid waste gasification forenergy production. Waste Manag. **33**, 1704–1713 (2013)
14. A.H. Pandyaswargo, H. Onoda, K. Nagata, Energy recovery potential and life cycle impact assessment of municipal solid waste management technologies in Asian countries using ELP model. Int. J. Energy Environ. Eng. **3**, 1–11 (2012)
15. F. Pinamonti, G. Stringari, F. Gasperi, andZorzi G., The use of compost: its effects on heavy metal levels in soil and plants. Resour. Conserv. Recycl. **21**, 129–143 (1997)
16. S. Kumar, S.R. Smith, G. Fowler, C. Velis, S.J. Kumar, S.R. Arya, R. Kumar, C. Cheesman, Challenges and opportunities associated with waste management in India. R. Soc. Open Sci. **4**, 160764 (2017)
17. Kaushal and Rajedra K., Municipal solid waste management in India-current state and future challenges: a review. Int. J. Eng. Sci. Technol. **4**, 1473–1489 (2012)
18. M. Niyati, A comparative study of municipal solid waste management in India and Japan. Gakken Ronshu **25** (2015). (Gakken Ronshu Vol. 25 2015 March of the year)
19. S. Kumar, J. Bhattachrya, A. Vaidya, T. Chakrobarty, S. Devotta, A. Akolkar, Assessment of the status of municipal solid waste management in metro cities state capitals, class I cities and class I towns in India: an insight. Waste Manage. **29**, 883–895 (2009)
20. K. Vikas, Solid waste management in Indian cities: issues and challenges. Int. J. Adv. Educ. Res. **5**, 241–248 (2017)
21. S. Kumar, S.R. Smith, G. Fowler, C. Velis, S.J. Kumar, R. Rena Kumar, C. Cheeseman, Challenges and Opportunities associated with waste management in India. R. Soc. Open Sci. **4**, 160764 (2017)
22. M. Niyati, A comparative study of municipal solid waste management in India and Japan. Shagakken J. (Gakken Ronshu) **25**, 48–61 (2015)

# Electrochemical Conversion of $CO_2$ into Useful Chemicals and PKL Electricity


**K. A. Khan, M. A. Mamun, Md. Israrul Adal, Sharif Mia, and M. Hazrat Ali**

## 1 Introduction

The main theme should be the addressing global challenges in the new era through research, innovations, and strengthening connections (Hasan and Khan 2017, 2019, 2020). PKL electricity is produced mainly using Zn/Cu-based electrodes and PKL extract. The performances are gradually decreased within a few months (Hazrat Ali et al. 2019; Khan et al. 2016a, 2017). To remain sustain of this PKL electricity, several techniques have been developed like the use of nanoparticles, dynamic method, use of secondary salt, etc. The use of $CO_2$ is a new technique for PKL electrochemical cells (Khan et al. 2016b, c, 2018a, b). To keep it in mind, the electrochemical conversion of $CO_2$ into useful chemicals and PKL electricity has been designed and developed (Khan et al. 2019a, b). The PKL electricity is a new, renewable energy and innovative technique across the globe (Khan et al. 2019c). So that R&D work should be done regularly on PKL electricity. This research work will also be an excellent avenue for collaborative work for more innovative research for the uplifting of the community and industrial development. The nominal voltage of a galvanic cell is fixed by the electrochemical characteristics of the active chemicals used in the cell (Khan et al. 2020). The actual voltage generated at the cell terminals at a particular time depends on the load current and the internal impedance of the cell, and this also varies with the temperature, the state of charge, and with the age of the cell. A comparative study of the voltage of the normal voltaic/galvanic cell, traditional PKL electrochemical cell, and $CO_2$-based PKL electrochemical cell has also been conducted (Ruhane et al. 2017a). The PKL electrochemical cell depends on some parameters (Ruhane et al. 2017b) which have been discussed here. The production and the use of $CO_2$ is an

K. A. Khan (✉) · M. A. Mamun · Md. I. Adal · S. Mia
Department of Physics, Jagannath University, Dhaka 1100, Bangladesh

M. H. Ali
European University of Bangladesh (EUB), Dhaka, Bangladesh



C. K. Chanda et al. (eds.), *Advanced Energy and Control Systems*, Lecture Notes in Electrical Engineering 820, https://doi.org/10.1007/978-981-16-7274-3_5

innovative technology for an electrochemical cell or battery. The different parameters of the PKL electrochemical cells both with and without $CO_2$ have been studied.

## 2 Methodology

In this section, the methodology of $CO_2$ production has been discussed. The methodology of the preparation of PKL electrochemical cell has also been studied. Finally, the use of $CO_2$ for PKL Electricity has been designed and fabricated.

### *2.1 Experimental Procedure*

The experimental setup of the $CO_2$ production device for practical utilization is shown (Fig. 1). The chemical reaction was $NaHCO_3 + HCl = NaCl + H_2O + CO_2$. The produced $CO_2$ goes out through a tube. Figure 1 also shows the collection of

**Fig. 1** Experimental setup of $CO_2$ production device

**Fig. 2** Experimental setup with a balloon for electrochemical conversion

$CO_2$ by a balloon. Figure 2 shows the utilization of $CO_2$ in a PKL electrochemical cell for getting more electricity for a long time duration.

## 2.2 *Application of $CO_2$ Gas into the PKL Electrochemical Cell: Preparation of $CO_2$ Gas*

About 2.0 g of powdered $NaHCO_3$ and 250 mL 0.1 M HCl solution were taken in a 500 mL conical flask. Then the mixture was heated very slowly, releasing $CO_2$ gas which was dried by passing through silica gel.

The methods of $CO_2$ gas preparation in the laboratory are shown in Fig. 3. Here, Fig. 3a shows the Schematic diagram of $CO_2$ gas preparation and Fig. 3b shows the Experimental setup of $CO_2$ gas preparation.

**Instrumentation and Apparatus**

Model CHI 660E electrochemical workstation, Graphite pencil electrode (GPE) as working electrode (Livo), GCE, modified GCE, carbon-based paper electrode and activated GPE electrode as working electrode, Pt wire auxiliary electrode, Ag/AgCl reference electrode, pH meter (Hanna), Digital Multimeter, Zn, Cu, Al, Ag, Fe electrodes, and Magnetic Stirrer.

**Chemicals and Reagents.**

Carbon dioxide ($CO_2$), Sodium bicarbonate solution ($NaHCO_3$), Hydrochloric acid (HCl), PBS solutions for various pH, Deionized water or double-distilled water, Graphite powder, Activated charcoal (Sigma Aldese), Nujol, Alumina powder, Silica gel, and Highly pure $N_2$ gas (Linde BD Ltd.).

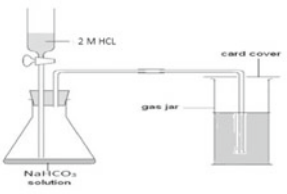


(a): Schematic diagram of $CO_2$ gas preparation

(b):Experimental set up of $CO_2$ gas preparation

**Fig. 3** Methods of $CO_2$ gas preparation

## 2.3 Zn and Cu Electrodes Preparation

To prepare a PKL (Pathor Kuchi Leaf) electrochemical cell, a cathode and an anode are needed. In our research article, it is shown that Zn (Zinc) plate is used as a cathode and the Cu (Copper) plate is used as an anode. The Zn and Cu plates are available in the local market. The price of the Zn plate is of low cost compared to the Cu plate. On the other hand, the longevity of the Cu plate is much more than the Zn plate. Moreover, the Zn plate is called a sacrificial element rather than the other metal plates. That is why the performance Zn/Cu-based PKL electrochemical cell is better than the other metals. The preparation technique of the Zn/Cu-based PKL electrochemical cell for practical utilization is shown in Fig. 4.

Figure 4a shows the Zn and Cu for a cell (Zn:Cu = 1:1). Figure 4b shows the keeping of Zn plate first (Zn:Cu = 2:2). Figure 4c shows the keeping of Cu plate

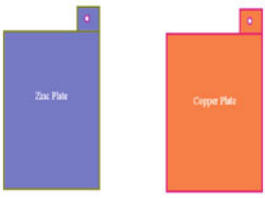


(a): Zn and Cu for a cell(1:1)

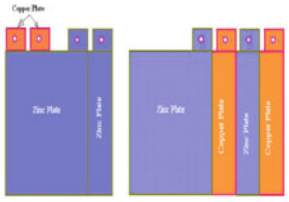

(b):Keeping Zn plate first (2:2)

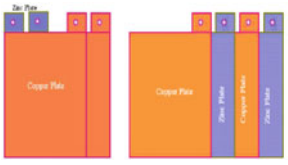

(c): Keeping Cu plate first(2:2)

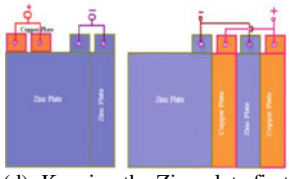

(d): Keeping the Zinc plate first(3:2)

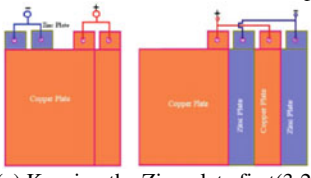

(e) Keeping the Zinc plate first(3:2)

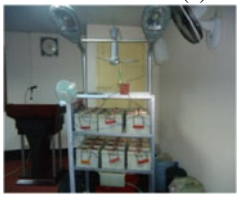

(f): Design and fabrication of 1KW PKL Power

(g): Practical application of 1KW PKL Power

**Fig. 4** Design and fabrication of Zn/Cu-based 1 KW PKL power for practical utilization

first (Zn:Cu = 2:2). Figure 4d shows the keeping of the Zinc plate first (Zn:Cu = 3:2). Figure 4e shows the keeping of the Zinc plate first (Zn:Cu = 3:23:2). Figure 4f shows the design and fabrication of 1 KW PKL Power and, finally, Fig. 4 g shows the Practical application of 1 KW PKL Power.

## *2.4 Chemical Reactions*

Since Zn is a sacrificial element, we have

$$Zn = Zn^{2+} + 2e^- \tag{1}$$

$$2e^- + Cu^{2+} = Cu \tag{2}$$

Adding (1) + (2), $Zn + 2e^- + Cu^{2+} = Zn^{2+} + 2e^- + Cu$

$$\text{Or} \quad Zn + Cu^{2+} = Zn^{2+} + Cu \tag{3}$$

where $Cu^{2+}$ = Reactant Ions and $Zn^{2+}$ = Product Ions.

$$\text{Again we have} \quad Zn = Zn^{2+} + 2e^- \tag{4}$$

$$2e^- + H^+ = H = H_2 \tag{5}$$

Adding (4) + (5), $Zn + 2e^- + H^+ = Zn^{2+} + 2e^- + H_2$

$$\text{Or} \quad Zn + H^+ = Zn^{2+} + H_2 \tag{6}$$

where $H^+$ = Reactant Ions and $Zn^{2+}$ = Product Ions.

$$NaHCO_3 + HCl = NaCl + H_2O + CO_2$$

Here, NaCl and $H_2O$ are the useful chemicals and $CO_2$ is the conversion/production product of electricity.

From Eq. (7), it is shown that the produced $CO_2$ can be used in the dead PKL electrochemical cell. The pH of the dead PKL electrochemical cell decreased than that of starting pH of the PKL electrochemical cell. When the produced $CO_2$ is applied to the dead PKL electrochemical cell, then the following chemical equation has occurred:

$$H^+ + CO_2 = H_2CO_3 \tag{8}$$

The $HCO_3$ will be produced in the dead PKL electrochemical cell. It is shown that the pH of the dead PKL electrochemical cell has been increased and then the dead PKL electrochemical cell has become reactive to generate electricity. In this case, $H_2$ gas will be produced as a byproduct.

## 2.5 Advantages of Electrochemical Reduction of $CO_2$

It is an easy process and the rate of electrochemical reduction of $CO_2$ is so much higher than the chemical reduction of $CO_2$. The advantages are as follows: (1) In presence of $CO_2$, it can easily convert into HCOOH (formic acid), CO (carbon monoxide), $CH_3OH$ (methanol), $(COOH)_2$ (oxalic acid), $C_2H_4$ (ethylene), $CH_4$ (methane), etc. (which are useful products). (2) During the electrochemical conversion of $CO_2$ without aqueous catholyte (electrolyte), other's reagent is not necessary as the chemical conversion of $CO_2$ into the same product. (3) Higher temperature and pressure is not necessary as the chemical conversion of $CO_2$:

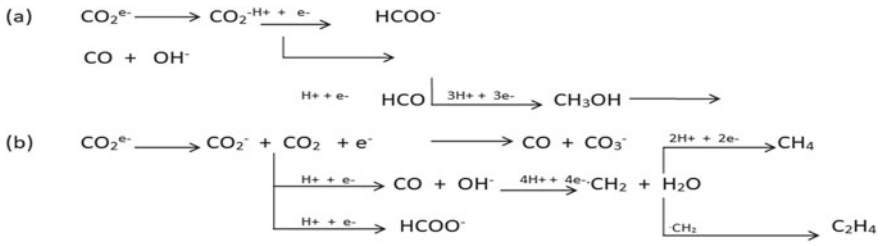


(4) In this process very low current (micro amp level) is needed to get the product. Because in this process, an electron is necessary (which is available here and obtained easily) for reduction. So this process is not expensive. (5) In this process, the reaction is carried out in the solution phase. Generally, the solution phase reaction is more easy than gas phase reaction.

## 2.6 Application of $CO_2$ Gas into the PKL Electrochemical Cell

During the preparation of the PKL electrochemical cell, the PKL extract was mixed with $H_2O$. In this case, $O_2$ was dissolved in water. So that $O_2$ should be neutralized before being applied to $CO_2$ gas into the PKL electrochemical cell.

# 3 Results and Discussion

## *3.1 Comparative Studies on Performance of Traditional Electrolytic Cells/Batteries*

The variation of the voltages for five different typical electrolytic cells/batteries has been studied. It is also shown the comparison of the variation of the voltages with the variation of percentage of capacity discharged among the five different typical electrolytic cells/battery like $Zn/MnO_2$, Ni–Cd, Ni–Zn, Lead Acid, and Lithium-Ion battery.

Figure 5 shows that the variation of the voltages with the variation of percentage of capacity discharged for $Zn/MnO_2$ electrolytic cells/battery. The change of voltage was (1.50–1.10 V) 0.40 V up to 100% of Capacity Discharged. Figure 6 shows that the voltages vary with the percentage of capacity discharged for Ni–Cd electrolytic cells/batteries. The change of voltage was (1.48–1.15 V) 0.33 V up to 100% of capacity discharged.

Figure 7 shows that the voltages vary with the variation of percentage of capacity discharged for Ni–Zn electrolytic cells/batteries. The change of voltage was (1.60–1.55 V) 0.05 V up to 100% of Capacity Discharged. Figure 7 shows that the voltages vary with the percentage of capacity discharged for lead acid electrolytic cells/batteries. The change of voltage was (2.01–1.73 V) 0.24 V up to 100% of Capacity Discharged (Figs. 8 and 9).

Figure 7 shows that the voltages vary with the percentage of capacity discharged for lithium-ion electrolytic cells/batteries. The change of voltage was (4.10–3.80 V) 0.30 V up to 100% of Capacity Discharged.

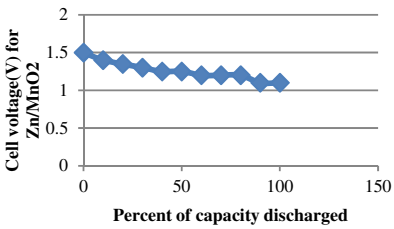


**Fig. 5** Cell voltage (V) for $Zn/MnO_2$ with percentage capacity of discharged

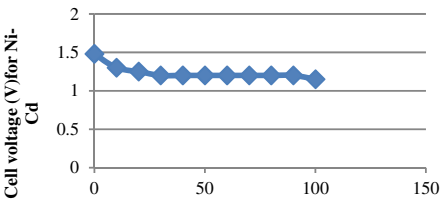


**Fig. 6** Cell voltage for Ni–Cd with percentage capacity of discharged

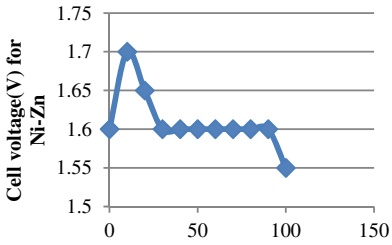


**Fig. 7** Cell voltage (V) for Ni–Zn with percentage capacity of discharged

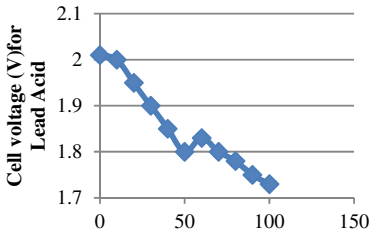


**Fig. 8** Cell voltage for Lead Acid with percentage capacity of discharged

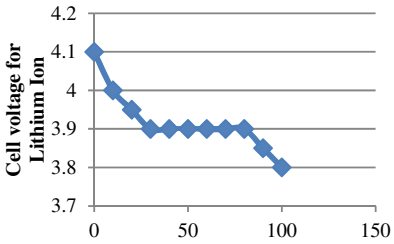


**Fig. 9** Cell voltage for Lithium Ion with percentage capacity of discharged

Figure 10 shows that the Cell voltages (V) vary with the percentage capacity of discharged for Lithium-Ion, Lead Acid, Ni–Zn, Ni–Cd, and Zn/$MnO_2$ electrolytic cells together.

## *3.2 Discharge Characteristics with Load for PKL Electrochemical Cell*

The discharge characteristics of PKL cell/module has been measured carefully. The fabricated PKL module was 6 V, which was used as a load for practical utilizations. A Light Emitting Diode (LED) lamp was used as a load of 6 V. For simplicity, it has been shown that the PKL module system is as shown in Fig. 11.

The observed values of load voltage, load current, and load power are tabulated. Taking the load tests for 120 h has been continued. It may be pointed out here that

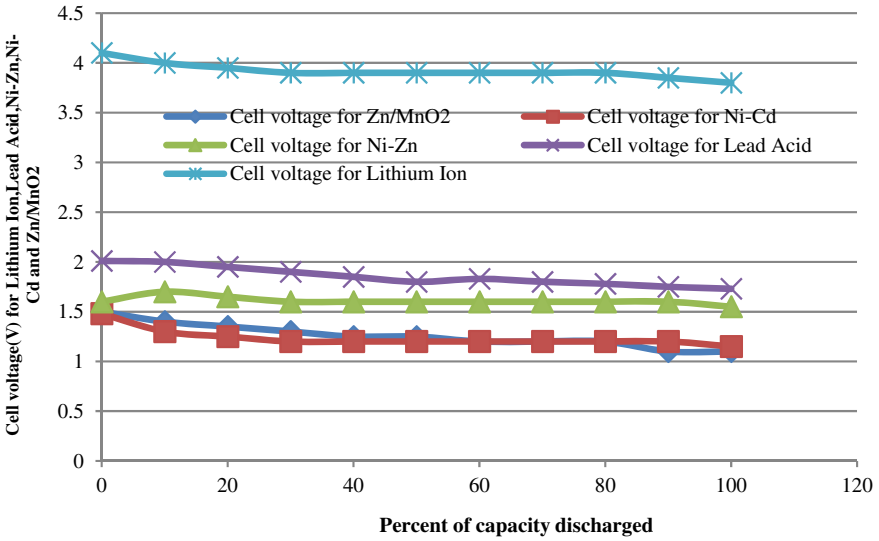


**Fig. 10** Cell voltage for Zn/MnO2, Ni–Cd, Ni–Zn, Lead Acid, and Lithium-Ion with percentage capacity of discharged

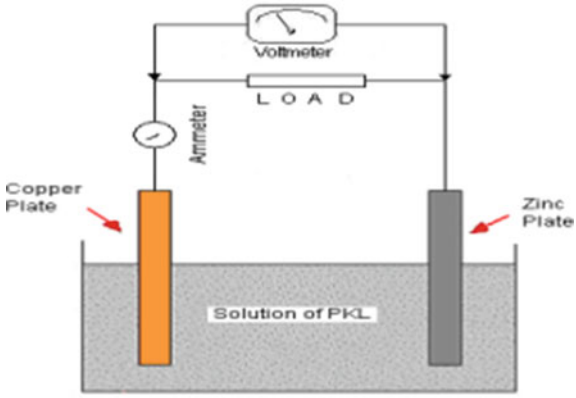


**Fig. 11** Experimental setup of discharge characteristics

initially when we connected the load, a substantial voltage drop occurs and this drop is 0.48 V which is around 8% of system voltage.

Voltage, Current, and power of PKL module under load conditions have been studied. The data was taken up to 120 h. The data has been tabulated very carefully. The discharge characteristics of a PKL electrochemical cell with the load are also shown. The Voltage, Current, and power without $CO_2$-based PKL module under load condition. It is shown that the change of load voltage for 120 h is 0.34 V, that the change of load current for 120 h is 0.32 A, and that the change of load power for 120 h is 1.9 W (Fig. 12).

**Fig. 12** PKL electricity without $CO_2$-based module

Figure 13 shows that the load voltage varies with the time duration. As per this graph, it is shown that the load voltage is reducing gradually as time duration. If we compare it with other cells, we find this change is relatively rapid. Figure 14 shows the variation of load current with the variation of time duration. As per this graph, it is seen that the load current is reducing gradually as time passes. If we compare it with other traditional cells, we find this change is relatively rapid.

Figure 15 shows the load power graph for the same system. According to the definition of load power, we have Power, P = V × I Watts, where V = Voltage (in

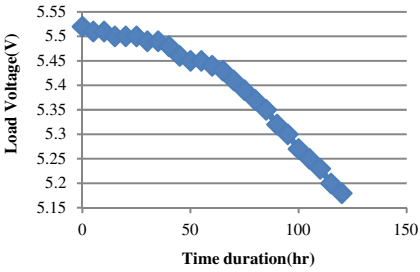


**Fig. 13** Load voltage versus time duration plot

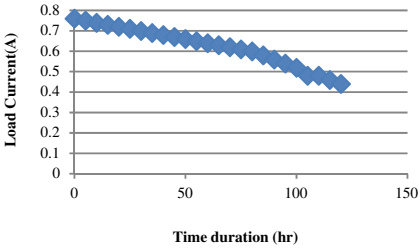


**Fig. 14** Load current versus time duration curve

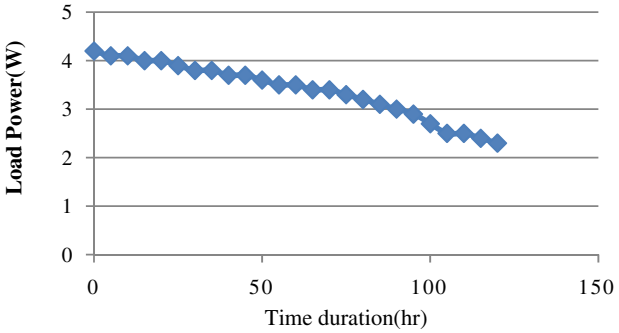


**Fig. 15** Load power (W) versus time duration (h) plot

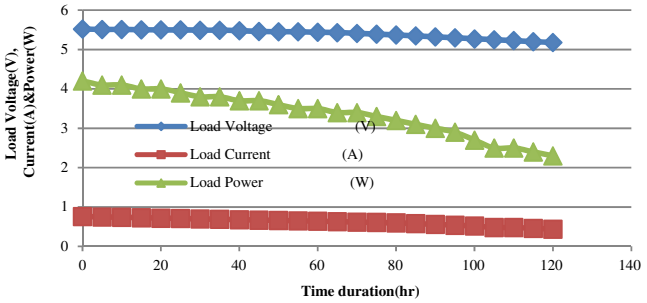


**Fig. 16** Load voltage (V), load current (A), and load power (W) versus time duration (h) plot

volts) and I = Current (in Amp). Since voltage and current are reducing with time duration, therefore, as per this graph, it is seen that the load power is also reducing gradually as time passes.

Figure 16 shows the observed results which have been plotted for three characteristics of PKL cells together. The variations of load voltage, load current, and load power with time duration have been discussed.

## *3.3 Discharge Characteristics with $CO_2$-Based PKL Electrochemical Cell for Load*

Figure 17 shows the methods of $CO_2$ Production for the PKL module. Figure 18 shows the method of $CO_2$-based PKL module for electricity production. Figure 19 shows the Measurement technique of pH of the PKL extract of a $CO_2$-based PKL unit cell. Figure 20 shows the appliance of $CO_2$-based PKL electricity with the load.

The Voltage, Current, and power of $CO_2$-based PKL (*Bryophillum pinnatum* Leaf) module under load conditions have been studied. It is shown that the change of load

**Fig. 17** Production of $CO_2$ for PKL module

**Fig. 18** $CO_2$-based PKL extract of a $CO_2$-based PKL unit cell

**Fig. 19** Measurement of pH of PKL module for electricity production

**Fig. 20** $CO_2$-based PKL electricity with load

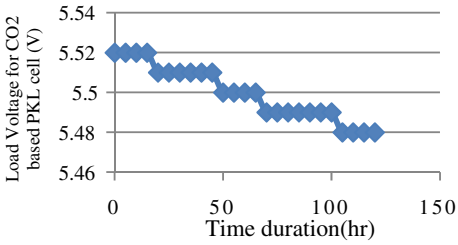


**Fig. 21** Load voltage for $CO_2$-based PKL cell (V) versus time duration (h)

voltage for 120 h is 0.04 V, that the change of load current for 120 h is 0.02 A, and that the change of load power for 120 h is 0.14 W.

Figure 21 shows that the Load voltage (V) for $CO_2$-based PKL cell varies with the time duration (h). It is shown that the load voltage was constant up to 15 h and then it decreased up to 0.01 V up to 45 h and then after it decreased 0.01 V up to 65 h and then it decreased 0.01 V up to 100 h, and finally, it decreased 0.01 V up to 120 h. Figure 22 shows that the Load current (A) for $CO_2$-based PKL electrochemical cell varies with the time duration (h). It shows that the load current was constant up to 35 h and then it decreased up to 0.01 A up to 100 h and finally, it decreased 0.01 A up to 120 h.

Figure 23 shows that the Load power (W) for $CO_2$-based PKL electrochemical cell varies with the time duration (h). It shows that the load power was constant up to 15 h and then it decreased up to 0.06 W up to 35 h and then after it decreased

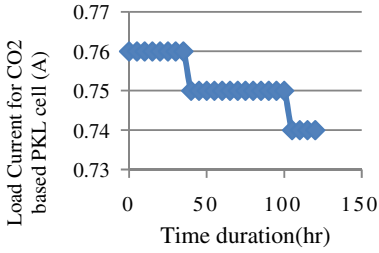


**Fig. 22** Load current for $CO_2$-based PKL cell (A) versus Time duration (h)

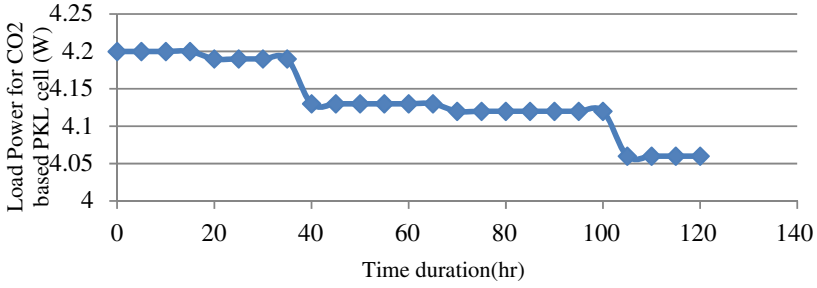


**Fig. 23** Load power for $CO_2$-based PKL cell (W) versus time duration (h)

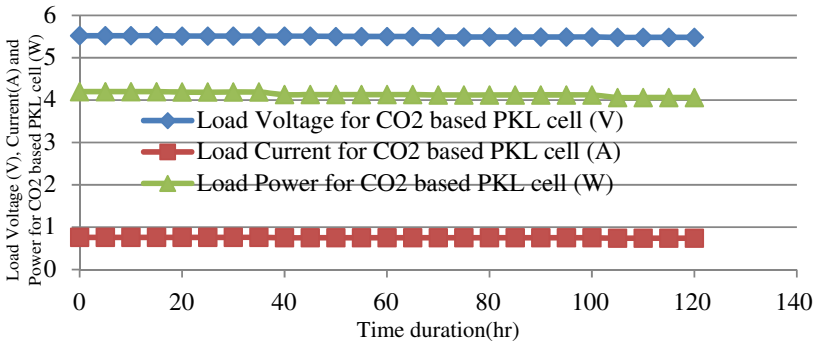


**Fig. 24** Load voltage (V), current (A), and power for $CO_2$-based PKL cell (W) versus time duration (h)

0.01 W up to 65 h and then it decreased 0.06 W up to 100 h, and finally, it decreased 0.01 W up to 120 h.

Figure 24 shows the variation of the voltage, current, and power of $CO_2$-based PKL module under load conditions. It is shown that the change of load voltage is 0.04 V, that the change of load current for 120 h is 0.02 A, and that the change of load power for 120 h is 0.14 W for 120 h.

## *3.4 Self-discharge Characteristics of a $CO_2$-Based PKL Electrochemical Cell*

Self-discharge characteristics of a $CO_2$-based PKL electrochemical cell are found. Using the Self-discharge characteristics, some data for open-circuit voltage ($V_{oc}$), Short circuit current ($I_{sc}$), maximum power ($P_{max}$), and internal resistance ($r_{in}$) has been collected and then tabulated carefully.

Figure 25 shows that the open-circuit voltage $V_{oc}$ (V) varies with and without $CO_2$-based PKL electrochemical cell with the time duration (h). It is found that the open-circuit voltage (Voc) is better with $CO_2$-based PKL electrochemical cell than without $CO_2$-based PKL electrochemical cell. Furthermore, the open-circuit voltage is more steady with $CO_2$-based PKL electrochemical cell than without $CO_2$-based PKL electrochemical cell. So that it can be said that the longevity has been increased for use in $CO_2$ with the PKL extract.

Figure 26 shows that the short circuit current $I_{sc}$ (A) with and without $CO_2$-based PKL electrochemical cell varies with the time duration (h). It is found that the short circuit current ($I_{sc}$) is better with $CO_2$-based PKL electrochemical cell than without $CO_2$-based PKL electrochemical cell. Furthermore, the short circuit current ($I_{sc}$) is more with $CO_2$-based PKL electrochemical cell than without $CO_2$-based PKL electrochemical cell. So that it can be said that the performance has been increased for use in $CO_2$ with the PKL extract.

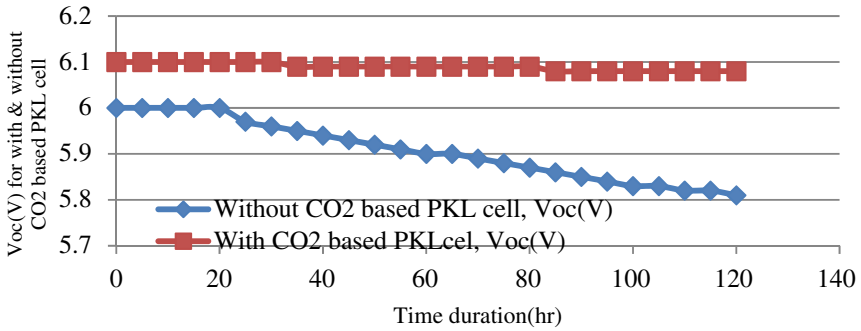


**Fig. 25** Variation of Voc (V) with and without $CO_2$-based PKL electrochemical cell with the variation of time duration (h)

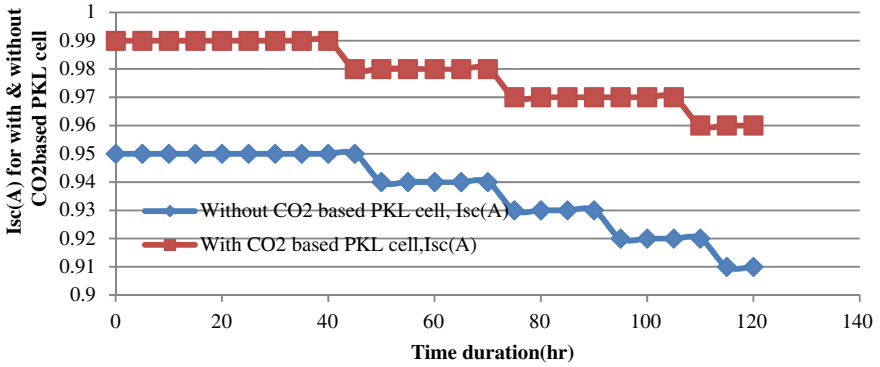


**Fig. 26** Variation of Isc (A) with and without $CO_2$-based PKL electrochemical cell with the variation of time duration (h)

Figure 27 shows that the maximum power $P_{max}$ (W) with and without $CO_2$-based PKL electrochemical cell varies with the time duration (h). It is found that the maximum power $P_{max}$ (W) is better with $CO_2$-based PKL electrochemical cell than without $CO_2$-based PKL electrochemical cell. Furthermore, the maximum power Pmax (W) is more with $CO_2$-based PKL electrochemical cell than without $CO_2$-based PKL electrochemical cell. So that it can be said that the performance has been increased for use in $CO_2$ with the PKL extract.

Figure 28 shows that the internal resistance, $r_{in}$ (ohm) with and without $CO_2$-based PKL electrochemical cell varies with the time duration (h). It is found that the internal resistance, $\mathbf{r_{in}}$ (ohm) is better with $CO_2$-based PKL electrochemical cell than without $CO_2$-based PKL electrochemical cell. Furthermore, the internal resistance, rin (ohm) is less with $CO_2$-based PKL electrochemical cell than without $CO_2$-based PKL electrochemical cell. So that it can be said that the performance has been increased for using $CO_2$ gas with the PKL extract .

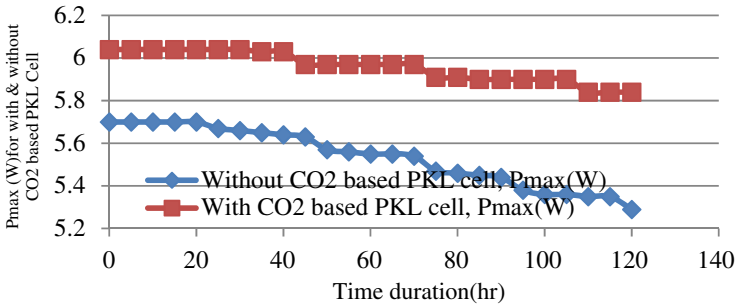


**Fig. 27** Variation of $P_{max}$ (W) with and without $CO_2$-based PKL cell with the variation of time duration (h)

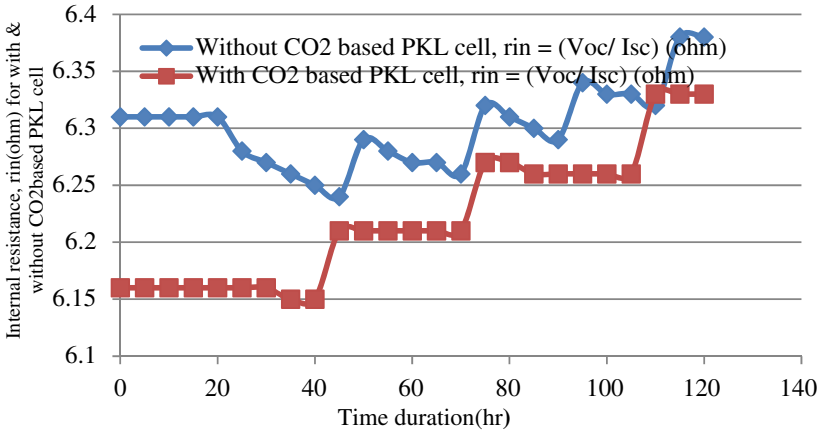


**Fig. 28** Variation of internal resistance, $r_{in}$ (ohm) with and without $CO_2$-based PKL electrochemical cell with the variation of time duration (h)

## 4 Conclusions

There are a lot of research papers on the electrochemical conversion of $CO_2$ into useful chemicals. But there was no use of $CO_2$ for electricity generation. This time the produced $CO_2$ has been used for electricity production. It is found that the performance of PKL electrochemical cell during electricity generation has been increased for using the produced $CO_2$. The variation of the voltage, current, and power of $CO_2$-based PKL module under load conditions has been studied. It is shown that the change of load voltage is 0.04 V, that the change of load current for 120 h is 0.02 A, and that the change of load power for 120 h is 0.14 W for 120 h. The Voltage, Current, and power without $CO_2$-based PKL module under load condition were found. It is shown

that the change of load voltage for 120 h is 0.34 V, that the change of load current for 120 h is 0.32 A, and that the change of load power for 120 h is 1.9 W. Finally, it is also found that the performances have been increased after adding $CO_2$ with the PKL extract. The life cycle of the PKL electrochemical cell has been increased. For a bigger size of the PKL electric plant, a $CO_2$ gas cylinder is needed. By using this $CO_2$ gas technology, the dead PKL electrochemical cell will get life for the generation of electricity. In this research work, the produced $H_2$ gas was a byproduct. Mallic acid increases during night time, Performances are better for night time collected PKL than the day time collected leaf. Reactant ion ($H+$) increases in the night time.

**Acknowledgements** The authors are grateful to the GARE (Grant of Advanced Research in Education) project, Ministry of Education, GoB for providing the financial support during the research work (Project/User ID: PS2019949).

## References

1. M. Hasan, K.A. Khan, Dynamic model of Bryophyllum pinnatum leaf fueled BPL cell: a possible alternate source of electricity at the off-grid region in Bangladesh. Microsystem Technologies (2018). Micro and Nanosystems Information Storage and Processing Systems, Springer, ISSN 0946–7076, Microsyst. Technol. (2017). https://doi.org/10.1007/s00542-018-4149-y
2. M. Hasan, K.A. Khan, Experimental characterization and identification of cell parameters in a BPL electrochemical device. SN Appl. Sci. **1**, 1008 (2019). https://doi.org/10.1007/s42452-019-1045-8
3. L. Hassan, K.A. Khan, A study on harvesting of PKL electricity. J. Microsyst. Technol. **26**, 1031–1041 (2020). https://doi.org/10.1007/s00542-019-04625-7. 26(3), 1032–1041 (2019)
4. M. Hazrat Ali, U. Chakma, D. Howlader, M. Tawhidul Islam, K.A. Khan, Studies on performance parameters of a practical transformer for various utilizations. Microsyst. Technol. (2019). https://doi.org/10.1007/s00542-019-04711-w
5. M.K.A. Khan, M.S. Rahman, T. Das, M.N. Ahmed, K.N. Saha, S. Paul, Investigation on parameters performance of Zn/Cu Electrodes of PKL, AVL, tomato and lemon juice based electrochemical cells: a comparative study, in *Electrical Information and Communication Technology (EICT), 2015 3rd International Conference on* (IEEE, 2017), pp. 1–6
6. K.A. Khan, A. Rahman, M.S. Rahman, A. Tahsin, K.M. Jubyer, S. Paul, Performance analysis of electrical parameters of PKL electricity (An experimental analysis on discharge rates, capacity & discharge time, pulse performance and cycle life & deep discharge of PathorKuchi Leaf (PKL) electricity cell), in *Innovative Smart Grid Technologies-Asia (ISGT-Asia), 2016 IEEE* (IEEE, 2016a), pp. 540–544
7. M.K.A. Khan, S. Paul, M.S. Rahman, R.K. Kundu, M.M. Hasan, M. Moniruzzaman, M.A. Mamun, A study of performance analysis of PKL electricity generation parameters: (An experimental analysis on voltage regulation, capacity and energy efficiency of pathorkuchi leaf (PKL) electricity cell), in *Power India International Conference (PIICON), 2016 IEEE 7th* (IEEE, 2016b), pp. 1–6
8. K.A. Khan, A. Rahman, M. Siddikur Rahman, A. Tahsin, K.M. Jubyer, S. Paul, Performance analysis of electrical parameters of PKL electricity (An experimental analysis on discharge rates, capacity & discharge time, pulse performance and cycle life & deep discharge of Pathor Kuchi Leaf (PKL) electricity cell), in *Innovative Smart Grid Technologies-Asia (ISGT-Asia), 2016 IEEE* (IEEE, 2016c), pp. 540–544

9. K.A. Khan, L. Hassan, A.K.M. Obaydullah, S.M. Azharul Islam, M.A. Mamun, T. Akter, M. Hasan, M. Shamsul Alam, M. Ibrahim, M. Mizanur Rahman, M. Shahjahan, Bioelectricity: a new approach to provide the electrical power from vegetative and fruits at off-grid region. Microsyst. Technol. (2018a). https://doi.org/10.1007/s00542-018-3808-3
10. K.A. Khan, M.S. Bhuyan, M.A. Mamun, M. Ibrahim, L. Hasan, M.A. Wadud, Organic electricity from Zn/Cu-PKL electrochemical cell, in *Contemporary Advances in Innovative and Applicable Information Technology, Advances in Intelligent Systems and Computing*, by ed. J.K. Mandal et al., vol. 812, Chapter 9, pp. 75–90 (Springer Nature Singapore Pvt. Ltd., 2018b)
11. K.A. Khan, M. Hazrat Ali, A.K.M. Obaydullah, M.A. Wadud, Production of candle using solar thermal technology. Microsystem Technologies Micro- and Nanosystems Information Storage and Processing Systems, Springer. ISSN 0946–7076, Microsyst. Technol. **25**(12) (2019a). https://doi.org/10.1007/s00542-019-04390-7(2019)
12. K.A. Khan, S.R. Rasel, M. Ohiduzzaman, Homemade PKL electricity generation for use in DC fan at remote areas, Microsystem Technologies Micro- and Nanosystems Information Storage and Processing Systems. ISSN 0946–7076. Microsyst. Technol. **25**(12) (2019b). https://doi.org/10.1007/s00542-019-04422-2
13. K.A. Khan, M.A. Mamun, M. Ibrahim, M. Hasan, M. Ohiduzzaman, A.K.M. Obaydullah, M.A. Wadud, M. Shajahan, PKL electrochemical cell: physics and chemistry. SN Appl. Sci. 1, 1335 (2019c). https://doi.org/10.1007/s42452-019-1363-x
14. K.A. Khan, M. Hazrat Ali, M.A. Mamun, M. Mahbubul Haque, A.K.M. Atique Ullah, M.N. Islam Khan, L. Hassan, A.K.M. Obaydullah, M.A. Wadud, Bioelectrical characterization and production of nanoparticles (NPs) using PKL extract for electricity generation, Received: 31 July 2018/Accepted: 4 February 2020. Microsyst. Technol. (2020). https://doi.org/10.1007/s00542-020-04774-0
15. T.A. Ruhane, M. Tauhidul Islam, M. Saifur Rahman, M.M.H. Bhuiyah, J.M.M. Islam, T.I. Bhuiyah, K.A. Khan, M.A. Khan,Impact of photo electrode thickness annealing temperature on natural dye sensitized solar cell. Sustain. Energy Technol. Assess. (2017a). https://doi.org/10.1016/j.seta.2017.01.012
16. T.A. Ruhane, M. Tauhidul Islam, M. Saifur Rahaman, M.M.H. Bhuiyan, J.M.M. Islam, M.K. Newaz, K.A. Khan, M.A. Khan, Photo current enhancement of natural dye sensitized solar cell by optimizing dye extraction and its loading period. Optik Int. J. Light Electron Optics (2017b)

# Graphical Approach to Recognize Optimal Distribution Network Reconfiguration


**Pushpanjalee Konwar, Dipu Sarkar, and Chandan Kumar Chanda**

## 1 Introduction

Reconfiguration of distribution networks is one of the core functions of the distribution monitoring framework. Reconfiguration of networks is assessed by activating and shutting switches [1]. The beauty of the methodology lies in its ability to locate the processing. In situations where the distribution network must experience individual geometrical changes, such as network reconfiguration, bus voltage magnitude appraisal can be calculated in much shorter numerical modules [2]. The problem of deciding which connections should indeed be enabled is alluded to here as network reconfiguration. The minimal loss or load management restructuring dilemma for the open-loop system radial distribution network is conceived as a hybrid configuration conundrum and is complicated to fix [3]. The suggested approach incorporates the minimum spanning tree (MST) algorithm with enhanced probabilistic principles. The local objective function, presented by the MST algorithm, offers a desirable initial condition for corresponding computation techniques. In addition to the strengthened genetic algorithm, the number of selected switching devices can be drastically decreased [4]. The radial load flow problem needs special attention, especially when resolving adaptive power system challenges, where the network topology influences the position of the link switching (multi-objective optimization issue). The proposed approach would assist in arranging line statistics for any variation of tie switch locations, checking the system's radiality, and ensuring that all

P. Konwar · D. Sarkar (✉)
Department of Electrical and Electronics Engineering, National Institute of Technology, Dimapur, Nagaland, India

C. K. Chanda
Department of Electrical Engineering, Indian Institute of Engineering Science and Technology, Shibpur, Howrah, India



C. K. Chanda et al. (eds.), *Advanced Energy and Control Systems*, Lecture Notes in Electrical Engineering 820, https://doi.org/10.1007/978-981-16-7274-3_6

nodes are associated with the source node [5]. The framework is particularly productive because it employs visualization strategies that provide semi-saving transformations from the current susceptibility matrix. The technology can be implemented to large networks and outperforms traditional network reconfiguration algorithms in terms of ensuring an optimal solution [6]. The Distribution Network Reconfiguration problem has arisen as a result of mixed-integer and complex nonlinear features. Two core components of meta-heuristic algorithms are explored in order to speed up the solution process: depiction of a solution and a strength and fitness evaluation [7]. Out of a large number of potential alternate configurations of lines and switches, an effort was made to identify the best possible radial. As a result of this combination, the network's overall voltage stability is maximized [8]. The switches' configuration was tweaked for optimal performance, and the best solution was chosen from a list of combinations with lower line losses. Optimal Power Flow (OPF) problems are concerned with achieving optimal efficiency while minimizing power loss, relying on other constraints to reduce the value that can fulfill the requirement [9]. Utilizing the assumption of parallel restructuring, the optimal route provided by the processor implementation was achieved. The Dijkstra algorithm was suggested as a means for finding an efficient link. The final position was reached by going across the in-between locations, which are assessed by filtering [10]. This study looks into the possibility of using assured synchronization particle swarm optimization in combination with graph theory to improve voltage stability and reduce power loss in distribution networks [11]. This research proposes a novel method for efficiently reconfiguring radial distribution networks. As part of the distribution system design, a graph theory-based load flow algorithm is implemented. By traversing the directed system graph to discover the depth-first query discovery sequence, the iterator approaches improvements in the system structure [12]. A technique for selecting the appropriate location and size of the DG must be established while at the same view ensuring appropriate combination. A lot of algorithm and synthetic processing approaches, reconfiguration of the optimal distribution network, size of DGs, and location have been suggested in the research. Integrating DG into the distributed generation at an inaccurate destination might well lead to higher power failures and voltage perturbations [13]. This study proposes a reconfiguration of the electrical power delivery network based on a mutualistic entity random search. The purpose here would be to achieve optimum reorganization of the power distribution network, which mitigates the real power losses due to a better power flow [14]. The conventional and colony optimization is modified by graph theory to constantly define viable radial architectures over the entire time. It's a newly discovered phenomenon. This eliminates time-consuming network searches, lowering operating costs [15]. This research presents a new Big Bang-Big Crunch (HBB-BC) hybrid simulation approach for efficiently reconfiguring imbalanced loss reduction delivery systems. Throughout the reconfiguration, restrictions such as being radial, avoiding load insulation, and voltage/current restrictions must be determined [16]. The purpose of the radial operational mechanism reconfiguration is to define a distribution network with a radial functional framework. This mitigates the reduction of the power of the delivery system under standard conditions. While they are arranged in a radial tree

structure during operation, delivery systems are normally expected to be intertwined meshed systems [17]. To meet the rising demand for power while minimizing power loss, a well-designed and effective distribution system needs the best mathematical layout This paper describes how a genetic algorithm based on graph theory was used to resolve the issue of power distribution network reconfiguration [18]. Reconfiguration is achieved by direct connections/estrangement of components and exchange of limits of autonomy. This journal proposes a new methodology for self-configuration scheduling for autonomous devices centered on domain signature and graph edit-distance [19]. This paper introduces a novel approach to the optimization process. Distribution system rearrangement uses the variation of Cycle Break optimization and optimization programming. The use of a combination cycle-break method and an evolutionary algorithm eliminates these problems and makes a real-size system execution [20]. This study proposes a new approach to increasing the dependability of the distribution system by reconfiguring it. In this context, an overall cost component is defined to comprise the cost of network active device malfunction as well as the cost of customer disruption at the same time [21]. In this study, the distribution system reconfiguration issue was subsequently studied compared to the graph theory and the functionality of the ant colony algorithm. It is recommended to use a fragmented circle approach to quickly have a network topology [22]. This study introduces a unique strategy toward solving the dynamic distribution network reconfiguration dilemma. A quick network topology identification methodology is built based on graph theory and efficient mathematical complexity recognition technology to resolve the device radiality limitation [23]. In this paper, a meta-heuristic approach based on Antlion's hybridization protocols and graph theory is anticipated to find the best DN distribution network combination by adjusting the switch position. The primary goal of network reconfiguration will be to find a network topology with the fewest possible disturbances within the constraints [24].

## 2 Description of the Issue

Structures in graph theory depict a relationship between entities in sequence. G (V, E) is a set of structures traced by a pair of vertices around the boundaries (E). If the vertices are intertwined around the ground, they have been shown to be neighbors. A tree T composed of all the vertices of graph G is defined as the spanning tree of the connected undirected graph G = (V, E). Each linked element in Graph G will provide a spanning tree if it is disconnected. There may be a number of spanning trees in a graph. The spanning trees can have different weights if each edge of the graph is assigned a weight. In a variety of scientific and technical areas, the minimum weighted spanning tree has a variety of implementations. In essence, modern approaches to resolving the minimum problem of the tree period are typically aggressive. The majority of traditional algorithms develop the MST edge-by-edge, including the necessary tiny edges while ignoring the larger ones.

## 2.1 Implementation of the Methodology

The feeder line with the lowest cost shall be brought into account with the preliminary evaluation of the vertex. The price specified shall be the load ability of the tracks. Restructuring does not manifest in a drastic shift in active power loss or reactive loss of power, but chooses another direction where another load-carrying potential has indeed been reduced. The stability index (L-INDEX) should be much closer to 0 if the system is to be stable. There is a significant chance of an illuminated voltage collapse if L-INDEX approaches 1 [25].

The suggested technique is centered on the Node Adaptive Cycle Identification System. Numerous sophisticated cycle detection techniques including almost standardized fashion can indeed be commonly obtained. The highest extent of the set of unidentified vertices (V-S), where S is the collection of known nodes, was chosen as vertex u. The selected endpoint which is a part of the loop is verified. If this is the case, we can define the much more problematic edge (i.e. the edge with the highest weighted graph) and eliminate it from the loop and also from the set of edges. If there is a tie, we choose the edge with the highest amounts of terminating edges. We proceed with this procedure with the chosen highest point u till the highest point is free of all the cycles associated. Because when a node is independent of all the related loops, we attach it to the collection of identified vertices S. Another endpoint will be selected and will expedite the method. The procedure ends when the quantity of edges remains equivalent to |V|-1, because a tree containing nodes comprises |V|-1 edges. The suggested methodology selects the highest degree vertex at each step. The reason behind such a concept is that the possibility that a vertex is part of a loop rises including its degree. The higher the vertex's degree, the more likely it is to be associated with a specific loop. When removing an edge, the additional tie is determined by the degree of the edge's marginal vertices. The greedy nature of the technique is reflected in the presumption that the maximum degree vertex is chosen at each point to check the parallelism of the loop.

**Control logic steps of the proposed algorithm:**

Step 1: Consider a weighted undirected graph G = (V, E).

Step 2: Initialize spanning tree S as a null set and tree (T) = graph (G).

Step 3: While edge > (vertex-1), choose a vertex whose degree is optimum.

Step 4: If step 3 is true and there exists a cycle, then remove the edge with the maximum weight.

Step 5: While performing step 4, if a tie occurs, select the edge with the maximum degree.

Step 6: Edge = Edge-(maximum edge).

Step 7: Minimum spanning tree is obtained.

This segment demonstrates the implementation of the procedure implemented on the reference graph depicted in Fig. 1. The implementation selects node C for the first time since it has the maximum degree. It then determines that vertex b is correlated with the C-A-D-C loop. Next, the relatively costly edge is selected and it is discovered that there is indeed a match, namely AD and CD. That said, the terminating nodes of CD have a maximum degree and thus BE is removed by dashed red lines as demonstrated in Fig. 2.

Now the methodology identifies that C is also a representative of the C-E-F-C loop and reduces the far more pricey CE edge (Fig. 3). Then another loop C-A-B-E-F-C is identified and BE is removed (Fig. 4). Since node C is currently free of all cycles, vertex C is attached to the list of identified nodes S. 'A' is the next node selected for experimentation. Vertex A is correlated with the loop A-B-D-A, and therefore the more costly side of the DB is erased as shown in Fig. 5. Next, A is assigned to the list of labeled nodes.

The number of sides represents one less than the set of nodes in this iterative procedure, so the method ends by restoring the corresponding minimum spanning tree, as shown in Fig. 6.

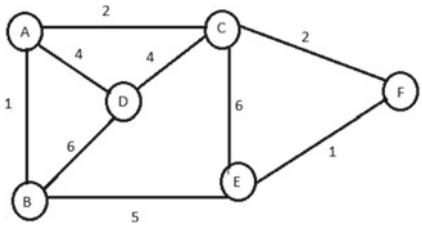


**Fig. 1** Graph

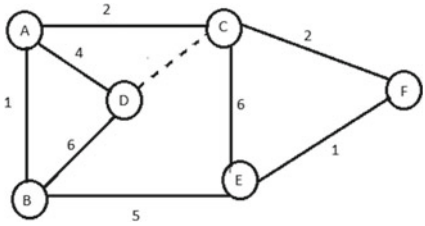


**Fig. 2** CD removed

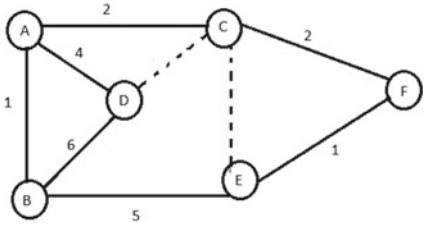


**Fig. 3** CE removed

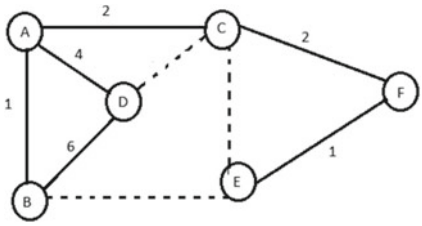


**Fig. 4** BE removed

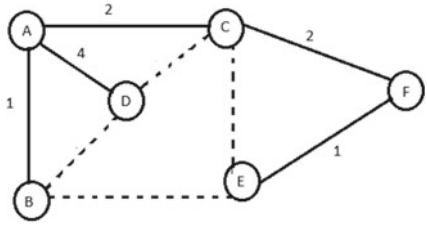


**Fig. 5** CD removed

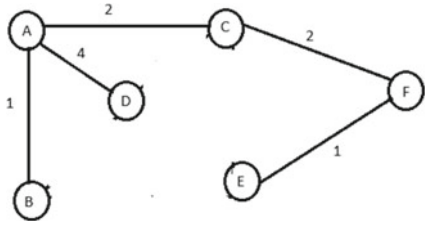


**Fig. 6** Minimal spanning tree

## *2.2 Analysis and Results of the Anticipated Optimization*

The suggested methodology selects the highest degree node at each step and the implementation of the proposed methodology is explained in the 5-node system as depicted in Fig. 7. The explanation for this is that as a node's degree increases, the likelihood of it being a member of a loop increases. The higher the vertex's degree, the more likely it is to be associated with a specific loop. The degree of terminal nodes on the sides is used to determine the additional tie when removing the edge. The greedy existence of this algorithm is embodied in the presumption that at each stage, the highest degree node possible is selected to verify the loop's parallelism. The optimal configuration for the 5-node network is obtained after implementing the cycle vertex algorithm, as shown in Fig. 8.

The suggested methodology was successfully implemented to rearrange the 14-node delivery network, as demonstrated in Fig. 9 simultaneously, the computed optimal graph is shown in Fig. 10. In the IEEE 14 bus system, the meshed network following the implementation of the cycle vertex method is depicted in Fig. 11.

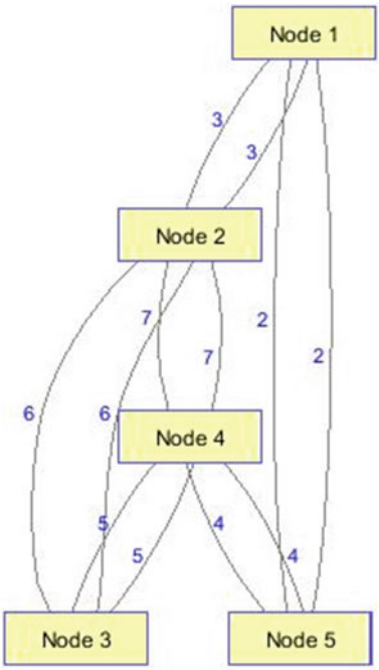


**Fig. 7** Cycle vertex algorithm on 5-node system

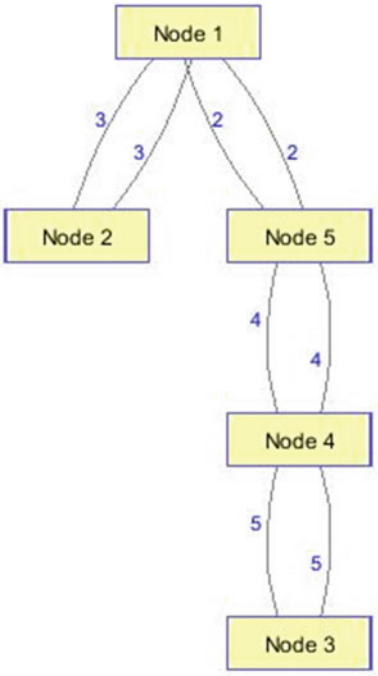


**Fig. 8** Optimal layout for a 5-node system

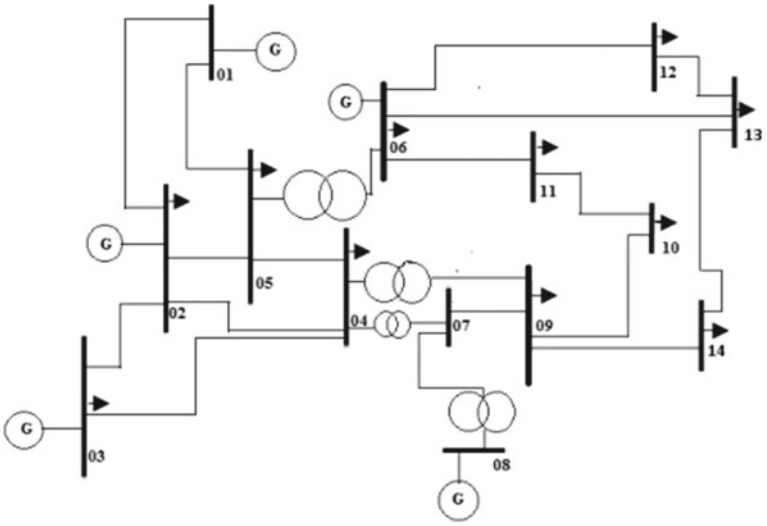


**Fig. 9** IEEE 14-bus system

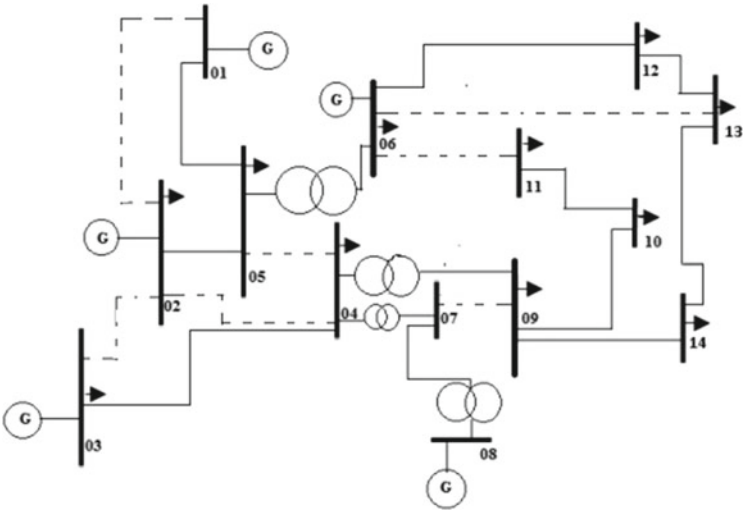


**Fig. 10** Cycle vertex optimal configuration

## 3 Validation Mechanism on 14-Bus System

Figure 9 shows the test system, which consists of a 14-node mesh network. Each feeder in the network has one series sectionalized turn and is labeled S1 through S20. As shown in the literature [8], the total requirement for a real and reactive

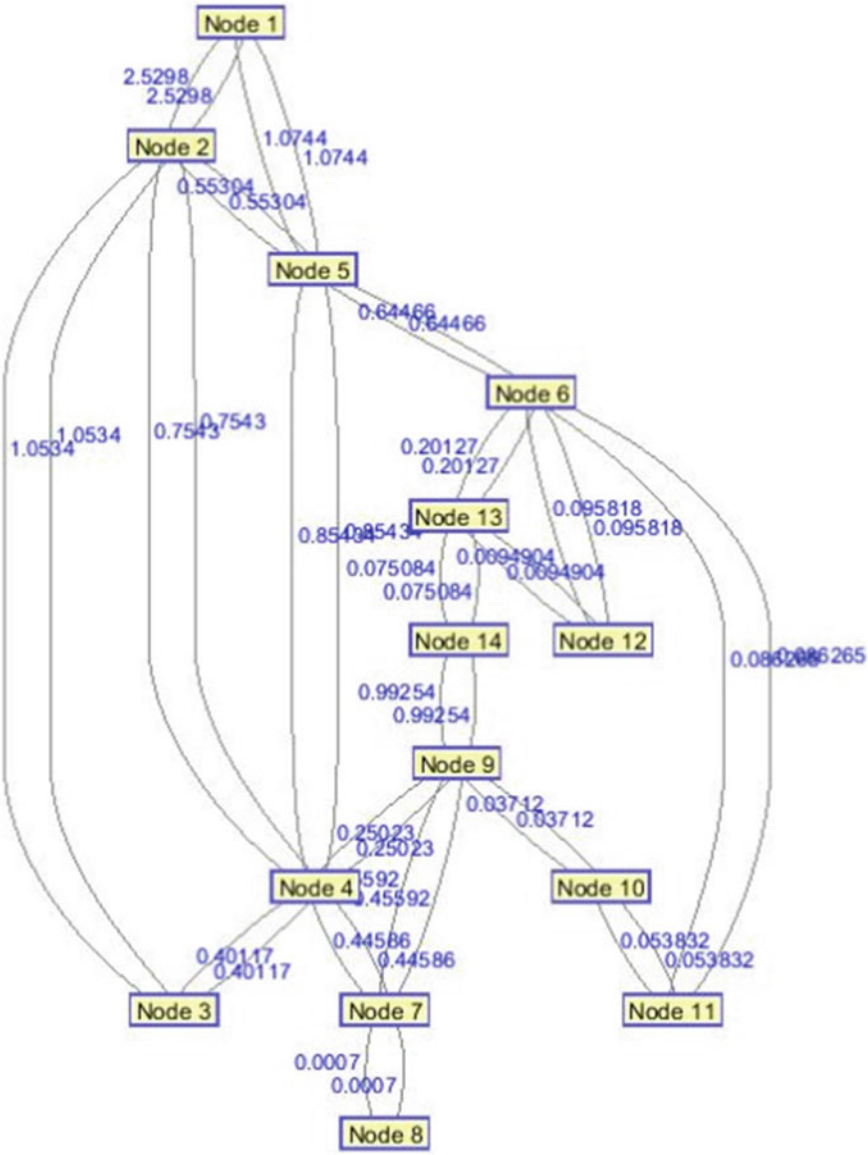


**Fig. 11** Meshed network through cycle vertex

power network is 362.6 MW and 113.96 MVAR until all the switches have been turned off by the Newton-Raphson load flow. To evaluate the cost matrix for the test unit, a load flow study is conducted. To evaluate the importance of the desired method's sides (feeder), a distribution load flow measurement is done. Since this is a 14-vertex network, the scale of the cost matrix will be 14 × 14. The proposed

cost-matrix algorithm parameters used for network simulation are the loadability maximum parameters extracted from the Newton-Raphson methodology. The price variables of the system sides are used to obtain the highest guided spanning tree that is the optimized radial system. The graph built in the next step is optimized using the Cycle Vertex algorithm defined in Sect. 2.1. The Ideal Graph is shown in Fig. 12.

To demonstrate the efficacy of the suggested implementation, the Kruskal Spanning Tree algorithm in the literature [8] and Edmonds' maximal spanning tree in the literature [25] were correlated with the outcome of cycle vertex methodology.

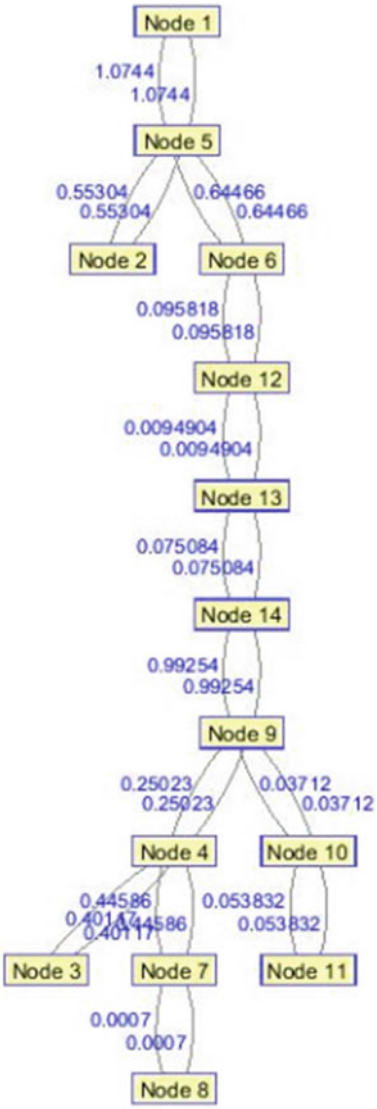


**Fig. 12** Cycle vertex graphical optimal configuration

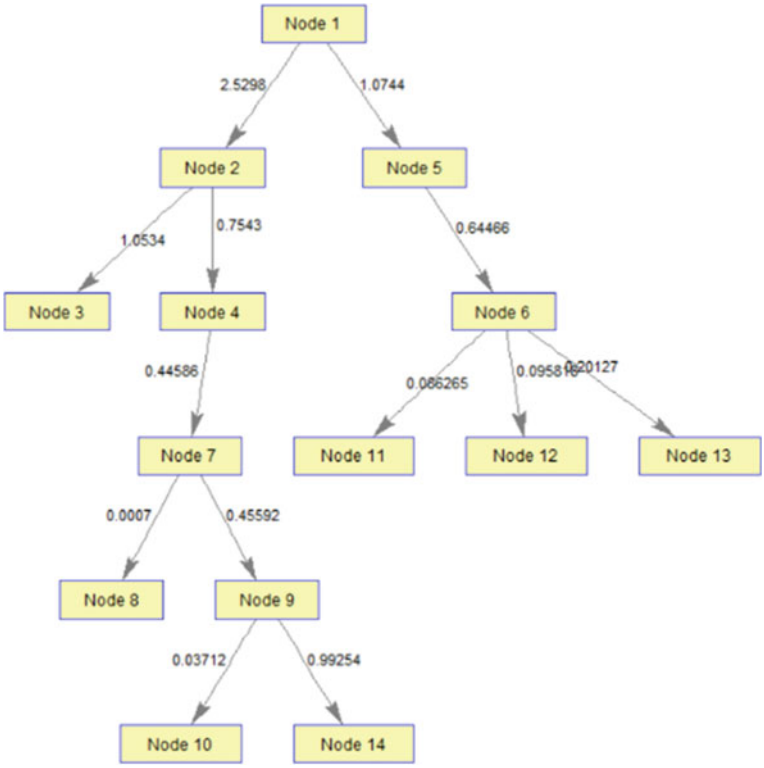


**Fig. 13** Edmonds' graphical optimal configuration

The optimal configuration obtained through the implementation of Edmonds' and Kruskal's Optimization techniques is depicted in Fig. 13 and Fig. 14, respectively. Some couple of observations of the voltage stability measurement and the data on active and reactive power loss referring to the various radial network switch configurations have been provided in Table 2. The optimum radial arrangement was found in an efficient manner using the recommended methodology showing the relative values acquired using a variety of methods: Cycle Vertex, Edmonds' algorithm, and Kruskal's 14-knot algorithm. The first parameter refers to the network configuration using the Cycle Vertex algorithm, the second configuration is achieved using Edmonds' algorithm [25], while the third example is the specification observed using the Kruskal Maximal Spanning Tree algorithm employed in [8]. The network graph is created after the computation is implemented leveraging the Cycle Vertex algorithm depicted in Fig. 12 obtained from meshed configuration as portrayed in Fig. 11. Sectionalized connections are detached as per the vertices not associated in the graph below as shown in Fig. 10. The voltage stability index is computed for the newly declassified sectionalized toggle layout. The results are clearly visible in the fact that the current algorithm, i.e. the Cycle Vertex algorithm, is much better than the

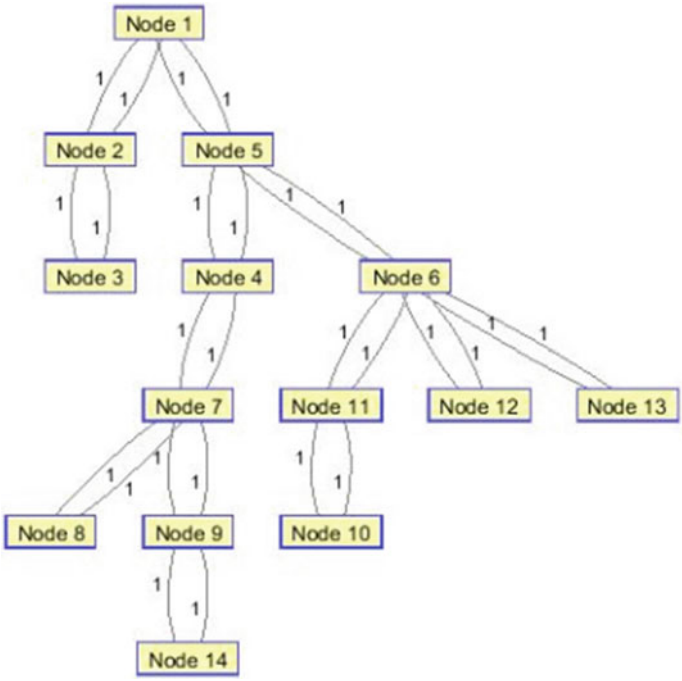


**Fig. 14** Kruskal's graphical optimal configuration

algorithms used in the literature [8, 25] since it has identified much better (efficient) switching configurations, as shown by the maximum voltage stable network conditions; the smallest the active and reactive power losses, the shortest the computation time for all the implementations evaluated as depicted in Table 2. The optimum framework for the 14 bus system is restructured and configured based on the evolving switch configurations as shown in Table 1.

## 4 Conclusion

To achieve a better operating environment, the paper attempted to change the topology of the Power Distribution Network by sectionalizing switches. Since the figure of alternate configurations is habitually large and the standard search takes an unacceptable amount of time, an efficient evaluation algorithm is critical. The paper introduces Cycle Vertex Spanning Tree methodology to provide a quick and efficient quest for optimized system configuration. The results are largely due to the fact that the current implementation is much superior to the algorithms used in the literature [8, 25] because it has identified even better (Optimal) switching configurations, as

**Table 1** Statistics for the 14-bus system's switch position

| End bus | Start bus | Button | End bus | Start bus | Button |
|---|---|---|---|---|---|
| 2 | 1 | S1 | 11 | 6 | S11 |
| 5 | 1 | S2 | 12 | 6 | S12 |
| 3 | 2 | S3 | 13 | 6 | S13 |
| 4 | 2 | S4 | 8 | 7 | S14 |
| 5 | 2 | S5 | 9 | 7 | S15 |
| 4 | 3 | S6 | 10 | 9 | S16 |
| 5 | 4 | S7 | 14 | 9 | S17 |
| 7 | 4 | S8 | 11 | 10 | S18 |
| 9 | 4 | S9 | 13 | 12 | S19 |
| 6 | 5 | S10 | 14 | 13 | S20 |

**Table 2** For a 14-bus structure, a correlation of various radial configurations acquired by Cycle Vertex (configuration 1), Edmonds' algorithm (configuration 2), and Kruskal's algorithm (configuration 3)

| Radial configuration no | Switches that are turned on | Active power loss (p.u) | Reactive power loss (p.u) | Voltage stability index | Computational time (sec) |
|---|---|---|---|---|---|
| 1 (Cycle index) | S1, S3, S4, S7, S15, S11, S13 | 5.82 | 40.23 | 0.144 | 1.3823 |
| 2 (Elmonds') | S5, S7, S9, S6, S18, S19, S20 | 8.6812 | 55.211 | 0.4610 | 1.928 |
| 3 (Kruskal's) | S4, S5, S6, S9, S16, S19, S20 | 7.2342 | 57.3341 | 0.6320 | 2.1538 |

evidenced by the lowest active and reactive power losses, as well as the most voltage stable network conditions of all the configurations tested. The optimal scheme is calculated based on the changing configurations of the Cycle Vertex.

## References

1. M. Mosbah, S. Arif, R.D. Mohammedi, A. Hellal, Optimum dynamic distribution network reconfiguration using minimum spanning tree algorithm, in *2017 5th International Conference on Electrical Engineering—Boumerdes (ICEE-B)* (Boumerdes), pp. 1–6 (2017). https://doi.org/10.1109/ICEE-B.2017.8192170
2. C. Ababei, R. Kavasseri, Efficient network reconfiguration using minimum cost maximum flow-based branch exchanges and random walks-based loss estimations. IEEE Trans. Power Syst. **26**(1), 30–37 (2011). https://doi.org/10.1109/TPWRS.2010.2052076
3. K. Nara, Y. Mishima, T. Satoh, Network reconfiguration for loss minimization and load balancing, in *2003 IEEE Power Engineering Society General Meeting (IEEE Cat.*

*No.03CH37491)*, vol. 4 (Toronto, Ontario), pp. 2413–2418 (2003). https://doi.org/10.1109/PES.2003.1271019
4. H. Li, W. Mao, A. Zhang, C. Li, An improved distribution network reconfiguration method based on minimum spanning tree algorithm and heuristic rules. Int. J. Electr. Power Energy Syst. **82**, 466–473 (2016). ISSN 0142-0615. https://doi.org/10.1016/j.ijepes.2016.04.017
5. M.M. Aman, G.B. Jasmon, A.H. Abu Bakar, H. Mokhlis, K. Naidu, Graph theory-based radial load flow analysis to solve the dynamic network reconfiguration problem. Int. Trans. Electr. Energy Syst. **26**, 783–808 (2016). https://doi.org/10.1002/etep.2108
6. A.B. Morton, I.M.Y. Mareels, An efficient brute-force solution to the network reconfiguration problem. IEEE Trans. Power Deliv. **15**(3), 996–1000 (2000). https://doi.org/10.1109/61.871365
7. S. Huang, V. Dinavahi, Fast distribution network reconfiguration with graph theory. IET Gener. Transm. Distrib. **12**(13), 3286–3295 (2018). https://doi.org/10.1049/iet-gtd.2018.0228
8. D. Sarkar, S. Goswami, A. De, C.K. Chanda, A.K. Mukhopadhyay, Improvement of voltage stability margin in a reconfigured radial power network using graph theory. Can. J. Electr. Electron. Eng. **2**(9) (2011)
9. E. Dolatdar, S. Soleymani, Soodabeh, B. Mozafari, A new distribution network reconfiguration approach using a tree model. World Acad. Sci. Eng. Technol. **58**(34), pp. 2480–2487 (2009)
10. H. Ishikawa, S. Shimizu, Y. Arakawa, N. Yamanaka, K. Shiba, New parallel shortest path searching algorithm based on dynamically reconfigurable processor DAPDNA-2, in *IEEE International Conference on Communications* (Glasgow), pp. 1997–2002 (2007). https://doi.org/10.1109/ICC.2007.332
11. M. Assadian, M.M. Farsangi, H. Nezamabadi-pour, GCPSO in cooperation with graph theory to distribution network reconfiguration for energy saving. Energy Convers. Manag. **51**(3), 418–427 (2010). ISSN 0196-8904. https://doi.org/10.1016/j.enconman.2009.10.003
12. A.R. Abul'Wafa, A new heuristic approach for optimal reconfiguration in distribution systems. Electr. Power Syst. Res. **81**(2), 282–289 (2011). ISSN 0378-7796. https://doi.org/10.1016/j.epsr.2010.09.003
13. O. Badran, S. Mekhilef, H. Mokhlis, W. Dahalan, Optimal reconfiguration of distribution system connected with distributed generations: a review of different methodologies. Renew. Sustain. Energy Rev. **73**, 854–867 (2017). ISSN 1364-0321. https://doi.org/10.1016/j.rser.2017.02.010
14. A. Boum, P. Ndjependa, J. Bisse, Optimal reconfiguration of power distribution systems based on symbiotic organism search algorithm. J. Power Energy Eng. **5**, 1–9 (2017). https://doi.org/10.4236/jpee.2017.511001
15. A. Swarnkar, N. Gupta, K. R. Niazi, *Efficient Reconfiguration of Distribution Systems Using Ant Colony Optimization Adapted by Graph Theory*, (IEEE Power and Energy Society General Meeting, Detroit, MI, USA), pp. 1–8 (2011). https://doi.org/10.1109/PES.2011.6039006
16. S. Ahmadi, S. Abdi, Optimal reconfiguration of unbalanced distribution systems using a new hybrid big bang-big crunch algorithm for loss reduction, in *20th Conference on Electrical Power Distribution Networks Conference (EPDC)* (Zahedan), pp. 53–59 (2015). https://doi.org/10.1109/EPDC.2015.7330473(2015)
17. J. Zhu, X. Xiong, J. Zhang, G. Shen, Q. Xu, Y. Xue, A rule based comprehensive approach for reconfiguration of electrical distribution network. Electr. Power Syst. Res. **79**(2), 311–315 (2009). ISSN 0378-7796. https://doi.org/10.1016/j.epsr.2008.07.001
18. U. Raut, S. Mishra, Power distribution network reconfiguration for loss minimization using a new graph theory based genetic algorithm, in *IEEE Calcutta Conference (CALCON)* (Kolkata), pp. 1–5 (2017). https://doi.org/10.1109/CALCON.2017.8280684
19. M. Asadpour, A. Sproewitz, A. Billard, P. Dillenbourg, A.J. Ijspeert, Graph Signature for Self-Reconfiguration Planning, in *IEEE/RSJ International Conference on Intelligent Robots and Systems, Nice, 2008*, pp. 863–869 (2008). https://doi.org/10.1109/IROS.2008.4650673
20. R. Čađenović, D. Jakus, P. Sarajčev, J. Vasilj, *Optimal Reconfiguration of Distribution Network Using Cycle-Break/Genetic Algorithm.* (IEEE Manchester PowerTech, Manchester), pp. 1–6 (2017). https://doi.org/10.1109/PTC.2017.7980842

21. A. Kavousi-Fard, T. Niknam, Optimal distribution feeder reconfiguration for reliability improvement considering uncertainty. IEEE Trans. Power Deliv. **29**(3), 1344–1353 (2014). https://doi.org/10.1109/TPWRD.2013.2292951
22. Y. Yuehao, Z. Zhongqing, B. Wei, X. Jun, Q. Limin, D. Yaoheng, Optimal distribution network reconfiguration for load balancing, in *China International Conference on Electricity Distribution (CICED)* (Xi'an), pp. 1–4 (2016). https://doi.org/10.1109/CICED.2016.7576313
23. C. Xiaoming, C. Yongjin, W. Zhaolong, Y. Yingqi, R. Huixian, Flexible distribution system reconfiguration using graph theory and topology identification technology, in *International Conference on Power System Technology (POWERCON)* (Guangzhou), pp. 2008–2014 (2018). https://doi.org/10.1109/POWERCON.2018.8602307
24. M. Mosbah, S. Arif, R. D. Mohammedi, R. Zine, Optimal algerian distribution network reconfiguration using antlion algorithm for active power losses, in *3rd International Conference on Pattern Analysis and Intelligent Systems (PAIS)* (Tebessa), pp. 1–6 (2018). https://doi.org/10.1109/PAIS.2018.8598534
25. D. Sarkar, P. Konwar, A. De, S. Goswami, A graph theory application for fast and efficient search of optimal radialized distribution network topology. J. King Saud Univ. Eng. Sci. **32**(4), 255–264 (2019)

# PKL Backup LED Bulb—An Alternative Source of Electricity During Load Shading


**K. A. Khan, Shahinul Islam, Salman Rahman Rasel, M. A. Saime, Syful Islam, and M. Hazrat Ali**

## 1 Introduction

Energy sources are divided into two parts: Renewable energy sources and Non-renewable energy sources [1, 2]. Oil, gas and coal are the non-renewable energy sources [3, 4]. It is not an unlimited source. It will be finished within 2100. Then after that, what will happen, actually nobody knows. That is why it is very much necessary to conduct research on renewable energy sources [5, 6]. A renewable energy source is a type of source which is not limited. It can be used again and again and will never run out. Examples of renewable energy sources are solar energy, wind energy, biogas energy, biomass energy, geothermal energy, water energy, tidal energy, wave energy and OTEC [7, 8]. Now, we should increase the use of renewable energy resources for practical utilizations. To keep it in mind, research has been conducted on biomass energy [9]. The PKL power is part of biomass energy. We have conducted research on PKL electricity for many years through an extract base. But this research work is different from that process. In this research paper, living and fresh PKL backup LED bulb has been used. research has been conducted for power production from PKL

K. A. Khan (✉)
Department of Physics, Jagannath University, Dhaka 1100, Bangladesh

S. Islam
Department of Physics, Uttara University, Dhaka, Bangladesh

S. R. Rasel
Local Government Engineering Department (LGED), Fulbaria, Mymensing, Bangladesh

M. A. Saime
Dinajpur Polytechnic Institute, Dinajpur, Bangladesh

S. Islam
Government Louhajang University College, Louhajang, Munshigonj, Bangladesh

M. H. Ali
European University of Bangladesh (EUB), Dhaka, Bangladesh



C. K. Chanda et al. (eds.), *Advanced Energy and Control Systems*, Lecture Notes in Electrical Engineering 820, https://doi.org/10.1007/978-981-16-7274-3_7

leaf directly in 3 different forms like PKL extract, living PKL and fresh PKL [10]. During load shading, this PKL backup LED bulb can help people both in urban and rural areas. Some similar research works have been done entitled "Development of cells for generation of potential difference from Aloe Vera" by Wajire and Gandole [11]. Similar works have also been done by the Massachusetts Institute of Technology (MIT) and University of Washington (UW), USA. They have found that it is possible to generate 250 mV when the electrodes are placed between two points in a tree. They have also found that if one electrode is placed in a living plant and other is placed into the soil, then electricity is produced [12]. Furthermore, previously we got 1.1 V for Zn/Cu single pair electrodes using PKL extract, whereas we got 1.00 V for Zn/Cu single pair electrodes using living PKL and 0.9 V for Zn/Cu single pair electrodes using fresh PKL. These are alternative sources of energy. Scientists are assuming that global climate change will not be controlled artificially. It needs to stop burning natural different renewable energy sources like biomass energy. If we start electricity generation from living trees or plants, then everyone wants to be plant in one's surroundings. Our Governments are motivated to the people such a process of plantation of trees and plants. As a result, a number of different trees are increasing in our countries [13]. This type of plantation will help to save our planet indirectly from the dangerous issue of global warming. This plant and tree energy is improbable to replace the power sources for most applications. Furthermore, After R&D, this type of energy could be of low cost, environmentally friendly, pollution-free and a natural option of the electricity or power source [14]. These research outputs may be the guid line for different practical utilizations in near future.

## 2 Materials and Method

### *2.1 Working Principle of PKL Backup LED Bulb*

(i) **Electroluminescence:**

When electricity passes through the diode, the diode emits photons and finally creates light through the principle of electroluminescence. The mechanism of electroluminescence is the recombination of electron-hole pairs due to the flow of Electricity through the diode. The emission of light (in the form of photons) is the Output of the release of energy due to excited electrons. There is an adaptor in the Electronic circuit, and it converts alternating current (AC) to direct current (DC). The Diode gets DC by a bridge rectifier from the grid or from the PKL electricity produced by PKL extract-based source and emits photons and finally light is produced. In the unelectrified areas, an inverter is needed (DC to AC converter for proving AC Electricity to the PKL backup LED bulb). But during load shading, PKL backup LED bulb did not get grid electricity. Then the PKL extract-based electricity with an Inverter can be the alternative for grid electricity. At that moment to face the load shading, fresh PKL and living PKL can back up the LED bulb instantly.

(ii) **Chemiluminescence:**

As a chemical reaction, emission of light which is called Chemiluminescence occurs. Some emission of heat in a limited manner also occurs.

**Principle of Chemiluminescence:**

Due to a chemical reaction, electromagnetic radiation is generated as light by the release of energy. The light can be emitted into 3 parts: ultraviolet, infrared and visible light. Among them, visible light is most common. Let us consider the two reactants A and B, with an excited intermediate $\varphi$, then the chemical reaction of the Chemiluminescence is $[A] + [B] \rightarrow [\varphi] \rightarrow [\text{Products}] + \text{light}$.

(iii) **Principle of Bioluminescence:**

The production and emission of light by a living organism is called bioluminescence (Fig. 1). It is nothing but one of the forms of chemiluminescence. It occurs through a chemical reaction that produces light energy within an organism's body. For any reaction to happen, a species must contain a molecule named luciferin, which reacts with oxygen and produces light. Many organisms also produce luciferase which works as a catalyst to speed up the reaction.

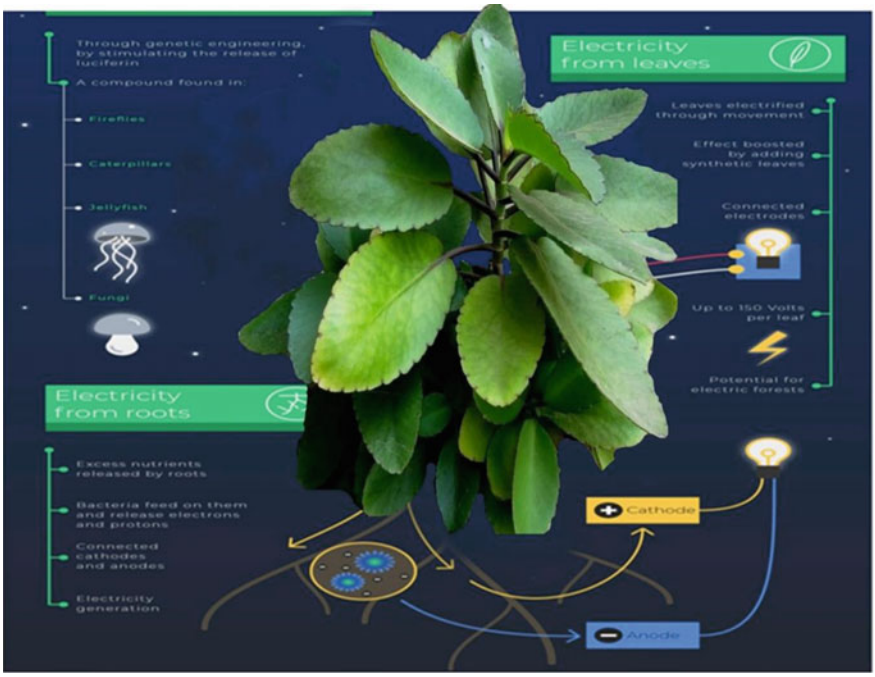


**Fig.1** Methods of production and emission of light by a living organism

## 2.2 Types of Luminescence and Their Energy Sources

Luminescence is nothing but the emission of light by electromagnetic waves of a substance which does not arise from heating. Luminescence is divided into 7 parts:

(1) Photoluminescence (absorption of photons) → Fluorescence and Phosphorescence.
(2) Cathodoluminescence (bombardment by electrons).
(3) Chemiluminescence (initiated by chemical reactions) → Bioluminescence, Electroluminescence, Candoluminescence and Lyoluminescence.
(4) Electroluminescence (applied by electric field).
(5) Mechanoluminescence (through mechanical action) → Triboluminescence, Fractoluminescence, Plazoluminescence and Sonoluminescence.
(6) Radioluminescence (bombardment by ionizing radiation).
(7) Thermoluminescence (activated by heating).

## 2.3 Materials for PKL Backup LED Bulb

The required materials are (i) Fresh PKL, (ii) Living PKL, (iii) PKL extract, (iv) An electronic circuit inside the LED bulb, (v) A small storage battery inside the LED bulb, (vi) A small charge controller inside the LED bulb, (vii) A small Printed Circuit Board (PCB) inside the LED bulb, (viii) Inverter, (ix) Bridge rectifier, (x) Transformer and (xi) Lux meter.

1st Step: An electronic circuit is designed and fabricated inside the LED bulb where there is a small storage battery, a small charge controller, and a small Printed Circuit Board (PCB).

2nd Step: A PKL battery and an inverter are taken to light a 20 W LED bulb. Then the LED bulb is used for 1 h.

3rd Step: Then the LED bulb is set up under short-circuit condition by a fresh and living PKL. The time duration is collected by a stopwatch.

It is shown from Fig. 2 that the LED bulb lights up with short-circuit condition by a single fresh Pathor Kuchi Leaf (PKL). The LED bulb is connected with one single fresh leaf only. The intensity is measured by a lux meter.

It is shown from Fig. 3 that the LED bulb lights up with short-circuit condition by a single garden living Pathor Kuchi Leaf (PKL). The LED bulb is attached with

(a) (b)

**Fig. 2** Experimental setup for 20 W PKL backup LED bulb with a single fresh Pathor Kuchi Leaf


**Fig. 3** PKL backup LED bulb lights with short-circuit condition by a garden living Pathor Kuchi Leaf (PKL)

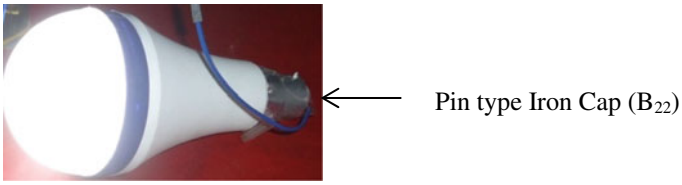


**Fig. 4** LED bulb lights with self-short-circuit condition

only one single living leaf from a living PKL tree. The intensity was measured by a Lux meter.

It is shown from Fig. 4 that the battery LED bulb lights up with a self-short-circuit condition without any fresh or living Pathor Kuchi Leaf (PKL). The intensity was measured by a Lux meter.

The data of the intensity of light was collected by a Lux meter (shown in Fig. 11) with time duration. With the help of this data a curve for the variation of Intensity has been drawn with time duration without the 20 W PKL backup LED bulb.

Ag Nanoparticles (NPs) have been synthesized and characterized for monitoring of power production. Figure 5 shows that firstly the voltage was collected from living PKL using Zn/Cu electrodes without Ag NPs and secondly the voltage was collected from living PKL using Zn/Cu electrodes with Ag NPs. The Ag NPs were in liquid form.

Figure 12 shows the data for voltage collection using the living PKL tree and the effect of Ag NPs. The voltages were measured by a calibrated multimeter. The time duration for data collection was 100 min.

## *2.4 Block Diagram for Charging and Discharging of the Experimental Setup of the PKL Backup LED Bulb*

The block diagram for charging and discharging is given below.

Figure 6 shows that the PKL electricity which is generated from the leaf extract is DC and is converted to AC by an inverter. By using AC, the LED bulb has to be

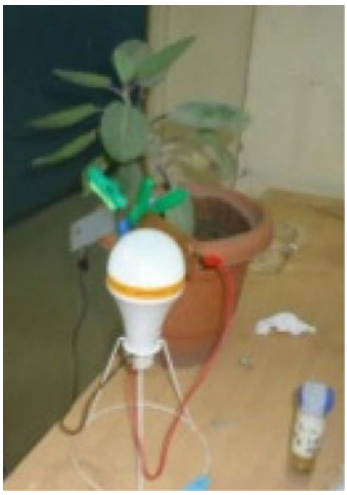

**Fig. 5** Experimental setup for voltage measurement with and without NPs

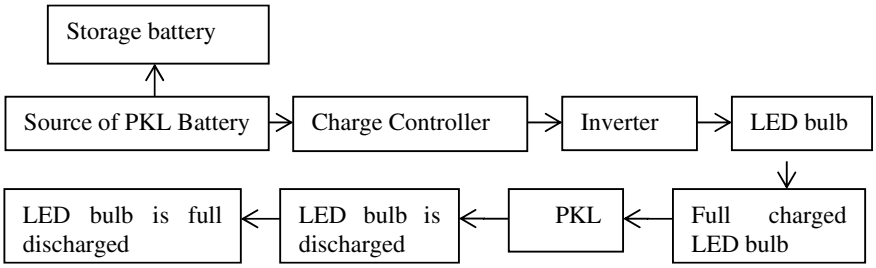


**Fig. 6** Block diagram of the experimental setup of the PKL backup LED bulb during charging and discharging

fully charged with the help of an adaptor. A living or fresh PKL has been set up with the two ends of a designed and fabricated lead bulb. The time duration (measured by stopwatch) and intensity (measured by Lux meter) of the LED bulb have been recorded.

## *2.5 Circuit Diagram of the Experimental Setup of the PKL Backup LED Bulb*

Figure 7 shows the experimental circuit diagram of the PKL backup LED bulb. There is a digital Printed Circuit Board (PCB). There are total 47 diodes (36 AC diodes and 11 DC diodes), 2 Integrated Circuits (ICs) and 1PWM (Pulse Width Modulation)

IC which controls drop voltage and drop current and then power. Finally, the PWM IC-1 acts as a power control IC and IC-2 works for battery charging and discharging. The 5 resistors, Resistors $R_3$ acts as a shunt resistor which converts drop voltage to current, Diode ($D_1$) is the Silicon Carbide Diode which is the series of ES1J or, ES2J high speed switch (kHz to MHz range), 1 Socket which is a SSD (Solid State Device). Here, Power IC controls the power of the circuit. There is a Bridge rectifier which converts from 220 AC to 310 DC and this is also called high-speed diode. The surface mounted device (SMD) LED converts electrical energy into optical energy. The socket is used to control the different connections. The 5 resistors is used for current sensing. Here, N indicates negative and L indicates positive terminals. The resistors R3 is used for feedback voltage but PWM IC converts current. There is a charge controller on the PCB also. There is a small transformer on the PCB. There is a small rechargeable battery under the PCB. It can be charged by the alternating current (AC) with the connection of a transformer, rectifier, charge controller, storage battery, inverter and then LED light. The LED light and the storage battery are connected with the charge controller. The block diagram can be summarized by the following.

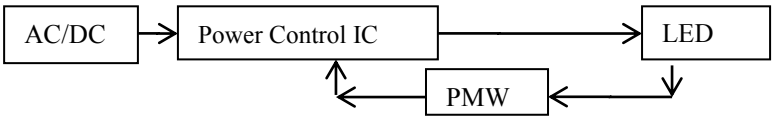


A DC-to-DC buck converter needs high voltage into low voltage. A DC-to-DC boost converter needs low voltage into high voltage. AcBuck-Boost Converter can also be used. The Iron cap can be pass type ($E_{27}$) and Pin type ($B_{22}$). The Pin type ($B_{22}$) has been used in our research work. The array mismatch factor has been considered here.

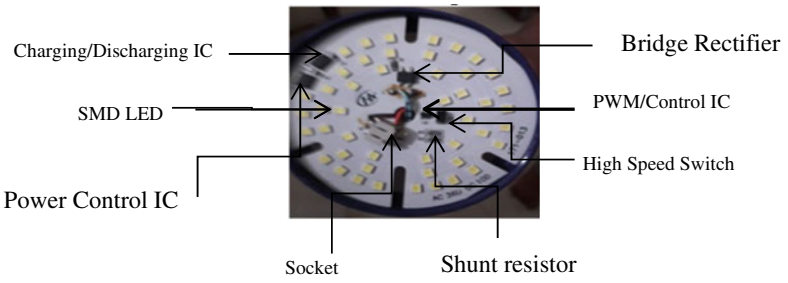


**Fig. 7** Experimental setup of different electronic components of the experimental setup of the PKL backup LED bulb

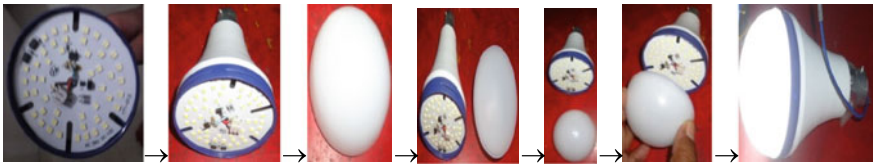


**Fig. 8** Different steps of the Experimental setup of the PKL backup LED bulb

## *2.6 Experimental Setup of the PKL Backup LED Bulb*

Figure 8a shows the circuit with PCB for LED bulb; Fig. 8b shows that covered by a back cover where there is a small storage mobile phone battery. Figure 8c shows the outer cover of the bulb and Fig. 8d shows the LED bulb and outer cover side by side together. Figure 8e shows the LED bulb and outer front cover made of plastic face to face together. Figure 8f shows the LED bulb and outer cover face to face moving along each other for finish product and Fig. 8g shows the final and fresh product of the LED bulb.

## *2.7 Peukert's Law for PKL Backup LED Bulb*

In 1897, the German scientist W. Peukert expressed the capacity of a lead–acid battery with respect to the rate of discharging the battery. As the rate increases, the battery's available capacity decreases. Peukert's law can be written as

$$t = H(C/IH)^k \tag{1}$$

where H = the rated discharge time (h), C = the rated capacity at that discharge rate (Ah), I = the actual discharge current (A) and k = Peukert's constant (dimensionless). The value of k lies between 1.1 and 1.3 and t = the actual time to discharge the battery or cell ( h) through the fresh or living PKL or self-discharge.

# 3 Results and Discussion

Figure 9 shows the variation of Intensity with time duration for 20 W PKL backup LED bulb with a single fresh Pathor Kuchi Leaf. The total time duration was 1200 min. The 20 W PKL backup LED bulb was charged by a PKL module with the help of an inverter. Then, it was discharged with the help of a single fresh Pathor Kuchi Leaf (PKL). It is shown that the intensity decreases slowly up to 185 min.

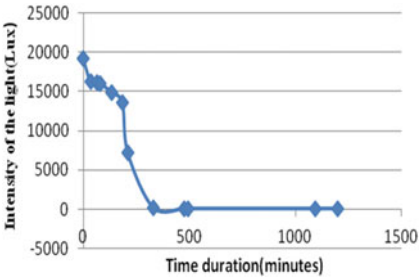


**Fig. 9** Variation of Intensity with time duration for 20 W PKL backup LED bulb with a single fresh Pathor Kuchi Leaf (PKL)

Then it decreases rapidly up to 1200 min. It is concluded that the discharge through the fresh PKL follows Peukert's law, $t = H(C/IH)^k$.

Figure 10 shows the variation of Intensity with time duration for 20 W PKL backup LED bulb with a single living Pathor Kuchi Leaf. The total time duration was 1200 min. Firstly, the 20 W PKL backup LED bulb was charged by a PKL module with the help of an inverter. Then, it was discharged with the help of a single Pathor Kuchi Leaf (PKL). It is shown that the intensity decreases slowly up to 185 min. Then it decreases rapidly up to 1200 min. It is concluded that the discharge through the fresh PKL follws Peukert's law, $t = H(C/IH)^k$.

Figure 11 shows the variation of Intensity with time duration without 20 W PKL backup LED bulb. The total time duration was 1200 min. Firstly, the 20 W PKL backup LED bulb was charged by a PKL module with the help of an inverter. Then, it was discharged without the help of a single living or fresh Pathor Kuchi Leaf (PKL). It is shown that the intensity decreases rapidly up to 185 min. Then it decreases very

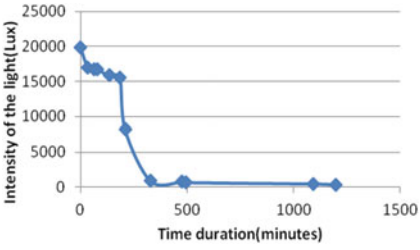


**Fig. 10** Variation of Intensity with time duration for 20 W PKL backup LED bulb with a single living Pathor Kuchi Leaf (PKL)

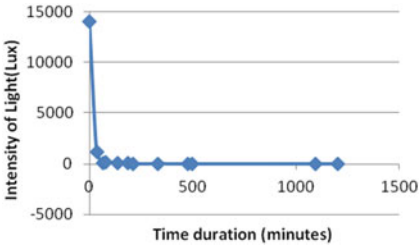


**Fig. 11** Variation of Intensity with time duration for a LED bulb with short-circuit condition

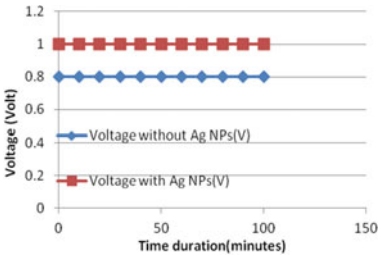


**Fig. 12** Variation of voltage with the time duration for using with and without Ag NPs

rapidly up to 1200 min. It is concluded that the discharge through the fresh PKL follows Peukert's law, $t = H(C/IH)^k$.

Figure 12 shows the variation of voltage with the variation of time duration with and without Ag NPs. Firstly, the voltage was collected without Ag NPs. The collected voltage was 0.8 V. It is also shown that the voltage was constant for 100 min. Zinc and Copper plates were used between two sides of a single living PKL leaf. Then the liquid Ag NPs were used between the Zinc and single living PKL & Copper and single living PKL. It is also shown that the collected voltage for using Ag NPs was 1.00 V. This voltage was also totally constant for 100 min.

## 4 Conclusions

This type of research work has not been done yet. The output of this research work can be used both in rural and urban areas during load shading. For R&D, work should be continued to get better performance. Double or triple living and fresh leaves should be used instead of single living or fresh leaf. The effect of different NPs should be used to get better performance. Ultra-low-cost electrodes should be used for further works to get better performance. Using single or double PKL, anybody can face the load shading problem both in urban and rural areas. If the researchers start conducting research on living trees and fresh leaves, then our dependence on conventional sources (oil, gas and coal) may be reduced to a great extent. If we start to use the living PKL trees and PKL fresh leaves surrounded by us for lighting our PKL backup LED bulb, then our imagination can cross the boundaries.

## References

1. P.E. Coombe, Visual behaviour of the greenhouse whitefly. Trialeurodes vaporariorum. Physiol Entomol **7**, 243–251 (1982)
2. H.S. Costa, K.L. Robb, C.A. Wilen, Field trials measuring the effects of ultraviolet-absorbing greenhouse plastic films on insect populations. J Econ Entomol **95**, 113–120 (2002)
3. K.A. Khan, Copper oxide coatings for use in a linear solar Fresnel reflecting concentrating collector, Published in the Journal of Elsevier, Renewable Energy, An International Journal,

WREN (World Renewable Energy Network), UK, RE: 12.97/859,1998, Publication date 1999/8/1, J. Renewable Energy **17**( 4), 603–608. Publisher-Pergamon (1999)

4. T.A. Ruhane, M. Tauhidul Islam, M.D. Saifur Rahman, M.M.H. Bhuiyah, Jahid, M.M. Islam, T.I. Bhuiyah, K.A. Khan, M.A. Khan, Impact of photo electrode thickness annealing temperature on natural dye sensitized solar cell, in *Sustainable Energy Technologies and Assessments* (Elsevier, 2017). https://doi.org/10.1016/j.seta.2017.01.012
5. T.A. Ruhane, M. Tauhidul Islam, M.D. Saifur Rahaman, M.M.H. Bhuiyan, Jahid, M.M. Islam, M.K. Newaz, K.A. Khan, M.A. Khan, Photo current enhancement of natural dye sensitized solar cell by optimizing dye extraction and its loading period. Optik – Int. J. Light Electron Opt. Elsevier (2017)
6. M. Hasan, K.A. Khan ,Dynamic model of Bryophyllum pinnatum leaf fueled BPL cell: a possible alternate source of electricity at the off-grid region in Bangladesh, in Microsystem Technologies Micro - and Nanosystems Information Storage and Processing Systems, Springer, ISSN 0946–7076, Microsyst. Technol. (2018). https://doi.org/10.1007/s00542-018-4149-y
7. K.A. Khan, M. Hazrat Ali, A.K.M. Obaydullah, M.A. Wadud, Production of candle using solar thermal technology, Microsystem Technologies Micro- and Nanosystems Information Storage and Processing Systems, Springer, ISSN 0946–7076, Microsyst. Technol. **25**(12) (2019). https://doi.org/10.1007/s00542-019-04390-7
8. K.A. Khan, S.R. Rasel, M. Ohiduzzaman, Homemade PKL electricity generation for use in DC fan at remote areas, Microsystem Technologies Micro- and Nanosystems Information Storage and Processing Systems, ISSN 0946–7076, Microsyst. Technol., **25**(12) (2019). https://doi.org/10.1007/s00542-019-04422-2
9. M. Hasan, K.A. Khan, Experimental characterization and identification of cell parameters in a BPL electrochemical device. Springer, SN Appl. Sci. **1**, 1008 (2019). https://doi.org/10.1007/s42452-019-1045-8,(2019)
10. L. Hassan, K.A. Khan, A study on harvesting of PKL electricity. Springer J., Microsyst Technol. **26**(3), 1031–1041 (2020). https://doi.org/10.1007/s00542-019-04625-7
11. K.A. Khan, M.A. Mamun, M. Ibrahim, M. Hasan, M. Ohiduzzaman, A. K.M. Obaydullah, M.A. Wadud, M. Shajahan, PKL electrochemical cell: physics and chemistry. Springer J., SN Appl. Sci. **1**, 1335 (2019).| https://doi.org/10.1007/s42452-019-1363-x
12. M. Hazrat Ali, U. Chakma, D. Howlader, M. Tawhidul Islam, K.A. Khan, *Studies on Performance Parametersof a Practical Transformer for Various Utilizations, Microsystem Technologies*, Springer, Accepted:03 Dec 2019, https://doi.org/10.1007/s00542-019-04711-w
13. K.A. Khan, L. Hassan, A.K.M. Obaydullah et al., Bioelectricity: a new approach to provide the electrical power from vegetative and fruits at off-grid region. Microsyst Technol (2018). https://doi.org/10.1007/s00542-018-3808-3
14. K.A. Khan, M.S. Bhuyan, M.A. Mamun, M. Ibrahim, L. Hasan, M.A. Wadud, Organic electricity from Zn/Cu-PKL electrochemical cell, in *Contemporary Advances in Innovative and Applicable Information Technology, Advances in Intelligent Systems and Computing*, ed. by J.K. Mandal et al. (eds.), © Springer Nature Singapore Pvt. Ltd., 2018, vol. 812, Chapter 9 (2018), pp. 75–90

# A Study of Nanomaterials Application for Future Energy Storage Devices


**Silpee Talukdar and Rudra Sankar Dhar**

## 1 Introduction

Energy resources and storage are the future of industrial growth and developments. Seeing the ongoing energy crisis, scientists have started focusing their research activities on energy-related novel materials. Energy storage devices compete in upgradation of the electronic gadget industry. Besides, high capacity and high power rated systems are favorable for static appliances like load-leveler in power plants and mobile appliances like electric vehicles [1, 2].

The search for a longer life cycle, capacity and secured energy storage system is quickly advancing. With the growing interest toward environment-friendly technology owing to population and global economy, renewable and clean energy has become a genuine concern for today's society [3]. Since electricity is one of the most convenient energy forms among all the energy for it is easily convertible to other energy forms, long-lasting research and industrial fervor catch an eye for electrical energy storage system, specially rechargeable battery and supercapacitor which are mostly used in stationary and mobile application [4, 5]. In 1991, Sony as a company has succeeded in the marketing of lithium-ion batteries (LIB). Since then, LIBs has been used in cell phones, laptops, hybrid and electric vehicle market. Nanotechnology has been attracted toward future energy improvement technology to offer environment compatible, large consumer distribution, higher security and lesser manufacturing cost. Nanomaterials are used as electrode material and thin film membrane in energy storage devices to make them superior and highly compatible. Nanostructures

S. Talukdar · R. S. Dhar (✉)
Department of Electronics and Communication Engineering, National Institute of Technology Mizoram, Mizoram 796012, India
e-mail: rudra.ece@nitmz.ac.in

S. Talukdar
e-mail: silpee.ece.phd@nitmz.ac.in



C. K. Chanda et al. (eds.), *Advanced Energy and Control Systems*, Lecture Notes in Electrical Engineering 820, https://doi.org/10.1007/978-981-16-7274-3_8

show some unique and fascinating properties due to which they are used in upcoming technology for energy storage systems [6–8].

### *1.1 Unique Properties of Nanomaterial*

i. Nanomaterials exhibit remarkable optical, electronic, mechanical and magnetic characteristics for quantum effect.
ii. Reactive responses of Nanomaterials are significantly distinctive to their macroscopic geometry.
iii. Surface area per unit mass is vastly increased for Nanoscale materials.
iv. Novel structured geometry can be obtained, e.g., fullerenes, CNT, $TiO_2$, ZnO and other composites.

## 2 Application

Some of the nanostructures that are extensively used in various energy storage has briefed below.

### *2.1 CNT Application in Energy Storage*

Carbon nanotubes (CNT) are auspicious materials for electrodes in energy storage. CNTs are of two types, single-wall nanotube (SWNT) and multi-wall nanotube (MWNT). The carbon atoms are arranged in a hexagonal pattern in CNT [9–11]. CNTs show notable features of excellent conductivity, high ion transfer capacity, more surface domain, more mesoporosity and superior electrolytic accessibility, for which they are desirable materials for lithium-ion batteries [12, 13]. Currently, CNTs are considered for conductive additive and host nanostructure. The higher capability of CNT can be obtained by fissuring or fragmenting the CNTs. On charging and discharging, carbon-based materials experienced irreversible capability [14, 15].

### *2.2 Silicon Nanoparticles Application in Energy Storage*

Since Si exhibits high theoretical capacity, it is considered as an excellent anode material for energy storage systems. Upon lithiation, Si changes to large volume which is headed to Si pounding and capacity loss [16, 17]. One-dimensional Si nanostructures show higher capacity and durability for three reasons: (i) more volume vs surface ratio, (ii) more specific surface area and (iii) nanosized radial dimension.

Si nanotubes are in current research for their hollow structure which offers large volume change accommodation. The mesoporous Si nanorod improves Columbic efficiency and cycling performance by magnetiothermic reduction process [18, 19].

## 2.3 Metal Nanoparticles and Composites Application in Energy Storage

Due to the low Free State energy and specific capacity of the metal oxides, they are undoubtedly promising materials for energy storage systems. The energy density of LIBs could be almost doubled within 10 years using metal compounds (such as the compounds $LiNi_xCo_yAl_zO_2$; NCA) as cathode material. Using metal phosphates nanocomposites (e.g., $LiXPO_4$ where X represents Ni, Fe, Mn and Co), considerably $LiMnPO_4$, $LiCoPO_4$ or $LiFePO_4$, the energy density of Li-ion battery can also be enhanced [20, 21]. In lithium sulfur battery or sodium sulfur battery, Nanomaterials like compounds of silicon and tin are used to increase cycling performance. Recent technology of printed battery shows that use of Nanomaterials like silver, copper, aluminum and nickel and metallic compounds, generally ZnO can make it translucent and steady in ion intercalation state. In nanocapacitors, during the implementation of extremely organized porous $Al_2O_3$ nano-film fabricated with TiN conductive nanoshape, the potentiality of nanocapacitors can be increased [22, 23]. Research is going on hydrogen storage cells in nanolevel for confining abundant hydrogen in a lesser area. Depository materials like $BH_6N$ as well as CNT, metallic compounds or Ti, Fe or Ni alloys are employed with chemical and physical reversible bond of hydrogen, and for that, the chance of outbursting can be restrained [24]. Nanocubes of metal–organic composites which are crisscrossed in the intensified network of nanosized pores are essentially used for the abundant surface domain in accessible storage. Metal Nanomaterials are also used in smart windows to make them transparent to translucent (and vice versa). Metal oxides or composites of metals of titanium, vanadium, chromium, manganese, iron, cobalt, nickel, molybdenum, tantalum, tungsten, rhodium and iridium are used as electrodes in electrochromic devices. Besides some metal nanoparticles like silver (Ag), iron (Fe) compounds are used as suspended nanoparticles on thin film for enhancing the efficiency of smart electrochromic devices [25].

## 2.4 Polymer Application in Energy Storage

Conducting polymers are used in energy conversion and storage materials for their desirable physical property, large surface areas and diminished path length. CNT and Polyaniline nanofibers exhibit high capacity (147mAh/g) and more lifespan (over 10,000 cycles) [26, 27]. $MnO_2$ and PEDOT are treated as the cathode in LIBs

for their high capability and capacity retention. Poly (3, 4-ethylenedioxythiophene) (PEDOT) nanotubes processed in an electrochemical template approach used in supercapacitors exhibit high power performance [27, 28].

## 3 Discussion

The capacity of energy storage device from charge–discharge can be obtained by using the following formula:

1. For linear charge–discharge curve,

$$C = I\Delta s/\mu(M_f - M_i) \tag{1}$$

where C is the capacity, I is current intensity, $\Delta s$ is discharge time, $\mu$ is the electrode mass and $(M_f - M_i)$ is the functional potential frame.

2. For non-linear charge–discharge curve,

$$C = 2I \int K dx \Big/ \mu\left(M_f - M_i\right)^2 \tag{2}$$

where $\int K dx$ is area under charge–discharge curve.

The transmittance of the device can be formulated as follows:

$$\rho = I/I_0 \tag{3}$$

where $\rho$ is the transmittance, I is light intensity running through the sample and $I_0$ is initial intensity.

The optical density (OD) can be formulated as follows:

$$OD = log_{10}\frac{I_o}{I} \tag{4}$$

Some of the Nanomaterial used in batteries and supercapacitors are given below with their morphology, synthesis strategy and capacity in Table 1 [9].

Kartick et al. [23] presented the charge–discharge patterns of $WS_2$, MWCNT and $WS_2$-MWCNT (1:1) compound when the current density is 50 $mAg^{-1}$. The observations from the graph are as follows:

- MWCNT revealed an initial ion transportation capacity of 500 (discharge) and 261 $mAhg^{-1}$ (charge), respectively.
- $WS_2$ are found to be 579 (discharge) and 424 $mAhg^{-1}$ (charge). The first discharge graph in $WS_2$ conveys the presence of two plateau domains at ~1.5 V and 0.54 V.

**Table 1** Some nanostructures used in energy storage (swnt = single-wall nanotube, mwnt = multi-wall nanotube, nw = nanowire, nr = nanorod, nt = nanotube, ce = chemical etching, e = electrospinning, t = template assisted, l = liquid state, cd = chemical deposition)

| Nanomaterial | Structured | Methods | Capacity in mAh/g |
|---|---|---|---|
| C | MWNT | T | 400 |
| C | SWNT | CE | 700 |
| N-doped C | NW | E | 632 |
| Silicon | NR | T | 2411 |
| Sn-doped $TiO_2$ | NT | L | 252 |
| $Co_3O_4$ α $Fe_2O_3$ | NW | L | 980 |
| $MnO_2$/ PEDOT | NW | T | 300 |
| $NiCo_2O_4$ | NT | E | 1756 |
| ZnO/$Mn_3O_4$ | NT | T | 4412 |
| PANI | NW | CD | 950 |
| C/NiO | NT | CD | 1657 |
| PANI/C | Hybrid | L | 448 |

- The profile of $WS_2$-MWCNT (1:1) hybrid manifests as like $WS_2$, this indicates appreciably elevated initial discharge capacity (925 $mAhg^{-1}$) and charge capacity (483 $mAhg^{-1}$).

It is observed that in the presence of MWCNT with metal compounds, the capacity as well as ion storage within the device improves due to the morphology of MWCNT and metal compound composites and enhances electron transportation in charge–discharge process, i.e., cathode to anode and anode to cathode [23]. Because of the presence of MWCNT, storage of $Li^+$ gets enhanced and this improves the capacity of the energy system. The charge–discharge profile of $WS_2$, MWCNT and composition of $WS_2$-MWCNT is represented in Fig. 1. At 100 $mAg^{-1}$, cyclic reversibility of $WS_2$, MWCNT and $WS_2$-MWCNT had been observed which is stated as follows:

- MWCNT possessed reversible cyclic performance at a specific capacity of ~260 $mAg^{-1}$ after 20 cycles.
- $WS_2$ held 350 mAh/g capacity in the first cycle and gradually degraded with the cycle at a rate of 10.4 mAh/g.
- $WS_2$-MWCNT was detected with 430 mAh/g in the first cycle and after 20 cycles, the specific capacity was at 346 mAh/g.

Chen et al. [9] noticed retained capacity over cycle time of Si NT without oxide, Si NW and DWSi NT. The findings are stated as follows:

- After 6000 cycles, DWSiNT shows 88% capacity retention at a 10C rate. In spite of the Coulombic efficiency of DWSiNT at first cycle is 76%, the average Coulombic efficiency is 99.938% from 2nd to 6000 cycles.
- The observations clearly show that double-walled silicon nanotube (DWSiNT) has more capacity than Si Nanowires and Si nanotube without oxide. DWSiNT has 88% capacity retention after 6000 cycles at a 10C rate, which indicates the device will be capable of storing more charge, and thereby energy storage for

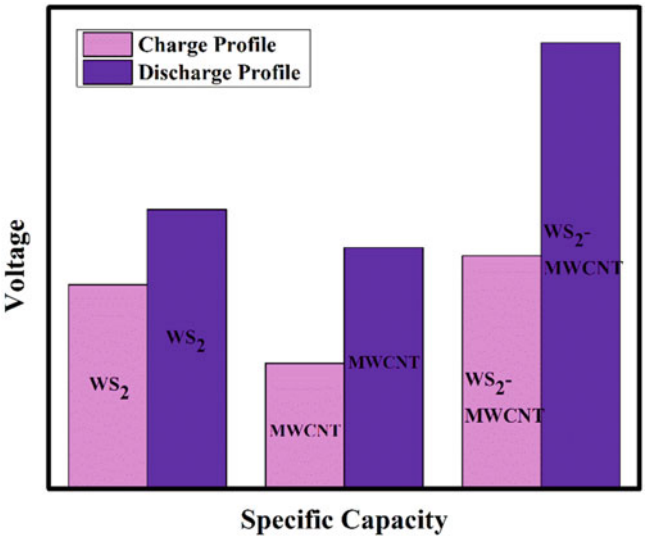


**Fig. 1** Charge–discharge profile of $WS_2$, MWCNT and $WS_2$-MWCNT

further usage may be a better alternative in comparison to Si nanotubes without oxide.

- DWSiNT holds stable electrochemical effect on charge–discharge profile.
- The nanorange and steady SEI DWSiNT allows swift $Li^+$ ion transportation through SEI making the energy device highly capacitive. The average Coulombic efficiency of DWSiNT specifies that the material is a highly desirable option for future energy storage devices.

Gillaspie et al. [29] worked on the transmittance of Li$x$Ni$_{1-x}$O at different annealing temperatures. The studies of Li$x$Ni$_{1-x}$O transmittance are as follows:

- As the film of Li$x$Ni$_{1-x}$O crystallites is annealed, the film bleaches strongly.
- Because the amount of lithium in the film presumably does not change drastically at this temperature and time scale, there is a reduction of the film due to oxygen loss at the grain boundaries. The opposite effect is seen in nickel oxide films exposed to ozone.
- As the oxidation reaction goes on the film, transmittance slashes making the device translucent.

Yan et al. [30] forwarded the V–T curve of PSLC devices in under 1 kHz square wave AC operation. The revelations are as follows:

- The peak transmittance of all PSLC devices is found to be 95%.
- It is seen that the optical transmittance in both positive and negative conditions reduced with Ag NW doping of 0.01 wt% and when Ag NW concentration increases to 0.1 wt%, the transmittance also improved. It happened due to the rich

concentration where Ag NW was randomly distributed in LC and agglomerate together, showing inter-connection between the Ag NW.

- When voltage continuously grows, aggregation of silver nanowires will form a local short-circuit, which affects device efficiency and increases the transmittance.
- At specific voltage, the current of PSLC device doped with 0.01wt% and 0.02wt% Ag nanowires decreases as Ag nanowire concentration enriches.
- When the Ag nanowire doping concentration is 0.02 wt%, the current is the lowest due to impurity in PSLC compounds surrounded by Ag NW.
- At lower LC conductivity, the liquid crystal molecules experience powerful electric force resulting in minimal threshold voltage and rapid response.
- The consequences of minimal doping of Ag NW help to drop impurity and electrical response rises excellently, developing a device having superior electro-optical response.

Zhou et al. [31] represented the plots of charge density at 630 nm and 1100 nm and CE of the as-synthesized $WO_3$/Ag NW (89 Ω/sq.) and $WO_3$ /ITO. It is stated as follows:

- The CEs of $WO_3$/Ag NW are 50 and 86.9 $cm^2$/c at 630 nm and 1100 nm.
- A high CE of 86.9 $cm^2$/c is obtained at the NIR region of 1100 nm for EC $WO_3$ materials.
- $WO_3$/ITO film CE are 57.5 and 43.7 $cm^2$ $C^{-1}$ at 1100 and 630 nm, respectively.
- The Electrochromic Device (ECD) comprising of glass/Ag NW/$LiClO_4$ + PC + PMMA/ $WO_3$/Ag NW/glass bleaching transmittance was found to ~47% in visible and ~58% in the NIR domain.
- Another ECD consisting of ITO deposited glass/ $WO_3$/$LiClO_4$ + PC + PMMA/ITO deposited glass was investigated for transmittance results at ~78% over visible and ~65% over NIR spectra.

Wang et al. [32] disclosed the FTIR characteristics of P (TMC-DLLA) for in-vivo application for 4 weeks. The findings are as follows:

- Stretching bands at 3514/cm from OH groups enhanced while compared with existing analysis.
- P (TMC-DLLA) hydrolytically degraded and regenerated numbers of OH groups.
- After 2 weeks mass loss was 2.6%, 4 weeks 5.6% and 8 weeks mass loss approached 12.6%.

Li et al. [33] forwarded the transmittance plot of mono-, bi- and tri-structured graphene. The observations are stated as follows:

- Transmittance of mono-, bi- and tri-layer graphene are 97.5%, 94.9% and 92.4%, respectively. The representation is plotted in Fig. 2.
- Due to suspended graphene, a minor deviation is observed at 1000 nm. The deviation is due to chemical residue for ion transfer.
- At 600–1200 nm, transmission is constant, outside of which it begins to deviate.
- More than 300 nm, spectra show consistency in both Visible light and UV light.

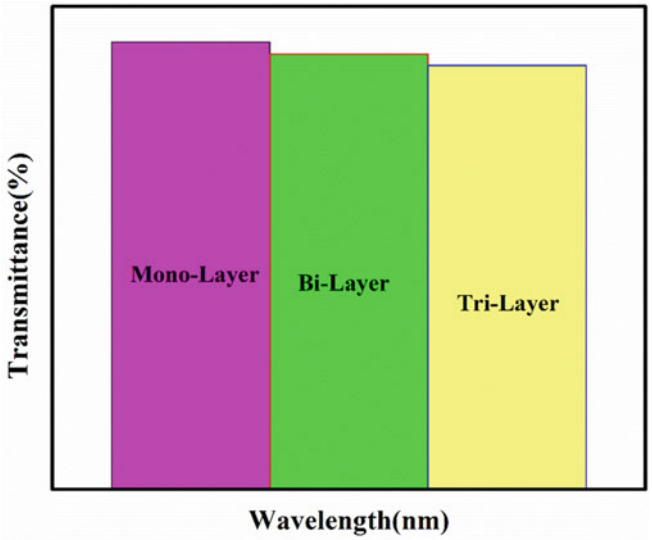


**Fig. 2** Difference of transmittance in mono-, bi- and tri-layer Graphene

Kuhaili et al. [34] investigated the transmittance spectra of $Cr_2O_3$ thin film on unheated (RS) and heated (HS) substrates fitted for the optical constants. The estimations are as follows:

- From transmittance maximum and minimum, the thickness value was estimated and refined by fitting procedure.
- The transmittance spectra of $Cr_2O_3$ thin film were fitted over the wavelength region with error less than 4%.
- The transmittance on RS substrate was found at 76% in visible and 93% in the infrared region.
- HS deposited $Cr_2O_3$ film transmittance appeared at ~78% and ~95% in visible and infrared regions, respectively.
- The refractive index of $Cr_2O_3$ thin film on unheated (RS) and heated (HS) substrates was established at 2.08 and 2.37, respectively.

All the values of each and every material are calculated by using Eqs. (1), (2), (3) and (4). From Kartick et al. [23], the statements are of $WS_2$-MWCNT (1:1) hybrid which appears to possess remarkably higher initial discharge and charge capacity than the other profiles. This is due to enriched ion intercalation in charge–discharged process. Chen et al. [9] explored about DWSiNT which has 88% capacity retention after 6000 cycles whereas Si Nanowires and Si nanotube without oxide are not highly desirable options for energy storage. $Lix Ni_{1-x}O$ film annealed at 438 °C transmittance is found to be ~95% which implies as the temperature rises, the film optical properties also increase as stated by Gillaspie et al. [29]. The doping of Ag NW in the $WO_3$ film effect is described by Yan et al. [30]. The analysis of CEs $WO_3$/Ag NW is

measured as 50 and 86.9 $cm^2/c$ at 630 nm and 1100 nm studied by Zhou et al. [31]. Likewise, the transmittance spectra of P (TMC-DLLA) (Wang et al. [32]), mono-, bi- and tri-layer graphene (Li et al. [33]) and $Cr_2O_3$ thin film (Kuhaili et al. [34]) lighten up the possible reinforcement of Nanotechnology in future Energy Storage Devices. All the nanomaterials can be accomplished to get soaring performance and stability in Nanotechnology-based advanced Energy Storage Systems.

## 4 Conclusion

This paper discusses the nanomaterials that have attracted growing research interest in energy storage applications due to their electrical, mechanical, chemical, morphological and topographic properties. Research has been going on to obtain more capability, rapid charging and discharging accomplishment and life stability of energy storage devices. Nanostructures with a broader surface area such as multi-walled carbon nanotubes exhibit extraordinary charge storage performance boosting up the capacity of accommodating volume change which is associated with the electrochemical reaction.

**Acknowledgements** The authors are obliged to DST-NanoMission for the funding of the research work as well as all the supporting hands of the Dept. of ECE, NIT Mizoram.

## References

1. D. Larcher, T. Jean-Marie, Towards greener and more sustainable batteries for electrical energy storage. Nat. Chem. **7**(1), 19–29 (2015)
2. M.F.L. De Volder, S.H. Tawfick, R.H. Baughman, A.J. Hart, Carbon nanotubes: present and future commercial applications. Science **339**(6119), 535–539 (2013)
3. B. Dunn, K. Haresh, T. Jean-Marie, Electrical energy storage for the grid: a battery of choices. Science **334**(6058), 928–935 (2011)
4. Q. Wei, F. Xiong, S. Tan, L. Huang, E.H. Lan, B. Dunn, L. Mai, Porous one-dimensional nanomaterials: design, fabrication and applications in electrochemical energy storage. Adv Mater. **1602300**, 1–39 (2017)
5. L. Dai, D.W. Chang, J.B. Baek, W. Lu, Carbon nanomaterials: carbon nanomaterials for advanced energy conversion and storage. Small **8**, 1130–1166 (2012)
6. Y. Xiao, D. Hao, H. Chen, Z. Gong, Y. Yang, Economical synthesis and promotion of the electrochemical performance of silicon nanowires as anode material in li-ion batteries. ACS Appl. Mater. Interfaces **5**(5), 1681–1687 (2013)
7. J.B. Goodenough, P. Kyu-Sung, The li-ion rechargeable battery: a perspective. J. Am. Chem. Soc. **135**(4), 1167–1176 (2013)
8. S.W. Kim, D.H. Seo, X. Ma, G. Ceder, K. Kang, Electrode materials for rechargeable sodium-ion batteries: potential alternatives to current lithium-ion batteries. Adv. Energy Mater. **2**, 710–721 (2012)
9. C. Cheng, F. Yuqi, G. Jianhang, W. Liming, P. Stefano, M. Liqiang, One-dimensional nanomaterials for energy storage. J. Phys. D: Appl. Phys. **51**(11), 1–27 (2018)

10. F. Cheng, J. Liang, Z. Tao, J. Chen, Functional materials for rechargeable batteries. Adv. Mater. **23**(15), 1695–1715 (2011)
11. L. Qu, A.V. Rich, D. Liming, Multilevel, multicomponent microarchitectures of vertically aligned carbon nanotubes for diverse applications. ACS Nano **5**(2), 994–1002 (2011)
12. Z. Guangmin, X. Lin, H. Guangwu, M. Liqiang, C. Yi, Nanowire electrodes for electrochemical energy storage devices. Chem. Rev. **114**(23), 11828–11862 (2014)
13. D. Zilli, P.R. Bonelli, A.L. Cukierman, Effect of alignment on adsorption characteristics of self-oriented multi-walled carbon nanotube arrays. Nanotechnology **17**(20), 5136–5141 (2006)
14. W. Lu, L. Qu, K. Henry, L. Dai, High performance electrochemical capacitors from aligned carbon nanotube electrodes and ionic liquid electrolytes. J. Power Sourc. – J Power Sourc. 189, 1270–1277 (2009)
15. K. An, W. Kim, Y. Park, J.M. Moon, D. Bae, S.C. Lim, Y.-S. Lee, Y.H. Lee, Electrochemical properties of high-power supercapacitors using single-walled carbon nanotube electrodes. Adv. Funct. Mater. **11**, 387–392 (2001)
16. T. Jean-Marie, A. Michel, Issues and challenges facing rechargeable lithium batteries. Nature **414**, 359–367 (2001)
17. U. Kasavajjula, W. Chunsheng, A.J. Appleby, Nano- and bulk-silicon-based insertion anodes for lithium-ion secondary cells. J. Power Sources **163**(2), 1003–1039 (2007)
18. C.K. Chan, H. Peng, G. Liu, K. Mcllwrath, X.F. Zhang, R.A. Huggins, Y. Cui, High-performance lithium battery anodes using silicon nanowires. Nat. Nanotechnol. **3**(1), 31–35 (2009)
19. N. Hung, F. Yao, Z. Mihai-Robert, C. Biswas, K.P. So, Y.H. Lee, S. Kim, S. Cha, J. Kim, D. Pribat, Highly interconnected si nanowires for improved stability li-ion battery anodes. Adv. Energy Mater. **1**, 1154–1161 (2011)
20. M. Armand, T. Jean-Marie, Building better batteries. Nature **451**, 652–657 (2008)
21. W. Zhou, C. Cheng, J. Liu, Y. Tay, J. Jiang, X. Jia, J. Zhang, H. Gong, H.H. Hng, T. Yu, H. Fan, Epitaxial growth of branched α-Fe2O3/SnO2 nano-heterostructures with improved lithium-ion battery performance. Adv. Func. Mater. **21**, 2439–2445 (2011)
22. L. Jiang, H. Liu, L. Yuan, Recent advances in metal oxide-based electrode architecture design for electrochemical energy storage. Adv. Mater. **24**, 5166–5180 (2012)
23. K. Bindumadhavan, S. Srivastava, S. Mahanty, Tungsten disulfide-multiwalled carbon nanotube hybrid anode for lithium-ion battery. J. Nanosci. Nanotechnol. **14**, 3758–3764 (2014)
24. B. Wang, X. Li, X. Zhang, B. Luo, M. Jin, M. Liang, S.A. Dayeh, S.T. Picraux, L. Zhi, Adaptable silicon carbon nanocables sandwiched between reduced graphene oxide sheets as lithium ion battery anodes. ACS Nano **7**(2), 1437–1445 (2013)
25. H. Jiang, M. Jan, L. Chunzhong, Mesoporous carbon incorporated metal oxide nanomaterials as supercapacitor electrodes. Adv. Mater. **24**(30), 4197–4202 (2012)
26. Z.Kai, L.Z. Li, W. Zhao, Graphene/polyaniline nanofibre composites as supercapacitor electrodes. Chem. Mater. **22**(4), 1392–1401 (2010)
27. S. Cho, B.L. Sang, Fast electrochemistry of conductive polymer nanotubes synthesis, mechanism, and application. Accounts of Chem. Res. **41**(6), 699–707 (2008)
28. J. Huang, W. Kai, W. Zhixiang, Conducting polymer nanowire arrays with enhanced electrochemical performance. J. Mater. Chem. **20**(6), 1117–1121 (2010)
29. G. Dane, N. Andrew, C.T. Edwin, P.J. Roland, L. Se-Hee, D. Anne, Nanocomposite counter electrode materials for electrochromic windows. J. Electrochem. Soc. **157**(3), 1–5 (2010)
30. Y. Xudong, L. Wei, Z. Yong, Y. Dong, H. Xiaowen, Z. Wei, Z. Guofu, Improvement of electro-optical properties of PSLC devices by silver nanowire doping. Appl. Sci. **9**(145), 1–11 (2019)
31. Z. Kailing, H. Wang, S. Zhang, J. Jiu, J.B. Liu, Y.Z. Zhang, H. Yan, Electrochromic modulation of near-infrared light by WO3 films deposited on silver nanowire substrates. J. Mater. Sci. **52**, 12783–12794 (2017)
32. M. Zhengyu, W. Yi, W. Jing, L. Changsheng, In vitro and in vivo degradation behavior of poly (trimethylene carbonate-co-D, L-lactic acid) copolymer. Regenerat. Biomater. 207–213 (2017)
33. L. Wei, C. Guangjun, L. Yiran, T. Boyuan, L. Xuelei, P. Lianmao, A.R.H. Walker, J.G. David, V.N. Nhan, Broadband optical properties of graphene by spectroscopic ellipsometry. Carbon **99**, 348–353 (2015)

34. M.F. Al-Kuhaili, S.M.A. Durrani, Optical properties of chromium oxide thin films deposited by electron-beam evaporation. Opt. Mater. **29**, 709–713 (2007)

# Performance Analysis of Latency on Wide Area Monitoring and Control for a Smart Power Grid


**Suman Ghosh, J. K. Das, and Chandan Kr. Chanda**

## 1 Introduction

Wide Area Monitoring System (WAMS) became one of the most recent technologies for upgrading the traditional electric grid. The basic components of WAMS are PMUs, PDCs, and communication networks. The first basic component of WAMS that is the Phasor Measurement Unit (PMU) is used in the Indian smart grid for the collection of the real-time synchronized phasor data over a time span from different parts of any power grid and delivers the snapshots of the power system. If the time span reduces, then it will be more helpful for better monitoring, control, and protection over the system. There are several projects conducted worldwide for better and efficient utilization of synchrophasor data received from PMUs. In WAMS, the quality of control actions and the stability of the system can decrease due to latency or time delays in the communication network. Hence, the impact of latency in the PMU measurements and the communication between grids is an important factor for power system stability. All the measurements from PMUs are synchronized and time stamped, and from this, we can easily obtain the snapshot of the power system (Synchronized Phasor, Frequency, and Rate of Change of Frequency (ROCOF) estimates from the voltage and/or current signals and a time synchronizing). This is important for the aforementioned WAMS like Wide Area Monitoring System (WAMS), Wide Area Protection System (WAPS), and Wide Area Control Systems (WACS) and combined methodologies like Wide Area Monitoring and Control Systems (WAMCS).

S. Ghosh (✉) · J. K. Das
Department of Electrical Engineering, GNIT, Panihati, Kolkata, India
e-mail: suman.ghosh@gnit.ac.in

C. Kr. Chanda
Department of Electrical Engineering, IIEST, Shibpur, Kolkata, India



C. K. Chanda et al. (eds.), *Advanced Energy and Control Systems*, Lecture Notes in Electrical Engineering 820, https://doi.org/10.1007/978-981-16-7274-3_9

Latency or time delay associated with the communication system is one of the major challenges in the wide area technology. It impacts the Wide Area Monitoring System (WAMS), Wide Area Control System (WACS), and Wide Area Protection System (WAPS). Depending on the length of the network, medium of communication, and bandwidth of the channel, a typical communication time could span over from 10–100 ms.

## 2 Latency or Time Delay in a Wide Area System

Latency or time delay mainly occurred in a PMU-based Wide Area Monitoring System which includes time delays associated with voltage and/or current transducers and actuators, communication delay, and processing delay. The total delay associated with the transducer and actuator is nearly about 10 ms and the communication delay and processing delay together comes nearly about 500 ms. There are four types of communication delay like serial delays, between packets serial delays, routing delays, and propagation delays.

- Serial delays occurred in between each of the one bit sent. Basically, time span over which bit of one communication data packet is coordinated at a specified transmission speed is called serial delay.
- Between packets serial delays occur between two consecutive packets sent.
- Routing delay is the time delay over which the data are sent or resent through the router which also includes the waiting time and service time at any node. Under light network traffic, routing delay can be ignored.
- Propagation delays are the time delays over which data are transmitted over a communication medium. This type of delay mainly depends on the distance of communication and type of communication medium. While it is independent of network bandwidth.

Delays associated with Wide Area System are shown in Fig. 1.

## 3 Major Researches on Time Delay or Latency Analysis and Its Impact on Wide Area Technology System

N. R. Chaudhuri et al. proposed a compensation technique using a phasor Power Oscillation Damping (POD) controller for continuously variable latency in a wide area system. In this compensation technique, the concept of rotating coordinates was utilized [1]. V. P. Singh et al. proposed a linear matrix inequality-based quadratic regulator and a decentralized controller to reduce the mean square error of the power system state variable estimation under topological changes. In this paper, the service quality of the communication infrastructure is also described for the application

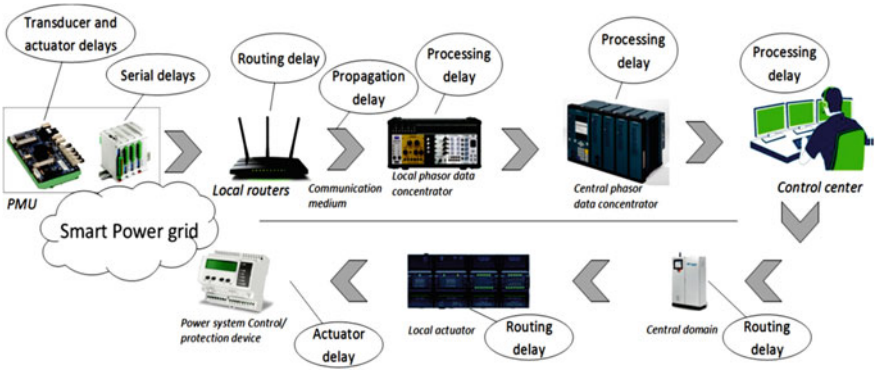


**Fig. 1** Delays associated with wide area system

of load frequency control in a smart grid environment [2]. Lu et al. proposed a methodology for frequency restoration which is based on the secondary control level under a communication network with a single time delay. In this paper, the author presented a mathematical model incorporating the effects of stochastic time delay for analysis of wide area control system [3]. E. A. A. Coelho et al. studied and validated that the impact of time delay was under the hardware-in-the-loop schemes and software-in-the-loop schemes. The author also described the time delay and its variation due to communication in an islanded microgrid system [4]. S. Musleh et al. described the impact of latency on the stability of a smart grid in a Wide Area Monitoring and Control Systems (WAMCS) [5]. B. Chaudhuri et al. presented a technique and control strategy for latency compensation by using USP (Unified Smith Predictor), which can be used for designing a synchrophasor assisted wide area damping controller with a static VAR compensator [6]. J. W. Stahlhut et al. presented a case study and show that latency due to control signals may significantly reduce the efficiency and performance of wide area control system [7].

S. Wang proposed a methodology to calculate latency by comparing the time stamped feedback signals and the GPS receiver clock. Then the latency data are used to anticipate the trajectories of the particular power system so that the impact of latency can be compensated [8]. M. Mokhtari et al. proposed a Wide Area Damping Controller (FLWADC) based on Fuzzy Logic to damp inter-area oscillations and for continuous latency compensation. With the help of the proposed controller, one case study was performed and validated for its robustness against input signal variations [9]. B. P. Padhy et al. employed the Modified Extended Kalman Filter (MEKF) for compensation of the communication latency in a synchrophasor-based WAMCS [10]. W. Shaobu et al. proposed a controller with wide area information and linear matrix inequality concepts as a feedback signal that can undergo various delays, communication disorders, and dropouts of data packets in the wide area measurement systems to improve the power system efficiency and performance [11]. B. P. Padhy

et al. proposed a wide area centralized damping controller considering packet dropout under variable latency in the communication network to improve the power system stability [12].

W. Yao et al. employed a time delay-dependent criterion and model reduction technique based on the Lyapunov theory. Stability analysis of a power system based on time delay and with a Wide Area Damping Controller (WADC) is described in this paper. Delay margin is defined as the maximum delay within which the closed-loop power system can retain stability. Based on Linear Matrix Inequality (LMI) technique and reduced order model, calculation of the delay margin of a power system was presented in this paper [13]. B. Naduvathuparambil et al. provide the data regarding various delays in the communication network associated with the wide area technologies. The authors also presented various alternatives and latency profiles for communication systems for application in WAMS [14].

## 4 Impact of Latency on Wide Area Control (WAC) System

The main focus of a Wide Area Control (WAC) system is on the slow nature dynamics of the power system. Here, the normal transient system dynamics is not considered which is assumed as instantaneous, so the control scheme used here is not a systematic one. This is because the Wide Area Control (WAC) system has a higher step time compared to the local area controller. That's why power flow equations considering steady-state behavior are used in the WAC. In large-scale power grids, decoupled power flow systems are considered to improve computing efficiency by reducing the requirements of storage. In the decoupled power flow analysis, the relation between voltage and reactive power magnitude can be represented as follows:

$$\begin{pmatrix} \Delta Q_1 \\ \vdots \\ \Delta Q_n \end{pmatrix} = -\begin{pmatrix} B_{11} & \cdots & B_{1n} \\ \vdots & \ddots & \vdots \\ B_{n1} & \cdots & B_{nn} \end{pmatrix} \begin{pmatrix} \Delta V_1 \\ \vdots \\ \Delta V_n \end{pmatrix} \tag{1}$$

where $Q_i$ represents the reactive power of the ith bus, $|V_i|$ is the voltage magnitude of the ith bus, and B is the susceptance of the lines. The main aim of considering the decoupled power flow equation is to develop an estimated mathematical modeling of a power grid that can relate the variation of the reactive power with the voltage magnitude at every bus in the grid as well as elsewhere in the grid. In other words, if the voltage varies at one bus, then how it affects the other busses of the system.

Now voltage deviation ($\Delta|V|$) can be expressed as follows:

$$\Delta V = V_{Set} V_{PMU} \tag{2}$$

where $|V_{Set}|$is the set-point of the voltage magnitude considered as 1PU and $|V_{PMU}|$is the voltage magnitude measured by the PMUs. The decoupled power flow equation no. 1 can be expressed by separating the controlled and uncontrolled busses:

$$\begin{pmatrix} \Delta Q_C(t) \\ \Delta Q_u(t) \end{pmatrix} = -\begin{pmatrix} B_{cc} & B_{cu} \\ B_{uc} & B_{uu} \end{pmatrix} \begin{pmatrix} \Delta V_c(t) \\ \Delta V_u(t) \end{pmatrix} \tag{3}$$

where 't' is the wide area protection time instant, 'u' for voltage-uncontrolled busses, and 'c' for voltage-controlled buses (with the help of FACTS). At the upcoming time-step, the voltage of the uncontrolled bus can be expressed from the above equation as follows:

$$(\Delta V_u(t+1)) = -(B_{uu}u)^{(-1)}((B_{uc}(\Delta V_c(t+1))) + (\Delta Q_u(t))) \tag{4}$$

From the above expression, we can conclude that the upcoming time-step mainly depends on the input at the present time-step denoted by $(\Delta Q_u(t))$ (reactive power perturbation at the voltage-uncontrolled busses'). Hence, employing the present disturbance, the forthcoming control action is designed $(\Delta|V_c(t+1)|)$ (voltage set-point at the voltage-controlled busses) for minimizing the deviation in the power system denoted as $(\Delta|V_u(t)|)$ (voltage deviation at the voltage-uncontrolled busses). For every time-step, the calculation of present voltage deviation is done to design the set-points of the voltage-controlled busses for the coming time-step. $(\Delta|V_u(t)|)$ is calculated from the PMU measurements. $(\Delta|V_c(t)|)$ is the voltage at the voltage-controlled busses which are collected from the respective local controller. For the stable system, the uncontrolled bus voltage deviation $(\Delta|V_u(t)|)$ should be minimum. This can be obtained by optimizing the function.

$$\text{Min}\,|-(B_{uu})^{(-1)}((B_{uc}(\Delta V_c(t+1)|)) + (\Delta Q_u(t)))|$$

subjected to

$$\begin{cases} |V_c^{min}(t+1)| \le |V_c(t+1)| \le |V_c^{max}(t+1)| \\ Q_c^{min}(t+1) \le Q_c(t+1) \le Q_c^{max}(t+1) \end{cases}$$

The optimization function represented in the above equation needs to be solved with minimum time to maintain the system stability. Different optimization techniques and algorithms are there to achieve this goal. Interior Point Algorithm (IPA) is one of the most important and unique optimization techniques. IPA provides a much better solution to the convex programming problems than the simplex method. By traversing the interior of the feasible region through iterations, IPA reaches the optimal solution which is in contradiction to the simplex method. There is another approach that received the attention of many researchers which is the Genetic Algorithm (GA). In this approach, a set of possible solutions are developed in the form of

random chromosomes and then evaluated. Then with the help of the crossover and mutation process, we can find the best solutions among the different generations. In presence of latency or time delay $t_d$, the optimization problem discussed above (Eq. 4) is represented by

$$(\Delta V_u(t+1)) = -(B_{uu})^{(-1)}((B_{uc}\Delta(V_c(t+1))) + (\Delta Q_u(t-t_d))) \tag{5}$$

Now the optimizing function will be

$$\text{Min}\,|-(B_{uu})^{(-1)}((B_{uc}(\Delta|V_c(t+1)|)) + (\Delta Q_u(t-t_d)))|$$

subjected to

$$\begin{cases} |V_c^{\min}(t+1)| \le |V_c(t+1)| \le |V_c^{\max}(t+1)| \\ Q_c^{\min}(t+1) \le Q_c(t+1) \le Q_c^{\max}(t+1) \end{cases}$$

From the above expression, we can observe the impact of time delay on voltage estimation and voltage control. Thus, the latency should be as minimum as possible to maintain the system stability of a power grid.

## 5 Optimized Routing Estimation

In the time delay analysis, identifying the shortest route between the PMU and the control center is one of the major challenges. Combining data propagation delays and router processing delays, we can achieve optimized routing estimation. An optimized channeling period from each of the PMU to the control center is obtained by using Dijkstra's Algorithm. In the year 1959, E. W. Dijkstra developed an algorithm to estimate the optimum distance of traveling between two nodes of a grid [13]. For the optimized routing estimation problem, this length can be replaced by the time delay between two nodes in a communication network.

The data sending time span between the sensor device and the control center is defined as the sending time delay ($T_{send}$). This time span is basically the combination of the individual router processing delay and the propagation delay between the routers. The new propagation delay can be represented as follows:

$$T^i_{l_j new} = \begin{cases} T^i_{l_j}, & \text{for } i = 1 \\ T^i_{l_j} + T_{router}, & \text{for } i = 2, 3, \ldots, N_{l_j} \end{cases}$$

where $T^i_{l_j new}$ is the combined new propagation time of the ith link in $l_j$. l is the link of the shortest communication time between PMU and PDC. The total number of links is represented by $N_{l_j}$ and data processing time in a router is $T_{router}$. Thus, the total

data sending time between the sensor device and the control center can be expressed as follows:

$$T_{send} = \max_{l_1, l_2, \ldots, l_n \in l} \left\{ \sum_{i=1}^{N_{l_1}} T^i_{l_1 new}, \sum_{i=1}^{N_{l_2}} T^i_{l_2 new}, \ldots, \sum_{i=1}^{N_{l_n}} T^i_{l_n new} \right\}$$

In Fig. 2, a flowchart for Dijkstra's algorithm for finding the shortest communication link is shown.

## 6 Performance Analysis of Latency in a Wide Area Network

S. Musleh et al. focused on the impact of latency in a WAMCS on the power system stability analysis under different contingencies. Wide area control is achieved with the help of FACTS by controlling through the wide area controller. One case study was performed on a developed testbed in an RTDS system with the help of SIL (Software in Loop). Based on the voltage settling time and voltage profile index, we can assess the performance of a wide area controller. It was shown in the paper that with a delay of 0.2 s, an error of 0.078% occurred to the overall power grid voltage profile index. The error was increased to 0.23% when the time delay increased to 0.5 s [5].

J. J. Q. Yu et al. analyzed the impact of communication delay on power system state estimation. The author proposed a delay-aware synchrophasor recovery and prediction framework to minimize the problem. This framework mainly depends on the iteration using existing incomplete synchrophasor data [15].

I. Al-Anbagi et al. proposed Adaptive Quality of Service (AQoS) scheme, by which average end-to-end time delay can be reduced nearly 50% [16].

N. R. Chaudhuri analyzed the impact of latency in large power grids on wide area damping controllers employed for preventing the small signal oscillations. The case studies conducted on the power system model depict that with a communication latency of 1 s, the oscillating response of the power system stabilized the peak overshoot of about 75% [17].

C. Sharma et al. proposed a robust type-2 Fuzzy controller to reduce the impact of latency in a WACS. The author also mentioned the impact of latency on a power damping controller. When damping controllers are operated under latency, oscillations occur in the tie-line of the power system. To reduce the oscillations, the author proposed the position of the rotating vector method for phasor extraction [18].

A comparative study of recent trends on the performance of latencies is given in Table 1.

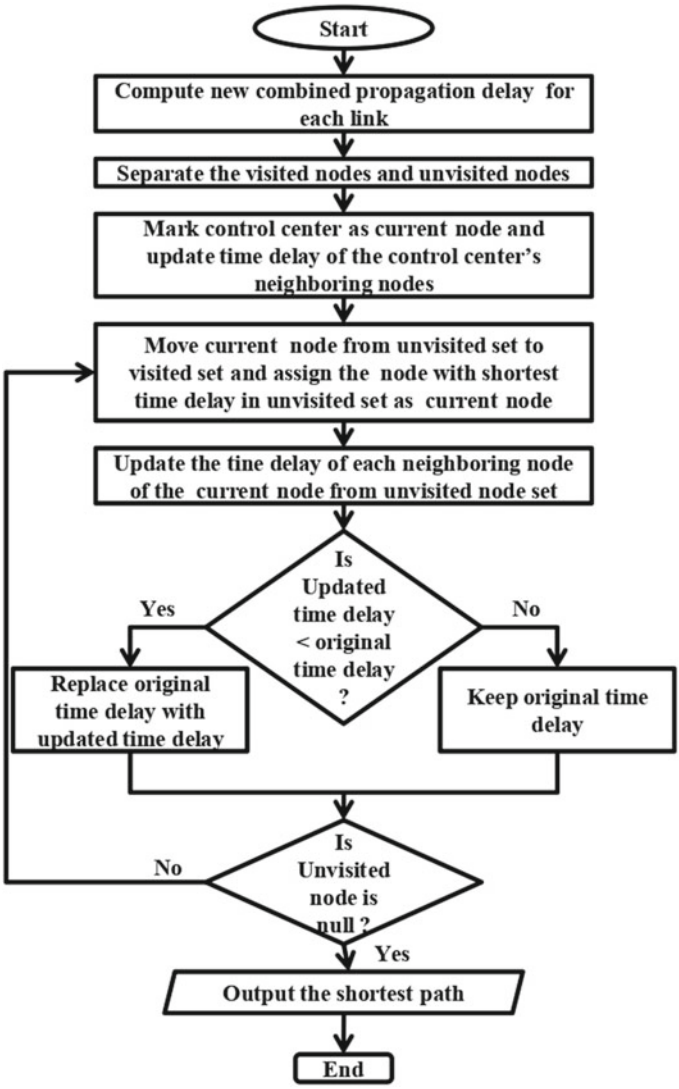


**Fig. 2** Flowchart for Dijkstra's Algorithm to find the shortest communication link

## 7 Conclusion

This paper investigates the various types of latency and their impact on Wide Area Monitoring and Control System (WAMCS). For effective wide area monitoring under contingencies, analysis of latency is very essential. Due to the presence of latency in the system, the quality of control actions and the stability of the power grid can be

**Table 1** Recent trends on performance of latency in wide area system

| Controller used in wide area system | Latency/time delay | Performance analysis considered | Proposed methodology overcome latency issue |
|---|---|---|---|
| FACTS [5] | 0.2–0.5 s | Under contingencies, performance of FACTS to maintain the voltage stability | |
| Wide area PMUs [15] | 0.05–0.1 s | Real-time state estimation | Synchrophasor recovery and prediction framework |
| Wireless sensor [16] | 0.42 s | Delay critical application | Adaptive QoS scheme (AQoS) and Adaptive Guaranteed Time Slot (AGTS) allocation |
| Phasor power oscillation damping controller [17] | 1 s | Damping of power through TCSC | Continuous compensation for time-varying delay |
| Damping controller [18] | 1 s | Dynamics of tie-line power flow | Fuzzy Type-2 Controller |
| Damping controller [20] | 0.1 s | Frequency and voltage angle deviation | Time-delayed Control (TDC) |
| Damping controller [22] | 0.2 s | Variable loop gain controller to ensure stability | Excessive Regeneration Detector (ERD) |
| Power system stabilizers [19] | 1 s | Damping factor, frequency deviation | |
| Wide area PMUs [21] | 30–60 ms | Voltage magnitude and angle measurements | Shortest path routing |

reduced. Thus latency or time delay is the key factor for choosing the communication channel for data communication through PMU in WAMS.

## References

1. N.R, Chaudhuri, S. Ray, R. Majumder, B. Chaudhuri, A new approach to continuous latency compensation with adaptive phasor poweroscillation damping controller (POD). IEEE Trans. Power Syst. **25**(2), 939–946 (2010)
2. V.P. Singh, N. Kishor, P. Samuel, Load frequency control with communication topology changes in smart grid. IEEE Trans. Ind. Inf. **12**(5), 1943–1952 (2016)
3. Z.X, Lu, X. Wang, Y. Han, Mathematical expectation modelling of wide-area controlled power systems with stochastic time delay. IEEE Trans. Smart Grid **6**(3), 1511–1519 (2015)
4. E.A.A. Coelho et al., Small-signal analysis of the microgrid secondary control considering a communication time delay. IEEE Trans. Indust. Electron. **63**(10), 6257–6269 (2016)
5. S. Musleh, S.M. Muyeen, A. Al-Durra, I. Kamwa, M.A.S. Masoum, S. Islam, Time-delay analysis of wide-area voltage control considering smart grid contingences in a real-time environment. IEEE Transa. Indust. Inf. **14**(3), 1242–1252 (2018)

6. B. Chaudhuri, R. Majumder, B.C. Pal, Wide-area measurement based stabilizing control of power system considering signal transmission delay. IEEE Trans. Power Syst. **19**(4), 1971–1979 (2004)
7. J.W. Stahlhut, T.J. Browne, G.T. Heydt, V. Vittal, Latency viewed as a stochastic process and its impact on wide area power system control signals. IEEE Trans. Power Syst. **23**(1), 84–91 (2008)
8. S. Wang, W. Gao, J. Wang, J. Lin, Synchronized sampling technology-based compensation for network effects in WAMS communication. IEEE Trans. Smart Grid. **3**(2), 837–845 (2012)
9. M. Mokhtari, F. Aminifar, D. Nazarpour, S. Golshannavaz, Wide area power oscillation damping with a fuzzy controller compensating the continuous communication delays. IEEE Trans. Power Syst. **28**(2) 1997–2005 (2013)
10. B.P. Padhy, S.C. Srivastava, N.K. Verma, A network delay compensation technique for wide-area SVC damping controller in power system. IEEE PES Trans. Distrib. Conf. Expo. (Chicago, 2014)
11. W. Shaobu, M. Xiangyu, C. Tongwen, Wide-area control of power systems through delayed network communication. IEEE Trans. Control Syst. Technol. **20**(2), 495–503 (2012)
12. B.P. Padhy, S.C. Srivastava, N.K. Verma, A wide-area damping controller considering network input and output delays and packet drop. IEEE Trans. Power Syst. **32**(1), 166-176 (2017)
13. W. Yao, L. Jiang, Q.H. Wu, J.Y. Wen, S.J. Cheng, Delay dependent stability analysis of the power system with a wide-area damping controller embedded. IEEE Trans. Power Syst. **26**(1), 233–240 (2011)
14. B. Naduvathuparambil, M.C. Valenti, A. Feliachi, Communication delays in wide area measurement systems, in *34th Southeastern Symposium System Theory* (2002), pp. 118–122
15. J.Q. Yu, A.Y.S. Lam, D.J. Hill, Y. Hou, O.V.K. Li, Delay aware power system synchrophasor recovery and prediction framework. IEEE Trans. Smart Grid **10**(4) (2019)
16. I. Al-Anbagi, M. Erol-Kantarci, H.T. Mouftah, Delay critical smart grid applications and adaptive QoS provisioning. IEEE Access **3**, 1367–1378 (2015)
17. N.R. Chaudhuri, B. Chaudhuri, S. Ray, R. Majumder, Wide-area phasor power oscillation damping controller: a new approach to handling time-varying signal latency. IET Gener., Trans. Distrib. **4**(5), 620–630 (2010)
18. C. Sharma, B. Tyagi, Fuzzy type-2 controller design for small signal stability considering time latencies and uncertainties in PMU measurements. IEEE Syst. J. **11**(2), 1149–1160 (2017)
19. X. Zhang, C. Lu, X. Xie, Z.Y. Dong, Stability analysis and controller design of a wide-area time-delay system based on the expectation model method. IEEE Trans. Smart Grid **7**(1), 520–529 (2016)
20. S. Roy, A. Patel, I.N. Kar, Analysis and design of a wide-area damping controller for inter-area oscillation with artificially induced time delay. IEEE Trans. Smart Grid, **10**(4) (2019)
21. R. Kateb, P. Akaber, M. Tushar, A. AL-Barakati, M. Debbabi, C. Assi, Enhancing WAMS communication network against delay attacks. IEEE Trans. Smart Grid (2019)
22. D. Roberson, J.F. O'Brien, Variable loop gain using excessive regeneration detection for a delayed wide-area control system. IEEE Trans. Smart Grid **9**(6) (2017)

# Analysis of Voltage Stability in Smart Grid System Due to Demand Load Variation


**Shouvik Kumar Samanta and Chandan Kumar Chanda**

## 1 Introduction

The distinct nonlinear and linear properties of power system engineering have consisted of various components in a composite system network which could be a radially distribution network of non-uniform systems. In electrical grid systems, many aspects of design gained advances of dynamic demand methodologies which are normally recognized as the development of stability response. In advance research, Smart Grid lags behind the conventional area of research despite demand-side management are dependent on load variation and load shifting of real-time scenarios. The identity of voltage stability [1] may be described as instability of the power system to utilize the non-uniform reactive power or system's own reactive power absorption. For power planning and security of voltage stability concerns, the contingency analyses are leading to the establishment of the assessment of voltage stability situation for developing countries. It is solely recorded at a complex system of a power network that the non-uniform load growth at demand-side management and the reactive power [2] interval management side also affect the region of stability. Due to the high R/X ratio at various branches, convergence problems create a critical stage of solving the traditional Newton–Raphson technique of a low voltage power distribution system.

From load flow studies, determination of current, voltage, active power and reactive power, etc. are carried out at various buses in power systems operating under normal steady-state or static conditions. It is used to plan the best operation and control of an existing system and for future expansion, to keep pace with load growth. Due to this information system, losses are minimized, and also check is provided on system stability. Traditionally, the load flow method [3, 4] is performed to examine the stability studies of the electric grid, and different numerical techniques were applied on various system phenomenons to solve the critical loading liabilities. Numerical

S. K. Samanta (✉) · C. K. Chanda
IIEST, Shibpur, Howrah, India



C. K. Chanda et al. (eds.), *Advanced Energy and Control Systems*, Lecture Notes in Electrical Engineering 820, https://doi.org/10.1007/978-981-16-7274-3_10

methods and geometrical data are needed for approximations of grid circuit parameters. Method of the successive displacement or the Liebmann method is known as Gauss–Seidel method [5, 6] and numerical technique, i.e. the Newton–Raphson method [7–13] depended on an iterative process that is verifying the complex system analysis to satisfy the stability concept. Bialek suggested in his paper [8] a modern technology to trace the active and reactive power flow measurement from the generator to a particular load established in 1996. "Proportional Principle" is applied here for bringing together generator units individually and obtaining individual loads contribution. The Principle concept primarily depends on comparative incoming and outgoing power flow study distributed among all parameters, and initials guessing are considered for all dimensions power flow concern.

According to research, exchanging load level or proposed load level is obtained on the IEEE 14 bus model for forecasting the load variation on dynamic demand due to distribution of reactive and active power flow under the steady-state method of load flow and transient stability analysis [14] to examine the actual circumstances with particular time band in the grid. At the arising point of stability, the load flow solution is the presented solution earlier than determined steady-state grid stability from smartly network control demand. The Transmission Systems have various levels of voltage generally, e.g. 11, 33 and 66 kV, and also higher range voltages are complementary forecasting to the utility networks in transmission lines. Suppose a transmission network [15] might be interconnected with other power generating stations drawing imported power for meeting the requirement of local load and utility power. Smart monitoring and control of the timely operational decisions in the power system are to bring down losses and outages. Energy interchange points are recorded for planning loss minimization and outgoing, and incoming feeders meter readings have been noted for pricing electricity of demand-side consumer.

## 2 Voltage Stability Indices and Smart Grid

The smart grid allows distributed generation for using all voltage levels [16] and smart meters, pricing at real-time and domestic customers might be able to install the distributed generator own. Domestic distributed generators such as photovoltaic cells or wind turbines reduce their energy bills to help out our customers and also trade extra power to the grid for minimizing electricity demand. The fluctuation of voltage is normally a dynamic circumstance with rather than slow dynamics and ranging a time domain from a few seconds to a few minutes or more. After all the smart grid will entirely upgrade consumer transactions as less time consuming from the conventional grid and permit also undertaking better of consumers to save their pricing of electrical energy.

## 2.1 Smart L-Type Voltage Stability Index

The stability margin of voltage could be determined from the index of voltage stability [19] and voltage stability index for the smart grid of the entire system has been formed. Let us consider n as the total number of buses in a system. Now system generator buses are 1,2,….,$g$ with PV buses are $g + 1$, $g + 2$,…..,$g + l$ and the remaining $g + l + 1$,……., $n$ are PQ buses. The simplified representation of the L index with the $j$th load bus is expressed as follows (the real part of Y-line matrix influence is neglected).

$$L_j = \left| 1 - \sum_{i=1}^{i=g} Fji \frac{Vi}{Vj} \right| \tag{1}$$

Within Σ the RHS of the above equation complex quantities are in all the terms from $j = g + l + 1$,……, to $n$. From [Y] bus matrix, Fji elements are calculated as follows for the network below:

$$[F] = -[K'']^{-1}[K_{LG}] \tag{2}$$

where [K″] is the imaginary part of the matrix [$Y_{LL}$] and [$K_{LG}$] is the imaginary part of the matrix [$Y_{LG}$]. The proximity voltage collapse indicator of a power system is $L_j$. Now at bus $j$, $L_j = 1$ indicates the condition of voltage collapse. Hence, in a complete system, L described as the global indicator of stability is given by

$$L = \text{for all } jth \text{ buses the load } Lj \text{ maximum} \tag{3}$$

For this Smart L-type index of stability is modified and proposed Smart L-type index of voltage stability equation is described below:

$$Lj|_t = \left| 1 - \sum_{i=1}^{i=g} F_{ji} \frac{\frac{\partial V_i}{\partial t}}{\frac{\partial V_j}{\partial t}} \right| \quad t = 1 \text{ to } 24 \tag{4}$$

For L = 1, a limit of stability will be attained.

Also, LQF and FVSI values must be kept <1.0 to maintain the system is stable.

During daily demand, load respond scale of 24 h L-type index value will hourly alter. In order to stabilize the system, the L index value will have reduced by controlling generating power through demand respond [17] management (DRM).

### 2.2 Stability Index

If any unbounded voltage at the nodal point is composed, it is led to as voltage instability [18], i.e. the system capacity is comparatively exceeded with respecting load and created mismatching power in the system. The $\frac{\partial V_i}{\partial |Q_i|}$ index [19] that is elucidated by the two reactive powers must be equal to each other at equilibrium that means the source and load sides both.

Degree of weakness implies in terms of $\frac{\partial Q_i}{\partial |V_i|}$ at the *i*th bus. If $\frac{\partial V_i}{\partial |Q_i|}$ became low, $\frac{\partial Q_i}{\partial |V_i|}$ being too high, that minimum change of $|V_i|$ indicates the reactive power (Q) level is varied at the particular bus. So $\frac{\partial Q_i}{\partial |V_i|}$ is being higher, at *i*th bus, degree of weakness becomes lesser.

## 3 Demand Load and Peak Load Availability of Smart Grid

In most cases, demand load response is indicated at peak demand to reduce the disturbances of the potential risk-avoiding additional cost of capital requirements for other operating networks [20]. If power generation source utilized greater cost of generation capacity, customers will be paid for greater prices of electricity.

Any serious imbalance brings about grid failures and could cause severe voltage fluctuations or grid instability. Therefore, the capacity of total generation is inspected corresponding for contingencies [21] and allowance to some error margin (such as during peak demand periods, plants are off-line) with total peak load demand. Operators want to use commonly the least expensive power generating plant at certain period of time (considered as marginal cost) and in the time of demand expansion, additional capacity is managed from overpriced plants.

The daily basis about 24 h scale demand responds characteristics is illustrated in Fig. 1:

Some references of data are taken, respectively, on daily demand load from southern and northern region data of India. At last our aim is to determine the voltage

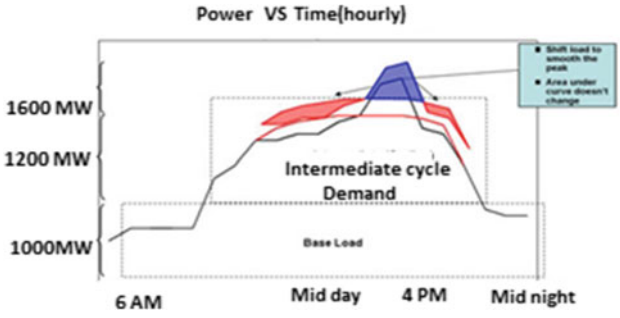


**Fig. 1** A figure of daily basis about 24 h demands response illustration

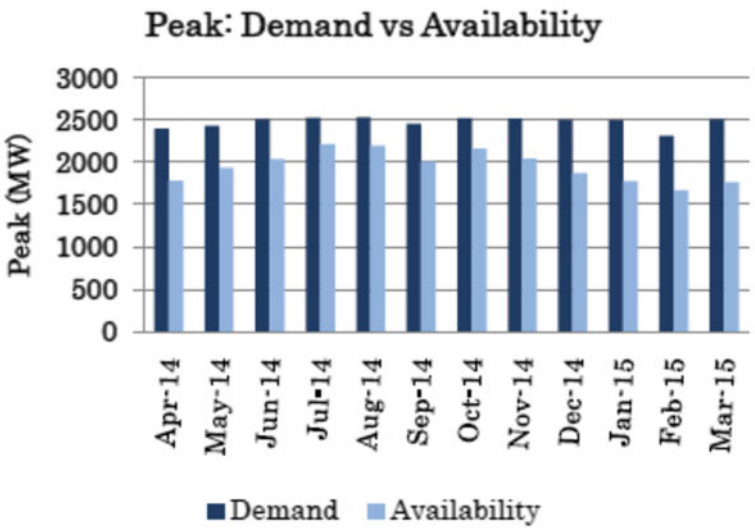


**Fig. 2** A figure of Peak demand against peak availability

stability in respect of demand load variation in West Bengal with smartly control the grid and adequately investigates the economic load power factor.

**North–East Region of India**:

See Fig. 2.

**Southern Region of India**:

See Fig. 3.

Digital technologies will approach the smart grid due to the incorporation of real-time information enabling from distributed energy resources (DER), generating stations and demand resources for coordination with stakeholder as well as consumers and operators. Distributed generation allows the smart grid for using all voltage levels and smart meters (Table 1).

From the analytical perspective contour of the power model, IEEE 14 bus smart system is described in Fig. 4. The stability process is to analyze on upper band variation of large load that depended on dynamic demand load variation subject to the percentage of loading located in different load buses. The objective is to determine stability analysis of smart model through different voltage stability indexing for every response of demand load variation in West Bengal.

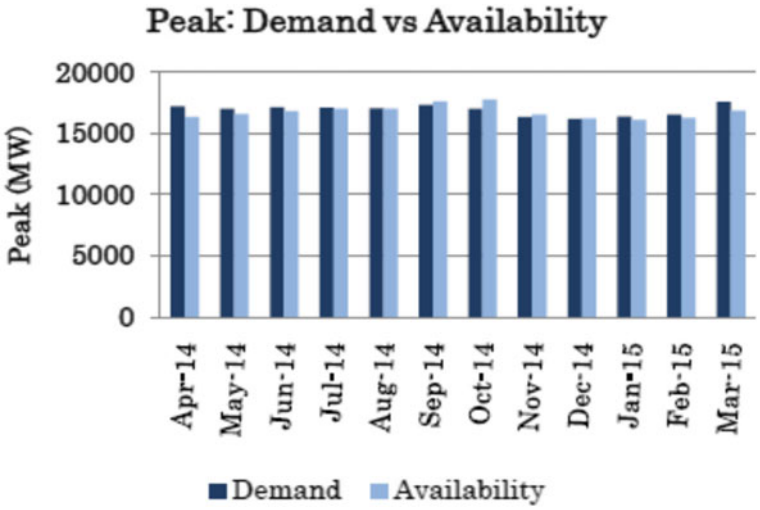


**Fig. 3** A figure of Peak demand against peak availability

**Table 1** Data analysis of demand-side load variation in West Bengal during the year 2014–15

| Sl. no. | Months | Time period | Availability shortfall (MW) | Loading percentage (%) | Location of bus loading (MW) | Voltage stability factor |
|---|---|---|---|---|---|---|
| 1 | March | Summer | 50.8 | 80 | Bus 3 | 0.2617 |
| 2 | April | | | 60 | Bus 12 | 0.1244 |
| 3 | May | | | 40 | Bus 14 | 0.3265 |
| 4 | June | | | 20 | Bus 6 | 0.1132 |
| 5 | July | | | 10 | Bus 3 | 0.2246 |
| 6 | August | Autumn | 32.54 | 50 | Bus 5 | 0.3244 |
| 7 | September | | | 30 | Bus 6 | 0.4458 |
| 8 | October | | | 10 | Bus 12 | 0.3256 |
| 9 | November | Winter | 24 | 60 | Bus 14 | 0.4538 |
| 10 | December | | | 40 | Bus 3 | 0.2677 |
| 11 | January | | | 30 | Bus 6 | 0.2282 |
| 12 | February | | | 20 | Bus 7 | 0.1248 |

## 4 Case Study and Analysis of System Model

In most cases, demand load response [22] is indicated at peak demand to reduce the disturbances of potential risk. In these model analyses, yearly peak load demands are divided into three groups alternately. Summer, autumn and winter are indicated groups in this analysis. Primarily, it was analyzed here as input data taking the load

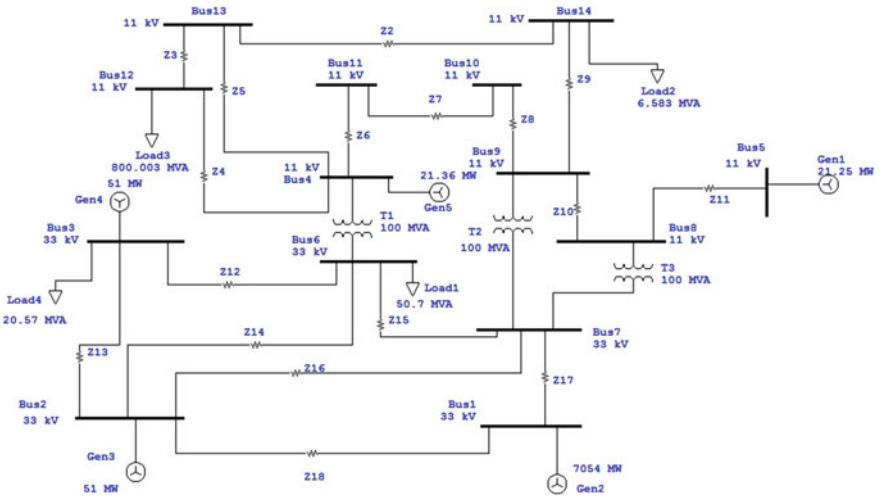


**Fig. 4** A figure of IEEE 14 bus smart model

variation of different kinds of seasons that examine on IEEE 14 bus smart system with the peak to peak load demand. If the generator produced energy in the fixed mode in this study case, we surveyed different average sample data for the calculation of load flow analysis. If any system suddenly goes through the collapse point, analysis of transient stability is needed to examine the generator frequency and rotor angle response status. Due to demand shifting or demand variation, how to respond to change in the generator for variation of different seasons was also affecting the grid network.

## *4.1 Direct Load Forecasting*

According to classical load modeling [23], direct load control (DLC) is that different kinds of loads are operated fully controlling the mode of the controller, i.e. they what to do, they are told as to do. An intelligent smart grid controls the load ideally. Employing the GPS incentive charge is saved at emergency through an automatic intelligent server which provides the prompt message of demand variation to the server.

## *4.2 Demand Shifting*

When load modeling is applied, demand shifted to another desire point [24]. Moving of load in a critical point causes various possibilities of system instability. If tomorrow

**Table 2** Voltage stability indexes analysis

| Various indexes | Time frame | | |
|---|---|---|---|
| | Summer | Autumn | Winter |
| $LQF_{ij}$ | 0.39284 | 0.34333 | 0.31736 |
| $FVSI_{ij}$ | 0.298602 | 0.28548 | 0.27658 |
| Smart L-type | 0.99784 | 0.98534 | 0.97682 |

by weather and other forecasts grid emergency is created, an intelligent system can plan their action of safety.

### *4.3 Smart L-type Voltage Stability Index*

If the smart L-type voltage stability index is determined by some process of the above described proposed technique, it will show more efficiency improvement practically than other indexes of voltage stability. By the numerical technique, the Newton–Raphson process is applied on the grid network through simulating mode to solve the nonlinear equations and analyzes the load flow process. Assume base active power ($P_{base}$) = 100 MW and base reactive power ($Q_{base}$) = 100 MVAR as system base parameters. All these solutions are calculated in p.u. data. For this smart L-type index, we should also compare between the $LQF^t$ and $FVSI^t$ to analyze the voltage stability at a particular band of the time. In every case, one sampled data is verified (Table 2).

### *4.4 Voltage Stability Index*

It is investigated from the $\partial V_i/\partial|Q_i|$ values in Table 3 that are illustrated on the weakest bus. Now connecting bus no. 5–8 of IEEE 14 bus system model is the weakest bus of the system in Table 3. In the test system, theoretical outcomes indicated that the collapse point of generator 1 is most severely approaching the system. The practical results from the simulation of the test system pointed that point of collapse of generator 1 was most dangerous hence proving among all results.

## 5 System Results and Report Analysis with Discussion

The operation of dynamic demand load is subject to alter at interchanging point and load shifting in critical point is subject to risk being analysis of stability that system operated at the variety of large load. Three models are taken into reference as summer, autumn and winter in West Bengal during the year 2014–15. In illustrating

**Table 3** Stability index for IEEE 14 bus system

| Sl. no. | Connecting bus ID | $\frac{dv_i}{dq_i}$ |
|---|---|---|
| 1 | 1–2 | $-j4.16 * 10^{-3}$ |
| 2 | 1–7 | $-j2.16 * 10^{-4}$ |
| 3 | 2–3 | $-j1.35 * 10^{-3}$ |
| 4 | 2–6 | $-j1.68 * 10^{-6}$ |
| 5 | 2–7 | $-j3.18 * 10^{-6}$ |
| 6 | 3–6 | $-j1.2047 * 10^{-7}$ |
| 7 | 4–11 | $-j1.75 * 10^{-8}$ |
| 8 | 4–12 | $-j2.58 * 10^{-6}$ |
| 9 | 4–13 | $-j5.16 * 10^{-3}$ |
| 10 | 5–8 | −j0.01123 |
| 11 | 6–7 | $-j2.44 * 10^{-5}$ |
| 12 | 8–9 | $-j7.75 * 10^{-7}$ |
| 13 | 9–10 | $-j1.63 * 10^{-8}$ |
| 14 | 9–14 | $-j1.32 * 10^{-8}$ |
| 15 | 10–11 | $-j8.69 * 10^{-4}$ |
| 16 | 12–13 | $-j6.69 * 10^{-3}$ |
| 17 | 13–14 | $-j5.76 * 10^{-3}$ |

pursuance on every kind of distributed generator, effects have been investigated into smart grid [25]. Steady-state as well as transient stability technique performs analysis of stability. Validating voltage pattern, the Newton–Raphson Method is employed for estimating load flow study to analyze the steady-state profiles, and overloading as well as convergence points are mapped. When G V, G IV, GIII and GI are co-ordinated into the smart grid, transient stability analysis, i.e. short-circuited condition, has been investigated notably. The parameters, i.e. power angle, frequency and voltage are being determined. Different kinds of model are considered as below.

The transient stability assessment was particularly executed when perturbation or fault occurs in the transmission grid network. The response of load flow is indicated in Fig. 5.

Fault created on a system at bus 7 with initial step time 0.000010. In complex process, variation of load demand at West Bengal has simulated the system model to clarify the season of summer to winter profiles. Hence, the set value indicates precisely the solution of load flow with the small step value. All the cases step time for a solution is 0.0000100000 and the simulation process runs up to five seconds during faults. If in a system any disturbance occurs, to decide how much to vary for demand variation or demand shifting, therefore, it is needed to analyze the transient stability. The various characteristics like rotor angle and frequency of generator variation are recorded down. The Electrical Transient Analyzer program may help to resolve the programed solution (Fig. 6).

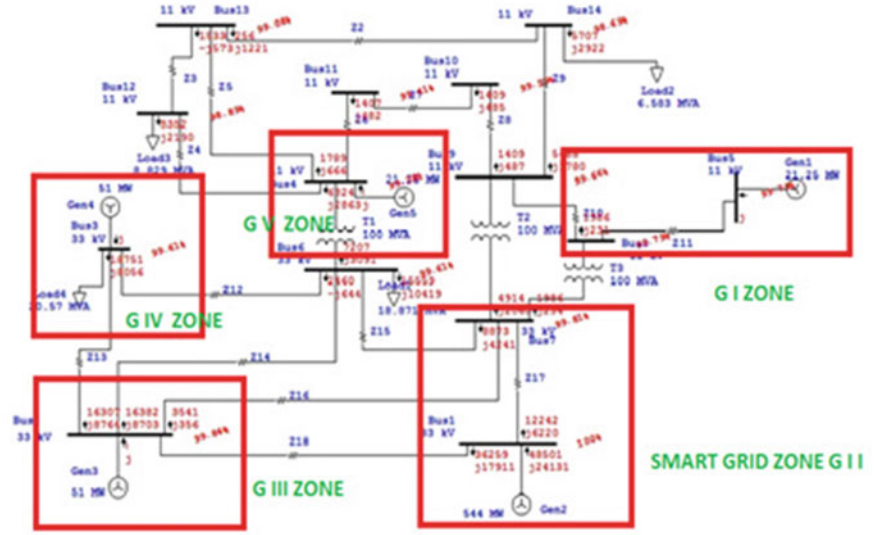


**Fig. 5** A figure of load flow solution on IEEE 14 bus illustration

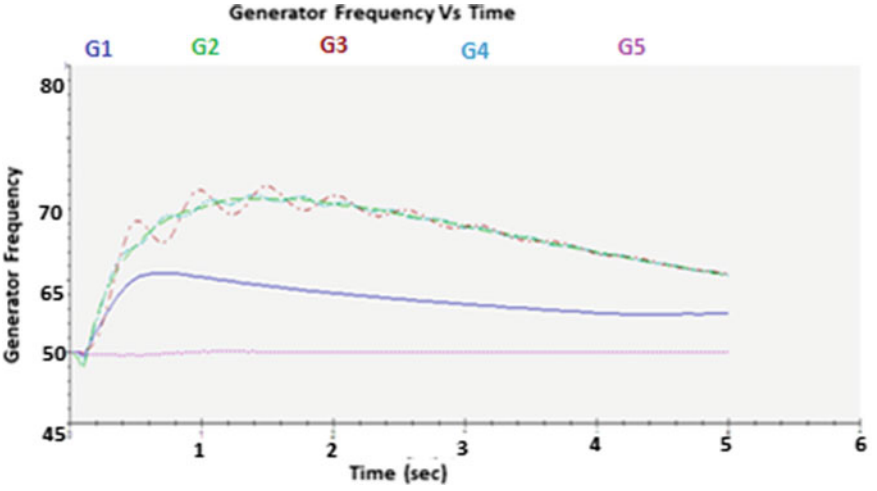


**Fig. 6** A figure of generator frequency variation in summer

From Fig. 7 Gen 2, 3 and 4 suffer rapidly with massive fluctuation in the angle of rotor and negative swing mode broadly. Hence, generators 5 and 1 are oscillating in high magnitude and zero-crossing abruptly in summer load.

$$\Delta\delta = \sin^{-1}\left\{\left(\frac{\partial P_e}{\partial X}\right)_0\right\}\frac{W_F}{\Delta P_e} \tag{5}$$

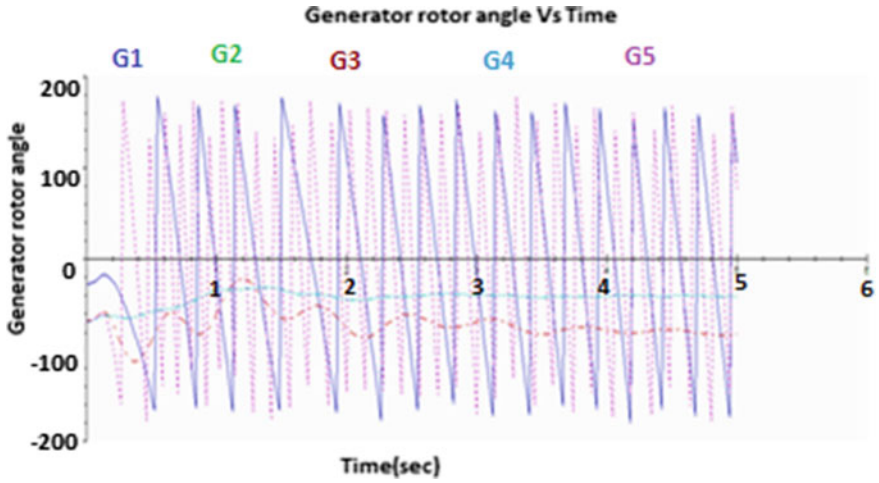


**Fig. 7** A figure of the angle of generator rotor variation in summer

$W_F$ is the weather forecasting time function and $\Delta\delta$ is the rotor swing angle.

In Fig. 8, for generators 5 and 1, the angle of the rotor widely swings in oscillatory at autumn whereas for the other generators, negative swings almost occurred in nature.

In Fig. 9, frequency of generator 1 reflection is maximum taking place with respect to other generators' load response in winter.

In Fig. 10, Generator 1 is fluctuating and other generators except 5 persist no change in nature, and the rotor angle of generator 5 has drooping characteristics in winter load demand.

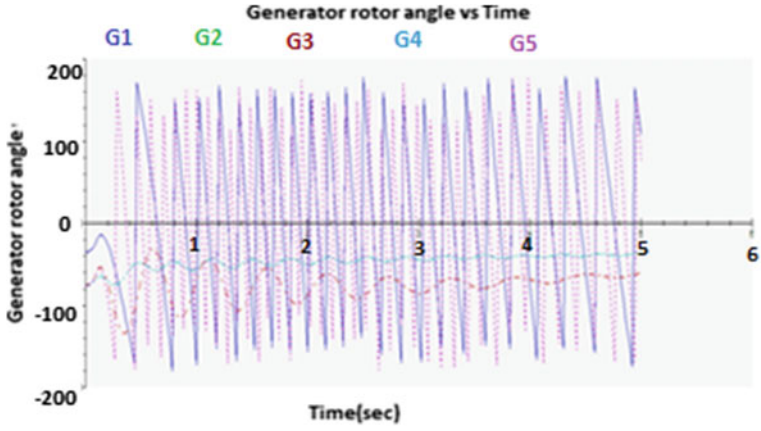


**Fig. 8** A figure of the angle of generator rotor variation in autumn

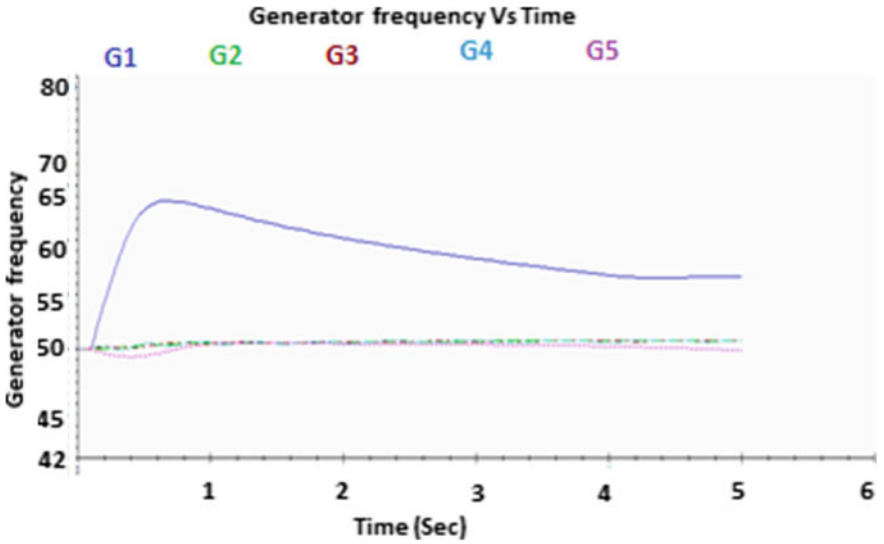


**Fig. 9** A figure of generator frequency variation in winter

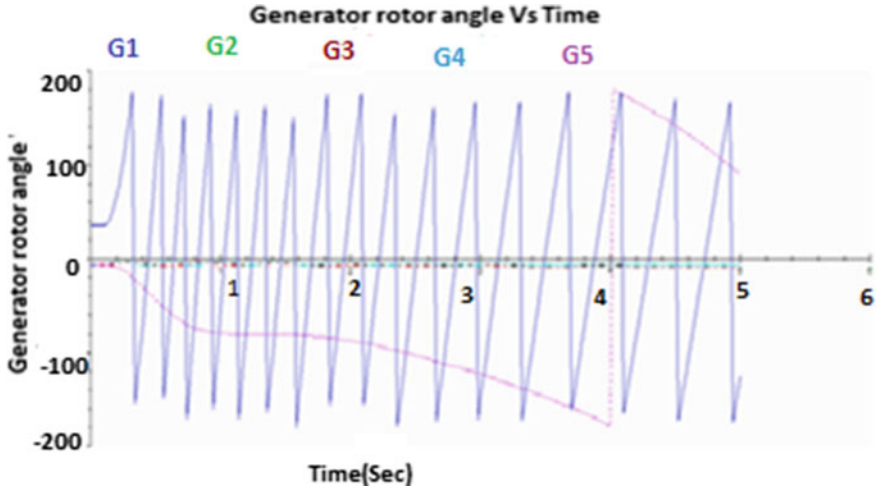


**Fig. 10** A figure of the angle of generator rotor variation in winter

## 6 Conclusion

The outcome of visional figures of temperature, pressure and other parameters is improved for an approximation of solution technique which is low cost, fast forward and advanced too. Minimizing the losses, interruption level of energy interchange

points is convenient to collect meter readings in incoming or outgoing feeders and smart decisions are taken for corrective action of voltage stability.

Finally, weighted consideration network analysis of the real data in simulation mode that indicates various existing complex networks (communication and transport) validated the idea of efficiency diffusion both locally and globally which explained the voltage indices in power networks as the essential need of the balanced system. If the original network frequency changes to adjust the demand load input variation, synchronic balance in the power network is also faulty, and within the specified time limit, corrective actions are taken in generating station. Otherwise, voltage instability occurs due to power mismatch and the point of converging area does not meet for actual system match.

In the whole year, voltage index changes with the demand variation of peak load as well as reactive and active power changes in each bus in due time drawn the significance of stability profile all along with security and reliability. The line quality factor of summer is found to be maximum as regards variation of winter load factor at the different combination of buses. These stability factors will implement to be acknowledged in the future through a better way of many objectives consideration and constraint criteria concurrently are considering the dynamic model.

## References


1. B. Gao, G.K. Morison, P. Kundur, Voltage stability evaluation using modal analysis. IEEE Trans. Power Syst. **7**(4), 1529–1539 (1992)
2. "Assessment of Demand Response and Advanced Metering", Federal Energy Regulatory Commission, February 2011. [Online]. http://www.ferc.gov/legal/staff-reports/2010-dr-report.pdf.
3. A. Chakraborty, A. De, C.K. Chanda, Development of a unique network equivalencing technique for determining voltage stable states in a multi-bus longitudinal power system using load flow analysis. IE(I) J. **85**, 196–202, March 2005
4. M. Morimoto, K. Harada, M. Sagamihara, H. Sawami, The Gauss-Seidel iterative method with the preconditioning matrix. Jpn. J. Indus. Appl. Math. **21**(1), 25–34. https://doi.org/10.1007/BF03167430
5. D. Holmberg, "Demand response and standards, BACnet® today & the smart grid"—A supplement to Ashrae Journal, pp. 823–828, November 2011
6. D.A. Haughton, S. Member, G.T. Heydt, L. Fellow, A linear state estimation formulation for smart distribution systems. IEEE Trans. Power Syst. 1–9 (2013)
7. L G.B. R Report, Govt of India, 2014–15
8. J. Bialek, Tracing the flow of electricity. IEEE Proc. Generat. Transmission Distrib. **143**(4), 313–320 (1996)
9. R.N. Patel, T.S. Bhatti, D.P. Kothari, Matlab/Simulink—based transient stability analysis of a multi-machine power system analysis. Int. J. Electr. Eng. Educ. **39**(4), 320–336 (2002)
10. S. Dey, C.K. Chanda, A. Chakraborty, Concept of a global voltage security indicator (VSI) and role of SVC on it in longitudinal power supply (LPS) systems. Electr. Power Syst. Res. **68**, 1–9 (2004)
11. G. Walsh, H. Ye, L. Bushnell, Stability analysis of networked control systems. IEEE Trans. Control Syst. Tech. **10**, 438–446 (2002)
12. "Report of NIST on the Smart Grid Interoperability Standards Roadmap" June 17, 2009

13. D. Yang, B. Zhou, X. Du, A simplification method of power flow calculation based on Newton–Raphson. J. Shenyang Inst. Eng. (Nat. Sci.) **4**(1), 37–40 (2008)
14. P.K. Iyambo, R. Tzonova, Transient stability analysis of the IEEE 14-bus electrical power system. IEEE Conf. (2007)
15. M. Stubbe, A. Bihain, J. Deuse, Simulation of voltage collapse. Electr. Power Energy Syst. **15**(4), August 1993
16. D. Nguyen, Y. Shen, M. Thai, Detecting critical nodes in interdependent power networks for vulnerability assessment. IEEE Trans. Smart Grid **4**(1), 151–159 (2013)
17. R. Earle, E. Kahn, E. Macan, Measuring the capacity impact of demand response. Electr. J. **22**(6), 47–58 (2009)
18. G.B. Jasmon, L.H.C. Lee, Distribution network reduction for voltage stability analysis and load flow calculations. Electr. Power Energy Syst. **13**(1), 9–13 (1991)
19. K. Seethalekshmi, S.N. Singh, S.C. Srivastava, A synchro phasor assisted frequency and voltage stability based load shedding scheme for self-healing of power system. IEEE Trans. Smart Grid **2**(2), 221–230 (2011)
20. C. Zhang et al., An interpretative structural modeling base network reconfiguration strategy for power systems. Int. J. Elect. Power Energy Syst. **65**, 83–93 (2015)
21. J. Blazewics, P. Erwin, S. Margozata, W. Frank, The two-machine flow-shop problem with weighted late work criterion and common due date. Eur. J. Oper. Res. **165**, 408–415 (2005)
22. Z. Baharlouei, M. Hashemi, Efficiency-fairness trade-off in privacy-preserving autonomous demand side management. IEEE Trans. Smart Grid **5**(2), 799–808 (2014)
23. D. Das, H.S. Nagi, D.P. Kothari, Novel method for solving radial distribution networks. IEE Proc. Gener. Transmission Distrib. **141**(4), 291–298 (1994)
24. D. Hurley, P. Peterson, M. Whited, Demand response as a power system resource (2013)
25. W. Qi, J. Liu, P.D. Christofides, A distributed control framework for smart grid development: energy/water system optimal operation and electric grid integration. J. Process Control **21**, 1504–1516 (2011)

# 3R Economy of a PKL Electrochemical Cell


**K. A. Khan, Shahinul Islam, Md. Delowar Hossain Munna, S. M. Zian Reza, M. Hazrat Ali, and Farhana Yesmin**

## 1 Introduction

The traditional sources of energy are very limited in the world which will soon run out in the near future [1–6]. Therefore, it needs alternative renewable energy sources that are environmental friendly. As a continuation of such investigation, an abandoned PKL (Pathor Kuchi Leaf) module was chosen where the basic principle of the module is a simple galvanic cell system consisting of Zinc (Zn) and Copper (Cu) electrodes, and the PKL extract is used as an electrolyte [7–12]. The age of the electrolyte was almost 8 years. It is noted that the production of electricity from PKL was invented in 2008 by Dr. Md. Kamrul Alam Khan, Ex-Dean (Faculty of science, Jagannath University), Ex-Chairman, Department of Physics, Jagannath University, Dhaka, Bangladesh [12–15]. The 3R economy is very popular nowadays [16–18]. The term 3R means reduction, recycle and reuse. To develop the economy of the country, the 3R economy is very necessary for any country. To keep it in mind, an old-aged PKL electrochemical cell has been designed and developed by the authors.

K. A. Khan (✉)
Department of Physics, Jagannath University, 9-10 Chittaranjan Avenue, Dhaka 1100, Bangladesh

S. Islam · Md. Delowar Hossain Munna · S. M. Zian Reza
Department of Physics, Uttara University, Dhaka, Bangladesh

M. Hazrat Ali
European University of Bangladesh (EUB), Dhaka, Bangladesh

F. Yesmin
Department of Civil Engineering, Dhaka Polytechnic Institute, Dhaka, Bangladesh



C. K. Chanda et al. (eds.), *Advanced Energy and Control Systems*, Lecture Notes in Electrical Engineering 820, https://doi.org/10.1007/978-981-16-7274-3_11

## 2 Methodology

### *2.1 Methods for Performances of Electricity Generation Using 50% PKL Extract in the Battery Box Made by Glass*

The PKL module was filled with PKL extract 50% of the box volume. When the box was filled with PKL extract, the open circuit voltage was 5.9 V and the short circuit current was almost 1A. Then with the help of this module, four types of 12 V fans and a 12 V LED lamp had been run. Here, the 12 V LED lamps were used as the load of the experimental setup (Figs. 1 and 2). After running these fans and LED lamps, the open circuit voltage of the module became 5.67 V. The experimental observations have been given in Table 1.

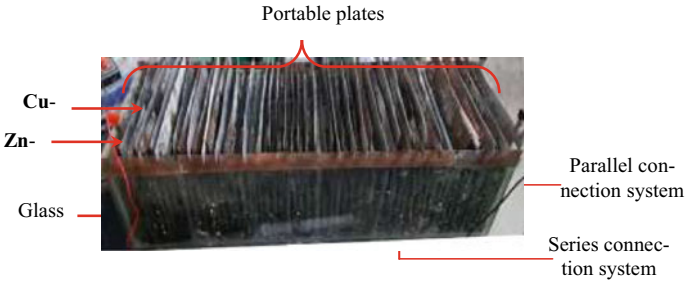


**Fig. 1** An abandoned portable plate PKL module

**Fig. 2** LED lamp is switching on by the abandoned portable electrode PKL module

**Table 1** Experimental results of a PKL module for using 50% PKL extract of the box

| No. of observations | Local time (PM) | Time duration (min) | Open circuit voltage, $V_{oc}$ (V) | Load voltage, $V_L$ (V) | Short circuit current, $I_{sc}$ (A) | Load Current, $I_L$ (mA) |
|---|---|---|---|---|---|---|
| 1 | 6:54 | 00 | 5.67 | 5.35 | 0.95 | 60 |
| 2 | 7:04 | 10 | 5.65 | 5.33 | 0.90 | 60 |
| 3 | 7:14 | 20 | 5.65 | 5.33 | 0.90 | 60 |
| 4 | 7:24 | 30 | 5.64 | 5.33 | 0.85 | 60 |
| 5 | 7:34 | 40 | 5.64 | 5.33 | 0.90 | 50 |
| 6 | 7:44 | 50 | 5.65 | 5.33 | 0.90 | 50 |
| 7 | 7:54 | 60 | 5.67 | 5.33 | 0.90 | 50 |
| 8 | 8:04 | 70 | 5.68 | 5.33 | 0.85 | 50 |
| 9 | 8:14 | 80 | 5.70 | 5.32 | 0.90 | 50 |
| 10 | 8:24 | 90 | 5.71 | 5.32 | 0.85 | 50 |
| 11 | 8:34 | 100 | 5.71 | 5.32 | 0.90 | 50 |
| 12 | 8:44 | 110 | 5.70 | 5.32 | 0.90 | 50 |
| 13 | 8:54 | 120 | 5.70 | 5.31 | 0.90 | 50 |

## *2.2 Methods for Performances of Electricity Generation Using 100% PKL Extract in the Battery Box Made by Glass*

After the experiment IIA, the Zn-plates were withdrawn but the Cu-plates were remaining in the module. After 46 h later, the Zn-plates were dipped again into the module. But this time, PKL extract was taken 100% of the box volume and similar readings were taken as like experiment IIA. The experimental observations have been given in Table 2.

## *2.3 Electricity Generation Performance Using a Load (LED Lamp) for 21 h*

After the end of the experiment IIB, the whole experimental setup was unchanged for 21 h that means the LED lamp was switched on for 21 h. After 21 h later, similar readings were taken as like experiment IIA. The experimental observations have been given in Table 3.

**Table 2** Experimental results of a PKL module for using 100% PKL extract of the box

| No. of observations | Local time (PM) | Time duration (min) | Open circuit voltage, $V_{oc}$ (V) | Load voltage, $V_L$ (V) | Short circuit current, $I_{sc}$ (A) | Load current, $I_L$ (mA) |
|---|---|---|---|---|---|---|
| 1 | 6:50 | 2756 | 5.69 | 5.31 | 0.90 | 45 |
| 2 | 7:00 | 2766 | 5.71 | 5.31 | 0.90 | 40 |
| 3 | 7:10 | 2776 | 5.71 | 5.31 | 0.95 | 40 |
| 4 | 7:20 | 2786 | 5.71 | 5.31 | 0.90 | 40 |
| 5 | 7:30 | 2796 | 5.70 | 5.31 | 0.95 | 40 |
| 6 | 7:40 | 2806 | 5.69 | 5.31 | 0.95 | 40 |
| 7 | 7:50 | 2816 | 5.68 | 5.31 | 0.90 | 40 |
| 8 | 8:00 | 2826 | 5.67 | 5.30 | 0.90 | 40 |
| 9 | 8:10 | 2836 | 5.67 | 5.30 | 0.90 | 40 |
| 10 | 8:20 | 2846 | 5.66 | 5.30 | 0.85 | 40 |
| 11 | 8:30 | 2856 | 5.66 | 5.30 | 0.85 | 40 |
| 12 | 8:40 | 2866 | 5.67 | 5.30 | 0.90 | 35 |
| 13 | 8:50 | 2876 | 5.66 | 5.30 | 0.85 | 35 |

**Table 3** Experimental results of a PKL module for switching on the load for 21 h

| No. of observations | Local time (PM) | Time duration (min) | Open circuit voltage, $V_{oc}$ (V) | Load voltage, $V_L$ (V) | Short circuit current, $I_{sc}$ (A) | Load current, $I_L$ (mA) |
|---|---|---|---|---|---|---|
| 1 | 5:50 | 4136 | 5.48 | 5.17 | 0.60 | 17 |
| 2 | 6:00 | 4146 | 5.48 | 5.17 | 0.60 | 17 |
| 3 | 6:10 | 4156 | 5.48 | 5.17 | 0.60 | 17 |
| 4 | 6:20 | 4166 | 5.49 | 5.17 | 0.60 | 15 |
| 5 | 6:30 | 4176 | 5.49 | 5.17 | 0.62 | 15 |
| 6 | 6:40 | 4186 | 5.49 | 5.17 | 0.60 | 17 |
| 7 | 6:50 | 4196 | 5.48 | 5.17 | 0.60 | 17 |
| 8 | 7:00 | 4206 | 5.47 | 5.17 | 0.60 | 17 |
| 9 | 7:10 | 4216 | 5.49 | 5.17 | 0.60 | 17 |
| 10 | 7:20 | 4226 | 5.49 | 5.17 | 0.60 | 17 |
| 11 | 7:30 | 4236 | 5.49 | 5.17 | 0.60 | 17 |
| 12 | 7:40 | 4246 | 5.49 | 5.17 | 0.63 | 17 |
| 13 | 7:50 | 4256 | 5.48 | 5.17 | 0.63 | 17 |

**Table 4** Experimental results of a PKL module for withdrawing the load for 22 h

| No. of observations | Local time (PM) | Time Duration (min) | Open circuit voltage, $V_{oc}$ (V) | Load voltage, $V_L$ (V) | Short circuit current, $I_{sc}$ (A) | Load current, $I_L$ (mA) |
|---|---|---|---|---|---|---|
| 1 | 5:50 | 5576 | 5.46 | 5.17 | 0.55 | 15 |
| 2 | 6:00 | 5586 | 5.45 | 5.17 | 0.60 | 14 |
| 3 | 6:10 | 5596 | 5.44 | 5.17 | 0.55 | 14 |
| 4 | 6:20 | 5606 | 5.44 | 5.17 | 0.60 | 15 |
| 5 | 6:30 | 5616 | 5.44 | 5.16 | 0.55 | 15 |
| 6 | 6:40 | 5626 | 5.44 | 5.16 | 0.50 | 14 |
| 7 | 6:50 | 5636 | 5.44 | 5.16 | 0.50 | 15 |
| 8 | 7:00 | 5646 | 5.44 | 5.16 | 0.50 | 15 |
| 9 | 7:10 | 5656 | 5.44 | 5.16 | 0.55 | 14 |
| 10 | 7:20 | 5666 | 5.44 | 5.16 | 0.55 | 14 |
| 11 | 7:30 | 5676 | 5.45 | 5.16 | 0.55 | 14 |
| 12 | 7:40 | 5686 | 5.44 | 5.16 | 0.55 | 14 |
| 13 | 7:50 | 5696 | 5.44 | 5.16 | 0.55 | 14 |

### *2.4 Electricity Performance Withdrawing the Load (LED Lamp) for 22 h*

After the end of the experiment IIC, the whole experimental setup was unchanged except for the load. The load (LED lamp) was withdrawn and 21 h later, the load (LED lamp) was switched on again and similar readings were taken as like experiment IIA. The experimental observations have been given in Table 4.

## 3 Results and Discussion

Figure 3 shows the variation of open circuit voltage, $V_{oc}$ (V), with the variation of time duration (min) for four types of experiments. It was found that for the experiment 2A (PKL extract 50% of the box volume), $V_{oc}$ was changing very slightly (5.67–5.71 V) with the increase of time duration. The change of $V_{oc}$ was almost periodic. But it was interesting that for the experiment IIB (PKL extract 100% of the box volume), the change of $V_{oc}$ was almost like experiment 2A. That means the change of $V_{oc}$ is independent of the amount of PKL extract. Although $V_{oc}$ is more flat (stable) for experiment IIB.

It was also found that after switching on the LED lamp for 21 h (experiment 2C), the open circuit voltage, $V_{oc}$, was dropped for about 0.2 V. But in this case, $V_{oc}$ was almost constant with the increase of time duration. $V_{oc}$ was changed from 5.47 to 5.49 V. It was interesting that for the experiment 2D (Withdrawing the load for 22 h),

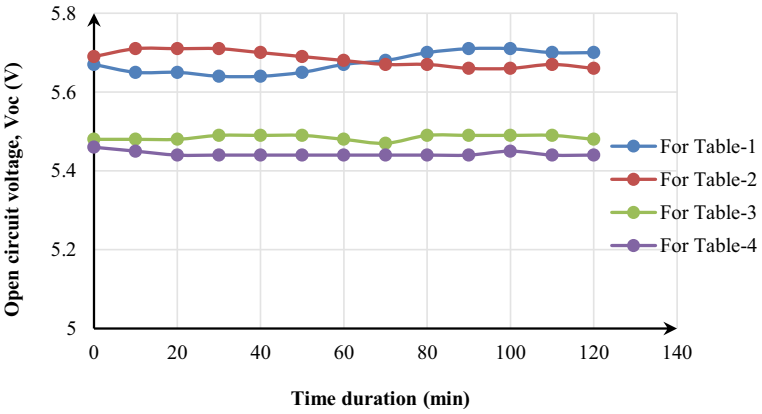


**Fig. 3** Variation of open circuit voltage, $V_{oc}$ (V), with the variation of time duration (min)

$V_{oc}$ was almost constant too with the increase of time duration. In this case, $V_{oc}$ was changed from 5.44 to 5.46 V.

Figure 4 shows the variation of load voltage, $V_L$ (V), with the variation of time duration (min) for four types of experiments. It was found that for the experiment IIA (PKL extract 50% of the box volume), the initial value of $V_L$ was 5.35 V. But with the increase of time duration, $V_L$ was changing very slightly and the minimum value of $V_L$ was 5.31 V. But in the experiment IIB (PKL extract 100% of the box volume), $V_L$ was almost constant and it was confined between 5.30 and 5.31 V.

It was also found that after switching on the LED lamp for 21 h (experiment 2C), the load voltage, $V_L$, was dropped by about 0.16 V. But in this case, $V_L$ was just constant with the increase of time duration. This constant voltage was 5.17 V.

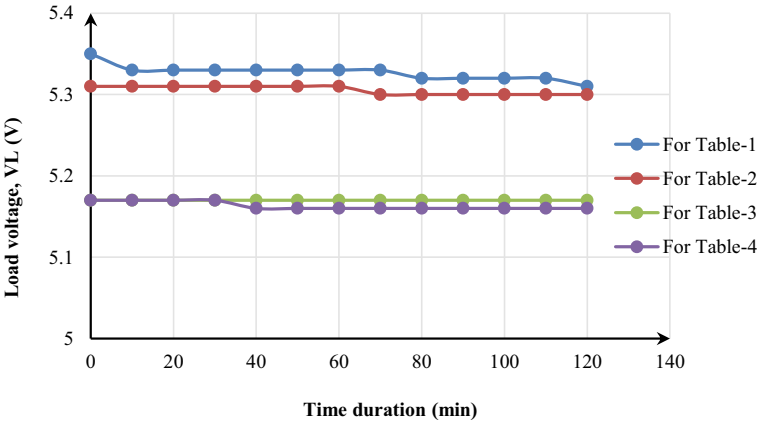


**Fig. 4** Variation of load voltage, $V_L$ (V), with the variation of time duration (min)

It was interesting that for the experiment 2D (Withdrawing the load for 22 h), $V_L$ was almost constant too with the increase of time duration. But sometimes it deviated from 5.16 to 5.17 V.

Figure 5 shows that the variation of short circuit current with the variation of time duration for four different conditions. It is shown that the short circuit current decreases for different conditions of the different tables. It is also shown that the short circuit current was almost constant for Table 3.

Figure 6 shows the variation of load current with the variation of time duration for four different conditions. It is shown that the load current decreases for different conditions of the different tables. It is also shown that the load currents were almost constant for Tables 3 and 4.

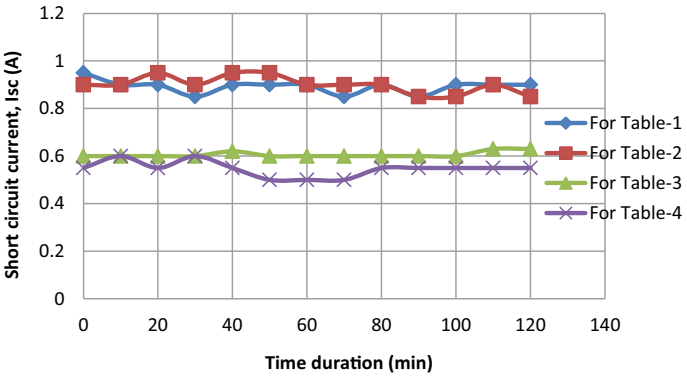


**Fig. 5** Variation of short circuit current, $I_{sc}$ (A), with the variation of time duration (min)

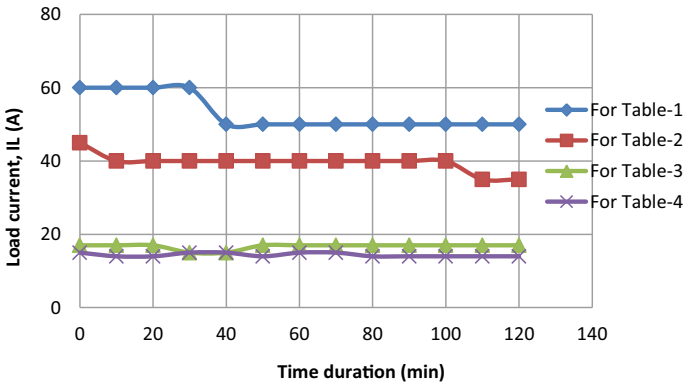


**Fig. 6** Variation of load current, $I_L$ (A), with the variation of time duration (min)

## 4 Conclusions

From this research work, it can be concluded that the 3R economy is feasible and viable for PKL electrochemical cells. In this research work, it is shown that both the Zn/Cu-based electrodes and PKL electrolyte can be used as a 3R economy.

## References


1. P.E. Coombe, Wavelength specific behaviour of the whitefly Trialeurodes vaporariorum (Homoptera: Aleyrodidae). J. Comp. Physiol. **144**, 83–90 (1981)
2. P.E. Coombe, Visual behaviour of the greenhouse whitefly Trialeurodes vaporariorum. Physiol. Entomol. **7**, 243–251 (1982)
3. H.S. Costa, K.L. Robb, C.A. Wilen, Field trials measuring the effects of ultraviolet-absorbing greenhouse plastic films on insect populations. J. Econ. Entomol. **95**, 113–120 (2002)
4. K.A. Khan, Copper oxide coatings for use in a linear solar Fresnel reflecting concentrating collector, Published in the Journal of Elsevier, Renewable Energy, An International Journal, WREN (World Renewable Energy Network), UK, RE: 12.97/859,1998, Publication date 1999/8/1, J. Renewable energy, **17**(4):603–608. Publisher-Pergamon (1999)
5. T.A. Ruhane, M. Tauhidul Islam, M. Saifur Rahman, M.M.H. Bhuiyah, J.M.M. Islam, T.I. Bhuiyah, K.A. Khan, M.A. Khan, Impact of photo electrode thickness annealing temperature on natural dye sensitized solar cell. Sustain. Energy Technol. Assess. Elsevier (2017). https://doi.org/10.1016/j.seta.2017.01.012
6. T.A. Ruhane, M. Tauhidul Islam, M. Saifur Rahaman, M.M.H. Bhuiyan, J.M.M. Islam, M.K. Newaz, K.A. Khan, M.A. Khan, Photo current enhancement of natural dye sensitized solar cell by optimizing dye extraction and its loading period. Optik—Int. J. Light Electron Opt. Elsevier (2017)
7. M. Hasan, K.A. Khan, Dynamic model of Bryophyllum pinnatum leaf fueled BPL cell: a possible alternate source of electricity at the off-grid region in Bangladesh, in *Microsystem Technologies Micro- and Nanosystems Information Storage and Processing Systems* (Springer, 2018). ISSN 0946-7076, Microsyst. Technol. https://doi.org/10.1007/s00542-018-4149-y
8. K.A. Khan, M. Hazrat Ali, A.K.M. Obaydullah, M.A. Wadud, Production of candle using solar thermal technology, in *Microsystem Technologies Micro- and Nanosystems Information Storage and Processing Systems* (Springer, 2019). ISSN 0946-7076. Microsyst. Technol. **25**(12). https://doi.org/10.1007/s00542-019-04390-7
9. K.A. Khan, S.R. Rasel, M. Ohiduzzaman, Homemade PKL electricity generation for use in DC fan at remote areas, in *Microsystem Technologies Micro- and Nanosystems Information Storage and Processing Systems* (2019), ISSN 0946-7076. Microsyst. Technol. **25**(12). https://doi.org/10.1007/s00542-019-04422-2
10. M. Hasan, K.A. Khan, *Experimental Characterization and Identification of Cell Parameters in a BPL Electrochemical Device.* Springer, SN Appl. Sci. **1**:1008 (2019). https://doi.org/10.1007/s42452-019-1045-8
11. L. Hassan, K.A. Khan, A study on harvesting of PKL electricity. Springer J. Microsyst. Technol. **26**, 1031–1041 (2020). https://doi.org/10.1007/s00542-019-04625-7, **26**(3),1032–1041 (2019)
12. K.A. Khan, M.A. Mamun, M. Ibrahim, M. Hasan, M. Ohiduzzaman, A.K.M. Obaydullah, M.A. Wadud, M. Shajahan, PKL electrochemical cell: physics and chemistry. Springer J., SN Appl. Sci. **1**,1335 (2019). https://doi.org/10.1007/s42452-019-1363-x
13. M. Hazrat Ali, U. Chakma, D. Howlader, M. Tawhidul Islam, K.A. Khan, Studies on performance parameters of a practical transformer for various utilizations, in *Microsystem Technologies* (Springer, 2019). https://doi.org/10.1007/s00542-019-04711-w, Accessed 3 Dec 2019

14. K.A. Khan, L. Hassan, A.K.M. Obaydullah et al., Bioelectricity: a new approach to provide the electrical power from vegetative and fruits at off-grid region. Microsyst. Technol. (2018). https://doi.org/10.1007/s00542-018-3808-3
15. K.A. Khan, M.S. Bhuyan, M.A. Mamun, M. Ibrahim, L. Hasan, M.A. Wadud, Organic electricity from Zn/Cu-PKL electrochemical cell, in *Contemporary Advances in Innovative and Applicable Information Technology*, Advances in Intelligent Systems and Computing, vol. 812, ed. by J.K. Mandal et al. (Springer Nature Singapore Pvt. Ltd., 2018), Chapter 9, pp. 75–90
16. T. Cowan, G. Gries, Ultraviolet and violet light: attractive orientation cues for the Indian meal moth. Plodia interpunctella. Entomol Exp Appl **131**, 148–158 (2009)
17. M.F. Day, Pigment migration in the eyes of the moth, Ephestia kuehniella Zeller. Biol. Bull. **80**, 275–291 (1941)
18. Emura K, Tazawa S, The development of the eco-engineering insect control technology-physical control of insect behavior using artificial lights. Eco-engineering **16**, 237–240 (2004) (in Japanese with English abstract)

# Embedded Control Systems and Sensors

# Multilevel Inverters Operating with Improved Harmonic Performance Using SVPWM


**Mohammed Asim, Mohd Suhail Khan, Raj Kumar Yadav, H. S. Mewara, and Nivedita Sethy**

## 1 Introduction

As we all know that cascaded H-bridge inverter consists of a large number of switches, and due to these large numbers of switches, the question arises of how we switch them to obtain the desired output waveform. In a cascaded H-bridge inverter, there are cells in the leg, and in one leg, there will be three legs, i.e. phase 1, phase 2 and phase 3, and in each cell, there are four switches. So due to this complex construction model, we have to switch from converter for which we have to use to techniques, that is phase shift PWM (PSPWM) and level shift PWM (LSPWM). PSPWM and LSPWM have more similar characteristics, the harmonics performances of LSPWM are slightly better, however, this matters for any level like more than five levels [1–4]. There are substantially different disadvantages of using these two techniques if we talk about the LSPWM, the distribution of loss will be uneven, and there are many other techniques to solve this uneven distribution of loss. Another method is to use modified space vector PWM in which we have to ensure that in three nearest vectors, a multilevel space vector diagram will be switched. By understanding PSPWM and LSPWM, we find more possible ways to implement these techniques in a space vector diagram by a simple modification in PSPWM and LSPWM to make changes we center the zero vector for any n-level space vector diagram. Let us first see what is the general approach for PWM by taking a very simple example. So, when we talk about phase shift PWM or when we talk about level shift PWM, let us see what the main or basic idea is. The phase shift PWM does that very easily by asking each

M. Asim · M. S. Khan
Department of Electrical Engineering, Integral University, Lucknow, India

R. K. Yadav (✉) · H. S. Mewara · N. Sethy
Department of Electronics Instrumentation and Control Engineering, Government Engineering College, Ajmer, Rajasthan, India

H. S. Mewara
e-mail: hsmewara@ecajmer.ac.in



C. K. Chanda et al. (eds.), *Advanced Energy and Control Systems*, Lecture Notes in Electrical Engineering 820, https://doi.org/10.1007/978-981-16-7274-3_12

of these H-bridges to produce 1 by *n* times the amplitude of the sine wave. So, for example, if this sine wave has an amplitude between 1 and minus 1 per unit then in phase shift PWM what do we do? We ask each of these H-bridges to produce an identical sine wave like the one we want to produce here all of them are identical, but each has 1 by *n* times the amplitude of the big sine wave that means, where *n* is the number of H-bridges. So, that means, each H-bridge is as if taking up the responsibility of producing 1 by *n* so that we have the output of the first H-bridge as this one, the second one is identical to it, the third one is identical to it and the fourth one is identical to it like that so that we at the end get a big sine wave which is this waveform here. So, each H-bridge is like producing one by n times the amplitude of the required waveform at the output. This will do this by comparing this sine wave with a high-frequency triangle.

## 2 Multilevel Converter Topologies

Multilevel converters are the family members of power electronics converter the output waveform produced by these converter consist of three or more discrete level voltage. Voltage steps of multilevel are smaller as we compare it with two-level waveform with the same fundamental component, due to smaller voltage steps, there should be less stress on the switching device and at lower rating devices, they allow to produce higher voltage waveform [5–9]. The harmonic distortion in multilevel is less as compared with two-level. By increasing the level of the converter, the output waveform increases, further reducing the voltage steps more closely the sinusoidal waveform can be obtained. The improved waveform quality can be obtained at the expense of increasing the complexity in designing and modeling the converter and with the increase in the level of converter, the controlling of the converter becomes more difficult in which the converter requires more switching devices and energy storage components. Cascaded H-bridge converter topology has been considered in this paper, the converter is made up of a single-phase, and the full-bridge inverter is connected in series with it. The modular structure decreases the commissioning cost, maintenance and it increases the tolerance of fault if the converter is controlled. A cascaded H-bridge 5 level inverter includes two cells per phase in which each cell contains an isolated voltage source, and the output voltage across the cell each of which can be –E, 0 and E, the output voltage of a phase leg can be shown as:

$$V_{ao} = E \sum_{n}^{N-1} Sn \tag{1}$$

where $N$ shows the number of converter cells, the result is that the $N$ cell produced $2N-1$ level. In a Cascaded H-Bridge converter, there is a redundancy of the switching state of a single-phase leg like any other converter. For medium voltage, speed drives

and STATCOM. For drive application, the DC link is supplied by the rectifier for separate winding of the complex input transformer. For such applications, the complexity and expense of the transformer limit the number of cells. The topology that has been most suited for the STATCOM application is the cascaded H-Bridge because it contains only a DC link without the need to deliver real power.

There are several ways of modulation techniques, some of which are presented here in this paper. The switching frequencies are subdivided into fundamental and high switching frequency [10–13]. In the case of fundamental switching frequency, switch commutation is produced at the output of fundamental frequency to target this frequency, which is used to cancel some particular low-frequency harmonics. In other divisions, there are selective harmonics and space vector control, which are also presented, In case of SHE, the output is in the form of a staircase wave, the duration of steps can be optimized to cancel some specified harmonics, the harmonics that are being eliminated are proportional to levels of the converter. Whereas, in SVC, the complex plane is divided into numerous hexagonal zones, which define the proximity of the reference to the closest applied vector. High switching frequencies' modulation of about 10–20 kHz is the adaptation of standard PWM to multilevel Modulation (SCSM), and Carrier-Based Space Vector Modulation (CBSVM) is reviewed for CMI. In general, for high power applications, most low-frequency methods are preferable because of the reduction in the switching losses, while at a higher dynamic range of applications, the better output quality and higher bandwidth of high switching frequency are more suitable [14–18].

## 3 Phase Shift Modulation Techniques for Three-Phase Cascaded H-Bridge Converter

Assume the number of cells in each phase is equal to 5 and then a total number of levels which is possible from this converter is 11 that is $2n + 1$, where n is the number of level cells. So, for this case, as I had earlier told that all the cells will require their carriers, but each carrier is shifted, phase-shifted from each other will require L−1 that is 10 carriers. Here, where the phase shift between the carriers is 360° divided by L−1, which is equal to 36°. So, this is the phase shift that is required between the carriers, it is equal to 360° divided by L minus 1, which is equal to 36°. Now, this angle of 360° is with respect to the carrier or the triangle frequency. If there is one cell then, these are the carriers for the two legs of one cell left leg and right leg, and they are 180° phase shifted. The left leg alone for all the 5 cells have these five carrier waveforms. It can be seen that these carriers are slightly phase-shifted from each other, this phase shift is 36° and 360° is the duration. We have taken 5 cell CHB with each cell having 1000 V DC bus and so, the output of cell one. So, each of these cells is given the same modulating waveform. Remember, each of these cells is given

the same modulating waveform, they are all having the same modulating waveform, but their carriers are slightly phase-shifted.

### A. Simulation and Modeling of Phase Shift Multicarrier PWM

In phase-shifted PWM (PSPWM), carrier waves are phase-shifted from each other by a certain angle. The angle by which the phase is shifted is given by 180/$n$ where $n$ $s$ number of H bridge cell in the given circuit. In the given case $n = 3$ so the required angle is 60°. The block diagram, simulation diagram and output waveforms of the three-phase CHB multilevel converter is shown in Figs. 1, 2 and 3. The simulation parameter for the output voltage level produced by CHB is $2n + 1$, where $n$ is the number of H-Bridge.

### B. Simulation and output results

The triangular pulse is compared with the sinusoidal wave, and the output is sent to the switch.

The equation of output voltage for each phase is $V_{an}$, $V_{bn}$, $V_{cn}$.

$$V_{an} = \frac{(2 \times V_{ao} - V_{bo} - V_{co})}{3} \tag{2}$$


**Fig. 1** General block diagram of the proposed technique

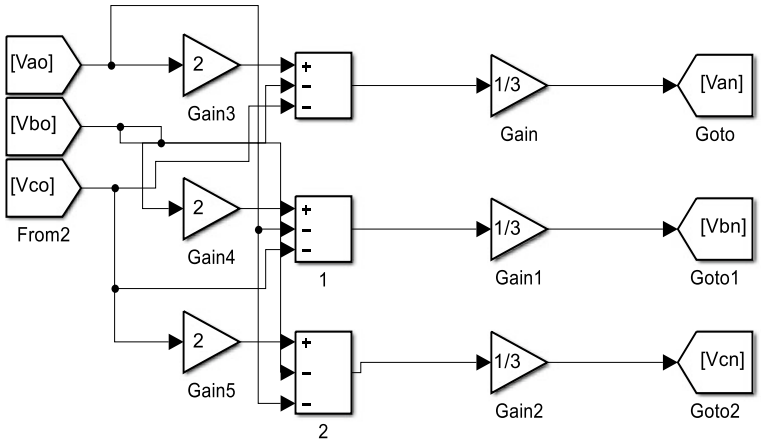


**Fig. 2** Simulink model of three-phase CHB multilevel converter

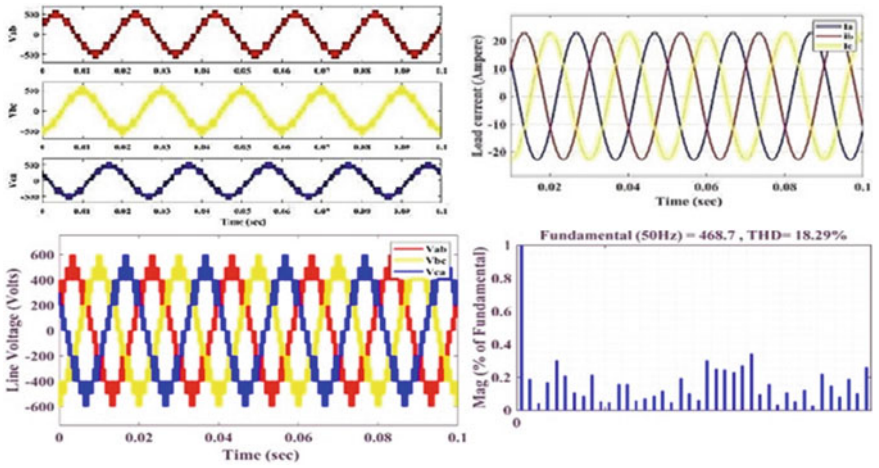


**Fig. 3** Individual line voltage, individual phase voltage, three-phase line voltage and THD profile

$$V_{bn} = \frac{(2 \times V_{ao} - V_{bo} - V_{co})}{3} \tag{3}$$

$$V_{cn} = \frac{(2 \times V_{ao} - V_{bo} - V_{co})}{3} \tag{4}$$

where,

$V_{ao}$ = Individual phase voltage for R phase

$V_{bo}$ = Individual phase voltage for Y phase

$V_{co}$ = Individual phase voltage for B phase.

The equation of load current of each phase is

$$i_a = \frac{(V_{an} - i_a + R)}{L \times s} \tag{5}$$

$$i_b = \frac{(V_{bn} - i_a + R)}{L \times s} \tag{6}$$

$$i_c = \frac{(V_{cn} - i_a + R)}{L \times s} \tag{7}$$

## C. Result and Discussion

In phase-shifted PWM, carrier waves are phase-shifted from each other by a certain angle that is given as 180/*n*, where *n* is the number of H bridge cells in the circuit. In this case, *n* is 3 so the phase shift angle is 60°. The simulation results of three-phase CHB multilevel converter are shown in Fig. 3.

## 4 Level Shift Pulse Width Modulation for Multilevel Cascaded H-Bridge Converter

In level shift PWM, the carriers for each cell are identical, they are all vertically phase-shifted or vertically shifted from one another. So we have only one carrier here, second carrier, third carrier, fourth carrier and so on, and that is why the term level shift comes, and hence it is a level shift PWM. The carriers in which the modulating waveform is shown spanning between minus 0.5 to plus 0.5 and the carriers are also vertically shifted from one another, the fundamental voltage from each cell gets added up because it's a series connection of H bridges. So, the fundamental voltages by its connection itself will get added up. Now, let us take the example of the five levels of CHB and for a five-level CHB, we will need four carriers, L minus 1, four carriers, and these are shown here with the different-colored carriers in this diagram. The total height of the modulating on the reference wave is 1, then the height of each carrier is 1 by 4 or 1 by the total number of carriers used. So, 1 by 4 is equal to 0.25, which means that if this is the modulating waveform its total height is 1. The idea is that the carrier should span the entire waveform, ultimately we need to produce the sine wave and if we do not have the pulse width modulation, we cannot produce the variable voltage which is part of the sine wave. The sine wave is continuously varying and we need the pulse width modulation to mimic or to produce this varying sine wave. So, wherever the modulating wave is present, the carrier should also be present so, that we can replicate the varying nature of the sine wave and therefore, the carriers should span the entire height of the modulating waveform.

### A. Result and Discussion

In level-shifted PWM, carrier waves are level shifted from each other. These are Phase Disposition (PD), Phase Opposite Disposition (POD) and Alternate Phase Opposition Disposition (APOD). In this simulation, the PD pulse width modulation technique is used. The simulation results of three-phase CHB multilevel converter is shown in Fig. 4.

## 5 Conclusion

In this work, a three-phase CHB multilevel converter is simulated and analyzed by using multicarrier pulse width modulation techniques. These multicarrier-based pulse width modulation techniques are level-shifted and phase-shifted pulse width modulation. CHB multilevel converter is one of the widely used multilevel converters in industries because it is easy to scalable and because of its fault-tolerant operation properties. The results obtained in this study show that these multicarrier-based pulse width modulation techniques provide greater control over the output of the CHB. The phase voltage produces five levels of output voltage, hence, it is named as five-level CHB. Simulation work is carried out by using MATLAB software. In this study,

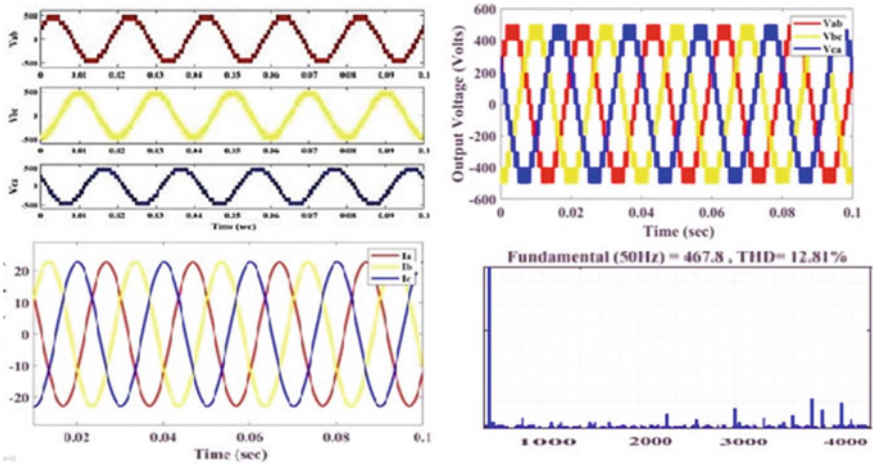


**Fig. 4** Individual line voltage, individual phase voltage, three-phase line voltage and THD profile

it is found that the THD of the output phase voltage is 18.29% in case of phase-shifted pulse width modulation, and THD is 12.81% in the case of level-shifted pulse width modulation. For a three-phase system, triplen harmonics get eliminated in the line voltage. The other advantage of level-shifted pulse width modulation is that it provides greater control in terms of lower order harmonic reduction from the output voltage waveform for different modulation values. This work can be extended in the future for CHB with more number of cells producing more levels at the output voltage. For further reducing the lower order harmonics, the same model can be used with selective harmonic elimination where the harmonic performance of the converter output can be improved.

## References

1. L.M. Tolbert, F.Z. Peng, Multilevel converters as a utility interface for renewable energy systems, in *IEEE Power Engineering Society Summer Meeting*, vol. 2 (2000), pp. 1271–1274
2. J. Rodriguez, J.-S. Lai, F.Z. Peng, Multilevel inverters: a survey of topologies, controls, and applications. IEEE Trans. Indus. Electron. **49**(4), 724–738 (2002)
3. H. Parveen, M. Asim, I. Ahamad, Efficiency analysis of bridgeless PFC boost converter. Int. J .Sci. Res. Dev. **4**(01) (2016)
4. B.P. McGrath, D.G. Holmes, Multicarrier PWM strategies for multilevel inverters. IEEE Trans. Indus. Electron. **49**(4), 858–867 (2002)
5. B.P. McGrath, D.G. Holmes, T. Meynard, Reduced PWM harmonic distortion for multilevel inverters operating over a wide modulation range. IEEE Trans. Power Electron. **21**(4), 941–949 (2006)
6. B.P. McGrath, D.G. Holmes, Multicarrier PWM strategies for multilevel inverters. IEEE Trans. Ind. Electron. **49**(4), 858–867 (2002)
7. B.P. McGrath, D.G. Holmes, T. Lipo, Optimized space vector switching sequence for multi-level inverters. IEEE Trans. Power Electron. **18**(6), 1293–1301 (2003)

8. A. Mehrizi-Sani, S. Filizadeh, An optimized space vector modulation sequence for improved harmonic performance. IEEE Trans. Ind. Electron. **56**(8), 2894–2903 (2009)
9. T.A. Meynard, H. Foch, P. Thomas, J. Courault, R. Jakob, M. Nahrstaedt, Multi cell converters: basic concepts and industry applications. IEEE Trans. Ind. Electron. **49**(5), 955–964 (2002)
10. R. Naderi, A. Rahmati, Phase shifted carrier PWM technique for general cascaded inverters. IEEE Trans. Power Electron. **23**(3), 1257–1269 (2008)
11. R.L. Naik, K.R.Y. Udaya, A novel technique for control of cascaded multilevel inverter for photovoltaic power supplies, in *Proceedings of European Conference Power Electronics and Applications* (2005)
12. G. Narayanan, D. Zhao, H.K. Krishnamoorthy, R. Ayyanar, V.T. Ranganathan, Space vector based hybrid PWM techniques for reduced current ripple. IEEE Trans. Ind. Electron. **55**(4), 1614–1628 (2008)
13. V. Naumanen, J. Luukko, T. Itkonen, O. Pyrhonen, J. Pyrhonen, Modulation technique for series-connected H-bridge multilevel converters with equal load sharing. IET Power Electron **2**(3), 275–286 (2009)
14. I. Ahamad, M. Asim, P.R. Sarkar, F.A. Khan, Comparison of conventional PFC boost converter and bridgeless PFC boost converter. Int. J. Innov. Res. Electr. Electron. Instrum. Control Eng. **4**(5) (2016)
15. L.G. Franquelo, J. Rodriguez, J.I. Leon, S. Kouro, R. Portillo, M.A.M. Prats, The age of multilevel converters arrives. IEEE Indus. Electron. Mag. **2**(2), 28–39 (2008)
16. A.K. Gupta, A.M. Khambadkone, Synchronous space vector modulation based closed-loop flux control of a grid-connected cascaded multilevel inverter, in *IEEE Power Electronices Specialists Conference* (2008), pp. 1358–1364
17. A.R. Beig, G. Narayanan, V.T. Ranganathan, Modified SVPWM algorithm for three-level VSI with synchronized and symmetrical waveforms. IEEE Trans. Indus. Electron. **54**(1), pp. 486–494 (2007)
18. N. Filho, J. Pinto, L. da Silva, B. Bose, Simplified space vector PWM algorithm for multilevel inverters using Non-Orthogonal moving reference frame, in *IEEE Industry Applications Society Annual Meeting 2008* (2008), pp.1–6

# Smart Blind Stick

**Tuhin Das, Soumit Das, Jaydip Nandi, Mrinal Dutta, Abhishek Purkayastha, Arunava Banerjee, and Arijit Ghosh**

## 1 Introduction

Eyesight is one of the most key aspect of human life. Blindness is a state where any person lacks visual perception due to physiological/neurological or any other factors. About 90% of the world's dim-sighted people live in the developing countries. India is now home to 12 million blind people, and India needs approximately 40,000 ophthalmologists, where as it has only 8,000.

House, factory, office, and school are the few closed premise areas where a visually impaired person needs to travel, just like a sighted one. Currently available solutions like sonic path finder, sonic torch etc. are not appropriate to use inside a closed site. The person has to take help from someone or use some equipment to reach at the destination. Generally, the white canes are noted as the best companion of dim-sighted people. But often this is not helpful. In an unknown surrounding, the person might get demented. So, this limits their mobility, making them depending on others. This paper comes up with a proposal to design and develop a mobile unit (stick) for them to easily navigate around in public places. The blind stick is equipped with a servo motor which can rotate up to 180°, also light sensing and water sensing system without any sensor. This paper first uses ultrasonic sensors to detect obstacles. Sensor passes the data of obstacle detection to the microcontroller. The proximity of the obstacle is calculated internally by the microcontroller using this data. If the obstacle is within the threshold, the microcontroller fires the buzzer. If water is detected, then it alerts the user with a different buzzer. Thus, the approach empowers detection of obstacles comprehensively.

T. Das (✉) · S. Das · J. Nandi · M. Dutta · A. Purkayastha · A. Banerjee · A. Ghosh
Department of Applied Electronics and Instrumentation Engineering, RCC Institute of Information Technology, Canal South Road, Kolkata 700 015, India



C. K. Chanda et al. (eds.), *Advanced Energy and Control Systems*, Lecture Notes in Electrical Engineering 820, https://doi.org/10.1007/978-981-16-7274-3_13

## 2 Literature Review

With the intuition of developing smart cities, it is required for the people to be more advanced and this can be done by using better technologies. Today there are over 39 million people in the world [1], where over 12 million people are visually impaired in India. Out of the 12 million people, 3 million people have inevitable blindness. So, there is a serious need for the development of smart technologies to help these dim-sighted people.

Many research papers indicate that many scientists all around the globe are trying to develop new algorithms and models to provide efficient smart sticks for blind people [2]. One of the papers has also designed a smart blind stick with ultrasonic sensors, and PIC Microcontroller 16F877A for object detection around the blind person to help them to walk with more safe navigation. But there is a deficiency that this type is least modified. Another paper came up with the scheme of obstacle avoidance by creating the blind stick with smart equipment. For potholes within a 20 cm detection radius of the stick one ultrasonic sensor was used, another one for detection below-knee obstacles, and one for detecting the knee above obstacles. These all are connected with either buzzer or with the vibration motor. The RF module has been used for finding the stick in case if it is lost. Although this model is more modified, it makes the stick heavy while carrying on all the equipment [3]. These problems can be reduced by the setup of the same smart stick with ultrasonic sensors and microcontroller whereas the 3D CAD application and Up-Mini 3D printer were used for designing and printing the sensor holder and were mounted on the walking stick for safer navigation [4].

The Global Positioning System (GPS) based navigation aid is one of the latest ones which has been developed for giving a better and safer life. Therefore, MSP430 Microcontroller, GSM Module for location detection, water sensor, Ultrasonic sensor for object detection, and RF module have been used in case of losing the blind stick [5]. Sometimes making the buzzer sound by detecting the obstacles is not enough for a blind person to understand the circumstances. So, it is more convenient if the smart accessories can make a voice alert by either loudspeaker or earphone and this is exactly what is proposed in [6]. Another paper proposed a convenient and easy navigation aid for dim-sighted people by using infrared sensors along with an ultrasonic range finder for obstacle detection and GPS navigation along with Bluetooth connectivity and an Android application, which will provide voice assistance to desired location and in panic situations, will notify registered mobile numbers using SMS [7]. In another paper, an automated smart stick which consists of an IR sensor, ultra-sonic sensors, GPS module and GSM module has been used for object detection and position monitoring of a blind person if the person loses his/her location [8].

The research proposed in [9] gives the blind cane a modified form rather than the traditional usage. They have used XBee Pro S2C, USR-BLE10, and NRF24L01 for better communication and location detection. Maybe the XBee Pro S2C module is expensive, but it gives a high communication performance in the development of a blind person's life [9]. Another research has proposed a solution using Low Latency

Communication where the ATMEGA-16 microcontroller has been used along with buzzer, vibration motor, Ultrasonic sensors, GPS, and smartphone application with the nearest base station. The ultrasonic sensors help to detect the objects, GPS for real-time monitoring location, and the smartphone application connected with the nearest base station in case of emergency [10]. Now for the improvement of blind person's lifestyles, the paper [11] developed a speed Gablind app connected with a smart glass that has the max sonar sensor to identify the hurdles. Initially, the said sensor can detect the obstacles 1–6 m ahead within a capture range of 45° to 145°. The users should have the Gablind App installed on their smartphones. The device worked effectively at speeds 21–66.8 cm/s and was able to detect obstacles with a distance of 123–63 cm. Instead of the traditional stick and smart blind stick designed a new element named "The Assistor" uses ultrasonic sensors and image sensors to detect obstacles and identifying them by echo sound waves and image processing respectively [12].

A Smartphone application is used to guide the user's predefined trajectory using GPS (Global Positioning System) and maps. The main drawbacks are that the users must carry a smartphone for navigation and GPS monitoring. Another research has proposed a solution to identify any obstacle using a mobile real-time dangling objects sensing (RDOS) prototype, which is located on the cap [13]. In the research paper of [14], the advancement of mobility aid devices without including various items has made the blind stick by including an SOS navigation system. They have used the Raspberry Pi with a portable camera which helps the blind person in the way that if the individual notices any kind of pain then he can press an e-SOS distress call button on the stick to give a video call to user's family member. The video is streamed in an Android mobile via an Android application. The Android application also shows the location of the blind person to user's family member [14]. It is true that as the technology increases and ideas develop the bulkiness of the smart stick increases (Fig. 1).

## 3 Architecture Diagram

The following components have been used.

### *3.1 Chlorinated Polyvinyl Chloride (CPVC) Pipe*

Chlorinated polyvinyl chloride (CPVC) is a thermoplastic, which is more pliable and can resist higher temperatures compared to standard PVC. The inside and outside diameter of the CPVC Pipe used are 0.622 and 0.84 inches respectively. Weight of the CPVC Pipe is 17 lb/100 ft.

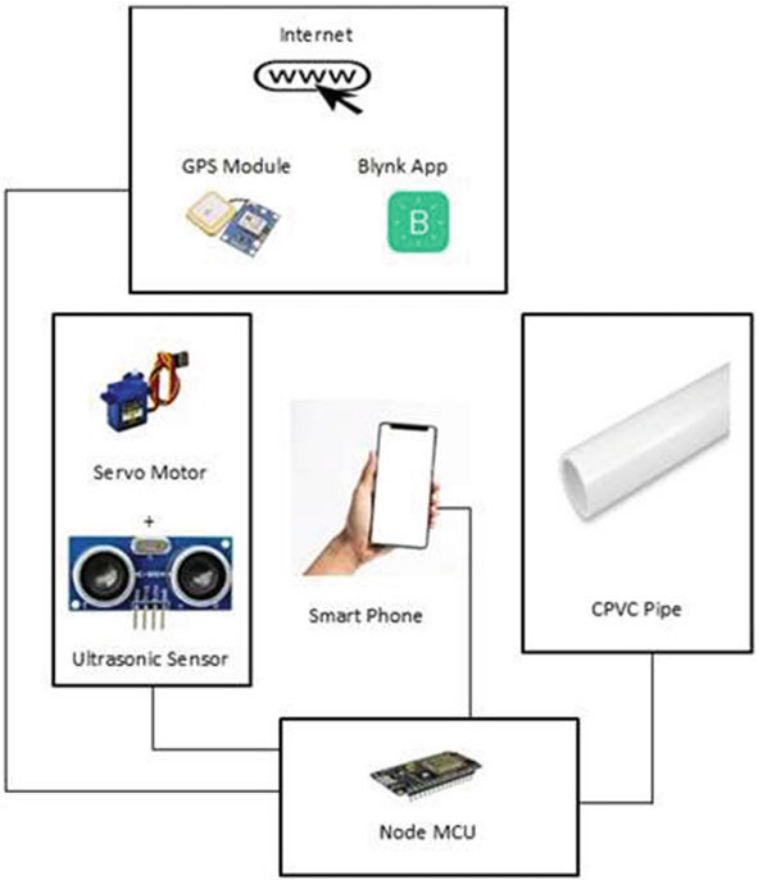


**Fig. 1** Architecture diagram of the system

## *3.2 NodeMCU*

The latest version of the NodeMCU board (V1.0) has been used. The specification of the board is as follows: Flash- 4 MB, SRAM is up to 50 KB, Clock Speed is between 24 and 52 MHz, GPIO pins are 17 in number, and ADC is 1.

## *3.3 Ultrasonic Sensor*

The sensor used is an Ultrasonic sensor that calculates the gap to an entity using ultrasonic sound waves. It uses a transducer to emit ultrasonic pulses and convert the reflected pulse into electrical quantity to detect object's proximity. It requires a

supply voltage of 5 V. The present consumption is 15 mA. The utmost range varies from 3 to 400 cm. The dimension is 43*20*15 mm.

### *3.4 Servo Motor*

The Ultrasonic sensor is made rotational with the help of a servo motor which is an electrical device which is placed beneath the servo motor so as to make it rotational. The servo motor is made of simple motor which run through servo mechanism with great precision. The model used is SG90 which weighs 9 gm. It operates within 3 to 7.2. The stall torque is 1.2 kg-cm.

### *3.5 Light Dependent Resistor (LDR)*

It is used to detect darkness/lightness of a particular surrounding where the person is. LDR is a passive component that drops resistance with respect to luminosity strikes on the component's light sensitive surface. Typically, > 1 MΩ when dark and < 1kΩ in high light levels. It has a response time of 2–50 ms.

### *3.6 GPS Module*

A Neo-6 m V2 GPS module has been used to locate the stick, which has an operating temperature ranging from −40 to 85 °C. A rechargeable battery for back-up and a separate 18*18 mm GPS antenna are also present. A supply voltage of 3.3 V has to be applied. Baud rate ranges from 4800 to 115,200 (default 9600). Indoor GPS tracking sensitivity is 162 dBm.

### *3.7 RF Transmitter and Receiver*

A RF Transmitter and Receiver (TSOP 1738) is used to detect where the stick has been kept. The person can find the stick by a remote, which works as a transmitter. It requires a consumption of 0.4–1.0 mA of current. It requires a supply voltage of 5 V. The dimension of the case in mm is 12.5*10*5.8. The temperature ranges from −25 to 85° C (Fig. 2).

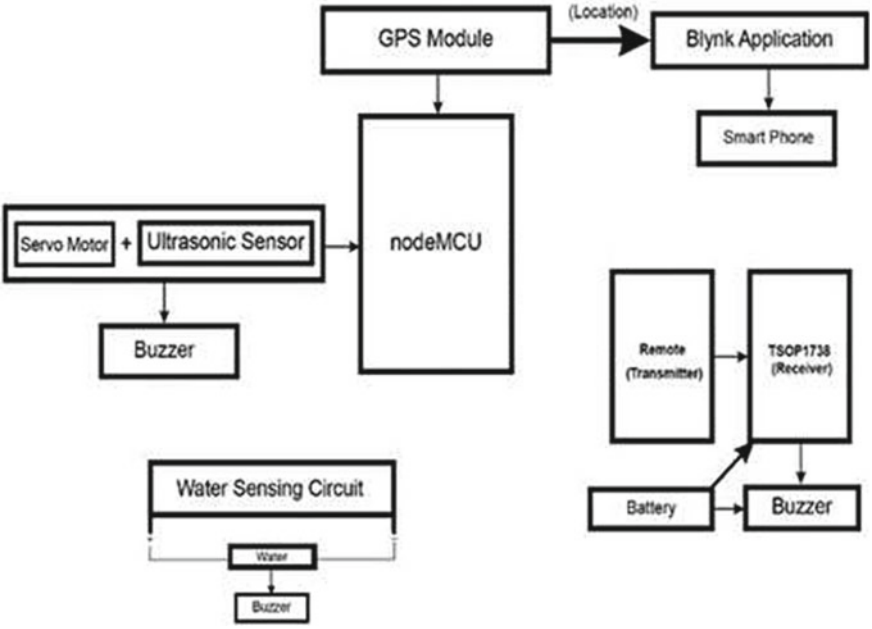


**Fig. 2** Block diagram of the system

## 4 Working Principle

This paper proposes an ingenious design of an advanced stick that allows dim-sighted people to navigate easily. The blind stick is equipped with an ultrasonic sensor along with a servomotor which allows the ultrasonic sensor to rotate up to 180°. At first, the ultrasonic sensors detect the obstacles around using ultrasonic waves. As soon as obstacles are sensed, the sensor passes the acquired data to the Node MCU. The microcontroller then processes this data and calculates if the obstacle's distance is within the threshold limit or not. If it is not, then the circuit remains silent otherwise, the microcontroller triggers a signal to sound a buzzer. It also triggers a separate buzzer if the water is within the threshold range of the stick to alert the blind person. The user also gets alerted regarding the darkness inside a room using an LDR circuit system. A wireless radio frequency-based remote was used to find the stick nearby.

## 5 Results and Discussion

The Ultrasonic Sensor and Buzzer were connected with NodeMCU (as per the block diagram) and shown in Fig. 3. An artificial obstacle was placed in front of the sensor and then the actual distance of the obstacle was compared with the measured distance.

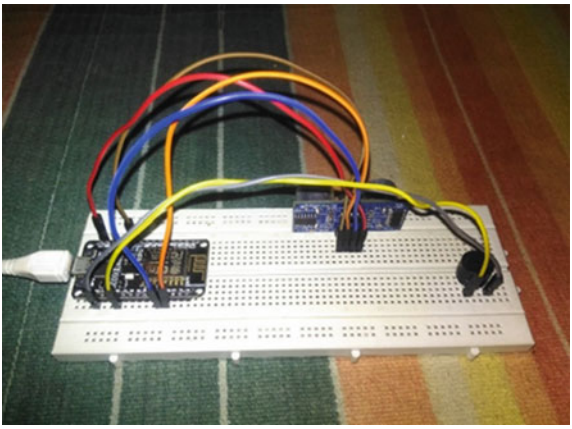

**Fig. 3** Connection of ultrasonic sensor and buzzer with nodeMCU

The same process was repeated several times by changing the distance of the obstacle which has been plotted in Table 1 and hence percentage error was found out. The following formula was used to calculate distance of the object from the ultrasonic sensor:

$$Distance = (Time \times Speed\ of\ Sound) / 2 \quad (1)$$

where

Speed of Sound = 340 m/second (approx.).

Time = The time required to travel ultrasonic waves from the sensor to the obstacle and then return to it after bouncing back from the obstacle in seconds.

The GPS module was connected with NodeMCU (as per the block diagram) and is shown in Fig. 4, and the location coordinates were logged on the serial monitor of Arduino IDE as displayed in Fig. 5.

The same location coordinates were marked on the map and displayed on the Blink app as shown in Fig. 6.

**Table 1** Distance error calculation

| Sl. No | Input (Barrier distance) mm | Sensor output (Barrier distance) mm | Error (%) |
|---|---|---|---|
| 1 | 10 | 12 | 20 |
| 2 | 15 | 17 | 26.66 |
| 3 | 20 | 21 | 5 |
| 4 | 25 | 23 | 16 |
| 5 | 30 | 31 | 3.33 |

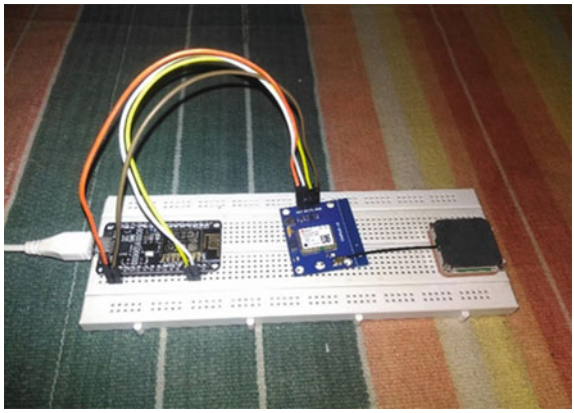

**Fig. 4** Connection of GPS module with NodeMCU

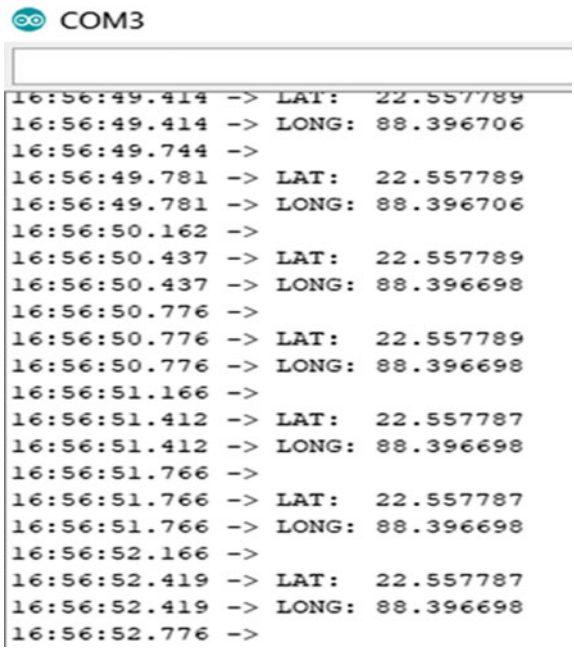


**Fig. 5** Serial monitor output of location coordinates

## 6 Conclusion

The main idea of this paper is not only to provide the unsighted or sight challenged people for safer movement through obstacles but also overcoming the hurdles that they have to face in their daily life. Independent mobility of the blind becomes much easier. It has been observed from the experimental results that the proposed system is precise in obstacle detection besides alerting the user to identify and bypass every obstacle and reach the destination. This prototype is ingenious and helps in energy

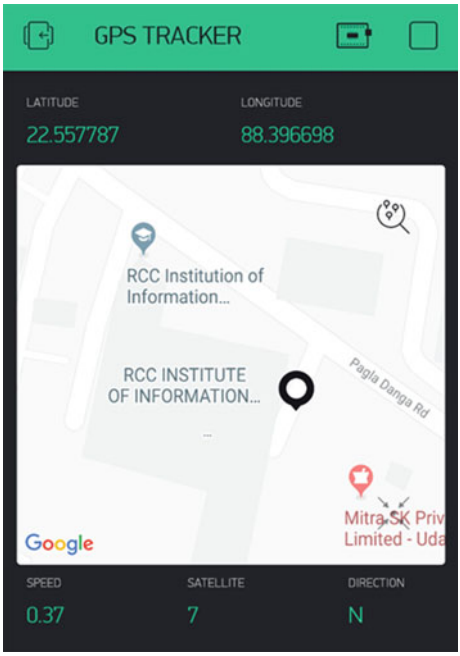


**Fig. 6** Location of the GPS Module

conservation. The cost-effectiveness and flexibility of the system make it handier and can be carried easily. A voice detection system can be implemented in place of the RF Transmitter–Receiver to relocate the smart stick in the future in case the user forgets the smart stick's last position. Similarly, a single button pressing mechanism (SOS) can be put into the stick to send an alert message to the user's family/friends in case the user falls into any crisis. Later, image processing can be used to detect objects more clearly and hence allow the person to know what is actually in front as a barrier.

## References

1. Visual impairment and blindness, World Health Organization Media Centre, https://www.who.int/news-room/fact-sheets/detail/blindness-and-visual-impairment last Accessed 10 Dec 2020
2. N. Dey, A. Paul, P. Ghosh, et al Ultrasonic sensor based smart blind stick, in 2018 International Conference on Current Trends towards Converging Technologies (ICCTCT) (2018), IEEE
3. M.A Ikbal, Rahman F, Kabir MH, Microcontroller based smart walking stick for visually impaired people, in *2018 4th International Conference on Electrical Engineering and Information & Communication Technology (ICEEICT)*, (IEEE, 2018)
4. M.P. Agrawal, A.R. Gupta Smart stick for the blind and visually impaired people, in *2018 Second International Conference on Inventive Communication and Computational Technologies (ICICCT)* (2018)
5. A.A. Nada, M.A. Fakhr, A.F. Seddik Assistive infrared sensor based smart stick for blind people, in *2015 Science and Information Conference (SAI)*. (IEEE, 2015)

6. A.S. Arora, V. Gaikwad Blind aid stick: Hurdle recognition, simulated perception, android integrated voice-based cooperation via GPS along with panic alert system, in *2017 International Conference on Nascent Technologies in Engineering (ICNTE).* (2017)
7. K.B. Swain, R.K. Patnaik, S. Pal, R. Rajeswari, A. Mishra, C. Dash Arduino based automated stick guide for a visually impaired person, in *2017 IEEE International Conference on Smart Technologies and Management for Computing, Communication, Controls, Energy and Materials (ICSTM).* (IEEE, 2017)
8. G.A. Mutiara, G.I. Hapsari, Periyadi (2017) Performance comparison of communication module against detection location for blind cane, in *2017 11th International Conference on Telecommunication Systems Services and Applications (TSSA).*
9. A. Shaha, S. Rewari, S. Gunasekharan SWSVIP-smart walking stick for the visually impaired people using low latency communication. in *2018 International Conference on Smart City and Emerging Technology (ICSCET).* (2018)
10. A.C. Frobenius, E. Utami, A. Nasiri analysis of speed gablind app in detecting obstacle-experiment results, in *2018 3rd International Conference on Information Technology, Information System and Electrical Engineering (ICITISEE).* (2018)
11. A. Krishnan, G. Deepakraj, N. Nishanth, K.M. Anandkumar Autonomous walking stick for the blind using echolocation and image processing, in *2016 2nd International Conference on Contemporary Computing and Informatics (IC3I).* (Noida, 2016)
12. C.H. Lin, P.H. Cheng, S.T. Shen Real-time dangling objects sensing: a preliminary design of mobile headset ancillary device for visual impaired, in *2014 36th Annual International Conference of the IEEE Engineering in Medicine and Biology Society.* (Chicago, IL, 2014)
13. A. El-Koka, G. Hwang, D. Kang Advanced electronics based smart mobility aid for the visually impaired society, in *2012 14th International Conference on Advanced Communication Technology (ICACT)*, (PyeongChang, 2012)
14. M.M. Kamal, A.I. Bayazid, M.S. Sadi, M.M. Islam, N. Hasan Towards developing walking assistants for the visually impaired people, in *2017 IEEE Region 10 Humanitarian Technology Conference (R10-HTC).* (IEEE, 2017)

# Home Security System Using RaspberryPi


**Pratik Banerjee, Parabi Datta, Suhankar Pal, Sangbit Chakraborty, Ankur Roy, Satwik Poddar, Soumya Dhali, and Arijit Ghosh**

## 1 Introduction

Home automation results in ease of work, increased efficiency, and security benefits aiding in improved personal satisfaction. The prevalence of system empowered home automation is continuously growing in safer and wider applications and is a lot more affordable nowadays. In addition, with rapid development of internet-enabled applications, the capability of remote control and network-enabled appliances are enhancing leaps and bounds. The use of a home automation system for controlling a wide range of devices from distant locations can be made possible through a number of communication options such as LAN, cellular network, satellite communication, and internet technologies. The main virtue of home automation can be in the security features where one gets notified and be alarmed if there is any threat to someone's privacy. Smart home systems tend to show its wonders when it comes to the accommodation of new devices and appliances along with newer technologies. Newer devices are being made each day and with it, and the older ones are being replaced. Home automation frameworks can associate motion detectors, surveillance cameras, automated entryway locks, and other important safety measures in house so that one may enact those from a cellular device. It will provide security alert on various gadgets depending upon the time of day and accordingly the alarm system operates. The paper is categorized as below: next section describes related work, Sect. 3 describe the system description, followed by the methodology in Sects. 4 and 5 elaborates the Haar Cascade algorithm, Sect. 6 shows the results, and this paper ends with a conclusion.

P. Banerjee (✉) · P. Datta · S. Pal · S. Chakraborty · A. Roy · S. Poddar · S. Dhali · A. Ghosh
Department of AEIE, RCC Institute of Information Technology, Canal South Road, Kolkata 700015, India



C. K. Chanda et al. (eds.), *Advanced Energy and Control Systems*, Lecture Notes in Electrical Engineering 820, https://doi.org/10.1007/978-981-16-7274-3_14

## 2 Literature Survey

### *2.1 Early Developments*

The rectangular features are used here and are reminiscent of Haar [1, 2] based functions. The suggested face recognition system detects the faces with low false positive rate. At the beginning, the face detection was done with 10 and 12 stage detector but due to poor detection accuracy and high false positive rate, it was discarded. The 14-stage detector gives good accuracy in face detection and very low false positive rates. The system works well on RaspberryPi with a 5MP camera and detects the face of captured image with the lowest resolution of 640 × 480 pixels and the highest resolution of 2560 × 1920 pixels with acceptable detection speed [3]. Patoliya and Desai developed ATM security system using embedded Linux platform, which is based on face detection system. RaspberryPi is used for implementation with extended capabilities of Computer Vision (OpenCV) software, which is used for processing images. One time password (OTP) technique is used which increases the security of this system. In an unauthorized condition, ATM door is locked and it opens only when security guard [4] enters the OTP. Pi Camera Module is added with RaspberryPi, which acts as a visual interface in case of face detection or recognition. This makes use of an interface, which is specially designed for associating with the cameras [5]. An algorithm known as Haar Cascade classifier is used for detection of the object, which is trained from the source [6]. In early 1990s, the consumer electronic devices were evolving into digital format, and so the need persists to interlink these home appliances through digital links. Other than that, main characteristics of the proposed network connection was digital access system because of which the home automation network could interact with the world outside [7].

### *2.2 Recent Developments*

In recent years, Internet of Things (IOT) has enabled innovation to make daily lives easier and comfortable. When home automation devices are remotely controlled through internet, it becomes an important virtue of IoT. High-end security system is the main feature of the present homes. Current patterns in home automation includes remotely controlled appliances, computerized gadgets, and remote video observation sensors, to name a few. In case of Java based home automation system, the World Wide Web is used to monitor and control [8]. Integrated residential gateway controller is used for home energy management system to obtain high performance from compact OS, and it lowers the memory space than traditional three-step plug and player arrangement [9]. It is used for saving power in the phone based remote control and office automation [10]. According to Ramlee, home automation using Bluetooth is the new development of automated technology, which is acting as a motivation for disabled persons and enable them to carry out their daily activity, safely and comfortably [11].

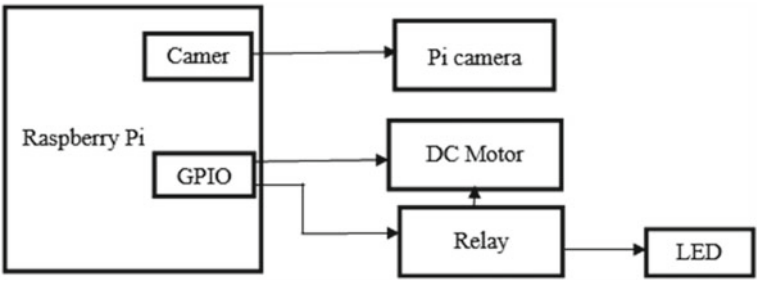


**Fig. 1** Block diagram of the system

## 3 Block Diagram and Flow Chart

### *3.1 Block Diagram*

In Fig. 1, the Pi camera is attached to the camera slot and the DC motor and Relay is attached to the GPIO pins of the RaspberryPi. As it is a two-channel relay, so it is connected to LED and DC motor that helps in driving them. Here, the DC motor drives a miniature door that is used as a door locking system for surveillance purpose. The door only opens after a successful recognition process, if the face is previously stored in the database and that image has the access to open the door. Otherwise, the system will not work, and the door will not be opened.

### *3.2 Hardware*

The hardware components that are required to develop the system are as follow:

**RaspberryPi**: A low priced, miniature computer that is connected into a computer monitor and uses normal peripheral devices like keyboard and mouse. It is a very powerful device, which allows people from all age groups to learn the basics of computing. It does everything a desktop computer is able to do, including browsing through internet. The RaspberryPi was first launched in the year 2012, and there have been some changes and variations performed from that time forward. The first model of Pi integrated a CPU of single core of frequency700MHz and 256MB RAM, and the most recent one has a quad core CPU of frequency 1.4GHz accompanied with 1GB RAM. Throughout the world, it is widely used for home automation as well as for running modern appliances. The RaspberryPi works in an open source environment: it runs on Linux and the most common working system called Raspbian is an open source application. It is having 40 GPIO (General Purpose Input Output) pins, used for wide range of purposes. There are two 5V and two 3.3V pins.

**RaspberryPi Camera:** The Pi camera comes with a flex cable. The flex cable is put into the connector positioned between the Ethernet and the HDMI port such that the silver connectors face the HDMI port. The flex cable gives input inside the connector firmly.

**Two Channel Relay**: This is a low-level 5V device, comprising of two-channels and having a driver current of 2mA. It is used to control any equipment involving high magnitude current. It can work under both DC and AC connection. The specifications include AC 250V and 10A for AC and DC 30V and 10A for DC. Relay is used here as a driver circuit for opening the miniature door.

*INPUT:* The two inputs are shown below.

IN1: This is the first signal triggering terminal of the relay module. It is connected to the GPIO 18 pin of RaspberryPi.

IN2: This is the second signal triggering terminal of the relay module. It is connected to the GPIO 17 pin of RaspberryPi.

*VCC:* It is connected to positive supply voltage terminal.

*GND:* It is connected to ground terminals.

*OUTPUT:* Each sub-module of the relay is having a Normal-close (NC), Normal-open (NO), and Common (COM) terminals each, so there are two-NC, two-NO, and two-COM.

**DC Motor:** A DC motor is a type of rotary electrical instrument that is used to transform DC electrical energy into mechanical energy. The most common types are based on the forces produced by magnetic fields. Almost all types of DC motors contain some internal mechanisms, either electro-mechanical or electronic, which periodically changes the direction of current flow in different parts of the motor. A coil of wire having current through it generates an electro-magnetic field positioned with the center of the coil. In this proposed scheme, the DC motor is connected to the relay and drives the miniature door after successful recognition process (Fig. 2).

**LEDs:** The LED is included for indicating that the face has been recognized successfully or not. The green LED shall denote the successful recognition, while the red LED shall denote wrong recognition of face.

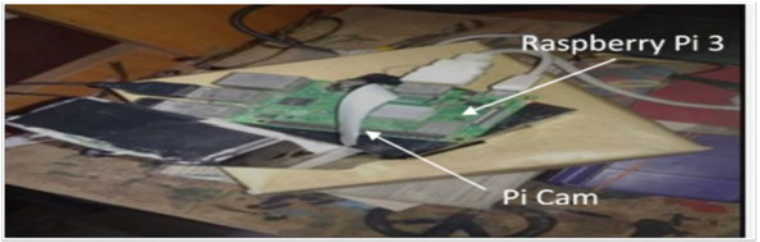


**Fig. 2** Setup of the system


**Fig. 3** Miniature door **a** Front view, **b** Side view

**Miniature door:** The miniature door shall open only when the face recognition is successful. The miniature door arrangement is a small-scale representation of the actual door as shown in Fig. 3.

## *3.3 Flow Chart*

In Fig. 4, the flow chart for the entire system is shown. The face data is collected and is stored. The Pi camera captures the real time image and is matched with the stored face images in the database. The decision box is shown for that purpose. If the answer is yes, the face is recognized successfully and the green LED glows. Whereas, if the face is not recognized, the red LED glows up.

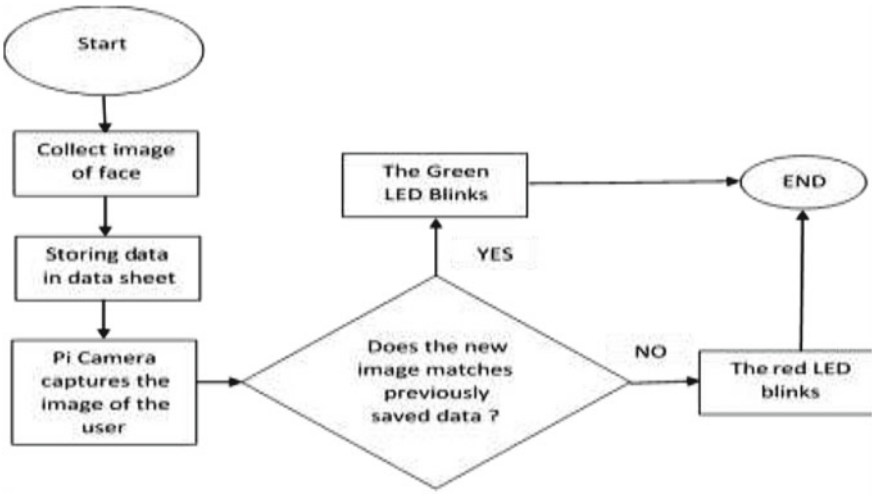


**Fig. 4** Flow Chart for the entire system

# 4 Methodology

The system is developed using the following methodology.

## *4.1 Installation of Raspbian on the RaspberryPi*

Raspbian is to be downloaded, the disc image is to be written to a micro SD card, and RaspberryPi is to boot from the micro SD card. For this, one needs a micro SD card (with no less than 8 GB), a PC with a space for it, a RaspberryPi, and fundamental peripherals like a screen, a mouse, a console, and a power source.

**Step1:** Downloading the Raspbian: The PC is turned on and the Raspbian disc image is downloaded. It will take some time, particularly in the event when one intends to utilize the conventional download alternative as opposed to other download sources.

**Step2:** Unzipping the file: As the Raspbian disc image is compressed, it should be unzipped. The file make use of the ZIP64 format, so on the basis of how present built-in utilities are, one needs to make use of certain programs to unzip it.

**Step3:** To write the disc image onto the micro SD card: One has to insert the micro SD card into computer and write the disc image on to it. We have to select each of these programs to select the destination and the disc image.

**Step 4:** Putting the micro SD card in the Pi and booting up: When the disc image is kept in touch with the micro SD card, it is prepared to run. We must put that micro SD into the RaspberryPi. The present release to Raspbian will boot straightaway to the desktop. The credentials will be the username as pi, and the password is raspberry by default here.

## *4.2 Installation of OpenCV*

**Step 1:** The first thing to do is to expand our file system to cover all the space available on the micro SD card.

Command—sudo raspi-config

**Step 2 (install dependencies):** Updating and upgrading any existing package is the next step.

Command—sudo apt-get update && sudo apt-get upgrade

**Step 3 Download the OpenCV source code**: We will now take the OpenCV archive version 3.3.0 from the OpenCV official repository after having the dependencies installed.

Command—cd ~wget -O opencv.zip

**Step 4 Python 2.7 package manager:** One needs to install a python package manager before the start of compiling OpenCV on our RaspberryPi 3.

Command—wget

**Step 5 Creation of Python virtual environment**: Python virtual environment is created with Python 2.7 that is put into use for development of computer vision based application.

Command—mkvirtualenv cv–p python2

**Step 6 Check 'CV' virtual environment:** When RaspberryPi is booted, we first get logged out and then get logged back in; or open up another terminal if anyone needs to utilize the 'work on' in order to get to the virtual environment of 'CV'.

Command—source ~/.profile work on cv.

**Step 7 Installation of the NumPy on Raspberry Pi:** NumPy is a Python package used for numerical data processing. Command—pip install numpy

**Step 8 Compiling and installing OpenCV:** OpenCV needs to be compiled and installed. First, one should check whether one is in virtual environment or not, then the execution of command 'work on' is to be done.

Command—work on cv.

**Step 9 Test the OpenCV 3.3.0:** A new terminal is opened, then the source is executed and 'work n' command, and Python + OpenCV binding is imported. The face recognition is done as the primary step for home security. The fact that authorized users shall be granted access is used here and based on this, a person shall be allowed to enter. The user shall train the Face Recognition algorithm using machine-learning techniques and based on the trained data, the user shall be allowed. The use of Haar Cascade Algorithm is used for face detection. The face once recognized shall sent a signal to the relay and that shall enable the DC motor to open the door.

Command—ls-l/usr/local/lib/python2.7/site-packages/ total 1852 rw-r--r-- 1 root staff 1895772 Mar 20 20:00 cv2.so

## 5 HAAR CASCADE Algorithm

The algorithm needs a number of positive pictures and negative pictures to prepare the Haar cascade classifier. Positive pictures are images having clear faces, whereas negative pictures are those with no countenances. It gives each feature as the single value, which is obtained as the difference between the sum of pixels in black region and the sum of pixels in white region. All the possible size and location of classifiers are used to calculate many features. With the increase in the number of classifiers, the computational time increases. The concept of integral image is put to use. We have used AdaBoost machine learning algorithm to avoid the complex calculations, which is inbuilt with OpenCV library. Any classifier, with a probability of 50% or more in detection, is taken as a weak classifier. By taking the sum of all the weak classifier, we get a strong classifier, which makes correct decision about detection. Classification takes place in stages, we have rejected if it fails in the first stage. The region, which passes all the stages, that is a strong classifier is considered for face

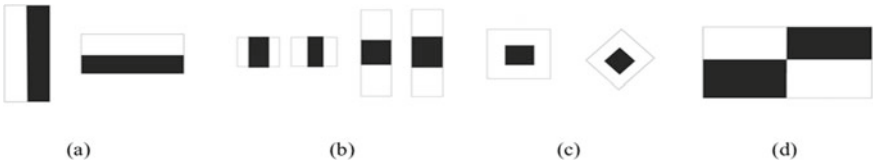


**Fig. 5** Haar cascade classifier features **a** Edge, **b** Line, **c** Center-surround, and **d** Special diagonal line

detection. Next, the detected faces are sent for face recognition. Local Binary Patterns Histogram algorithm (LBPH) is used for face recognition purpose. It is a lucid and very effective texture operator, which stores the pixels of an image by comparing with the adjacent pixels. There are four types of features in Haar Cascade classifier algorithm as indicated in Fig. 5.

## 6 Results and Discussion

The main objective of this work is to create a system where it will be easy to operate home appliances and equipment by making a user-friendly system. For the libraries of our work, we have used the Haar classifier and the LBPH face recognizer. Face recognition is ought to be successful if the matching index after recognition is more than 45%. Firstly, the pictures are captured and stored in the database. During the recognition process, the outcome shows the name of the person if it is stored in the database and it shows the matching index. In Fig. 6a one can see that the face is recognized as it is stored in the database and another face is not properly recognized


**Fig. 6** Real-time face recognition **a** successful detection and **b** unknown detection

**Table 1** Display message with recognition percentage

| Recognition percentage | Outcome | LED status |
|---|---|---|
| <45% | Message showing "UNKNOWN" | Red LED glows |
| >=45% | Recognized (name of person is shown) | Green LED glows |

and is shown in Fig. 6b. Here "UNKNOWN" means the data is not stored in the system, so the machine fails to recognize the face. If the matching index is 45% or more then only it is successful. The matching index in our model is nearly equal to 45% (the desired matching index) so we can say here that it is approximately a successful model.

In this proposed scheme, it was decided to introduce a smart door security system where a miniature door is to be used. The door will be driven by a relay and DC motor. The Pi Camera is connected to the camera slot and DC motor, and relay is connected to the GPIO pins of RaspberryPi. As it is a two-channel relay, so it is connected to LED and DC motor, which helps in driving them. Here the DC motor drives a miniature door. Firstly, the pictures are taken and stored in a database; then during the recognition process, the outcome shows name of the person if it is stored in the database and it shows the matching index. If it is 45% or more then, it is successfully detected otherwise not. When the face is detected successfully, then the door will open up. If the matching index is less than or equal to 29%, then face will not be detected, and in that case the door will not open and it will remain closed.

In Table 1, the relation between the recognition percentage, the outcome, and the LED status is shown. When the recognition percentage is less than 45%, the face cannot be detected and the message as "UNKNOWN" is shown. Therefore, the red LED is turned on and the door mechanism remains in off state. When the recognition percentage is greater than or equal to 45%, the face is recognized correctly and the name of the recognized person is displayed as stored in the database. Likewise, the green LED shall be turned on, so the door mechanism can be used and the door gets opened.

## 7 Conclusion

Home automation is presently the most trending technology and has almost brought a revolutionary change in handling or operating home appliances remotely. The designed system helps to perform face recognition with much accuracy by the help of a RaspberryPi camera that is used to take pictures of the faces and storing them in the database. Face recognition is done on OpenCV that is a library function in Python language. As for the libraries, we have used the Haar classifier, and the LBPH face recognizer. Face recognition is ought to be successful if the matching index after

recognition is more than 45%. The face detection and recognition can be put to use in the home security purpose. This would definitely modernize the lifestyle along with the added benefits of security. In different phases of life, the face detection plays a vital role in strengthening our security issues and has become an important field of research and development. The huge prospect of face recognition added with the ease of implementation has attracted many researchers around the globe to contribute in this field and make our lives smarter and comfortable.

## References

1. Electronics Industries Association, Consumer Electronics Group (1992) EIA Home Automation System: EIA/Is-60, EIA
2. D.L. Cross, C. Douligeris A fiber optic home automation system, in *Transactions on Consumer Electronics*, vol. 39 (IEEE, 1993), 636–645
3. C. Douligiris, Intelligent home systems, in *Communication Magazine* (IEEE, 1993), pp. 52–61
4. H. Fujieda, Y. Horiike, T. Yamamoto, T. Nomura A wireless home network and its application systems, in *Transactions on Consumer Electronics*, vol. 46, No. 2 (IEEE, 2000). pp. 283–290
5. H. Oh, H. Bahn, K.J. Chae, An energy-efficient sensor routing scheme for home automation networks, in *Transactions on Consumer Electronics*, vol. 51, No.3 (IEEE, 2005)
6. M. Kolberg, E.H. Magill, Using pen and paper to control networked appliances, in Communications Magazine (IEEE, 2006), pp. 148–154
7. A.R. Al-Ali, M. Al-Rousan, Java-based home automation system, in *Transactions on Consumer Electronics*, vol. 50, no. 2 (IEEE, 2003), pp. 498–504
8. N. Kushiro, S. Suzuki, M. Nakata, H. Takahara, M. Inoue, Integrated residential gateway controller for home automation system, in *Transactions On Consumer Electronics*, vol. 59, no. 3 (IEEE, 2003)
9. I. Cogkun, H.A.G. Universitesi, T.E. Fakultesi, E.E. Bolumu A remote controller for home and office appliances by telephone, in *Transactions on Consumer Electronics*, vol. 44, no. 4 (IEEE, 1998)
10. M. Narendra, M. Vijaylakshmi, Raspberry Pi based advanced scheduled home automation system through E-Mail, in *Proceedings of the IEEE International Conference on Computational Intelligence and Computing Research* (IEEE, India, 2014)
11. R.A. Ramlee, D.H.Z. Tang dan, M.M. Ismail, Smart home system for disabled people via wireless Bluetooth, in Proceeding of the IEEE International Conference on System Engineering and Technology, (IEEE, Indonesia, 2012), pp. 978–983

# FDTD Analysis of Nanowire Based InP/Ge Tandem Solar Cell for Enhanced Power Conversion Efficiency


**Suneet Kumar Agnihotri, D. V. Prashant, and Dip Prakash Samajdar**

## 1 Introduction

The photovoltaic (PV) modules with superior PCE and lower fabrication cost are required for harvesting the maximum of the available solar irradiance. There is an extensive research on thin film solar cells (SCs) due to its attractive qualities such as less stringent material quality, less material consumption, high light trapping possibilities over conventional PV, and possibility to manufacture SCs with a wide variety of materials using plasma enhanced chemical vapor deposition (PECVD) [1–3]. However, the thin film SCs need substantial improvement in terms of PCE which is 6–10% less than the conventional one [1]. In comparison to planar thin films, vertically aligned cylindrical NW arrays have emerged as potential candidates for PV applications because of its twin properties of better absorption and low reflection coupled with superior carrier collection efficiency along the radial direction of NWs owing to short carrier diffusion lengths, which increases the PCE of the SCs appreciably [4, 5]. Moreover, to increase the efficiency of SC, stack of two different materials with different band gap is chosen, which absorbs a wider band of the solar spectrum [6]. This type of SC is called a multi-junction or tandem SC. In this method, thermalization loss can be reduced due to high energy photons absorbed by a small band gap material and the loss of low energy photons which are transmitted by a high band gap material [6–8]. This principle is more easily applied to III-V compound semiconductor material SC because III-V materials possess superior carrier mobilities and more options to select lattice matched substrates through variation of mole fractions in case of ternary and quaternary materials [9]. In a double-junction tandem SC, top cell is a high band gap material and bottom cell is a low band gap material. Higher energy (low wavelength) photons are absorbed by the top cell (high band gap material), while the lower energy (high wavelength) photons transmitted by the

S. K. Agnihotri · D. V. Prashant · D. P. Samajdar (✉)
Nanoscale Device, Circuit and System Design Lab, Electronics and Communication Engineering Discipline, PDPM-Indian Institute of Information Technology, Jabalpur 482005, India



C. K. Chanda et al. (eds.), *Advanced Energy and Control Systems*, Lecture Notes in Electrical Engineering 820, https://doi.org/10.1007/978-981-16-7274-3_15

top cell are absorbed by the bottom cell (low band gap material), which helps to improve the absorption efficiency of the designed SC. The effective series combination of the two cells results in a higher $V_{OC}$ than either of the sub cells, which in turn increases the power conversion efficiency. Therefore, in this paper we have analyzed the performance of high band gap material in the form of InP nanowire, grown on low band gap Ge substrate in terms of $J_{sc}$, generation rate, absorption power and electric field.

## 2 Device Structure and Simulation Methodology

The schematic of InP NWs over Ge bottom substrate, which is subjected to solar radiation for optical simulation, is shown in Fig. 1. Note that we used only a single NW for simulation. The thickness of Ge substrate is 2 mm, and InP NW length is taken as 2 μm; whereas D of NW is optimized at 110 nm and P (period) at 360 nm for simulation purpose. 3D Finite Difference Time Domain (FDTD) method within the commercial software package of Lumerical Inc. is used for optical simulation [10] of the NW systems to have a deep understanding of the physics within the nanostructured tandem solar cell on illumination with AM 1.5G spectrum (Power Intensity, 100 mW/cm$^2$ and plane wave with wavelength spanning the regime 300–1600 nm). The ideal short circuit-current density ($J_{sc}$) is calculated as follows:

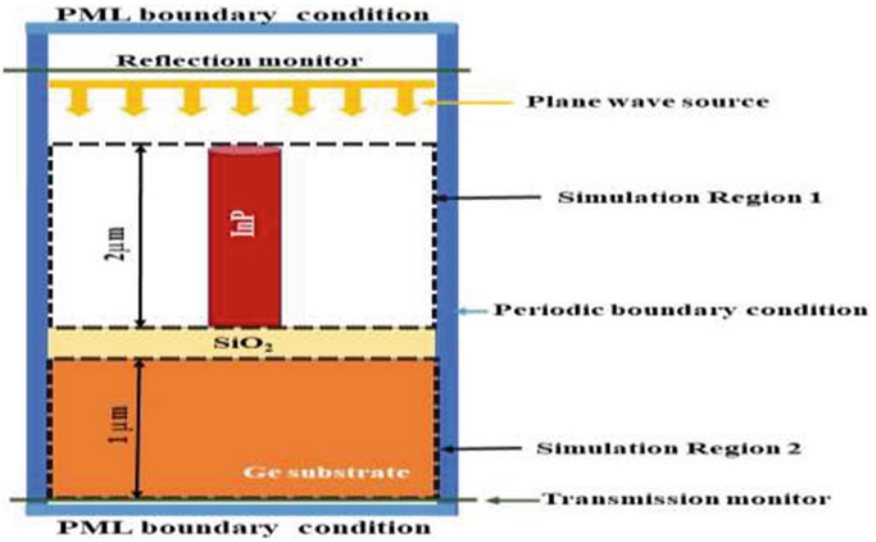


**Fig. 1** 2-D cross sectional diagram of InP NW/Ge tandem SC with the material specifications

$$J_{sc} = \frac{e}{\hbar c} \int_{300nm}^{1600nm} QE(\lambda)\lambda I_{AM1.5}(\lambda) d\lambda \quad (1)$$

For optical simulation, we have taken different simulation regions for top and bottom cell and placed reflection and transmission monitors accordingly. Periodic boundary condition is assumed along the x and y directions in order to obtain the response of the entire system by simulating only one unit cell and PML (Perfectly Matched Layer) condition is considered along z direction for impedance matching of the simulation region with the surrounding regions to minimize the reflection losses [10]. Absorption (A (λ)) can be computed from fundamental relation: A(λ) = 1-R(λ)-T(λ) by using the data of the frequency domain power monitors for reflectance (R (λ)) and transmittance (T(λ)). The parameters obtained from the optical simulations are ideal short circuit current density, photogeneration rate, and electric field distribution and absorption power.

## 3 Results and Discussions

Tandem SCs consist of stacks of multiple materials and the maximum efficiency of tandem SCs can be obtained by considering the perfect match of short circuit current densities between the top cell and the bottom cell. Therefore, in order to match the short circuit current density of the high band gap top cell with InP NWs and low band gap (LBG) bottom cell comprising of Ge substrate, optimization of the structure is done and from the analysis, it is found that $J_{sc}$ of the top cell and bottom cell is matched when diameter of the 2 μm long InP NW is 110 nm, and the length of the Ge substrate is 1 μm for a period of 360 nm. The matched $J_{sc}$ obtained from the simulation is ~24 mA/cm$^2$. The absorption plot for different simulation region over the wide wavelength regime (300–1600 nm) is depicted in Fig. 2. From the absorption plot, it has been observed that the top cell (InP NW) has higher absorption of incident photons in lower wavelength region of 300–800 nm. Whereas, the bottom cell (Ge substrate) which is a low band gap material has the higher absorption for higher wavelength range of 900–1600 nm. Therefore the total absorption of the tandem InP NW/Ge SC is the sum of the absorption spectra of top cell and bottom cell. The total generation rate of the InP NW and Ge substrate simulated separately and collectively are depicted in Fig. 3a, b and c, respectively. From the figures, it can be seen that the generation rate in top cell (InP NW) alone is $6 \times 10^{28}$ m$^{-3}$ s$^{-1}$ (28.8 in log scale) and for the bottom cell, it is $6 \times 10^{27}$ m$^{-3}$ s$^{-1}$ (27.2 in log scale). The significant difference in generation rate of top cell and bottom cell is because the photons transmitted by the top cell is absorbed by the bottom cell, and these transmitted photons help in the generation of electron hole pairs in the bottom cell. It can be verified from Fig. 2 that the absorption rate in the top cell is greater than the bottom cell, which contributes to the higher absorption rate in the top cell.

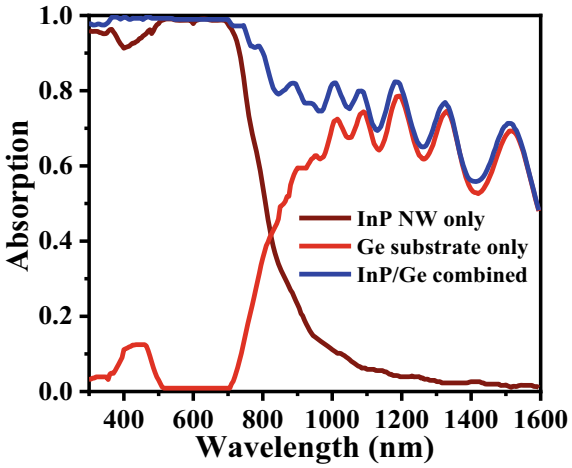


**Fig. 2** The absorption plots over the wavelength for InP NW alone, Ge substrate alone, and combined InP NW/Ge tandem SC

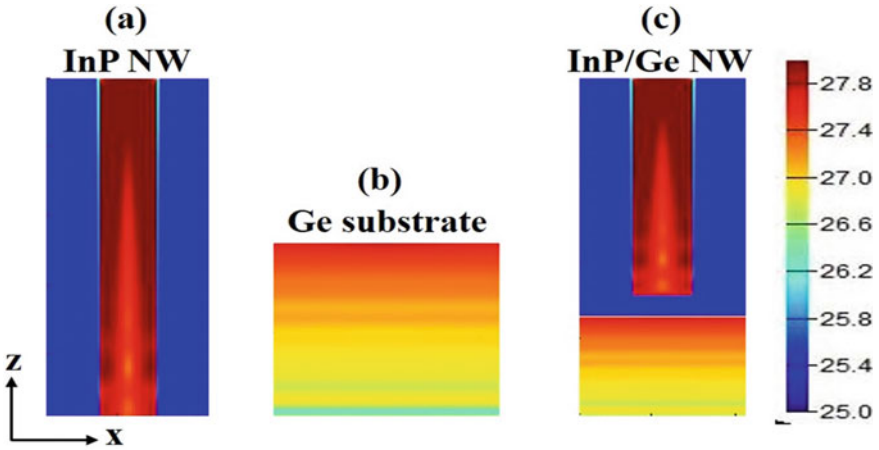


**Fig. 3** Normalized generation rate profiles in log scale of **a** InP NW alone, **b** Ge substrate alone, and **c** combined InP NW/Ge tandem SC

For better understanding of the absorption and generation in the top cell, bottom cell, and the combined cell, we have simulated the absorption power ($P_{abs}$) for individual and combined cells for different range of wavelengths. The normalized absorption power in log scale for top cell, bottom cell, and the tandem SC are depicted in Fig. 4a–g, h–n, and m–u, respectively. From the plots, it can be stated that for lower range of wavelengths of 300–800 nm, the absorption power in top cell (InP NW) is higher (nearly maximum), and for higher wavelength range of 900–1600 nm, it shows minimum values. However, the results are opposite in case of the bottom cell

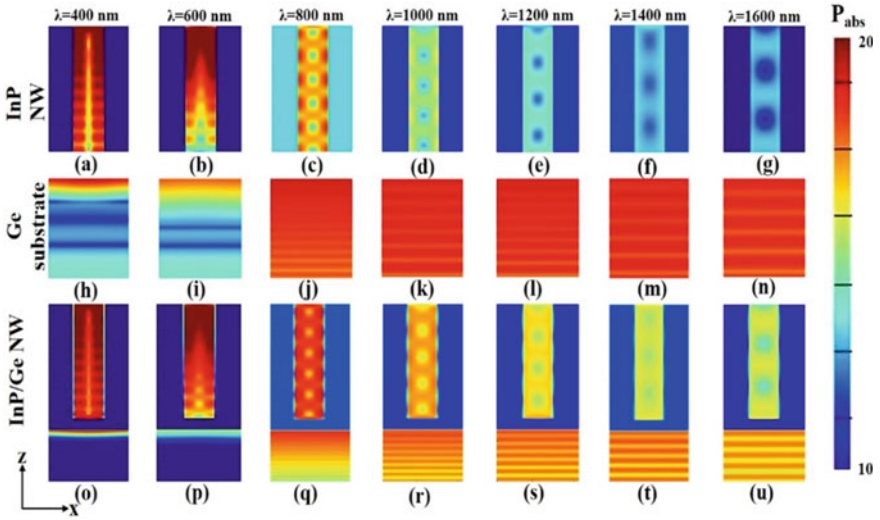


**Fig. 4** Normalized Power absorption plots in log scale for **a**–**g** InP NW only, **h**–**n** Ge substrate only, and **o**–**u** InP NW/Ge tandem SC

(Ge substrate). The combined effect of absorption power in InP NW/Ge tandem SC also depict the same results. The normalized electric-field distribution in InP NW, Ge substrate, and InP NW/Ge tandem SC is depicted in Fig. 5a–g, h–n, and m–u, respectively. It is evident that in InP NW, for lower wavelength region ranging from 400 to 600 nm, the electric field is concentrated mostly at the upper part of the NW, which shows the higher absorption in this range. However, from 800 to 1600 nm, the magnitude of the electric field along the length of the NW degrades, which results in less absorption and this is also evident from the absorption plots of the top InP NW SC. On the contrary, the electric field plot of Ge substrate shows reverse trend, exhibiting less absorption at lower wavelength regime and higher absorption for higher wavelengths. In case of the InP NW/Ge tandem SC, the electric field is concentrated along the length of the NW for lower wavelengths, and there is minimum electric field in the Ge substrate. However, for higher wavelengths, the electric gets evenly distributed between the NW and the Ge substrate, thereby maximizing the absorption throughout the entire wavelength regime.

## 4 Conclusions

In summary, we have proposed a tandem solar cell in which a top cell of high band gap material (InP NW) grown on the bottom substrate of low band gap material (Ge) to enhance the absorption over the entire wavelength regime under consideration. In this tandem solar cell structure, top cell absorbs the lower wavelength photons and

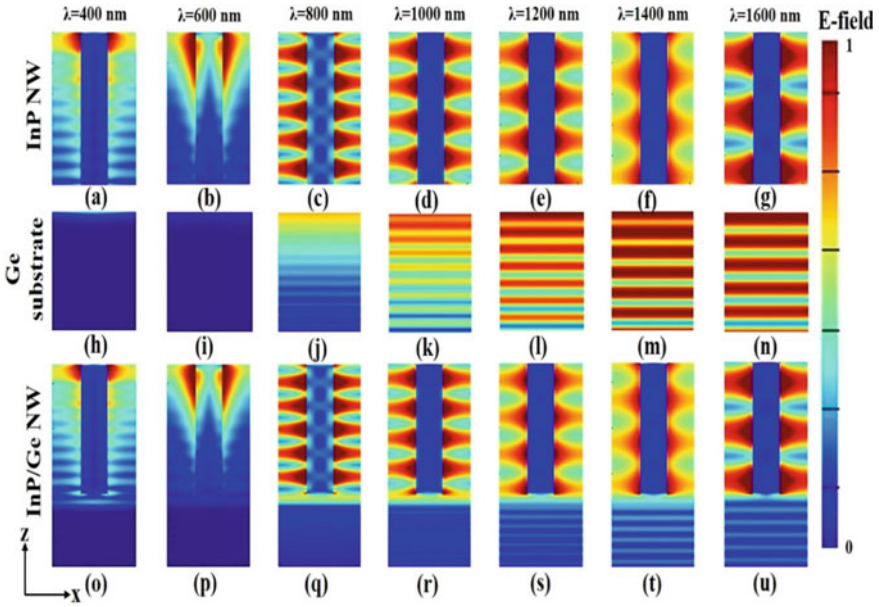


**Fig. 5** Normalized electric field plots in same scale for **a**–**g** InP NW only, **h**–**n** Ge substrate only, and **o**–**u** InP NW/Ge tandem SC

the higher wavelength photons transmitted by the top cell are absorbed by the bottom cell with low band gap. Optimization of the structure is performed such that the short circuit current densities could be matched in tandem SC. To verify the improved performance of the tandem SC, we have analyzed the absorption spectra and electric fields for individual cells as well as the combined one.

**Acknowledgements** This work is supported by the financial grant received from SERB for the project entitled "Analytical Modelling and Simulation of III-V nanostructure based Hybrid Solar Cells" under Grant No: ECR/2017/002369.

## References

1. T.D. Lee, A.U. Ebong, A review of thin film solar cell technologies and challenges. Renew. Sustain. Energy Rev. **70**, 1286–1297 (2017)
2. M. Powalla, S. Paetel, E. Ahlswede, R. Wuerz, C.D. Wessendorf, T. Magorian Friedlmeier, Thin-film solar cells exceeding 22% solar cell efficiency: an overview on CdTe-, Cu (In, Ga) Se2-, and perovskite-based materials. Appl. Phys. Rev. **5**(4), 041602 (2018)
3. C. Ballif, M. Despeisse, F.-J. Haug, Thin-film solar cells based on amorphous and micro-crystalline silicon, in ed. by M.A. Archer, 2nd edn. (World Scientific, Singapore, 2014), p. 140

4. D.V. Prashant, D.P. Samajdar, D. Sharma, Optical simulation and geometrical optimization of P3HT/GaAs nanowire hybrid solar cells for maximal photocurrent generation via enhanced light absorption. Sol. Energy **194**, 848–855 (2019)
5. L. Cao, P. Fan, A.P. Vasudev, J.S. White, Z. Yu, W. Cai, M.L. Brongersma, Semiconductor nanowire optical antenna solar absorbers. Nano Lett. **10**(2), 439–445 (2010)
6. M. Yamaguchi, K.H. Lee, K. Araki, N. Kojima, A review of recent progress in heterogeneous silicon tandem solar cells. J. Phys. D Appl. Phys. **51**(13), 133002 (2018)
7. V. Maryasin, Q. Rafhay, D. Bucci, J. Michallon, A. Kaminski-Cachopo, Opto-electrical simulation of III-V nanowire based tandem solar cells on Si, in *AIP Conference Proceedings*, vol. 1999, No. 1 (AIP Publishing LLC., 2018), p. 120001
8. K. Kumar, A. Das, U.K. Kumawat, A. Dhawan, Tandem organic solar cells containing plasmonic nanospheres and nanostars for enhancement in short circuit current density. Opt. Express **27**(22), 31599–31620 (2019)
9. S.K. Agnihotri, D.P. Samajdar, Z. Arefinia, Design of InP-based truncated nanopyramid solar cells with conformal coating of PEDOT: PSS for improved light harvesting efficiency. Optic. Mater. **110**:110475. (2020)
10. Nanophotonic FDTD Simulation Software—Lumerical FDTD."[Online]. https://www.lumerical.com/products/FDTD/. Accessed: 08 Dec 2020

# An Enhanced Tuning of PID Controller via Hybrid Stochastic Fractal Search Algorithm for Control of DC Motor


**Rita Saini, Girish Parmar, Rajeev Gupta, and Afzal Sikander**

## 1 Introduction

Nowadays, the celerity and position control of motors have become an active topic of research worldwide as it shows superb flexibility and versatility in terms of better speed control. It is a practical application used by many researchers as a test bud and is broadly used in areas like Automation Systems, Robotics, and many more [1].

PID controllers are commonly used for industrial processes because of ease of implementation, excellent performance, etc., and are generally used in industrial and robotic applications to improve the dynamic characteristics of a plant [2]. PID controllers attempt to correct the error between a measured process variable and a desired set point, first by calculating the error and then by outputting a corrective action. Among all kinds of controllers, PID controller is the most popular type of controller.

## 2 Literature Review

The improvement in the performance of PID controller has been carried out by tuning techniques. In general, optimum tuning of controller's parameters is a complex task and it indicates the tuning of its different parameters (KP, KI, and KD) to attain an optimized value of the well-desired response. The PID controller offers various time and frequency domain approaches for tuning which can be characterized in terms of Rule-based, classical, and artificial intelligence-based techniques [3]. Popular technique for tuning the parameters of PID in existing literature is Ziegler–Nichols

R. Saini (✉) · G. Parmar · R. Gupta
Rajasthan Technical University, Kota, Rajasthan 324010, India

A. Sikander
Dr. B. R. Ambedkar National Institute of Technology, Jalandhar, Punjab 144011, India



C. K. Chanda et al. (eds.), *Advanced Energy and Control Systems*, Lecture Notes in Electrical Engineering 820, https://doi.org/10.1007/978-981-16-7274-3_16

approach [4], in any case, this approach is most appropriate for online computations and is utilized as fundamental rules for tuning of PID parameters; however, it includes experimentation technique which makes the process as time consuming. In this way, the different optimizing algorithms based on artificial techniques are used as an option of Zeigler–Nichols technique and have come into the picture to diminish the time and endeavors, for example, Grey Wolf Optimization [5], Particle Swarm Optimization and Invasive Weed Optimization [6], and Stochastic Fractal Search [7], etc. The necessity of an intelligent PID controller for celerity control of DC motor has been found in [5–8] which controls the optimum speed of aforesaid motor and provides enhanced performance.

In the proposed work, HSFS has been applied to optimize the parameters of PID controller in aforesaid DC motor. The optimization of PID controllers utilizing HSFS has been denoted as HSFS-–PID approach throughout the proposed work. The proposed technique shows excellent results when compared with recently published popular approaches in the existing literature.

## 3 Background Concept

### *3.1 DC Motor*

The main mechanism behind DC motor is rotational motion, accomplished through attraction and repulsion of poles of the electromagnet and permanent magnet. Electrical energy is changed over into mechanical energy by methods for passing the DC current across the coil windings, creating electromagnetic poles. These poles interact through permanent magnet poles causing the motor to rotate and henceforth producing mechanical energy. Current speed is the primary factor in achieving the ideal/desired output, which can be accomplished either physically by methods for voltage deviation, armature resistance, and field flux or by methods of automation using controllers that direct the current speed for accomplishing desired outputs. The specifications of DC motor used in the present work have been depicted in Table 1. [7, 8].

**Table 1** Specification of DC motor

| Specifications value | Value |
|---|---|
| Resistance of armature; Ra | 0.40 Ω |
| Inductance of armature winding; La | 2.70 H |
| Moment of inertia of DC motor; J | 0.00040 kg $m^2$ |
| Equivalent friction coefficient of DC motor; B | 0.00220 N.m.sec/rad |
| DC Motor torque constant; Kt | 15 e-3 kg m/A |
| DC Motor Back EMF constant; Kb | 0.050 V.s |

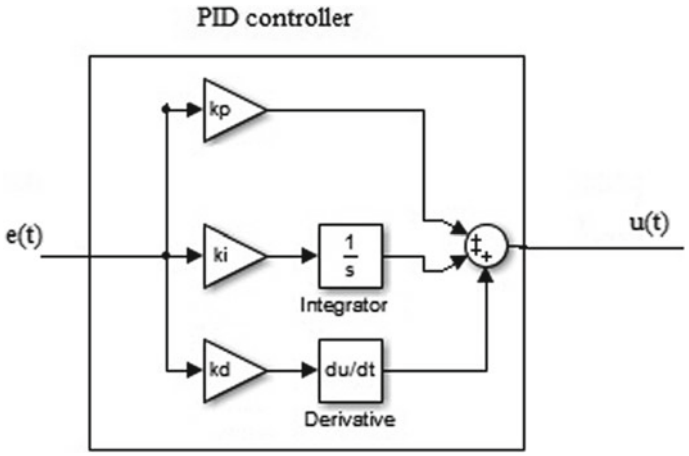


**Fig. 1** Structure of PID

### *3.2 PID Controller*

PID controller is very popular because of the following reasons: Simple controller structure, Easy to Implement, Robust performance over extensive range of operating conditions, and Clear physical significance of control parameter.

PID controller improves the time-domain characteristics, i.e., the transient and steady-state behaviors of a plant [2]. The main objective of the optimum tuning is to attain the output speed near to the set point. The transfer function of PID controller is

$$G_c = K_P + \frac{K_I}{s} + K_D s. \tag{1}$$

The weighted sum of these three proportional, integral, and derivative actions is used to adjust the process behaviors of a plant. Figure 1 shows the structure of PID controller.

## 4 Proposed Hybrid Stochastic Fractal Search

SFS has been proposed by Salimi et al. [9] and it utilizes diffusion property present inside random fractals to find out search space. In the SFS algorithm, there are four processes which are Initialization, Computation of fitness function, Diffusion, and Update. The Gaussian walk is widely used in SFS to change the iteration process for random fractals. The fitness of each individual particle has been estimated by this process and best particle has been selected and all other particles are discarded. More description of these processes for modeling of SFS can be found in [7–10]. The simulation parameters utilized in the implementation of SFS algorithm are

**Table 2** The simulation parameters used for SFS algorithm

| Parameters | Value |
|---|---|
| Number of population(particles) | 30 |
| Maximal iterations | 30 |
| S. diffusion | 3 |
| S. walk | 1 |
| Lower bounds ($K_P$, $K_D$, $K_I$) | [0 0 0] |
| Upper bounds ($K_P$, $K_D$, $K_I$) | [20 10 10] |

**Table 3** The simulation parameters used for PS algorithm

| Parameter | Value |
|---|---|
| MS (mesh size) | 1 |
| MEF (mesh expansion factor) | 2 |
| MCF (mesh contraction factor) | 0.5 |
| MFE (maximum no. of function estimation) | 10 |
| $I_{max}$ (maximum no. of iteration) | 10 |

shown in Table 2. This approach has been combined with Pattern Search (PS) optimization which is derivative free good evolutionary algorithm for solving the complex problems which could not have been solved with in the range of the standard optimization techniques. It utilizes balanced and adaptable operator to optimize local search excellently by enhancing global search [11–14]. The main benefits of PS are:

- Computationally efficient.
- Easy to Implement.
- Simple concept.

The parameters utilized in the implementation of PS algorithm are shown in Table 3. Here, the HSFS approach is combination of SFS and PS algorithmic applied to the DC Motor for celerity control consisting of PID controller by considering fitness/objective function ITAE. The HSFS approach is explained in the flow chart as depicted in Fig. 2 [15].

## 5 HSFS–PID Approach for Celerity Control of DC Motor

The program code that is needed for HSFS algorithm for designing of considered motor and simulations of its time response have been performed by utilizing MATLAB SIMULINK environment in a Dell laptop with Intel(R) Core(TM) i3-8145U CPU @ 2.10 GHz processor with 4 GB RAM and utilizing software version MATLAB (R2019b) with toolboxes. For designing a controller for considered motor, two main aims have been pondered. The first is the preference of a controller and the second is proposing the algorithm. The controller is a PID controller that is very

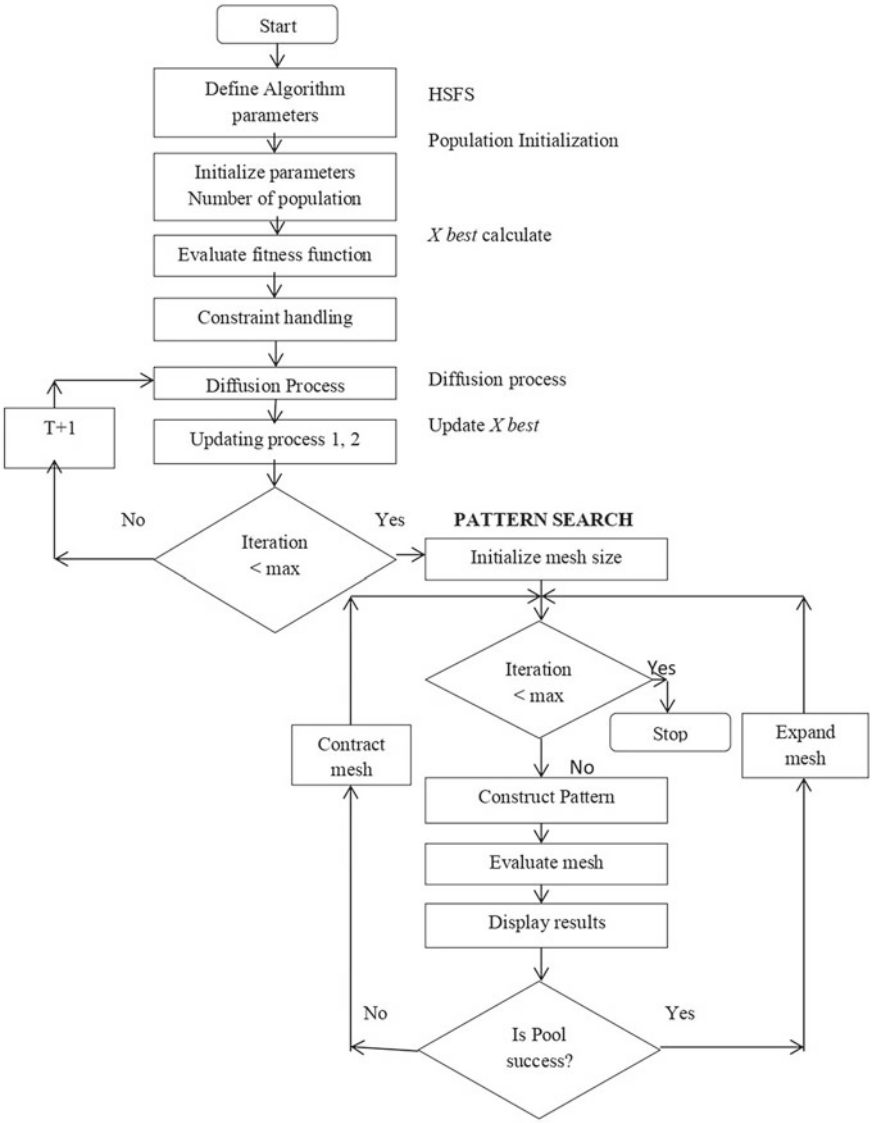


**Fig. 2** Flow chart of HSFS algorithm

popular and effective and the proposed algorithm, i.e., HSFS has excellent performance than other algorithms in the existing literature in terms of better intensification and diversification capabilities. The comprehensive Simulink model of DC Motor incorporating PID controller with ITAE fitness/objective function has been depicted in Fig. 3. The open-loop transfer function for celerity control of DC motor [7] is given by

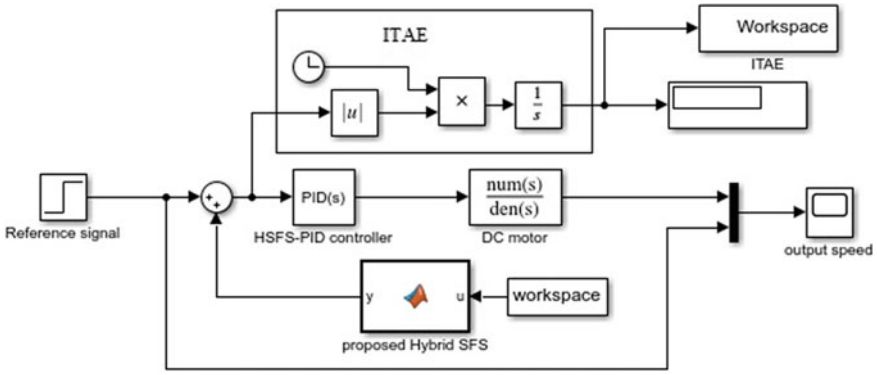


**Fig. 3** SIMULINK model of DC motor incorporating PID controller with fitness/objective function ITAE

$$G_M = \frac{15}{1.08s^2 + 6.1s + 1.63}. \tag{2}$$

The parameters of PID controller for celerity control of DC motor have been obtained using HSFS algorithm with ITAE as fitness/objective function. The obtained parameters of PID controller are

$$\mathrm{K_P} = 6.6315;\ \mathrm{K_I} = 0.212;\ \mathrm{K_D} = 0.5993 \tag{3}$$

$$G_c = 6.6315 + \frac{0.212}{s} + 0.5993s \tag{4}$$

$$G_{CL} = \frac{G(s)}{1 + G(s)H(s)} \tag{5}$$

$$G(s) = G_M \times G_C \tag{6}$$

$$G_{PIDOL} = \frac{8.99s^2 + 99.47s + 3.18}{1.08s^3 + 6.1s^2 + 1.63s} \tag{7}$$

$$G_{PIDCL} = \frac{8.99s^2 + 99.47s + 3.18}{1.08s^3 + 15.09s^2 + 101.1s + 3.18} \tag{8}$$

The optimum parameters of PID controller by HSFS for the considered motor have been given in Table 4, which the optimum parameters achieved by other popular approaches are also compared for validation.

The speed time response curves for comparison with existing different approaches in the literature have been given in Fig. 4. As described in simulation results, the

**Table 4** Comparison of unknown parameters obtained by different approaches

| Algorithm controller | $K_P$ | $K_I$ | $K_D$ |
|---|---|---|---|
| HSFS–PID (Proposed) | 6.6315 | 0.212 | 0.5993 |
| IWO–PID [6] | 1.5782 | 0.4372 | 0.0481 |
| PSO–PID [6] | 1.5234 | 1.3801 | 0.0159 |
| SFS–PID [7] | 1.6315 | 0.2798 | 0.2395 |

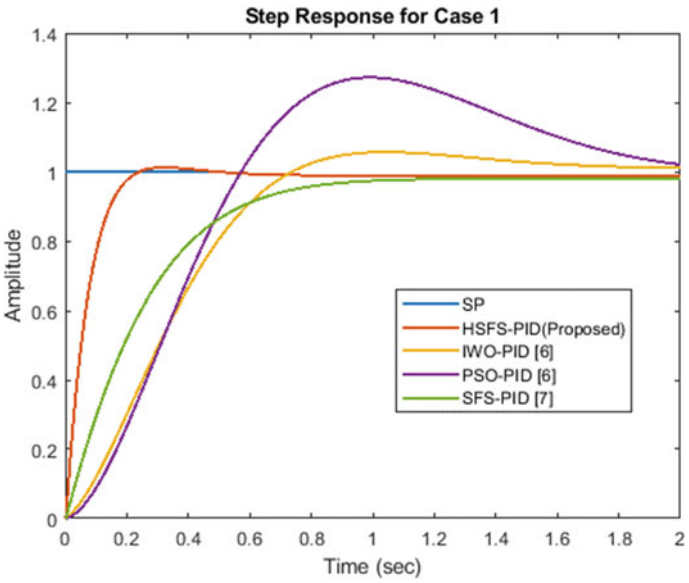


**Fig. 4** Step Response Comparison for Different Approaches for Case No. 1 (R = 0.040, Kt = 0.0150)

proposed controller HSFS–PID for celerity control of considered motor has no overshoot and improved rise and settling times compared to other approaches that are tuned with popular algorithms.

In Table 6, comparative analysis of HSFS–PID approach with IWO–PID [6], PSO–PID [6], SFS–PID [7] is depicted in terms of dynamic response performance measures.

## 6 Robust Analysis

In the robustness analysis, the step responses of the PID using HSFS and other algorithm for considered system has been studied with parametric variation of DC motor, i.e., variation in torque constant (kt) and the electrical resistance (R). There are two cases of parametric variations given in Table 5 for which the step responses

**Table 5** Different cases for parameters of DC motor

| Case No | Ra | Kt |
|---|---|---|
| 1 | 0.40 | 0.0150 |
| 2 | 0.20 | 0.0120 |

have been evaluated and shown in Figs. 4 and 5. The transient response parameters obtained for both the cases are given in Tables 6 and 7. These results justify the robustness of the HSFS-based PID controller for investigated system.

$$\text{Case No. 1: R} = 0.40 \text{ and Kt } = 0.0150 \tag{9}$$

$$G_M = \frac{15}{1.08s^2 + 6.1s + 1.63} \tag{10}$$

$$G_{CL(HSFS-PID)} = \frac{8.99s^2 + 99.47s + 3.18}{1.08s^3 + 15.09s^2 + 101.1s + 3.18} \tag{11}$$

$$G_{CL(IWO-PID)} = \frac{0.7215s^2 + 23.673s + 6.558}{1.08s^3 + 6.8215s^2 + 25.303s + 6.55} \tag{12}$$

$$G_{CL(PSO-PID)} = \frac{0.2385s^2 + 22.851s + 20.7015}{1.08s^3 + 6.3385s^2 + 24.481s + 20.701} \tag{13}$$

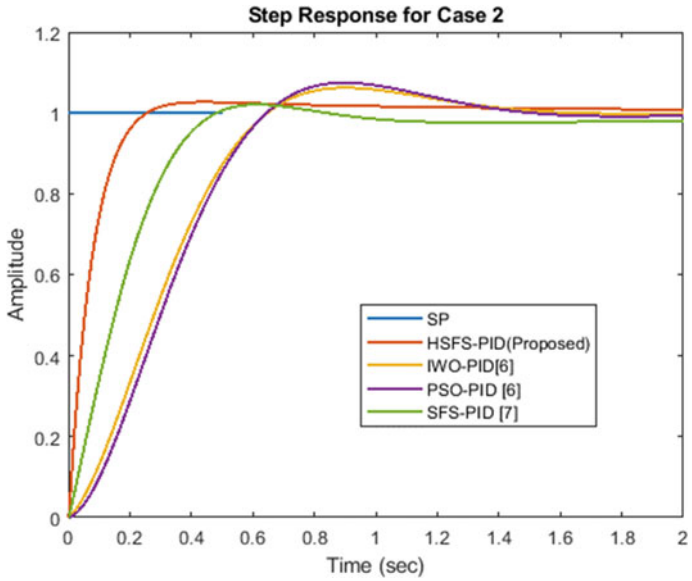


**Fig. 5** Step response comparison for different approaches for case no. 2 (R = 0.20, Kt = 0.0120)

**Table 6** Transient response parameters obtained by different approaches for case no.1; (R = 0.40, K t = 0.0150)

| Algorithm controller | Overshoot (%) | Settling time (s) | Rise time (s) |
|---|---|---|---|
| HSFS–PID (Proposed) | 1.64 | 1.345 | 0.27 |
| IWO–PID [6] | 7.16 | 1.95 | 0.493 |
| PSO–PID [6] | 25.5 | 2.38 | 0.409 |
| SFS–PID [7] | 0 | 1.06 | 0.638 |

**Table 7** Transient response parameters obtained by different approaches for case no. 2; (R = 0.20, Kt = 0.0120)

| Algorithm controller | Overshoot (%) | Settling time (s) | Rise time (s) |
|---|---|---|---|
| HSFS–PID (Proposed) | 1.84 | 1.045 | 0.37 |
| IWO–PID [6] | 7.16 | 1.95 | 0.493 |
| PSO–PID [6] | 25.5 | 2.38 | 0.409 |
| SFS–PID [7] | 0 | 1.06 | 0.638 |

$$G_{CL(SFS-PID)} = \frac{3.5925s^2 + 24.4725s + 24.197}{1.08s^3 + 9.6925s^2 + 26.1025s + 4.19} \tag{14}$$

Case No. 2: R = 0.20 and Kt = 0.0120 (15)

$$G_M = \frac{12}{1.08s^2 + 6.2s + 1.04} \tag{16}$$

$$G_{CL(HSFS-PID)} = \frac{7.192s^2 + 79.58s + 2.544}{1.08s^3 + 13.39s^2 + 80.62s + 2.544} \tag{17}$$

$$G_{CL(IWO-PID)} = \frac{0.5772s^2 + 18.9384s + 5.2464}{1.08s^3 + 6.5972s^2 + 19.9784s + 5.2464} \tag{18}$$

$$G_{CL(PSO-PID)} = \frac{0.1908s^2 + 18.2808s + 16.5612}{1.08s^3 + 6.2108s^2 + 19.3208s + 16.5612} \tag{19}$$

$$G_{CL(SFS-PID)} = \frac{2.874s^2 + 19.578s + 3.3576}{1.08s^3 + 8.894s^2 + 20.618s + 3.3576} \tag{20}$$

## 7 Conclusions

In present work, artificial intelligence technique based on natural growth phenomena such as HSFS algorithm have been utilized to develop more effective tuning of the controller so that enhanced optimized condition for the tuning can be derived. The obtained results display better-optimized values for the tuned controller and henceforth the performance of celerity control of DC motor is improved and comparable in terms of rise time, overshoots, and settling times, etc.

## References

1. P.C. Sen, *Principles of Electrical Machines & Power Electronics* (Wiley, USA, 1996)
2. B. Hekimoğlu, Optimal tuning of fractional order PID controller for DC motor speed control via chaotic atom search optimization algorithm. IEEE Access **7**, 38100–38114 (2019). https://doi.org/10.1109/ACCESS.2019
3. K..J. Astrom, PID controllers: theory, design and tuning. InstrtSoc Am, 1995.
4. J.G. Ziegler, N.B. Nichols, Optimum settings for automatic controllers. ASME Trans. **64**, 759–768 (1942)
5. J. Agarwal, G. Parmar, R. Gupta, A. Sikander, Analysis of grey wolf optimizer based fractional order PID controller in speed control of DC motor. Microsyst. Technol. **24**(12), 4997–5006 (2018). (Springer)
6. M. Khalilpour, N. Razmjooy, H. Hosseini and P. Moallem. Optimal control of DC motor using invasive weed optimization (IWO) algorithm, in *Proceedings of Maclesi Conference on Electrical Engineering, Maclesi New Town, Isfahan, Iran* (2011)
7. I. Khanam, G, Parmar. Application of stochastic fractal search in order reduction of large scale LTI systems, in *International Conference on Computer, Communications and Electronics (Comptelix) IEEE*, pp. 190–194 (2017)
8. R. Bhatt, G. Parmar, R. Gupta, A. Sikander, Application of stochastic fractal search in approximation and control of LTI systems. Microsyst. Technol. **25**(1), 105–114 (2018). (Springer)
9. H. Salimi, Stochastic fractal search: a powerful metaheuristic algorithm. Knowl Based Syst **75**, 1–18 (2015). (Elsevier)
10. R. Saini, G. Parmar, R. Gupta, SFS/PI approach for AGC of two area interconnected thermal power system, in *Energy Systems, Drives and Automations*, vol. 664, Lecture Notes in Electrical Engineering (Springer, Singapore, 2020)
11. U.K. Rout, R.K. Sahu, S. Panda, Design and analysis of differential evolution algorithm based automatic generation control for interconnected power system. Ain Shams Eng. J. **4**(3), 409–442 (2013)
12. R.K. Sahu, S. Panda, G.T. Chandra Sekher, A novel hybrid PSO-PS optimized fuzzy PI controller for AGC in multi-area interconnected power system. Int. J. Electric. Power Energy Syst. **64**, 880–893 (2015)
13. V. Soni, G. Parmar, M. Kumar, S. Panda, Hybrid grey wolf optimization-pattern search (hGWO-PS) optimized 2DOF-PID controllers for load frequency control (LFC) in interconnected thermal power plants. ICTACT J. Soft Comput. **6**(3), 1244–1256 (2016)
14. E.D. Dolan, R.M. Lewis, V. Torczon, On the local convergence of pattern search. SIAM J. Opt. **14**, 567–583 (2003)
15. S. Padhy, S. Panda, A hybrid stochastic Fractal Search technique based cascade PI-PD controller for automatic generation control of multi-source power system in presence of plugin electric vehicles. CAAI Transactions on Intelligence Technology (2017)

# Analysis and Fabrication of a Compact CPW-Fed Planar Printed UWB Antenna Using Isola Tera MT (R) Substrate for Medical Applications


**Soufian Lakrit, Sudipta Das, Apurba Chowdhury, MoussaLabbadi, and B. T. P. Madhav**

## 1 Introduction

Breast cancer is among the major widespread threatening diseases in the world. It may affect human beings of all genders. Every year, healthcare organizations reveal reports for the huge number of deaths of female persons. In women's breasts, in addition to fat, blood vessels, and skin tissues, there are exclusive glandular lobule cells that produce milk and a system of duct cells through which the milk transports and enters into the nipples. With any natural cells in the human body, the breast cells are renewing periodically and regularly where new cells replace the dead cells. However, in many cases, the breast cells (lobules/ducts) may reproduce unnaturally. The useful cells could transform into malignant lumps and tumors which could grow and spread over the whole breast tissues and finish to death.

Hopefully, an expert in medical care has proclaimed that early detection of breast cancer tumors followed by an immediate treatment could barely help to save the

S. Lakrit
Applied Mathematics and Information Systems Laboratory, EST of Nador, Mohammed First University, Oujda, Morocco

S. Das (✉)
Department of Electronics & Communication Engineering, IMPS College of Engineering & Technology, Malda, W.B, India

A. Chowdhury
Mallabhum Institute of Polytechnic, Bishnupur, Bankura, India

MoussaLabbadi
Engineering for Smart and Sustainable Systems Research Center, EMI, Mohammed V University in Rabat, Rabat, Morocco

B. T. P. Madhav
Department of Electronics and Communication Engineering, Koneru Lakshmaiah Education Foundation, Guntur, AP, India
e-mail: btpmadhav@kluniversity.in



C. K. Chanda et al. (eds.), *Advanced Energy and Control Systems*, Lecture Notes in Electrical Engineering 820, https://doi.org/10.1007/978-981-16-7274-3_17

cancerous woman's life. However, the danger of breast cancer resides in its non-external symptoms which make it hard to be diagnosed by doctors and even by the patients themselves. In human life, uncertain incidents are unpreventable but the panic created due to a serious disease like breast cancer leads to a lot of questions, how to identify whether a woman is already affected by breast cancer or not? How to minimize breast cancer risks? How to provide a cheap, largely available, and comfortable breast cancer diagnostic system for everybody and in every corner of the whole world? Yet, all those interrogations have been addressed for many years in conducted researches and still ongoing nowadays. Eventually, several technologies have been adapted to identify the existence of cancer tumors in a woman's breast. The most common techniques applied for the detection of breast cancer disease are X-Ray mammography and Magnetic Resonance Imaging (MRI) [1]. Nevertheless, they possess several weaknesses like some of them are inaccurate and expensive which made them less available on a large scale where some others are unsafe and cause negative effects on the human body like the heart and brain. All those miscellaneous problems pushed research to look after smarter and more accurate techniques. Microwave Imaging (MI) [2] technique has been solicited as the newest technique for breast cancer detection. Recently, it has received great research interest as it is more sensitive to cancer lumps and it has low deployment cost, high accuracy, high resolution, less magnetic field radiation risks, and also shows comfortable utility in comparison with the two precedents.

The MI technique is based on ultra-wideband (UWB) technology which is well involved in many medical applications nowadays [3–5]. In recent years, the popularity of the UWB technology has been raised due to the advancement of printed UWB antenna technology [6–9] The UWB antenna also plays an important role in medical applications [10–13]. After characterizing the breast contents, UWB transmitting antennas highlight the breast with low power signals when others receive the scattered signals. After an accurate analysis, the response of the tumor cells will be distinguished from the responses of the other breast cells. Since UWB antennas are focal elements in breast cancer microwave imaging systems, they received progressive development in the last years. In Ref. [10], a UWB antenna with T-Slot in the partial ground is proposed. Another UWB balanced antipodal Vivaldi antenna is proposed in Ref. [11] but it has a relatively large size. Also in Ref. [12], a UWB antenna with dual polarized squire ring slot for medical imaging systems is proposed. As well, just very recently, D. Shukla et al. have addressed a UWB antenna for microwave imaging [13]. All these designs possess a relatively large size which makes the system larger and less efficient. However, a small, low-cost and efficient UWB antenna may contribute to increase the efficiency of the MI system and reduce its size and cost of implementation. The cheap BC diagnostic system would be available for everybody, particularly poor people.

Therefore, this paper aims to design a smaller size, low cost, and efficient UWB CPW-Fed antenna applicable in breast cancer detection systems. The effort has been given to design a UWB antenna with an ultra-large impedance bandwidth. The designed antenna is purely planar with a simple structure, is flat, and its design

is simple and straightforward. A detailed discussion on the antenna geometry, simulation, and measurement results is presented in the subsequent sections. The design, simulation, and analysis of the results are performed by using High-Frequency Structure Simulator (HFSS) and Computer Simulation Technology-Microwave Studio (CST).

## 2 Design and Simulation

### *2.1 Structure of the Proposed Antenna*

As design constraints, a small volume (less than 44 × 38 × 0.762 $mm^3$) and ease of fabrication are targeted. Therefore, after exhaustive simulations using HFSS, the final structure is obtained as shown in Fig. 1. It has a simple configuration with a global volume of 44 × 38 × 0.762 $mm^3$. It consists mainly of a radiating patch and ground plane printed on one face of the Isola TeraMT (R*)* substrate with a dielectric constant $\varepsilon_r$= 3.45. The patch is made of a semi-elliptic shape of radiuses ($R_x$ = 10 mm and $R_y$ = 12 mm) integrated with a rectangular having the dimension of (21 × 20$mm^2$). A rectangular coplanar waveguide line of dimensions ($W_f$ = 3.5 mm, $L_f$ = 13.45 mm) is used to feed the designed patch. The structure of the ground plane is modified by incorporating two rectangular symmetrical wings having curved edges. Each wing has dimensions ($L_g$ = 14 mm, $W_g$ = 16.75 mm). Moreover, a small air gap (g = 0.5 mm) is incorporated between the designed wings in the suggested ground plane structure and the CPW feed.

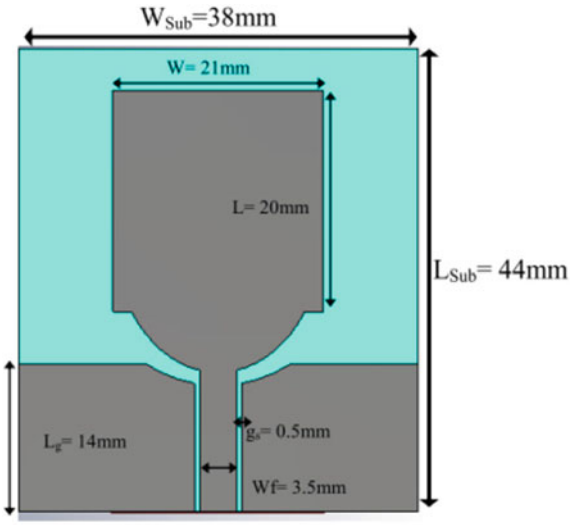


**Fig. 1** Geometry of the proposed antenna

## 2.2 Results and Discussions of the Proposed Antenna

This section demonstrates the obtained simulation results of the proposed CPW-fed UWB antenna. The results are presented in terms of impedance parameters (reflection coefficient, VSWR) and radiation parameters (gain and radiation patterns) which confirm its UWB characteristics with desirable radiation characteristics. In particular, the analysis of the $S_{11}$ parameter is displayed in Fig. 2a. It is very clear from the demonstration that the designed antenna is capable to cover an enormous band from 2 to 17.6 GHz for $S_{11} \leq -10$ dB. Thus, the proposed antenna offers an impedance bandwidth of 15.6 GHz (159.18% at the center frequency, 9.8 GHz). The suggested antenna confirm its candidature for several wireless applications such as RFID (2.4–2.5 GHz), WLAN(2.4–2.484 GHz, 5.15–5.35 GHz, 5.725–5.825 GHz), Wi–MAX

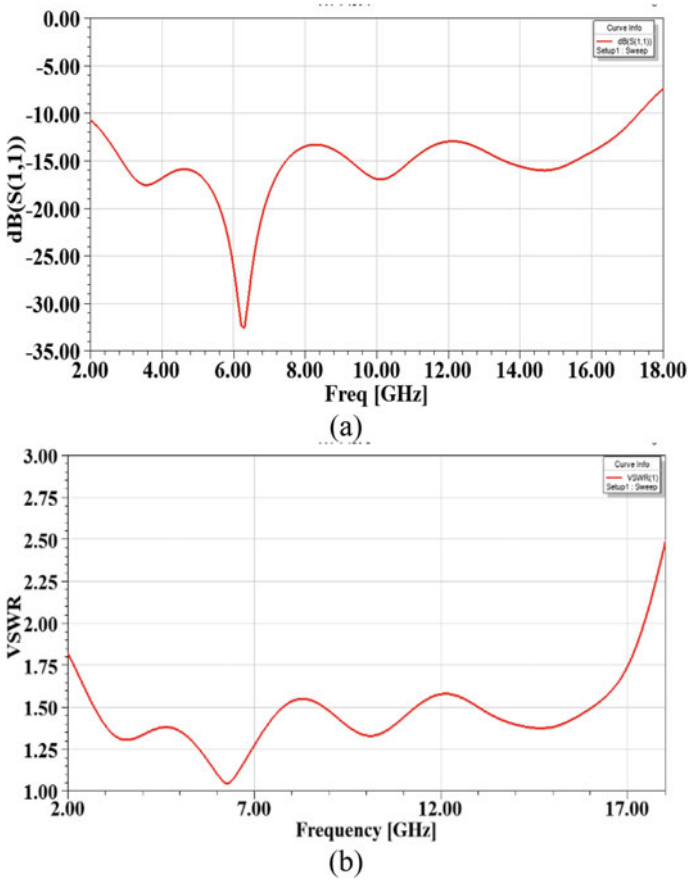


**Fig. 2** Demonstrations of **a** $S_{11}$ parameter and **b** VSWR of the CPW-Fed UWB antenna

(3.5–3.8 GHz, 5.25–5.85 GHz), ITU band (8–8.4 GHz), aeronautical radio navigation (10–10.7 GHz) band, X band satellite communication (7.25–7.75 GHz; 7.9–8.4 GHz), and Ku band (12–18 GHz). As shown in Fig. 2b, the VSWR is found within 2 for the whole operating bandwidth (2–17.6 GHz) which can assure minimum mismatch losses associated with the designed antenna.

Apart from impedance characteristics parameters, the radiation parameters are also important to investigate for the characterization of the UWB antenna. The radiation patterns for E- and H-planes representing co and cross-pol components of the fields are displayed in Fig. 3a–d. The simulated patterns are observed at four distinct frequencies (3, 5, 8, and 10 GHz) within the operating band. The suggested UWB antenna shows almost identical radiation patterns over the entire frequency band except for a slight deterioration at the higher operating frequency. At higher frequencies, the patterns are rather directional due to the excitement of higher order current mode. The desired omnidirectional patterns are observed in the H-plane, whereas E-plane patterns bidirectional. Compared to the co-pol components, the cross-pol components of the fields are suppressed and comparatively lower in the major planes. It is also very crucial to visualize the variations of gain as a radiation parameter because it reveals actually how much power the antenna can transmit or receive over all the operational bandwidth. The variations of gain for the designed CPW-fed UWB planar antenna are presented in Fig. 4. The realized gain has a variable value between 3.2 and 6.8 dB for the frequency band ranging from 2 to 18 GHz. The maximum peak gain (6.8 dB) is obtained at 11.3 GHz. So, it can be concluded that the proposed antenna offers significant gain and ration patterns of desired shapes as required for the intended applications in the UWB frequency spectrum.

## 3 Experimental Results and Validation

The final dimensions of the antenna are $44 \times 38 \times 0.762$ mm$^3$. The Isola TeraMT (R) substrate is utilized because of its commercial availability and excellent heat resistant properties for the realization of the antenna prototype model. The image of the realized antenna is displayed in Fig. 5. The measurement of the reflection coefficient of the manufactured antenna has been performed using E8634A VNA. The experimental results verify the simulation results and confirm the UWB resonance of the suggested antenna. An impedance bandwidth of 14.36 GHz (from 1.87 to 16.23 GHz) with $S_{11} \leq$-10 dB is recorded from the measurement results (see Fig. 6).

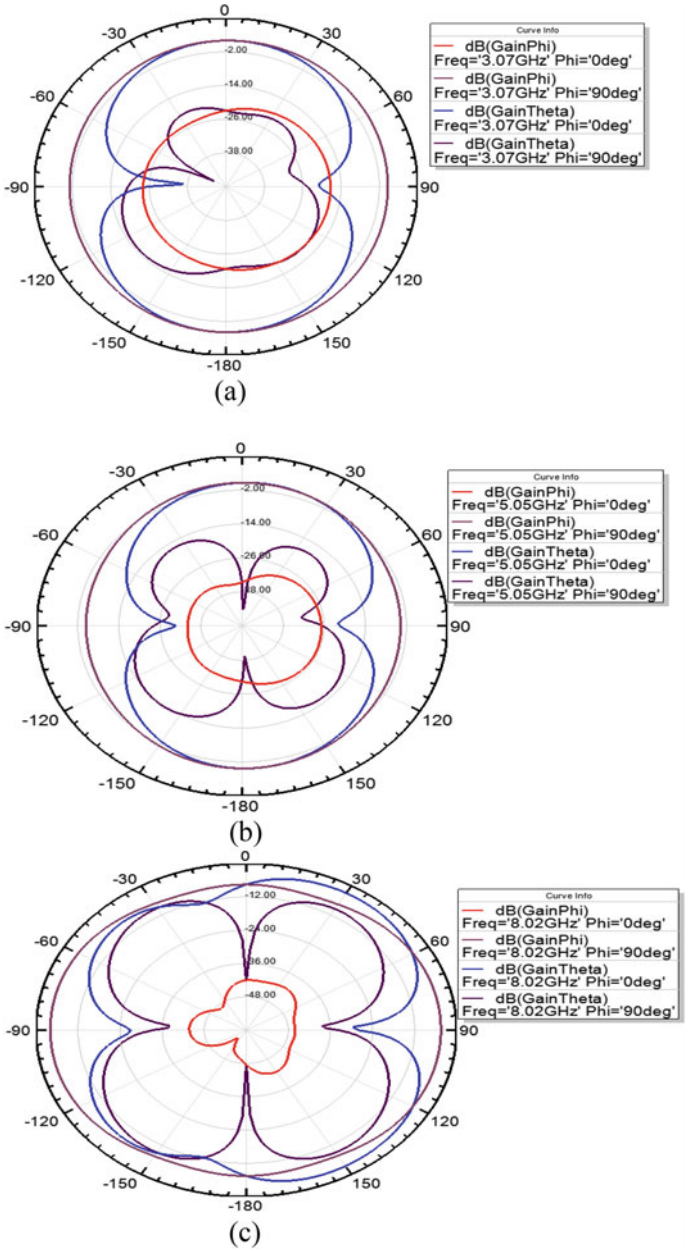


**Fig. 3** Radiation patterns in E- and H-plane representing Co- and Cross-polarization at frequencies **a** 3 GHz, **b** 5 GHz, **c** 8 GHz, and **d** 10 GHz

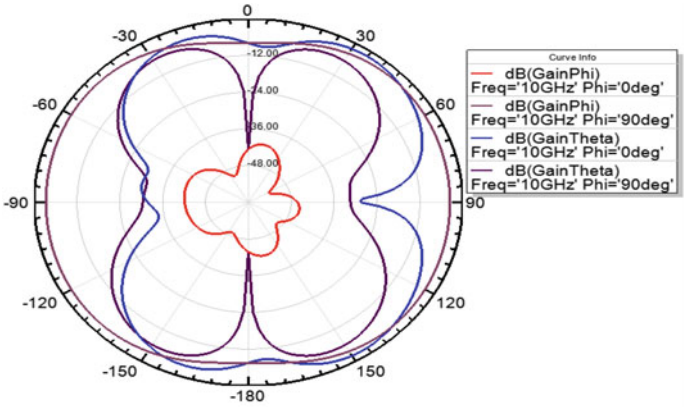


(d)

**Fig. 3** (continued)

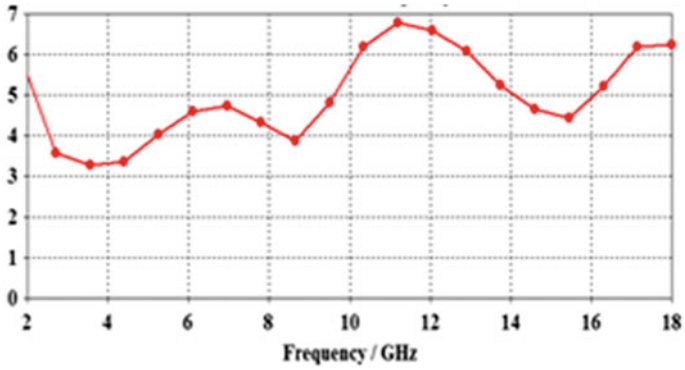


**Fig. 4** Variations of antenna gain over the operating band

**Fig. 5** The fabricated prototype of the proposed CPW-fed UWB antenna

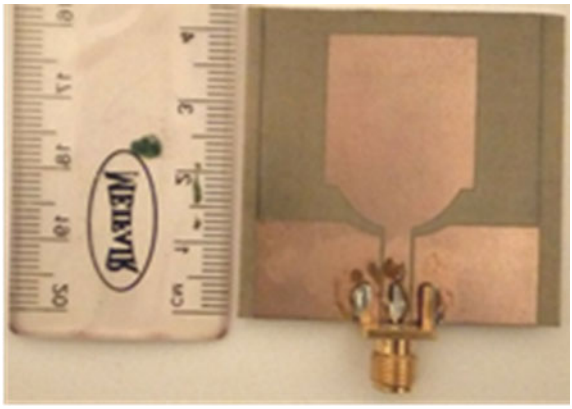

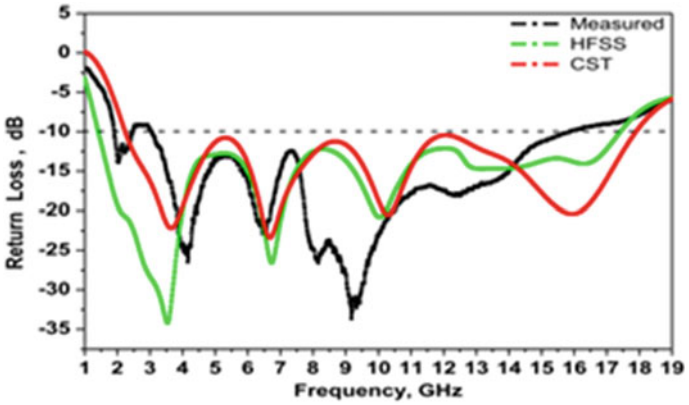


**Fig. 6** Simulated (using HFSS and CST) and measured return loss versus frequency

**Table 1** Comparison table

| References | Dimensions ($mm^2$) | Bandwidth (GHz) | Max. Peak Gain (dBi) |
|---|---|---|---|
| Zhong et al. [14] | 300 × 300 | 0.34–10.28 | – |
| Shafique et al. [15] | 86 × 72 | 3.5–10.6 | 4.89 |
| Sahnoun et al. [16] | 63.6 × 37 | 2–12 | 4.997 |
| Kikuta and Hirose [17] | 65 × 45 | 1.8–11 | – |
| Proposed work | 44 × 38 | 1.87–16.23 | 6.8 |

## 4 Comparison with Other UWB Antennas

The suggested UWB antenna is compared with some other reported antenna structures [14–17]. The comparative analysis is presented in tabular form in Table 1. It can be concluded from the comparison table that the designed proposed antenna furnishes maximum impedance bandwidth and gain characteristics in the smallest size.

## 5 Simulation Results of Breast with Tumor

The Specific Absorption Rate (SAR) is the most useful important parameter to measure the energy absorbed by the human tissue, organ, or body when exposed to the electromagnetic field. It can be expressed as [18].

$$SAR = \frac{d}{dt}\left(\frac{dW}{dm}\right) = \frac{d}{dt}\left(\frac{dW}{\rho dv}\right) \quad (1)$$

$$SAR = \frac{\sigma |E|^2}{\rho} \quad (2)$$

where σ the conductivity of the tissue (S/m), E is the electric field (V/m), and ρ is the mass density of the tissue (kg/m$^3$).

Signals in the microwave frequency range are capable of penetrating a diversity of biological materials including skin, muscle, fat, bone, and tumor, in general, systems with UWB technology achieve better material penetration. Each organ and tissue in the human body absorbs a quantity of microwave electromagnetic energy according to their dielectric properties and the rate of this absorption varies totally for every tissue. So, the challenge adopted in this study is to place our proposed antenna in contact with the breast to give more accuracy and precision for the studied concept in order to measure the SAR for breast tissues. The radius of the tumor is in the range from 2 mm to about 3 mm. The tumor was positioned at 20 mm away from the outer layer of the skin with a radius of 3 mm. After evaluating the optimized antenna, it is used to simulate the breast models developed in HFSS software as shown in Fig. 7 and the parameters of breast tissue are illustrated in Table 2. The proposed CPW UWB antenna is positioned in contact with the breast with a single tumor. The results obtained are illustrated in Figs. 8, 9, and 10. The results of the simulated current densities J in fat tissue, skin, and tumor are displayed in Figs.8a–c. It can be visualized from Fig. 8 that the current density J in the tumor is higher than in fat tissue and in the skin of the breast. In addition, the results presented in Figs. 9 and 10 indicate that the values of the SAR and the density of the current J are maximum at the level of the tumor compared to the other tissues.

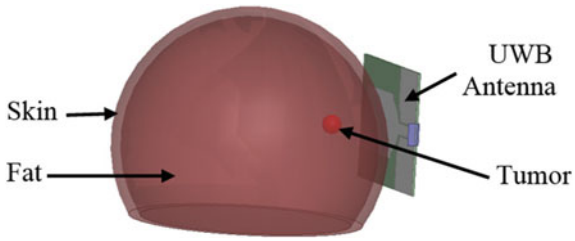


**Fig. 7** Model of Breast With Tumor

**Table 2** Parameters of breast tissues at 6 GHz

| Tissues type | Conductivité σ (S/m) | Relative permittivity (Ɛr) | Tissue density (ρ) |
|---|---|---|---|
| Skin | 1.74 | 36 | 1109 |
| Fat | 0.179 | 5.04 | 911 |
| Tumor | 4 | 50 | 84 |

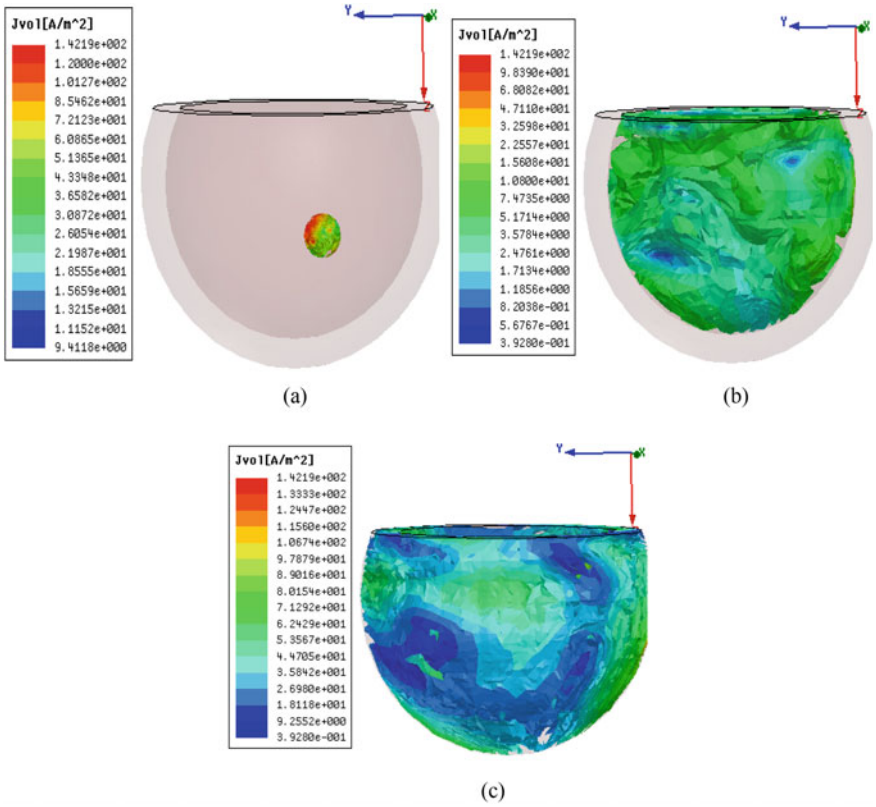


**Fig. 8** Distribution of the current density J, **a** Tumor, **b** Fat and **c** Skin

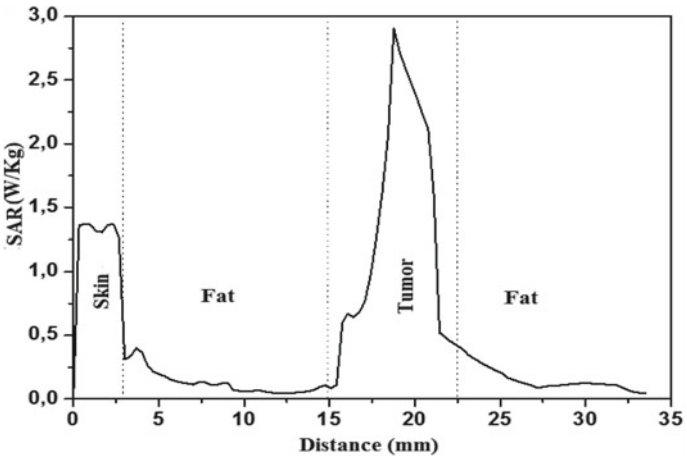


**Fig. 9** SAR distribution versus length of breast

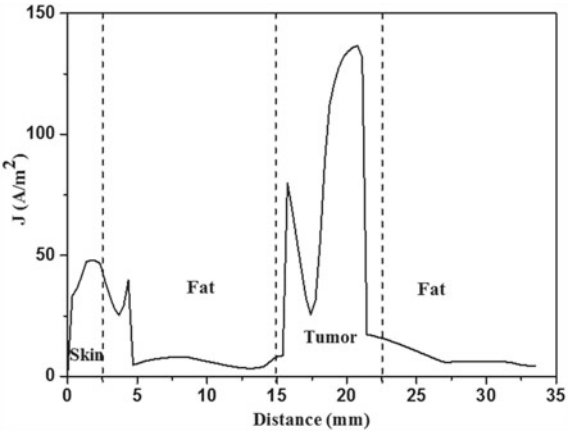


**Fig. 10** Current density J versus length of breast

## 6 Conclusion

A low-cost planar ultra-wideband antenna has been designed and presented for breast cancer detection. The simulation results are verified with experimental results. Both the theoretical and practical results assure the UWB characteristics of the suggested CPW feed printed antenna. The designed structure possesses a small size and less complex structure. The operating band of the antenna extends from 1.87 to 16.23 GHz with an ultra-wide bandwidth of 14.36 GHz for VSWR < 2. The proposed UWB antenna offers desirable radiation patterns and gain throughout the working band. Thus, the proposed UWB-printed antenna is a promising candidate for many wireless applications such as RFID systems, C-band, WiMAX, WLAN, ITU, X-band, aeronautical radio navigation Ku band, and European -UWB communication systems, etc. The proposed antenna can be implemented for breast cancer detection in medical science.

## References

1. W. Shao, B. Zhou, Z. Zheng, G. Wang, UWB microwave imaging for breast tumor detection in inhomogeneous tissue, in *IEEE Engineering in Medicine and Biology 27th Annual Conference Shanghai, China 2005* (2006), pp. 1496–1499, https://doi.org/10.1109/IEMBS.2005.1616715
2. D. Valderas, J.I. Sancho, D. Puente, C. Ling, X. Chen, *Ultrawideband Antennas: Design and Applications* (Imperial College Press, United Kingdom, 2010)
3. H.R. Khaleel, A. Issac, H.M. Al-Rizzo, A. Bihnam, Wearable printed monopole antenna for UWB and ISM applications, in *2014 USNC-URSI Radio Science Meeting (Joint with AP-S Symposium)*, Memphis, TN, USA, pp. 5–5, https://doi.org/10.1109/USNC-URSI.2014.6955387

4. A.I. Hammoodi, H.M. Al-Rizzo, A.A. Isaac, A proposed flexible elliptical ring monopole antenna for DSC and UWB with notch suppression for 5.8 GHz applications, in *2015 USNC-URSI Radio Science Meeting (Joint with AP-S Symposium)* (Vancouver, BC, Canada, 2015), pp. 10–10, https://doi.org/10.1109/USNC-URSI.2015.7303294.
5. M.Y. ElSalamouny, R.M. Shubair, Novel design of compact low-profile multi-band microstrip antennas for medical applications, in *Loughborough Antennas & Propagation Conference (LAPC)* (Loughborough, UK, 2015), pp. 1–4, https://doi.org/10.1109/LAPC.2015.7366015
6. S. Lakrit, S. Das, S. Ghosh, B.T.P. Madhav, Compact UWB flexible elliptical CPW-fed antenna with triple notch bands for wireless communications. Int. J. RF Microw. Comput.Aided Eng. **30**(7), e22201 (2020), 10.1002/ mmce.22201
7. S. Lakrit, S. Das, B.T.P. Madhav, Babu KV (2020) An octagonal star shaped flexible UWB antenna with band notched characteristics for WLAN applications. JINST **15**, P02021 (2020)
8. S. Lakrit, S. Das, A. El Alami, D. Barad, S. Mohapatra, A compact UWB monopole patch antenna with reconfigurable Band-notched characteristics for Wi-MAX and WLAN applications. Int. J. Electron. Commun. (AEÜ) **10**, 106–115 (2019)
9. S. Lakrit, H. Medkour, S. Das, B.T.P. Madhav, W.A.E. Ali, R.P. Dwivedi, Design and analysis of integrated wilkinson power divider-fed conformal high-gain UWB array antenna with band rejection characteristics for WLAN applications. J. Circuits Syst. Comput. (2020). https://doi.org/10.1142/S0218126621501334
10. S. Lakrit, H. Ammor, J. Terhzaz, A. Tribak, Realization and measurements of a miniature square patch antenna for ultra wideband applications. Int. J. Microw. Opt. Technol **10**, 307–313 (2015)
11. M.H. Bah, J.S. Hong, D.A. Jamro, UWB antenna design and implementation for microwave medical imaging applications, in *2015 IEEE International Conference on Communication Software and Networks (ICCSN),* (Chengdu, China, 2015), pp. 151–155, https://doi.org/10.1109/ICCSN.2015.7296144
12. R.R. Krishna, R. Kumar, A dual-polarized square-ring slot antenna for UWB, imaging, and radar applications. IEEE Antennas Wirel. Propag. Lett. **15**, 195–198 (2016)
13. D. Shukla, B.R. Dutta, B.K. Kanaujia, Design of microwave imaging based microstrip ultra-wideband antenna, in *Annual IEEE India Conference*, pp. 1–5, (Dec 2015)
14. Y.W. Zhong, G.M. Yang, L.R. Zheng, Planar circular patch with elliptical slot antenna for ultrawideband communication applications. Microw. Opt. Technol. Lett. **57**(2), 325–328 (2015)
15. K. Shafique, B.A. Khawaja, M.A. Tarar, B.M. Khan, M. Mustaqim, A. Raza, A wearable ultra wideband antenna for wireless body area networks. Microw. Opt. Technol. Lett. **58**(7), 1710–1715 (2016)
16. N. Sahnoun, I. Messaoudene, T.A. Denidni, A. Benghalia, Integrated flexible UWB/NB antenna conformed on a cylindrical surface. Prog. Electromag. Res. Lett. **55**, 121–128 (2015)
17. K. Kikuta, A. Hirose, Compact folded-fin tapered slot antenna for UWB applications. IEEE Antennas Wirel. Propag. Lett. **14**, 1192–1195 (2015)
18. N. Hammouch, H. Ammor, An accurate UWB technique for breast cancer detection using microwave specific absorption rate, vol. 13, no. 5 (2018)

# Applications of 555 Timer for Development of Low-Cost System


**Shadan AlShidani, Salim Alshabibi, Md Tabrez, Kanak Kumar, and Farhad Ilahi Bakhsh**

## 1 Introduction

Irrigation is the most important part of farming, and it requires daily labor works during the time of irrigation. Presently, the farmers mostly irrigate their fields or gardens through manual irrigation. In manual irrigation, farmers irrigate the land at regular intervals by turning the water pump ON/OFF as and when necessary. Wastage of water is seen often in this process, and the water supply to the field is delayed, consequently drying out of the crops occurred [1], until noticeable wilting occurs and water deficiency degrades plant growth. In addition to this sluggish growth, water deficiency is followed by lower fruit/crop production.

It is important for a farmer to know the amount of water and time of irrigation for economical farming. There may be wastage of water if the irrigation is unplanned [1]. The problem mentioned above can be perfectly addressed if an automated Irrigation System is used. In an Automatic Irrigation System, the most significant advantage is that watering is done only when it is required i.e., the water content of the field downs below a certain set value. Hence, automatic irrigation system minimizes water loss, maximizes productivity.

Many methods have already reported in the literature for automatic irrigation system. In each method sensor senses the soil moisture content with the help of a moister sensor. The suitability of each method depends on several issues such as

S. AlShidani · S. Alshabibi
Department of Engineering, Ibra College of Technology, Ibra, Oman

M. Tabrez (✉)
EEE Department, Motihari College of Engineering, Motihari 845401, India

K. Kumar
Electronics Engineering Department, IIT(BHU), Varanasi, India

F. I. Bakhsh
National Institute of Technology Srinagar, Srinagar, India



C. K. Chanda et al. (eds.), *Advanced Energy and Control Systems*, Lecture Notes in Electrical Engineering 820, https://doi.org/10.1007/978-981-16-7274-3_18

cost, accuracy, response time, installation cost, management, and durability [1–7]. The method presented here is the low cost design by employing easily available basic components. So it can be easily accessible to small farms as well.

Many people cannot turn ON lighting by hand such as differently abled persons, dwarfs, and children. This problem can be addressed by clap-switch, and switching is possible simply by clap sound [7]. Clap-switch enabled system can save time and effort by control the switch from away without movement. The switch can open and close the circuit by making sound to control the electric switches for devices. First sound commands to turn ON while subsequent clap shall toggle the switch. It is also useful for electric toys that need only clap to play [8].

This paper is organized in the following five sections. Section 1 is the introduction; Sect. 2 presents the materials and methods of the clap-switch and automatic irrigation system. Section 3 describes the design, simulation, and analysis of the proposed circuit, while Sect. 4 provides the results and discussion. The concluding remarks are given in Sect. 5.

## 2 Materials and Methods

### *2.1 IC555*

The 555 timer IC is one of the most essential part of electronic projects that require lesser or no computing. IC 555 can work as time delay circuits, as an oscillator, monstable, bi-stable, or astable multivibrator as below [9]. Figure 1 shows the internal circuit diagram of NE555.

*Astable mode of operation*

In this mode, the output is changing frequently between high and low; any state (LOW or HIGH) is not stable. This property of astable (unstable) output can be used as a clock pulse generation or square wave generation for different applications [10].

*Mono-stable mode of operation*

It consists of two configurations, one stable and the other unstable. The stable state can be selected by the user, either high or low. The output of the timer is high when the stable output is set to high (1). The timer output turns low when an interrupt is applied (0). Since the low state is unstable, after the interrupt passes, it goes to high (1) automatically. Similarly a mono-stable mode for stable low (logic 0) works [7].

*Bi-stable mode of operation*

In both, the output states (o and 1) are stable in Bi-stable mode of operation. At each interrupt, the output changes from low (0) to high (1) and vice versa and stays at that state (either 0 or 1).

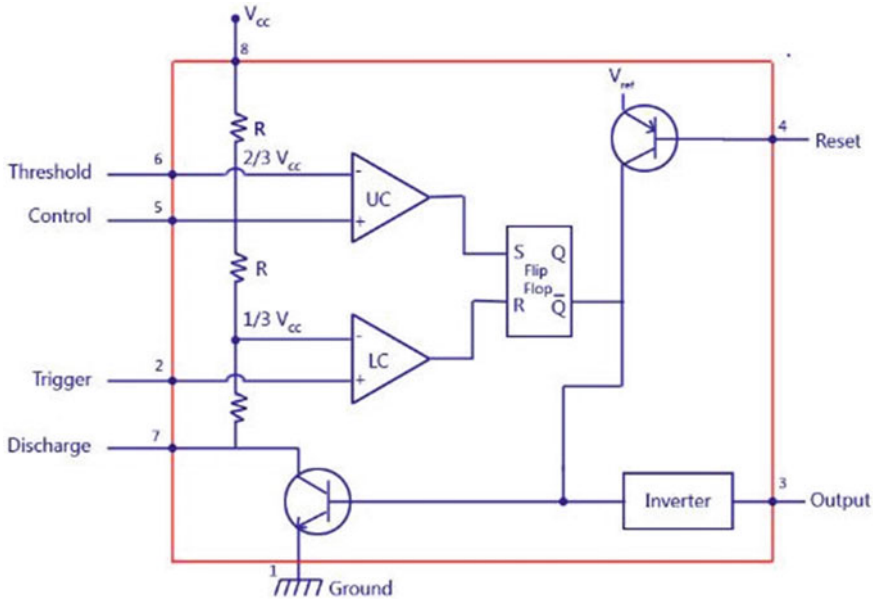


**Fig. 1** Internal circuit diagram of IC555

## *2.2 D Flip-Flop*

The "D flip-flop" shall store and gives output same as that of the input logic level applied to its input (D) terminal in so log the clock input is HIGH. When the clock input goes LOW the "SET" and "RESET" inputs of the flip-flop are both held at logic level "1" so it would not change the state and store whatever logic was available on its output before the clock transition happened. In other words, the output is "latched" at either logic level "0" or logic level "1" [11].

A D-type flip-flop only gives an output only when clock pulse change state from a logic 0 to logic (1). D flip-flop. Figure 2 shows the truth table of a D Flip-flop.

## *2.3 Working Principle of Clap-Switch*

Refer to Fig. 3, an electric Condenser Mic is utilized for identifying the sound signal, semiconductor switch Q1 to trigger the 555 timer IC. 555 IC output is used to SET and RESET the D-type flip-flop and D-type flip remembers the logic level (LED ON or OFF) until next Clap/sound shows up. From the start the semiconductor switch Q1 is in OFF condition in light of the fact that there is not sufficient (0.7v) base-emitter voltage to turn it ON. The detailed working is as demonstrated.

| Clk | D | Q | | Description |
|---|---|---|---|---|
| ↓ » 0 | X | Q | $\overline{Q}$ | Memory no change |
| ↑ » 1 | 0 | 0 | 1 | Reset Q » 0 |
| ↑ » 1 | 1 | 1 | 0 | Set Q » 1 |

**Fig. 2** Truth table of D flip-flop

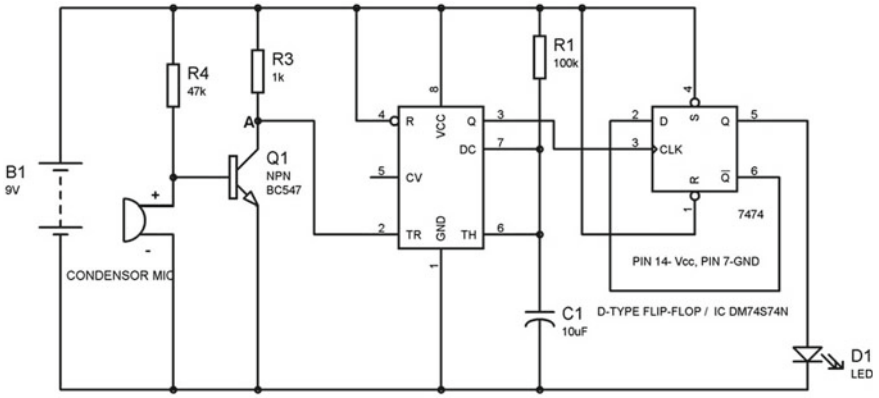


**Fig. 3** Schematic diagram of the clap-switch

The point A is at high potential as it is associated with Vcc, and simultaneously point A is associated with Trigger pin #2 of 555 IC, thus Trigger pin #2 is additionally at high potential. It is evident that, to trigger a 555 IC through Trigger pin #2, the voltage of the pin #2 should be beneath Vcc/3. So at this stage no output appears at OUT pin #3, it implies that no clock pulse for D-type Flip-flop (IC 7474), subsequently no reaction from D-type Flip-flop, thus LED light shall be switched OFF.

When the 555 IC first triggered by a Clap, sound energy of the clap converts into voltage and thus transistor Q1 turned ON due to enough voltage (0.7) across base-emitter junction. This shall bring the voltage of point A and thus pin #2 to zero. Consequently, pin #3 shall output HIGH (logic 1). The LED shall glows as output of pin #3 is the clock input of D flip-flop. The LED shall remain in ON state till the next positive clock pulse appears.

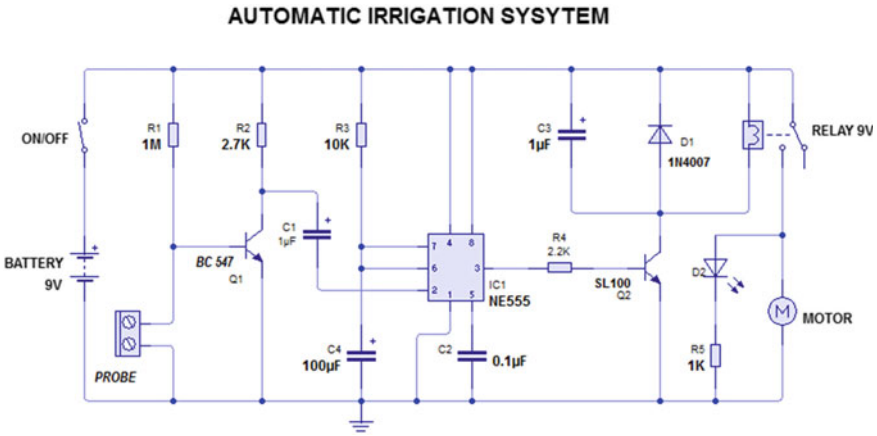


**Fig. 4** Schematic diagram of the IC 555 based automatic irrigation system

## *2.4 Working Principle of an Automatic Irrigation System*

Referring to Fig. 4, the automatic plant irrigation circuit, IC 555, is wired in a bi-stable multivibrator mode. The pin#2 here becomes the sensing pinout of the IC and is connected to the transistor Q1 through a moisture sensor and R1. A two metallic probe is used as a moisture sensor. When the soil is dry, probe is open circuit and base to emitter voltage high enough to drive the Q1 in saturation mode. Once Q1 switched ON, set pin 2 becomes LOW causing set the output HIGH. A high output at pin 3 shall drive transistor Q2 that in turn operate relay for pump motor. The relay activation turns ON the water pump motor, which now starts pumping water to the dry area of the soil via a water channel distribution network.

As this happen, the soil gradually gets wetter and as soon as the predetermined level of moisture is reached, the probes immediately sense the lower resistance and base to emitter voltage of transistor reduces below 0.7 V. Transistor shall be off and a high input shall appear at pin #2. Pin #4 is connected to Vcc so high Pin #4 shall reset the output (Pin #3) as soon as Pin #2 set to HIGH. Therefor transistor Q2 shall be switched OFF relay shall be OFF in absence of activation command switching OFF the water pump consequently. This cycle continues in between dry and wet soil.

## *2.5 Simulation of Clap-Switch for Differently Abled Person*

Refer to Fig. 5, the electric condenser mic is used as a sensor to receive clap sound. The condenser mic gets the sound energy of clap and convert into an electrical signal that thus is utilized to trigger 555 clock IC, through a semiconductor switch. The triggering of IC555 functions as a clock pulse signal for D-flip flop and would turn

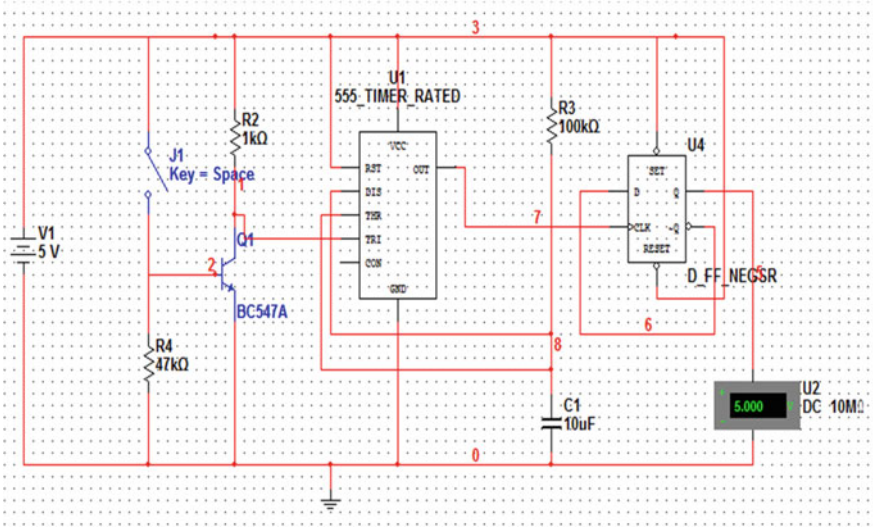


**Fig. 5** Clap-switch simulated in multisim

ON the load (LED in this situation), which shall stay ON until the following clock pulse (implies until the next applaud/sound). In this manner the clap-switch which shall turn ON with first applaud shall be turned OFF with the subsequent clap sound and so on.

## *2.6 Simulation of Automatic Irrigation System*

In this automatic irrigation process, moisture sensor shall detect the moisture and send the signal to NE555 through a transistor. NE555 sends an output command signal to relay for Turn ON/Turn OFF the pump according to the moisture content in the soil. If the soil is dry, NE555 send a command to turn ON the pump while Turn OFF command is sent as long as the soil is sufficiently wet.

MULTISIM, a software of National Instruments is a versatile schematic capture and simulation environment for engineers, students, and professors. It can be used to simulate electronic circuits and prototype Printed Circuit Boards (PCBs) [12]. Figure 6 shows the simulation model of the proposed automatic irrigation system circuit in MULTISIM before assembling on a PCB. Simulation results of the circuits found satisfactory.

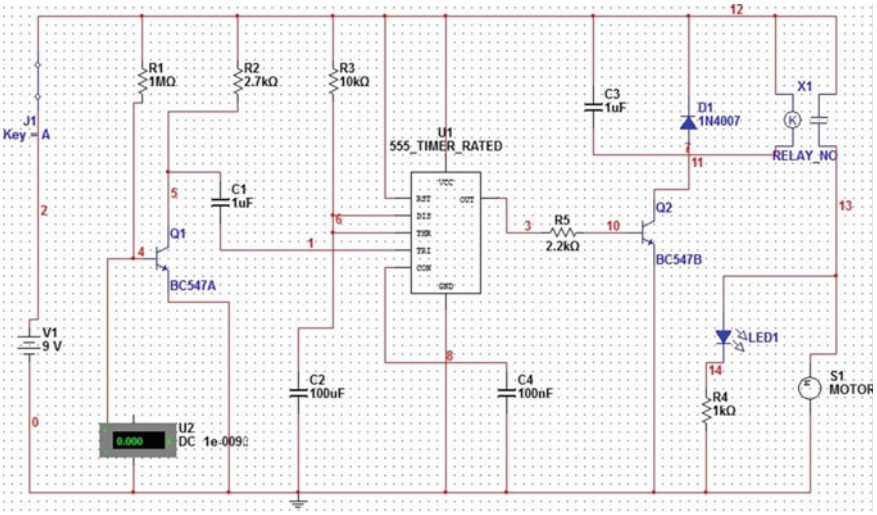


**Fig. 6** Automatic irrigation system simulated in multisim

## 3 Development of the Practical Model

At first, the circuit is designed and simulated in MULTISIM environment. Simulation results was satisfactory. After that printed circuit board is manufactured with the help of software in Engineering Department, Ibra College of Technology, Oman. The necessary electronic components are mounted and soldered on the board. Final working prototype of Automatic Irrigation System and Clap-Switch is shown in Figs. 7 and 8, respectively. The prototype has been tested after the complete design of the system. The expected results and the actual results are found to be very close.

## 4 Results and Discussions

After designing, the prototype model was tested to check that if it is working properly as per the designed specifications: The developed prototype model has tested to check the clap-switch is working properly as per the designed specifications. Performance test analysis is shown below in Tables 1 and 2 respectively. From the test results of Table 1, it is found that the distance of sensing is up to 50 cm only, which means the circuit shall not work more than 50 cm of distance.

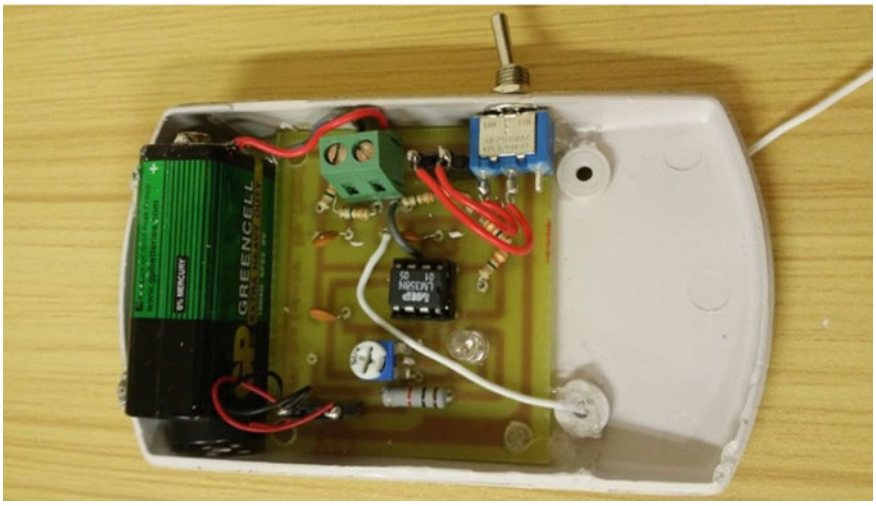


**Fig. 7** Automatic irrigation system prototype

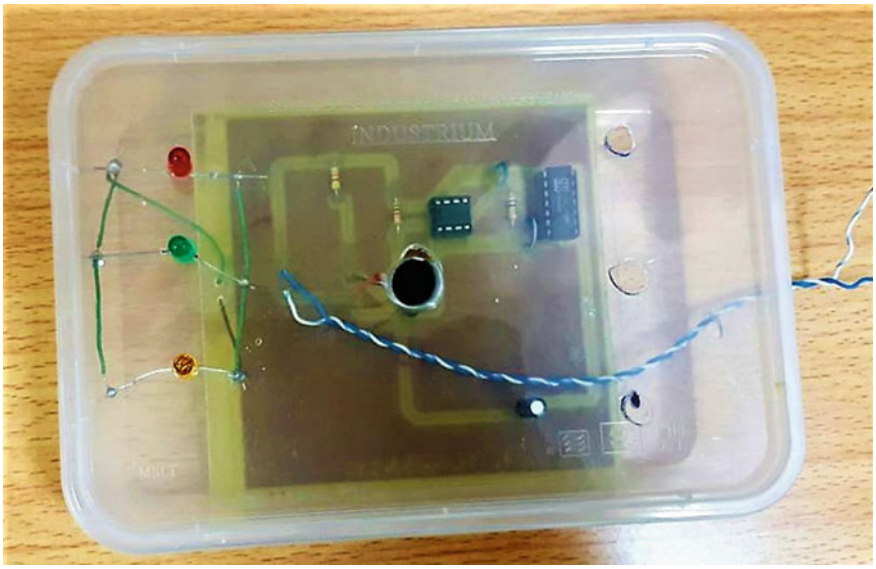


**Fig. 8** Clap-switch prototype

**Table 1** Performance test of clap-switch

| Distance (cm) | Light ON / OFF |
|---|---|
| 5 | Turn ON |
| 15 | Turn ON |
| 25 | Turn ON |
| 35 | Turn ON |
| 45 | Turn ON |
| 50 | Turn ON |
| 55 | Turn OFF |
| 60 | Turn OFF |

**Table 2** Performance test of automatic irrigation system prototype

| Moisture | Pump ON/OFF |
|---|---|
| No moisture | OFF |
| Very low moisture | OFF |
| Medium moisture | ON |
| Full moisture | ON |
| Flooded moisture | ON |

## 5 Conclusion

Proper and accurate irrigation can be used to minimize water losses. It is concluded that irrigation system presented in this can be used to automate the irrigation using low cost, easily available item. This automatic irrigation system shall help automation of Farms fields' irrigation and government places like airports, universities, colleges and schools, and parks irrigation system. Its response time is very fast overall cost is low power loss and requires fewer components. It shall help minimize water waste and improves plant growth. The circuit is designed to work automatically and hence there is no need for any human interference in the irrigation process. For large areas, more sensors has to be deployed for reliable operation of the system. For a better response, a sensor made of multiple metal probes connected together parallel have to be used.

Clap-switch is designed for the peoples with special needs (disabled persons) to control switching of home-appliances and toys (which need only clap to play). This switch help to minimize wastage of electricity. The reliability of the clap-switch depends on the proper functioning of the mic sensor. The clap-switch is unable to differentiate between a clap sound and sound of another origin of the same level leading to the faulty operation. Although this clap-switch is very basic in function, one can develop a more efficient clap-switch that can work on voice commands instead of clapping. Faulty operation of clap-switch may also be avoided if voice command based switch is employed.

## References


1. R.K. Sivanappan, Prospects of micro-irrigation in India. Irrig. Drain. Syst. **8**(1), 49–58 (1994)
2. V.N.R. Gunturi, Micro controller based automatic plant irrigation system. Int. J. Adv. Res. Technol. **2**(4), 194–198 (2013)
3. M.N. Sudha, M.L. Valarmathi, A.S. Babu, Energy efficient data transmission in automatic irrigation system using wireless sensor networks. Comput. Electron. Agric. **78**(2), 215–221 (2011)
4. P.B. Chikankar, D. Mehetre, S. Das, An automatic irrigation system using ZigBee in wireless sensor network, in *2015 International Conference on Pervasive Computing (ICPC)*, ( IEEE, 2015), pp. 1–5
5. D.S. Pavithra, M.S. Srinath, GSM based automatic irrigation control system for efficient use of resources and crop planning by using an Android mobile. IOSR J. Mech. Civil Eng. (IOSR-JMCE) **11**(4), 49–55 (2014).
6. G. Yang, Y. Liu, L. Zhao, S. Cui, Q. Meng, H. Chen, Automatic irrigation system based on wireless network, in *IEEE ICCA 2010*, (IEEE, 2010), pp. 2120–2125
7. S.K. Luthra, M.J. Kaledonkar, O.P. Singh, N.K. Tyagi, Design and development of an auto irrigation system. Agric. Water Manag. **33**(2–3), 169–181 (1997)
8. S.S. Olokede, Design of a clap activated switch. Leonardo J. Sci. **7**(13), 44–58 (2008)
9. H Goyal, Understanding of IC 555 timer and IC 555 timer tester. I. J. Inventive Eng. Sci. **3**(2) (2015)
10. L Chunling, Characteristics of 555 timer's function and application. Electron. Sci. Technol. **1** (2011)
11. M.R. Beigh, M. Mustafa, Design and analysis of a simple D flip-flop based sequential logic circuits for QCA implementation, in *2014 International Conference on Computing for Sustainable Global Development (INDIACom)* (IEEE, 2014)
12. J. Zhang, X. Li, Multisim based schematic design and simulation, in *Computer Simulation*, vol. 5 (2005), p. 032

# Optical Quadruple New Gate Using SLM and Savart Plate

**Supriti Samanta, Aranya Manna, Goutam Kumar Maity, and Subhadipta Mukhopadhyay**

## 1 Introduction

In recent years, the benefits of computer digital circuit technology have made feasible testing and implementation of electronic circuit's operation with over two discrete levels of signals. This provides the concept of multi-valued logic (MVL). Dubrova [1] et al. have proposed and presented MVL circuit design, revealing both the opportunities provided by them and also the challenges faced by them [2–4]. Different arithmetic operations like addition, multiplications in the Galois field and also addition, subtraction and multiplication in modulo-4 arithmetic are demonstrated in the MVL system by Patel and Gurumurthy [5]. Quaternary to binary and binary to quaternary converters are also designed for this purpose [6].

The benefits of technology during the last 20 years have generated an oversized demand for handling a large volume of knowledge at high speed. To fulfill up the wants, the concept of MVL has come forward from the status of the two-valued or binary logic system within the one hand, and on the other side, these include the concept of the optical processor for switches. Simultaneous operation is often performed using optical processors but it absolutely was also felt that it are often possible to represent multi-valued logic using the polarization states of the sunshine beam with the presence or absence of sunshine in the optical system [7]. Avizienis introduced a signed digit numeration system for proper utilization of parallelism of the optical beam rather than cascaded single-bit operating units [8]. The modified

S. Samanta (✉) · S. Mukhopadhyay
Department of Physics, Jadavpur University, Kolkata 700032, India

A. Manna
Department of Physics, Sabang Sajanikanta Mahavidyalaya, Paschim-Medinipur 721166, West Bengal, India

G. K. Maity
Department of Physics, Raipur Block Mahavidyalaya, Bankura 722134, West Bengal, India



C. K. Chanda et al. (eds.), *Advanced Energy and Control Systems*, Lecture Notes in Electrical Engineering 820, https://doi.org/10.1007/978-981-16-7274-3_19

signed digit [9–12] or modified trinary numeration system suggested the carry free operation. The ternary logic system supported three states which were introduced by Lukasiewicz, and further, it absolutely was modified by him to four states logic for a better proposition.

The irreversible operation produces information loss which ends up in energy dissipation. The energy dissipated for each irreversible bit operation is a minimum of KTln2 joules in keeping with Landauer's research; here, T is the operating temperature and K = 1.3806505 * $10^{-2}$ 3 $m^2$ $kgs^{-2}$ $K^{-1}$ joule/kelvin is Boltzmann's constant. The above-mentioned energy is often saved if the operation could be reversible operation as described by Bennett in 1973. Reversible operation means inputs also can be derived from the output.

Different applications for lossless data processing are often performed using reversible operation. The design of reversible logic optically is incredibly important for faster operation. With this aim, an optical quadruple new Gate using SLM and Savart Plate is presented in this paper. Savart plate is made with a double-plate device used to transmit polarized light where interference fringes of lights are formed which indicates the presence of a signal. There are two calcite plates of equal thickness, cut parallel to their natural cleavage faces with rotation and cemented together which forms a right angle to each other.

The proposed paper is organized as follows: Section 2 deals with the quadruple valued logic systems and their explanation. Section 3 describes briefly the truth tables of Di-bit representation. Section 4 presents the operation of the basic building block circuit using SLM and Savart Plate. The operating principle and design of Quadruple new Gate are represented in Sect. 5. Theological simulation results and final conclusion with the scope of future works are made in Sect. 6 and Sect. 7, respectively.

## 2 Quadruple Logic System

The four states of the quadruple logic system are represented as the right, partly right, wrong and the partly wrong. As the quadruple system with states {0, 1, 2, 3} does not satisfy the basic field conditions so, a Di-bit representation of the logic 00 0, 01 1, 10 2 and 11 3 is considered which is similar to basic two-valued logic system.

For quaternary logic, i.e., with four states, Galoisfield may be represented as GF($2^2$), i.e., k and r both are considered here 2. The elements and the states {0,1,2,3} of GF($2^2$) are represented by di-bit as {00, 01, 10, 11}, respectively. Table 1 represents the states of logic, representation of them and corresponding Di-bit representations and the state of polarization.

**Table 1** Quadruple logic system

| Logical state | Represented by | Dibit representation | State of polarization |
|---|---|---|---|
| False/wrong information | 0 | 00 | No light |
| Partial information | 1 | 01 | Vertical polarization |
| Partial information (complement of 1) | 2 | 10 | Horizontal polarization |
| True/complete information | 3 | 11 | The presence of both the horizontal annd vertical polarization |

## 3 Truth Tables Based on Di-Bit Representation

Truth tables of different quadruple logic gates are represented bit-wise in this section (Table 2).

**Table 2** Truth tables for **a** OR, **b** AND, **c** NOT **d** XOR, **e** NAND, **f** NOR and **g** XNOR Gates

| A / B | 00 | 01 | 10 | 11 |
|---|---|---|---|---|
| 00 | 00 | 01 | 10 | 11 |
| 01 | 01 | 01 | 11 | 11 |
| 10 | 10 | 11 | 10 | 11 |
| 11 | 11 | 11 | 11 | 11 |

(a)

| A / B | 00 | 01 | 10 | 11 |
|---|---|---|---|---|
| 00 | 00 | 00 | 00 | 00 |
| 01 | 00 | 01 | 00 | 01 |
| 10 | 00 | 00 | 10 | 10 |
| 11 | 00 | 01 | 10 | 11 |

(b)

| A | Ā |
|---|---|
| 00 | 11 |
| 01 | 10 |
| 10 | 01 |
| 11 | 00 |

(c)

| A / B | 00 | 01 | 10 | 11 |
|---|---|---|---|---|
| 00 | 00 | 01 | 10 | 11 |
| 01 | 01 | 00 | 11 | 10 |
| 10 | 10 | 11 | 00 | 01 |
| 11 | 11 | 10 | 01 | 00 |

(d)

| A / B | 00 | 01 | 10 | 11 |
|---|---|---|---|---|
| 00 | 11 | 11 | 11 | 11 |
| 01 | 11 | 10 | 11 | 10 |
| 10 | 11 | 11 | 01 | 01 |
| 11 | 11 | 10 | 01 | 00 |

(e)

| A / B | 00 | 01 | 10 | 11 |
|---|---|---|---|---|
| 00 | 11 | 10 | 01 | 00 |
| 01 | 10 | 10 | 00 | 00 |
| 10 | 01 | 00 | 01 | 00 |
| 11 | 00 | 00 | 00 | 00 |

(f)

| A / B | 00 | 01 | 10 | 11 |
|---|---|---|---|---|
| 00 | 11 | 10 | 01 | 00 |
| 01 | 10 | 11 | 00 | 01 |
| 10 | 01 | 00 | 11 | 10 |
| 11 | 00 | 01 | 10 | 11 |

(g)

## 4 The Basic Building Block

The basic building block performance of the rational processing quadruple valued logic system is shown in Fig. 1. Light output from laser source L after getting polarized at an angle of 45° with respect to the two orbits is incident on the Savart Plate $S_1$ as shown in Fig. 1. The Savart plate $S_1$ is used to split the light into two components. The output of $S_1$ is controlled by electrically addressable negative SLMs—$P_1$ and $P_2$. The SLMs are controlled by electrical signals applied on them. The negative SLM becomes opaque when an electric voltage is applied on it and then it becomes transparent when no electric voltage is applied on it. The operation of positive SLM is just the opposite of negative SLM. The outputs from SLM are finally combined by the Savart Plate S2. The flow chart of the basic building block is also provided in Fig. 2 to understand the operational process.

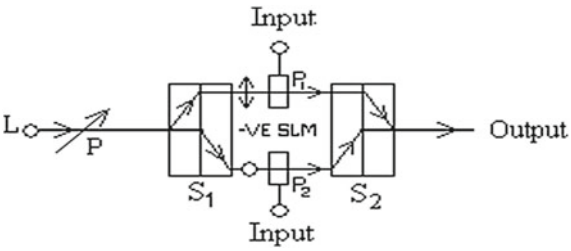


**Fig. 1** The basic building block

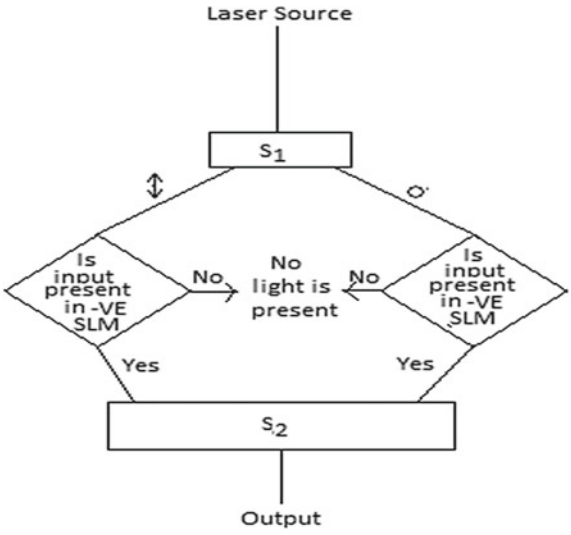


**Fig. 2** The flow chart of the basic structure block

## 5 Theoretical Principles of Design

A quadruple new gate is an integrated circuit of four logic gates. The gates can be of any type of AND, OR, NOT, NOR, NAND, XOR and XNOR. For any given quadruple new gate, all four of the individual gates are considered of the same types. A quadruple new gate is a unique building block of a digital circuit as the logic output mentioned in the truth table of Table 3. As the basic principle of gates, most of the basic logic gates have two inputs and one output. At any time, every gate is in one of the two binary states, low(0) or high(1), represented by different voltages as designed. Quadruple new gates can be used in various digital applications including flip flop, digital switches, voltage-controlled oscillator, waveform generator, etc.

### *5.1 The Operating Principle and Design of Quadruple New Gate*

A quadruple new gate (NG) has three inputs terminal (A, B, C) and three outputs terminal (P, Q, R). It is a combinational circuit of OR, XOR, XNOR, etc. logic gate, and these different types of logic gates are interconnected to each other. The quadruple NAND gate has diverse uses of particular interest, because other basic logic functions can be derived through multiple NAND gates developing different connections of circuits. This property makes the quadruple NAND gate a universal digital substitute for other gates. It satisfies the relations as follows (Fig. 3 and Table 4).

**Table 3** Truth table of new proposed gate

| Inputs | | | Outputs | | |
|---|---|---|---|---|---|
| A | B | C | P | Q | R |
| 0 | 0 | 0 | 0 | 0 | 0 |
| 0 | 0 | 1 | 0 | 1 | 1 |
| 0 | 1 | 0 | 0 | 0 | 1 |
| 0 | 1 | 1 | 0 | 1 | 0 |
| 1 | 0 | 0 | 1 | 0 | 1 |
| 1 | 0 | 1 | 1 | 1 | 1 |
| 1 | 1 | 0 | 1 | 1 | 0 |
| 1 | 1 | 1 | 1 | 0 | 0 |

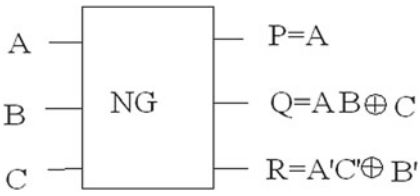


**Fig. 3** Schematic diagram of New Gate

## *5.2 Operating Principle*

The operating principle of the quadruple new gate is described in Fig. 4. Every input terminal is consisting of two components and every output terminal is consisting of two components. So, the result of output is of different types: true, partly true, partly false and false. It is evident that the output, P, is similar to that of the input, A, and the outputs of Q and R are dependent upon the inputs of A, B and C. We have described the inputs A, B and C and their corresponding outputs P, Q and R simultaneously.

I. If $A = B = C = 0$, as a result, no light comes out from $S_6$, $S_{10}$, $S_{14}$, $S_{20,}$ $S_{24}$, $S_{28}$ . So the final results are zero (i.e., $Q = R = 0$).

II. If $A = B = 0$ but $C = 1$ ($c_j = 0$, $c_i = 1$), as a result, light from $S_{10}$, $S_{14}$ and $S_{28}$ is perpendicular polarized and the final result is perpendicular polarized (i.e., $Q = R = 1$).

III. If $A = B = 0$ and $C = 2$ ($c_j = 1$, $c_i = 0$), as a result, light from $S_{10}$, $S_{14}$ and $S_{28}$ is straight polarized and the final result is straight polarized (i.e., $Q = R = 2$).

IV. If $A = B = 0$ but $C = 3$ ($c_j = 1$, $c_i = 1$), as a result, light from the $S_{10}$, $S_{14}$ and $S_{28}$has been perpendicular polarized. The final results are both straight and perpendicular polarized (i.e., $Q = R = 3$).

V. If $A = C = 0$ but $B = 1$ (i.e., $b_j = 0$, $b_i = 1$), as a result, no light comes out from the $S_6$, $S_{10}$ and $S_{14}$ but the output of $S_{20}$ is perpendicular polarized and the output, Q, is zero (i.e., $Q = 0$) but the output, R, is perpendicular polarized (i.e., $R = 1$). If $A = 0$ and $B = C = 1$, then the output of $S_{10}$is perpendicular polarized but no light comes out from the $S_{20,}$ $S_{24}$ and $S_{28}$. So the output, Q, is perpendicular polarized (i.e., $Q = 1$), and the output, R, will be zero (i.e., $R = 0$).

VI. If $A = 0$, $B = 1$ and $C = 2$, as a result, the light that comes out from the $S_{10}$ and $S_{14}$is straight polarized, and output, Q, is straight polarized (i.e., $Q = 2$). But the output of $S_{20}$ is perpendicular polarized and the output of $S_{28}$is both perpendicular and straight polarized. So the output, R, will be both (perpendicular and straight) polarized (i.e., $R = 3$).

VII. If $A = 0$, $B = 1$ and $C = 3$, as a result, the light that comes as output from $S_{10}$is both (straight and perpendicular) polarized and the output of $S_{14}$ will be straight polarized. So the output, Q, will be both (perpendicular and straight) polarized (i.e., $Q = 3$). The output of $S_{28}$ will be straight polarized. So the output, R, will be straight polarized (i.e., $R = 2$).

**Table 4** The truth table of proposed new gate

| Inputs | | | | | | | | | Outputs | | | | | | | | |
|---|---|---|---|---|---|---|---|---|---|---|---|---|---|---|---|---|---|
| A | $a_i$ | $a_j$ | B | $b_i$ | $b_j$ | C | $c_i$ | $c_j$ | P | $p_i$ | $p_j$ | Q | $q_i$ | $q_j$ | R | $r_i$ | $r_j$ |
| 0 | 0 | 0 | 0 | 0 | 0 | 0 | 0 | 0 | 0 | 0 | 0 | 0 | 0 | 0 | 0 | 0 | 0 |
| 0 | 0 | 0 | 0 | 0 | 0 | 1 | 0 | 1 | 0 | 0 | 0 | 1 | 0 | 1 | 1 | 0 | 1 |
| 0 | 0 | 0 | 0 | 0 | 0 | 2 | 1 | 0 | 0 | 0 | 0 | 2 | 1 | 0 | 2 | 1 | 0 |
| 0 | 0 | 0 | 0 | 0 | 0 | 3 | 1 | 1 | 0 | 0 | 0 | 3 | 1 | 1 | 3 | 1 | 1 |
| 0 | 0 | 0 | 1 | 0 | 1 | 0 | 0 | 0 | 0 | 0 | 0 | 0 | 0 | 0 | 1 | 0 | 1 |
| 0 | 0 | 0 | 1 | 0 | 1 | 1 | 0 | 1 | 0 | 0 | 0 | 1 | 0 | 1 | 0 | 0 | 0 |
| 0 | 0 | 0 | 1 | 0 | 1 | 2 | 1 | 0 | 0 | 0 | 0 | 2 | 1 | 0 | 3 | 1 | 1 |
| 0 | 0 | 0 | 1 | 0 | 1 | 3 | 1 | 1 | 0 | 0 | 0 | 3 | 1 | 1 | 2 | 1 | 0 |
| 0 | 0 | 0 | 2 | 1 | 0 | 0 | 0 | 0 | 0 | 0 | 0 | 0 | 0 | 0 | 2 | 1 | 0 |
| 0 | 0 | 0 | 2 | 1 | 0 | 1 | 0 | 1 | 0 | 0 | 0 | 1 | 0 | 1 | 3 | 1 | 1 |
| 0 | 0 | 0 | 2 | 1 | 0 | 2 | 1 | 0 | 0 | 0 | 0 | 2 | 1 | 0 | 0 | 0 | 0 |
| 0 | 0 | 0 | 2 | 1 | 0 | 3 | 1 | 1 | 0 | 0 | 0 | 3 | 1 | 1 | 1 | 0 | 1 |
| 0 | 0 | 0 | 3 | 1 | 1 | 0 | 0 | 0 | 0 | 0 | 0 | 0 | 0 | 0 | 3 | 1 | 1 |
| 0 | 0 | 0 | 3 | 1 | 1 | 1 | 0 | 1 | 0 | 0 | 0 | 1 | 0 | 1 | 2 | 1 | 0 |
| 0 | 0 | 0 | 3 | 1 | 1 | 2 | 1 | 0 | 0 | 0 | 0 | 2 | 1 | 0 | 1 | 0 | 1 |
| 0 | 0 | 0 | 3 | 1 | 1 | 3 | 1 | 1 | 0 | 0 | 0 | 3 | 1 | 1 | 0 | 0 | 0 |
| 1 | 0 | 1 | 0 | 0 | 0 | 0 | 0 | 0 | 1 | 0 | 1 | 0 | 0 | 0 | 1 | 0 | 1 |
| 1 | 0 | 1 | 0 | 0 | 0 | 1 | 0 | 1 | 1 | 0 | 1 | 1 | 0 | 1 | 1 | 0 | 1 |
| 1 | 0 | 1 | 0 | 0 | 0 | 2 | 1 | 0 | 1 | 0 | 1 | 2 | 1 | 0 | 3 | 1 | 1 |
| 1 | 0 | 1 | 0 | 0 | 0 | 3 | 1 | 1 | 1 | 0 | 1 | 3 | 1 | 1 | 3 | 1 | 1 |
| 1 | 0 | 1 | 1 | 0 | 1 | 0 | 0 | 0 | 1 | 0 | 1 | 1 | 0 | 1 | 0 | 0 | 0 |
| 1 | 0 | 1 | 1 | 0 | 1 | 1 | 0 | 1 | 1 | 0 | 1 | 0 | 0 | 0 | 0 | 0 | 0 |
| 1 | 0 | 1 | 1 | 0 | 1 | 2 | 1 | 0 | 1 | 0 | 1 | 3 | 1 | 1 | 2 | 1 | 0 |
| 1 | 0 | 1 | 1 | 0 | 1 | 3 | 1 | 1 | 1 | 0 | 1 | 2 | 1 | 0 | 2 | 1 | 0 |
| 1 | 0 | 1 | 2 | 1 | 0 | 0 | 0 | 0 | 1 | 0 | 1 | 0 | 0 | 0 | 3 | 1 | 1 |
| 1 | 0 | 1 | 2 | 1 | 0 | 1 | 0 | 1 | 1 | 0 | 1 | 1 | 0 | 1 | 3 | 1 | 1 |
| 1 | 0 | 1 | 2 | 1 | 0 | 2 | 1 | 0 | 1 | 0 | 1 | 2 | 1 | 0 | 1 | 0 | 1 |
| 1 | 0 | 1 | 2 | 1 | 0 | 3 | 1 | 1 | 1 | 0 | 1 | 3 | 1 | 1 | 1 | 0 | 1 |
| 1 | 0 | 1 | 3 | 1 | 1 | 0 | 0 | 0 | 1 | 0 | 1 | 1 | 0 | 1 | 2 | 1 | 0 |
| 1 | 0 | 1 | 3 | 1 | 1 | 1 | 0 | 1 | 1 | 0 | 1 | 0 | 0 | 0 | 2 | 1 | 0 |
| 1 | 0 | 1 | 3 | 1 | 1 | 2 | 1 | 0 | 1 | 0 | 1 | 3 | 1 | 1 | 0 | 0 | 0 |
| 1 | 0 | 1 | 3 | 1 | 1 | 3 | 1 | 1 | 1 | 0 | 1 | 2 | 1 | 0 | 0 | 0 | 0 |
| 2 | 1 | 0 | 0 | 0 | 0 | 0 | 0 | 0 | 2 | 1 | 0 | 0 | 0 | 0 | 2 | 1 | 0 |
| 2 | 1 | 0 | 0 | 0 | 0 | 1 | 0 | 1 | 2 | 1 | 0 | 1 | 0 | 1 | 3 | 1 | 1 |
| 2 | 1 | 0 | 0 | 0 | 0 | 2 | 1 | 0 | 2 | 1 | 0 | 2 | 1 | 0 | 2 | 1 | 0 |

(continued)

**Table 4** (continued)

| Inputs | | | | | | | | | Outputs | | | | | | | | |
|---|---|---|---|---|---|---|---|---|---|---|---|---|---|---|---|---|---|
| A | $a_i$ | $a_j$ | B | $b_i$ | $b_j$ | C | $c_i$ | $c_j$ | P | $p_i$ | $p_j$ | Q | $q_i$ | $q_j$ | R | $r_i$ | $r_j$ |
| 2 | 1 | 0 | 0 | 0 | 0 | 3 | 1 | 1 | 2 | 1 | 0 | 3 | 1 | 1 | 3 | 1 | 1 |
| 2 | 1 | 0 | 1 | 0 | 1 | 0 | 0 | 0 | 2 | 1 | 0 | 0 | 0 | 0 | 3 | 1 | 1 |
| 2 | 1 | 0 | 1 | 0 | 1 | 1 | 0 | 1 | 2 | 1 | 0 | 1 | 0 | 1 | 2 | 1 | 0 |
| 2 | 1 | 0 | 1 | 0 | 1 | 2 | 1 | 0 | 2 | 1 | 0 | 2 | 1 | 0 | 3 | 1 | 1 |
| 2 | 1 | 0 | 1 | 0 | 1 | 3 | 1 | 1 | 2 | 1 | 0 | 3 | 1 | 1 | 2 | 1 | 0 |
| 2 | 1 | 0 | 2 | 1 | 0 | 0 | 0 | 0 | 2 | 1 | 0 | 2 | 1 | 0 | 0 | 0 | 0 |
| 2 | 1 | 0 | 2 | 1 | 0 | 1 | 0 | 1 | 2 | 1 | 0 | 3 | 1 | 1 | 1 | 0 | 1 |
| 2 | 1 | 0 | 2 | 1 | 0 | 2 | 1 | 0 | 2 | 1 | 0 | 0 | 0 | 0 | 0 | 0 | 0 |
| 2 | 1 | 0 | 2 | 1 | 0 | 3 | 1 | 1 | 2 | 1 | 0 | 1 | 0 | 1 | 1 | 0 | 1 |
| 2 | 1 | 0 | 3 | 1 | 1 | 0 | 0 | 0 | 2 | 1 | 0 | 2 | 1 | 0 | 1 | 0 | 1 |
| 2 | 1 | 0 | 3 | 1 | 1 | 1 | 0 | 1 | 2 | 1 | 0 | 3 | 1 | 1 | 0 | 0 | 0 |
| 2 | 1 | 0 | 3 | 1 | 1 | 2 | 1 | 0 | 2 | 1 | 0 | 0 | 0 | 0 | 1 | 0 | 1 |
| 2 | 1 | 0 | 3 | 1 | 1 | 3 | 1 | 1 | 2 | 1 | 0 | 1 | 0 | 1 | 0 | 0 | 0 |
| 3 | 1 | 1 | 0 | 0 | 0 | 0 | 0 | 0 | 3 | 1 | 1 | 0 | 0 | 0 | 3 | 1 | 1 |
| 3 | 1 | 1 | 0 | 0 | 0 | 1 | 0 | 1 | 3 | 1 | 1 | 1 | 0 | 1 | 3 | 1 | 1 |
| 3 | 1 | 1 | 0 | 0 | 0 | 2 | 1 | 0 | 3 | 1 | 1 | 2 | 1 | 0 | 3 | 1 | 1 |
| 3 | 1 | 1 | 0 | 0 | 0 | 3 | 1 | 1 | 3 | 1 | 1 | 3 | 1 | 1 | 3 | 1 | 1 |
| 3 | 1 | 1 | 1 | 0 | 1 | 0 | 0 | 0 | 3 | 1 | 1 | 1 | 0 | 1 | 2 | 1 | 0 |
| 3 | 1 | 1 | 1 | 0 | 1 | 1 | 0 | 1 | 3 | 1 | 1 | 0 | 0 | 0 | 2 | 1 | 0 |
| 3 | 1 | 1 | 1 | 0 | 1 | 2 | 1 | 0 | 3 | 1 | 1 | 3 | 1 | 1 | 2 | 1 | 0 |
| 3 | 1 | 1 | 1 | 0 | 1 | 3 | 1 | 1 | 3 | 1 | 1 | 2 | 1 | 0 | 2 | 1 | 0 |
| 3 | 1 | 1 | 2 | 1 | 0 | 0 | 0 | 0 | 3 | 1 | 1 | 2 | 1 | 0 | 1 | 0 | 1 |
| 3 | 1 | 1 | 2 | 1 | 0 | 1 | 0 | 1 | 3 | 1 | 1 | 3 | 1 | 1 | 1 | 0 | 1 |
| 3 | 1 | 1 | 2 | 1 | 0 | 2 | 1 | 0 | 3 | 1 | 1 | 0 | 0 | 0 | 1 | 0 | 1 |
| 3 | 1 | 1 | 2 | 1 | 0 | 3 | 1 | 1 | 3 | 1 | 1 | 1 | 0 | 1 | 1 | 0 | 1 |
| 3 | 1 | 1 | 3 | 1 | 1 | 0 | 0 | 0 | 3 | 1 | 1 | 3 | 1 | 1 | 0 | 0 | 0 |
| 3 | 1 | 1 | 3 | 1 | 1 | 1 | 0 | 1 | 3 | 1 | 1 | 2 | 1 | 0 | 0 | 0 | 0 |
| 3 | 1 | 1 | 3 | 1 | 1 | 2 | 1 | 0 | 3 | 1 | 1 | 1 | 0 | 1 | 0 | 0 | 0 |
| 3 | 1 | 1 | 3 | 1 | 1 | 3 | 1 | 1 | 3 | 1 | 1 | 0 | 0 | 0 | 0 | 0 | 0 |

VIII. If $A = 0$, $B = 1$ and $C = 3$, then the output of $S_{10}$ will be both (perpendicular and straight) polarized, and the output of $S_{14}$is straight polarized. So the output, Q, will be both (straight and perpendicular) polarized (i.e., $Q = 3$). The output of $S_{28}$ will be straight polarized. So the output, R, will be straight polarized (i.e., $R = 2$).

IX. When $A = C = 0$ but $B = 2$(i.e ., $b_j = 1$, $b_i = 0$), then there will be no light at the output of $S_6$, $S_{10}$, $S_{14}$ but the output of $S_{20}$ will be horizontally

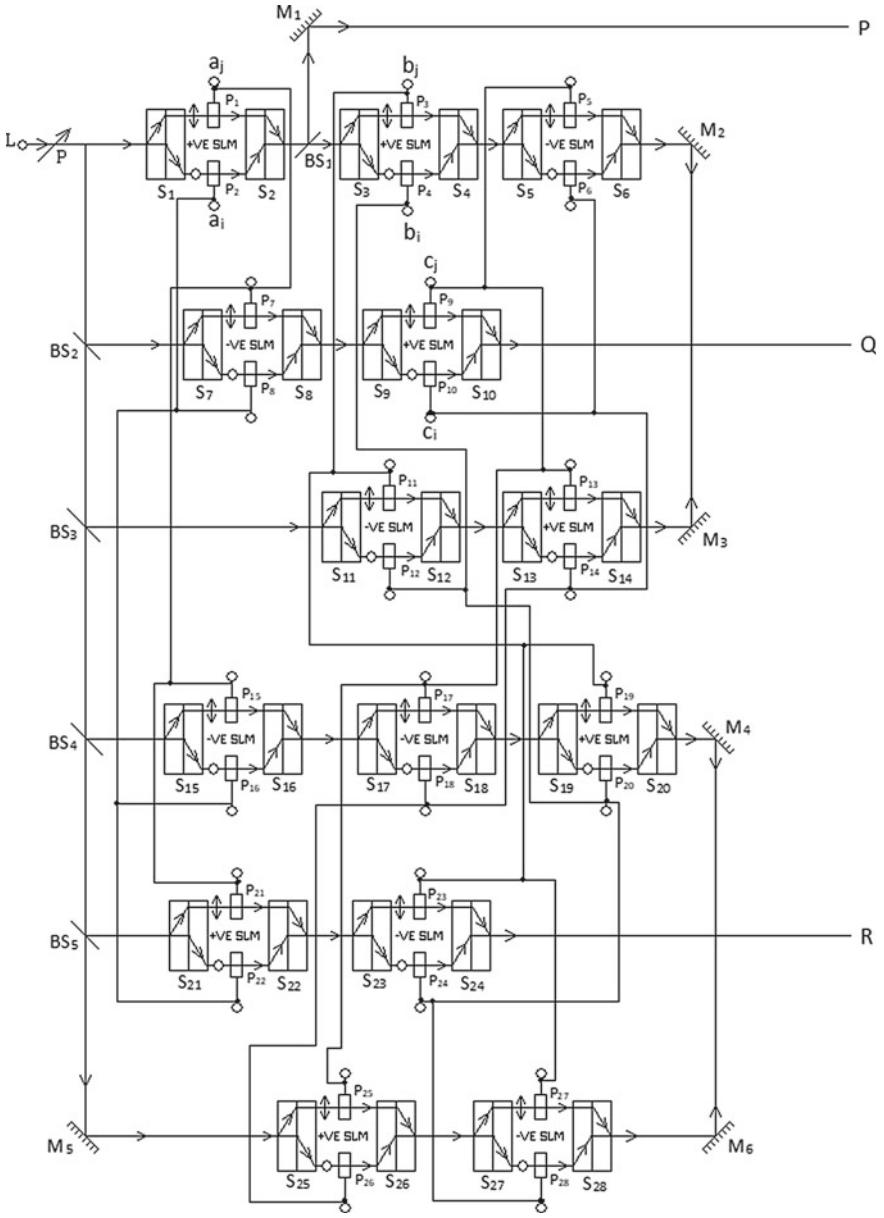


**Fig. 4** Circuit diagram of New proposed Gate

polarized. So the output, Q, will be zero (i.e., Q = 0) but the output, R, will be horizontally polarized (i.e., R = 2).

X. If A = 0, B = 2 and C = 1, then as a result, the output of $S_{10}$ and $S_{14}$ has been vertically polarized and output, Q, has been vertically polarized (i.e., Q = 1). But the output of $S_{20}$ has been horizontally polarized and the output of $S_{28}$ is vertically polarized simultaneously and output, R, has been vertically and horizontally polarized (i.e., R = 3).

XI. If A = 0, B = 2 and C = 2, then the output of the $S_{10}$ and $S_{14}$ has been horizontal polarized. As a result, the output Q is horizontally polarized (i.e., Q = 2). For this reason, there is no light at the output of $S_{20}$, $S_{24}$ and $S_{28}$. The output of R is zero (i.e., R = 0).

XII. If A = 0, B = 2 and C = 3, then the output of $S_{14}$ and $S_{10}$ is both vertically and horizontally polarized. So the output Q is both horizontally and vertically polarized (i.e., Q = 3). The Output of R is vertical polarized (i.e., R = 1).

Thus, the process will go on and the symmetrical results will be achieved for 64 steps of the new proposed gate.

## 6 Simulations and Results

Simulation is performed under Mathcad-7 and outputs are shown in Fig. 5 taking the different parameter values same as used in Chapter 2. Other constraints set in this experiment are the power of the input signals is taken as A = 1.13 dBm, B = 2.26 dBm and C = 1.13 dBm. In these experiments, 50:50 beam splitters were used.

The perpendicular orbit shown in Fig. 5 alludes to power in dBm, while straight orbit performs time scale in ps. The timing instances for the occurrence of the bit pattern are at 0, 5, 10, 15, 20, 25, 30 and 35 ps. In Fig. 5, the upper three sets of waveforms indicate the input bit sequences, 00001111, 00110011 and 01010101 for the input parameters of A, B and C, respectively.

## 7 Conclusion

This paper deals with the design of an optical quadruple Peres Gate circuit based on SLM and Savart Plate. The developed theoretical models are very much useful for the optical reversible logic computing system. This gate can be used to perform different logical and arithmetic operations in the reversible domain. This paper has presented and explored the quadruple logic system in four-state implementation which can process more information at a time. In the future, this gate can be used for the realization of various Boolean expressions in the form of system design, implementations and arithmetic operations of digital circuits.

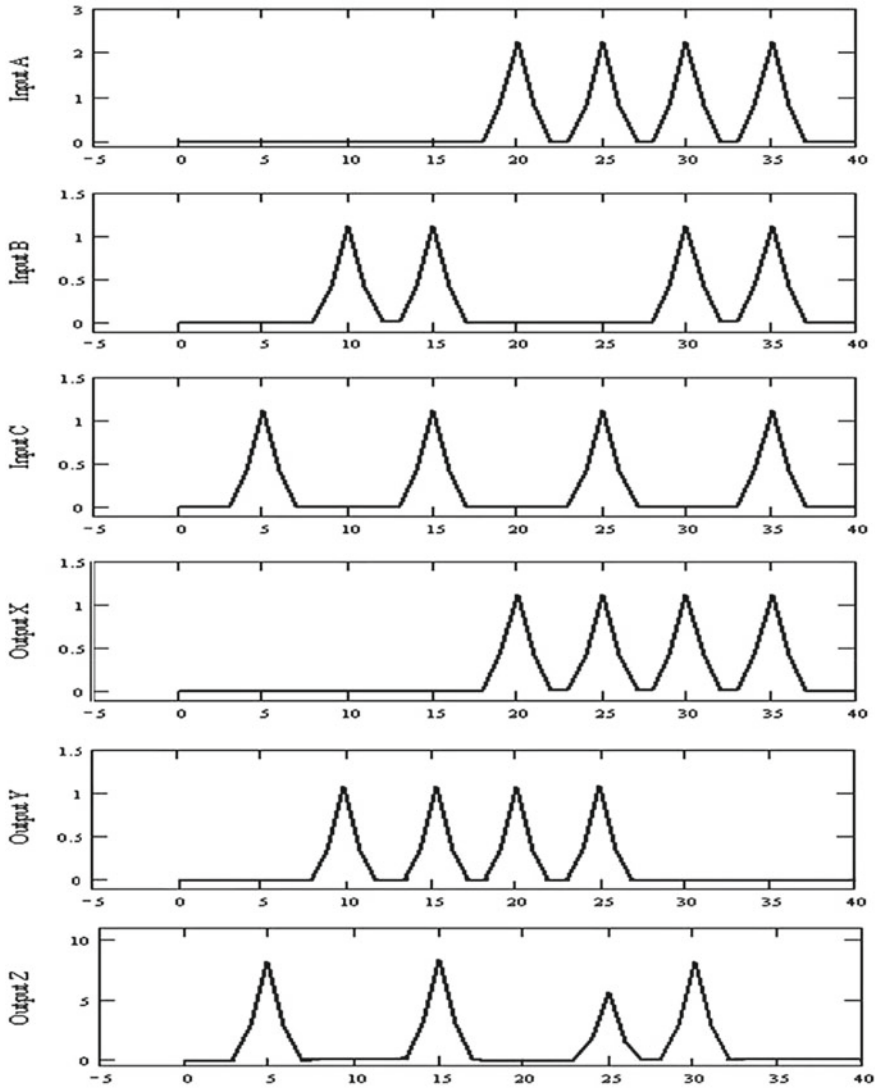


**Fig. 5** Simulation result of Fig. 4: [x-axis: Time (ps) and y-axis: Power (dBm)]

## References

1. E.V. Dubrova, *Multiple-Valued Logic in VLSI Design, Electronic System Design.* (Royal Institute of Technology, Sweden)
2. S. Liu, C. Li, J. Wu, Y. Liu, Optoelectronic multiple-valued logic implementation. Optics Lett. **14**(14), 713–715 (1989)
3. P. Ghosh, S. Mukhopadhyay, Implementation of tristate logic based all optical flip-flop with nonlinear material. Chin. Opt. Lett. **3**(8), 478–479 (2005)

4. T. Chattopadhyay, G.K. Maity, J.N. Roy, Designing of all-optical Tri-state Logic system withthehelpofopticalnonlinearmaterial. J. Nonlinear Optical Phys. Mater. World Sci. **17**(3), 315–328 (2008)
5. K.S.V. Patel, K.S. Gurumurthy, Arithmetic operation in multi valued logic. Int. J. VLSI Design Commun. Syst. (VLSICS) **1**(1) (2010)
6. A.W. Lohmann, Polarization and opticallogic. Appl. Opt. **25**, pp. 1594–1597 (1986)
7. T. Chattopadhyaya, J.N. Roy, All-optical conversion scheme: Binary to quaternary and quaternary to binary number. Optics Laser Technol **41**, 289–294 (2009)
8. A .Avizienis, Signed-digit number representation for fast parallel arithmetic. IRE Trans. Electron. Comp. EC-10, pp. 389–400 (1961)
9. B.L.Drake, R.P.Bocker,M.E.Lasher, R.H.Patterson, W.J.Miceli, Photonic computing using the modified-signed-digit number representation. Opt. Eng. **25**, 38–43 (1986)
10. R.P. Bocker, B.L. Drake, M.E. Lasher, T.B. Henderson, Modified signed-digit addition and subtraction using optical symbolic substitution. Appl. Opt. **25**(15), 2456–2457 (1986)
11. A.K. Cherri, M.A. Karim, Modified signed digit arithmetic using an efficient symbolic substitution. Appl. Opt. **27**(18), 3824–3827 (1988)
12. A.K. Ghosh, P.P. Choudhury, A. Basuray, Modified Trinary Optical Logic Gates and their Applications in Optical Computation, Innovations and Advanced Techniques in Systems, Computing Sciences and Software (Springer, 2008) pp. 87–92

# Design and Analysis of Asymmetric Cantilever Type Shunt Switch for L Band Applications


**Ch. Gopi Chand, Reshmi Maity, K. Girija Sravani, N. P. Maity, Koushik Guha, and K. Srinivasa Rao**

## 1 Introduction

RF-MEMS is a new technology that ensures the opportunity to revolutionize the introduction of radio-frequency and telecommunication applications [1]. MEMS technology allows the implementation of radio-frequency passive components with low losses, miniature size, huge customizable characteristics, and high linearity compared to an ordinary passive semiconductor [2]. RF-MEMS devices involve shifting capacitor MEMS, tunable MEMS Inductors, and RF-MEMS Switches. Over the past few years, MEMS switches designed to operate on radio frequencies should be the topic of active research, both in academia and in industrial organizations [3]. The MEMS devices are having low power consumption, best radio-frequency characteristics, wide tuning range, and combination capabilities which are important features that enable the implementation of a system with inherent developments in the area, value, and advanced functionality. The reliability of MEMS technology is important for industrial applications and a modern problem of intensive work [4]. RF-MEMS switch hass elevated potential and possibility to integrate into low and medium power applications as a replacement for modern switching technology, and potential for creating very flexible RF systems [5, 6]. The RF-MEMS switches are widely utilized in broadcast systems for routing the signal, and also the antenna signal is switching which enables to transmit and receive. MEMS Switches show more reliable performance than traditional semiconductor switches [7–9]. Though,

Ch. Gopi Chand (✉) · R. Maity · N. P. Maity
Department of ECE, Mizoram University, Aizawl, Mizoram 796004, India

K. G. Sravani · K. S. Rao
Department of ECE, Koneru Lakshmaiah Education Foundation, Vaddeswaram, Guntur, Andhra Pradesh 522502, India
e-mail: drksrao@kluniversity.in

K. G. Sravani · K. Guha
Department of ECE, National Institute of Technology, Silchar 788010, India



C. K. Chanda et al. (eds.), *Advanced Energy and Control Systems*, Lecture Notes in Electrical Engineering 820, https://doi.org/10.1007/978-981-16-7274-3_20

the view is further accompanied by any tradeoffs or defects in the micro-switches correlated over the solid-state outcomes [10–13]. The MEMS is currently growing more familiar with Radiofrequency uses owing to its engaging benefits, like low insertion loss and return loss.

This paper is formed as follows. In Sect. 2, the proposed switches and their dimensions are explained. In Sect. 3, results and discussions are given, and we have observed the analysis of theoretical calculations and simulation results, and finally, we concluded the paper in Sect. 4.

## 2 Structure of the Proposed Device

Here, we are considering a very simple RF-MEMS cantilever type capacitive shunt including electrostatic actuation to the proposed device. Consider these switches implemented in Au, Ti, and Al, and also analyse the characteristics of each of the specific metals as the material of the beam. The switch was analysed using electromechanical analysis between electrodes and membrane materials [14–20]. The switch was designed over substrate silicon semiconductor material. An oxide layer is located among the signal line and the substrate having a dielectric constant of 11.9 to overcome the DC losses. The device consists of two cantilever beams, such as the left and right beams along with meanders, end with fixed anchors, and the overall beam is placed on the upper part of the CPW as shown in Fig. 1.

For a good association between the cantilever and the signal line, the electrostatic force is utilized. The holes and meanders are used to reduce the minimum voltage, and also, to discharge the stiction obstacle among the lower cantilever beam and the electrode, a small layer $Si_3N_4$ is utilized to spread the electrode. Typically, these switches occur in the construction of deferred micro-cantilevers. The second type of non-uniform meander switch was designed as shown in Fig. 2.

A series of perforations are formed above the lower beam to decrease the damping of the compressed layer. The dielectric sheet is located above the signal line, which


**Fig. 1.** 3D view of uniform meander type switch

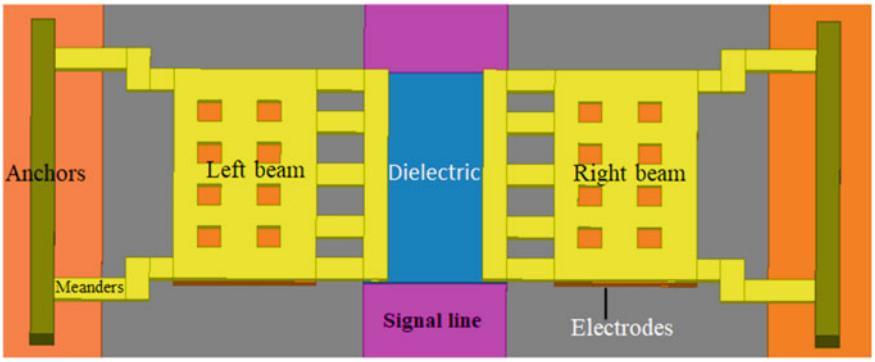


**Fig. 2** Top view of non-uniform type switch

makes a capacitance between them. The physics behind the electrostatic actuation is only the electrostatic force of attraction between the two parallel plates having opposing charges.

When a DC voltage is employed between the top and bottom electrodes, the beam touches the substrate due to electrostatic excitation. The device specifications are signify given in Table 1.

**Table 1** Specifications of the device

| Sl. no | Structural component | Length (μm) | Width (μm) | Height (μm) | Material |
|---|---|---|---|---|---|
| 1 | Substrate | 500 | 300 | 150 | Silicon |
| 2 | Ground | 150 | 300 | 2 | Gold |
| 3 | Right beam | 50 | 80 | 1.5 | Gold |
| 4 | Left beam | 50 | 80 | 1.5 | Gold |
| 5 | Cantilever blocks | 20 | 80 | 1.5 | Gold |
| 6 | Signal line | 70 | 300 | 1.5 | Gold |
| 7 | Perforation | 10 | 10 | 1.5 | – |
| 8 | Single meanders | 80 | 10 | 1.5 | Gold |
| 9 | Non-uniform meanders (1,2,3) | 10 | 10 | 1.5 | Gold |
| | | 10 | 20 | 1.5 | |
| | | 30 | 10 | 1.5 | |

## 3 Results and Discussions

### 3.1 A Spring Constant

The cantilever width has a direct impact on the spring rate and must be large adequate to provide a high MEMS beam rigidity. It depends on the meanders and area of the beam, thickness, and material properties like Young's modulus. Mainly, it means the stiffness of the switch. The specific equation is theoretically [21–23]

$$K = 3\frac{EI}{l^3} = \frac{EW}{4}\left(\frac{t}{l}\right)^3 \tag{1}$$

where E-Young's Modulus, 't'—thickness, and l—length of the beam, In this 'I' is the movement of inertia.

### 3.2 Actuation Voltage

When a bias charge is utilized over a pair of DC electrodes, the connection terminal moves down through the caused electrostatic force. The left and right beams are actuated and show the displacement for the supply voltage. The operating voltage depends on the spring constant and beam area [24–26].

$$V_P = \sqrt{\frac{8Kg_0^3}{27\varepsilon_0 A}} \tag{2}$$

where K-Spring constant, $g_0$—the gap between dielectric and beam, $\varepsilon_0$-Permittivity of free space, and A—actuated area. The simulation and graphical representation of prosed switch are as shown in Figs. 3 and 4.

### 3.3 Capacitance Analysis

When increasing the voltage source, the height will be reduced, and therefore, the capacitance, charge, and electric field are improved. The capacitance is depending on the switch ON and OFF conditions, and also dielectric material and thickness.

The upstate capacitance is calculated by using the following equation:

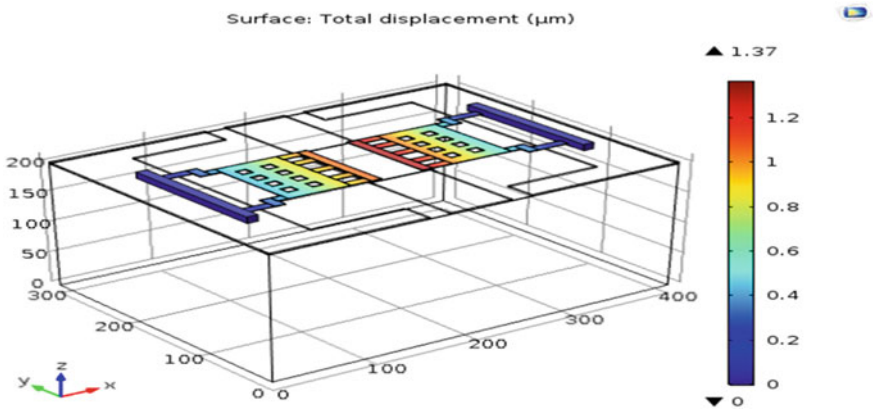


**Fig. 3** Displacement of non-uniform meander switch

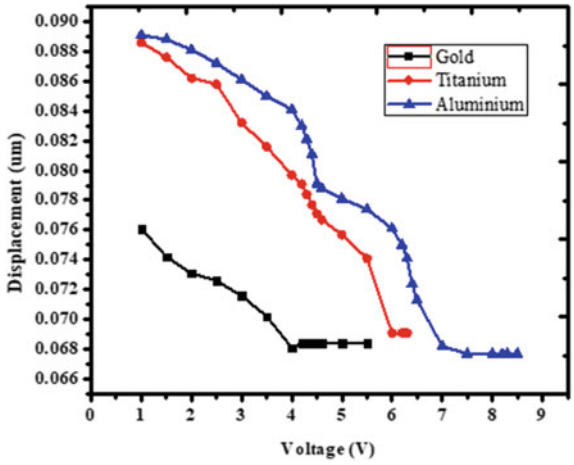


**Fig. 4** A graph view of second switch (non-uniform) voltages versus displacement

$$C_u = \frac{\varepsilon_0 A}{g_0 + \frac{t_d}{\varepsilon_r}} \tag{3}$$

where '$t_d$' is height, '$\varepsilon_r$' is permittivity, and 'A' implies the area between the actuation electrodes. The upstate capacitance is 5.42 and 8.26 fF (Fig. 5).

When there is no signal passed in that time, the downstate capacitance is generated, and also isolation is developed. In the down position, a capacitive switch drives to capacitance, while an ohmic switch leads to a junction resistance Rc and constant capacitance, which communicates to the aspired mode of operation. It is determined by the following equation:

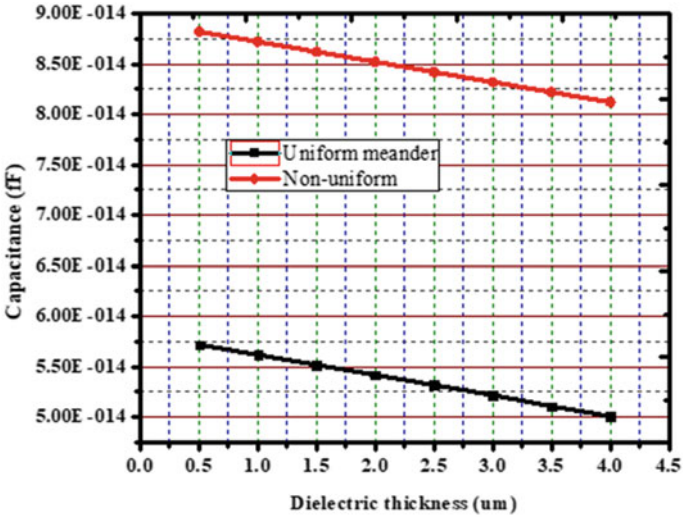


**Fig. 5** Upstate capacitance versus dielectric thickness for uniform meander switch

$$C_d = \frac{\varepsilon_0 \varepsilon_r A}{t_d} \tag{4}$$

The downstate analysis of the two switches is 3.68 and 6.43 pF.

## *3.4 Switching Time Analysis*

It is the time claimed to achieve pull-down, and the beam touches the bottom of the electrode. It depends on the supply voltage.

It is calculated by

$$t_{pull-down} = 3.67 \frac{V_{pull-down}}{V_s} \sqrt{\frac{m}{k}} \tag{5}$$

Here, K—spring constant, m—mass, and $V_s$—supply voltage.

The range of MEMS switches switching time is 1–300 μs. Figure 6 illustrates the switching time at different actuation voltages with both switches. The switching time is 9 and 12 μs.

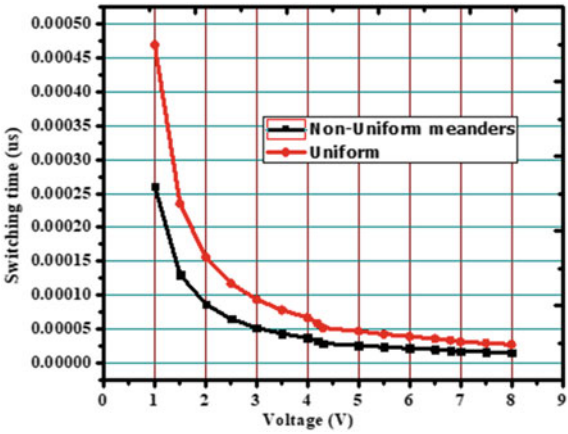


**Fig. 6** Switching time versus supply voltage for two switches

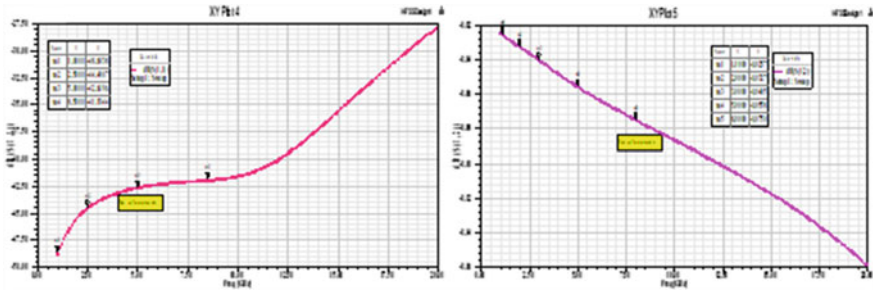

**Fig. 7** Measured return and insertion loss of non-uniform meander switch

## *3.5 RF-Performance Analysis*

The RF-performance is the foremost segment for obeying performance in a higher frequency range. The S-parameters are observed by using Electromagnetic analysis in HFSS software [27–30].

When one side cantilever switch is in an upstate while the shunt switches are in the downstate, in the cantilever type switch is down condition, the isolation was determined as −40.47 dB and −46.182 dB at 1–3 GHz, respectively. The switch exhibits return losses which are −36.24 dB and −48.69 and insertion losses are −0.057 and 0.0327 at 2–2.5 GHz. The results of the circuit simulation showed excellent assent with the computation result as shown in Figs. 7 and 8 (Table 2).

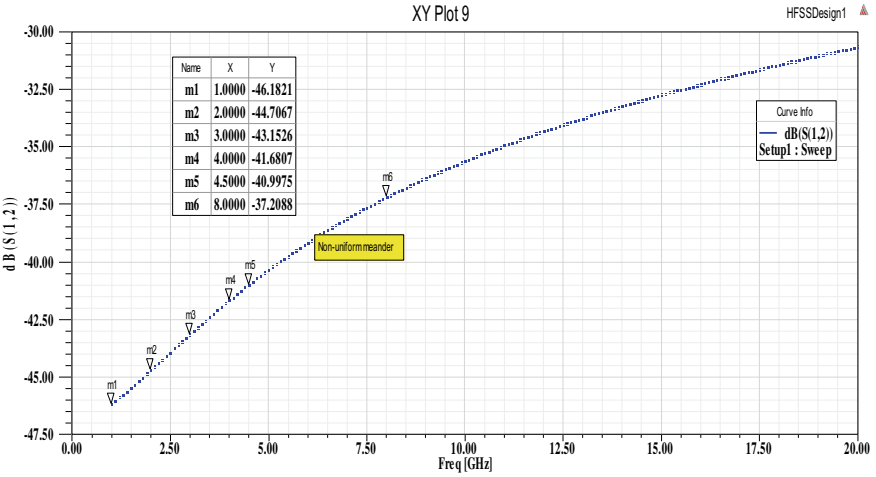


**Fig. 8** Isolation measured at 1 GHz frequency of the proposed device

**Table 2** Comparison of the proposed switch with existing work

| Parameters | Reference [6] | Reference [10] | Uniform meander switch | Non-uniform meander switch |
|---|---|---|---|---|
| Pull-in voltage | 18 V | 20 V | 6.8 V | 4.3 V |
| Return loss | −12 dB | −20 dB | −36.24 dB @ 1 GHz | −48.69 dB @1 GHz |
| Insertion | −0.92 dB | −0.9 dB | −0.0576 dB @ 2.5 GHz | −0.327 dB @2 GHz |
| Isolation loss | −29 dB | 14 dB | −40.473 dB @ 1 GHz | −46.182 dB @1 GHz |
| Switching time | – | 3 μs | 9 μs | 12 μs |
| Up-capacitance | – | 0.1–0.13 fF | 5.42 fF | 8.26 fF |
| Down-capacitance | – | 1.6–2 pF | 3.68 pF | 6.43 pF |

## 4 Conclusion

In this paper, an Asymmetric Cantilever type RF-MEMS shunt switch was presented. The proposed switch had non-uniform and uniform type meanders along with the perforations, which were used to decrease the actuation voltage. The non-uniform meander type switch obtained pull-in voltage is 4.3 V by compared uniform meander. The capacitance analysis and resonance frequency are evaluated. The electromagnetic simulations are done through HFSS software, return and insertion losses are having −48.69 dB and −0.032 dB and exhibit good isolation of −46.182 dB near

1–3 GHz frequency. So, this switch can be applicable in low-frequency L band and satellite applications.

**Acknowledgements** The authors are thankful to National MEMS Design Centre, NIT Silchar, Assam, for providing essential Finite Element Modelling tools.

## References

1. C.L. Goldsmith, Z. Yao, S. Eshelman, D Denniston, Performance of low-loss RF MEMS capacitive switches. IEEE Microw Guided Wave Lett. **8**(8), 269–271 (1998)
2. G.M. Rebeiz, *RF MEMS: Theory, Design, and Technology* (John Wiley & Sons, 2004)
3. D.R. Shah, R. Sharma, H.K. Varshney, S. Parveen, A. Akhtar, Study of RF-MEMS capacitive shunt switch for microwave backhaul applications. J. Electron. Commun. Eng. **12**(1), 57–65 (2017)
4. P.A. Kumar, K. Girija Sravani, B.V.S. Sailaja, K.V. Vineetha, K. Guha, K. Srinivasa Rao, Performance analysis of series: shunt configuration based RF MEMS switch for satellite communication applications. Microsyst. Technol. **24**(12), 4909–4920 (2018)
5. C.-H. Chu, W.-P. Shih, S.-Y. Chung, H.-C. Tsai, T.-K. Shing, P.-Z. Chang, A low actuation voltage electrostatic actuator for RF MEMS switch applications. J. Micromech. Microeng. **17**(8), 1649 (2007)
6. L. Muhua, J. Zhao, Z. You, G. Zhao, Design and experimental validation of a restoring force enhanced RF MEMS capacitive switch with Stiction-recovery electrodes. Microsyst. Technol. **23**(8), 3091_3096 (2017)
7. T. Singh, N. Khaira, High isolation single-pole four-throw RF MEMS switch based on series-shunt configuration. Sci. World J. (2014)
8. K.S. Rao, P.S. Mounika, P. Pavan, V. Guru, N. Dinesh, P. Ashok Kumar, K. Vineetha, K. Girija Sravani, Design, simulation and analysis of RF-MEMS shunt capacitive switch for 5G application. Microsyst. Technol. **25**(11), 4197–4208 (2019)
9. J. Sam, J. Kumar, E.A. Tetteh, E.P. Braineard, A study of why electrostatic actuation is preferred and a simulation of an electrostatically actuated cantilever beam for mems applications (2014)
10. Y. Mafinejad, A. Kouzani, Low insertion loss and high isolation capacitive RF MEMS switch with low pull-in voltage. Int. J. Adv. Manuf. Technol. (2017)
11. Y.-W. Yu, J. Zhu, S.-X. Jia, Yi. Shi, A high isolation series-shunt RF MEMS switch. Sensors **9**(6), 4455–4464 (2009)
12. M. Angira, K. Rangra, Performance improvement of RF-MEMS capacitive switch via asymmetric structure design. Microsyst. Technol. **21**(7), 1447–1452 (2015)
13. W.-B. Zheng, Q.-A. Huang, X.-P. Liao, F.-X. Li, RF MEMS membrane switches on GaAs substrates for X-band applications. J. Microelectromech. Syst. **14**(3), 464–471 (2005)
14. E.A. Savin, K.A. Chadin, R.V. Kirtaev, Design and manufacturing of X-band RF MEMS switches. Microsyst. Technol. **24**(6), 2783–2788 (2018)
15. A. Ziaei, S. Bansropun, P. Martins, M. Le Baillif, Fast high power capacitive RF-MEMS switch for X-Band applications.“ In *2015 45th European Solid State Device Research Conference (ESSDERC)*, (IEEE) pp. 153–155 (2015)
16. A.K. Ravirala, L.K. Bethapudi, J. Kommareddy, B.S. Thommandru, S. Jasti, P.R. Gorantla, A. Puli, G.S. Karumuri, S.R. Karumuri, Design and performance analysis of uniform meander structured RF MEMS capacitive shunt switch along with perforations. Microsys. Technol. **24**(2), 901–908 (2018)
17. T. Lakshmi Narayana, K. Girija Sravani, K. Srinivasa Rao, A micro level electrostatically actuated cantilever and metal contact based series RF MEMS switch for multi-band applications. Cogent Eng. **4**(1), 1323367 (2017)

18. K. Girija Sravani, G. Sudheer Babu, M. Ramesh, V. Prudhvi Raj, D. Prathyusha, K. Srinivasa Rao, Beam and dielectric materials impact on improvement of the performance of a novel capacitive shunt RF MEMS switch. Int. J. Numer. Model. Electron. Netw. Dev. Fields **32**(5), e2598 (2019)
19. K.S. Rao, C. Gopi Chand, K. Girija Sravani, D. Prathyusha, P. Naveena, G. Sai Lakshmi, P. Ashok Kumar, T. Lakshmi Narayana, Design, modeling and analysis of perforated RF MEMS capacitive shunt switch. IEEE Access 7, 74869–74878 (2019)
20. K.G. Sravani, D. Prathyusha, K. Srinivasa Rao, P. Ashok Kumar, G. Sai Lakshmi, C. Gopi Chand, P. Naveena, L.N. Thalluri, K. Guha, Design and performance analysis of low pull-in voltage of dimple type capacitive RF MEMS shunt switch for Ka-Band. IEEE Access **7**, 44471–44488 (2019)
21. A. Susmitha, T. Sravani, B. Yogitha, G. Keerthika, M. Sonali, P.A. Kumar, K.G. Sravani, K.S. Rao, Design and simulation of a MIM capacitor type RF MEMS switch for surface radar application. In *Microelectronics, Electromagnetics and Telecommunications.* (Springer, Singapore, 2019), pp. 443–452
22. K.S. Rao, P. Naveena, K.G. Sravani, Materials impact on the performance analysis and optimization of RF MEMS switch for 5G reconfigurable antenna. Trans. Electr. Electron. Mater. **20**(4), 315–327 (2019)
23. K.G. Sravani, K. Guha, K.S. Rao, Design and analysis of serpentine flexure based RF MEMS switch for high isolation with low pull-in voltage. Trans. Electr. Electron. Mater. **20**(2), 154–164 (2019)
24. K.S. Rao, P. Naveena, T.A. Swamy, P.A. Kumar, K. Guha, K.G. Sravani, Design and performance analysis of self-similar reconfigurable antenna by cantilever type RF MEMS switch. Microsyst. Technol. 1–12 (2019)
25. K.G. Sravani, T.L. Narayana, K. Guha, K.S. Rao, Role of dielectric layer and beam membrane in improving the performance of capacitive RF MEMS switches for Ka-band applications. Microsyst. Technol. 1–10 (2018)
26. K.G. Sravani, K. Guha, K.S. Rao, Analysis on selection of beam material for novel step structured RF-MEMS switch used for satellite communication applications. Trans. Electr. Electron. Mater. **19**(6), 467–474 (2018)
27. P.A. Kumar, K.S. Rao, K.G. Sravani, Design and simulation of millimeter wave reconfigurable antenna using iterative meandered RF MEMS switch for 5G mobile communications. Microsyst. Technol. 1–11 (2019)
28. K.G. Sravani, K. Srinivasa Rao. Analysis of RF MEMS shunt capacitive switch with uniform and non-uniform meanders. Microsyst. Technol. **24**(2), 1309–1315 (2018)
29. T.M. Vu, G. Prigent, J. Ruan, R. Plana, Design and fabrication of RF-MEMS switch for V-band reconfigurable application.“ Progress Electromagn. Res. **39**, 301–318 (2012)
30. K.S. Rao, L.N. Thalluri, K. Guha, K.G. Sravani, Fabrication and characterization of capacitive RF MEMS perforated switch. IEEE Access **6**, 77519–77528 (2018)

# Substrate Integrated Waveguide (SIW)-Based Filter for Ka Band Applications


**P. S. Ganaraj, Koushik Guha, and M. Kavicharan**

## 1 Introduction

Lately, the evolution in millimeter wave wireless communication has led to the development of low loss and miniature systems. The commercial 5G mobile communication is expected to provide a high data rate and large capacity compared to that of the present-day communication system. The commercial use of 5G has been deployed in countries like China, US, and European countries. Some countries are in the trial/testing and research/development phase. Thus, there is a lot of scope for improvement in the performance in Millimeter wave range of 5G [1]. The Millimeter waves are electromagnetic waves ranging from 30–300 GHz. The 3GPP which develop protocols for mobile communication has been proposed for two frequency band ranges for 5G communication, i.e. in the Frequency range 1(FR1), a sub 6 GHz range, and Frequency range 2(FR2) between the range 24.5–29.5 GHz and 37–40 GHz which is in millimeter wave Ka band range. Thus, there is a need for an advanced receiver, which would have a tunable filter that would facilitate large bandwidth with low insertion loss.

The tunable filters should have reduced insertion loss, have better stopband performance, and lesser footprint compared to the present counterparts. These tunable filters can be found in applications such as Mobile communication, RADAR, Air traffic control, and Satellite communication. The losses that occur in the filter include conduction loss, transmission loss, and dielectric loss. Tunable filters designed over

P. S. Ganaraj (✉)
KIIT Deemed to be University, Bhubaneswar 751024, India
e-mail: ganaraj.psfet@kiit.ac.in

K. Guha · M. Kavicharan
NIT Silchar, Silchar 788010, India
e-mail: koushik@ece.nits.ac.in

M. Kavicharan
e-mail: kavicharan@ece.nits.ac.in



C. K. Chanda et al. (eds.), *Advanced Energy and Control Systems*, Lecture Notes in Electrical Engineering 820, https://doi.org/10.1007/978-981-16-7274-3_21

the microstrip/stripline platform will produce an increase in a loss at the same time lower quality factor but have a low footprint. A waveguide offers very low loss and provides a high-quality factor also. But, the rectangular waveguide is bulky [2]. Substrate Integrated Waveguides (SIWs) have characteristics that are in between the microstrip or stripline and waveguide characteristics. SIWs bridge the technological gap between the microstrip or stripline and metallic waveguide [3]. Hence, Substrate Integrated waveguide is the best suitable platform over which tunable filters can be designed.

## 2 Design of Basic SIW Structure

The basic SIW structure has two metal layers forming the top and bottom layer and the dielectric material is embedded between them. A linear array of metallic vias are placed so as to connect the top and bottom layers. The SIW structures only support the $TE_{10}$ mode [4]. The width of SIW is based on the cutoff frequency. If periodicity between the two adjacent via is made large, the EM wave is not confined between the array of metallic via, leading to increased leakage loss. Design rules that need to be followed while designing SIW, in order to curtail the leakage loss and the Bandgap Effects over the entire bandwidth, are

$$d < \frac{\lambda_g}{5} \text{ and } d < p \leq 2d \text{ [5]} \tag{1}$$

where d is the diameter of metallic via, p is the periodicity between adjacent metallic vias, and $\lambda_g$ is the waveguide cutoff wavelength. The cutoff frequency of the SIW is calculated using

$$f_c = \frac{f_0}{1.5} \text{ and } a_{eff} = \frac{c}{2f_c\sqrt{\varepsilon_r}} \tag{2}$$

where $f_0$ is the centre frequency, $f_c$ is the cutoff frequency, and $a_{eff}$ is the effective width of SIW.

The Fig. 1 shows basic SIW structure having $a_{SIW}$ as the width of the SIW, d as the diameter of the metallic via, h as the height of the substrate whose dielectric coefficient is $\varepsilon_r$, and p is the pitch or the periodicity between two adjacent metallic vias. The choice of $\varepsilon_r$ plays a crucial role in deciding the size of the structure. If the $\varepsilon_r$ chosen is a higher value, there is a reduction in size. But, there is a compromise over the power handling capability of the structure.

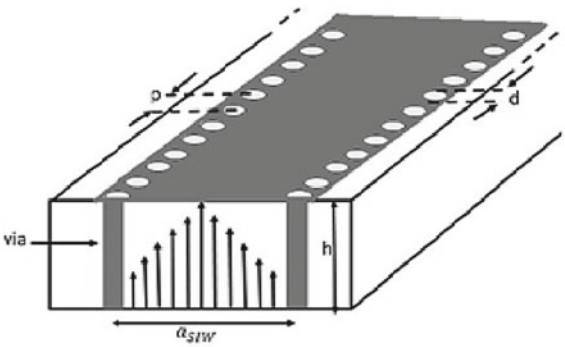


**Fig. 1** Substrate Integrated Waveguide with an array of metallic via with $TE_{10}$ mode shown

## 3 Design of SIW Filter Using Iris

The design of SIW-based filter for Ka band can be modelled with direct coupled cavities. The SIW waveguide cavities are cascaded by coupling iris on the common wall. The design of the SIW filter is identical to that of an air-filled rectangular metallic waveguide filter. Irises help in forming the cavities for the SIW filter which are resonating at $f_0$. The resonant frequency of the filter is given by the following equation:

$$f_{101} = \frac{c_0}{2\sqrt{\varepsilon_r}}\sqrt{\left(\frac{1}{a_{eff}}\right)^2 + \left(\frac{1}{l_{eff}}\right)^2} \tag{3}$$

$$\text{where } a_{eff} = a - \frac{d^2}{0.95p} \text{ and } l_{eff} = l - \frac{d^2}{0.95p} \tag{4}$$

where $a_{eff}$ and $l_{eff}$ are the effective width and length of a cavity. The dimensions $a$ and $l$ are the width and length of the SIW cavity, respectively. $p$ and $d$ are the periodicity or pitch between two vias and diameter of via hole, respectively.

The Chebyshev filter technique is used over the SIW structure to design a filter for a fractional bandwidth of 3.0% and 0.1 dB ripple. Fractional bandwidth, FBW, $w_\lambda = \frac{\lambda_{g1} - \lambda_{g2}}{\lambda_{g0}}$

$$\text{where } \lambda_{gi} = \frac{2}{\sqrt{\varepsilon_r\left(\frac{2f}{c}\right)^2 - \left(\frac{1}{a_{eff}}\right)^2}} \text{ for i } = 0, 1, 2 \tag{5}$$

Three resonators are formed using two input iris structures and two intermediate irises which form impedance inverters. The shape of the desired response is achieved by specifying the impedance-inverter parameters $K_{01}, K_{12}, K_{23}$, and $K_{n,n+1}$. The individual iris would represent an impedance-inverter [6]. The irises form an inductive obstacle with edges parallel to the electric field as shown in Fig. 2b.

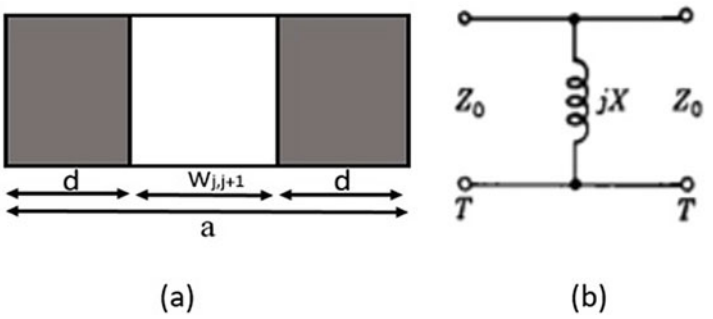


**Fig. 2** Iris Structure **a** Cross section of Iris **b** Equivalent circuit

The normalized impedances of the K-inverters are calculated as follows:

$$\frac{K_{01}}{Z_0} = \sqrt{\frac{\pi}{2}\frac{\omega_\lambda}{g_0 g_1}} \tag{6}$$

$$\frac{K_{j,j+1}}{Z_0} = \sqrt{\frac{\pi}{2}\frac{\omega_\lambda}{g_j g_{j+1}}} \tag{7}$$

$$\frac{K_{n,n+1}}{Z_0} = \sqrt{\frac{\pi}{2}\frac{\omega_\lambda}{g_n g_{n+1}}} \tag{8}$$

where $g_0$, $g_1$, $g_2$,……$g_n$,$g_{n+1}$ are the generalized element values of a Chebyshev filter for a 0.1 dB ripple.

The Chebyshev filter generalized elements used are $g_0 = 1$, $g_1 = 1.0316$, $g_2 = 1.474$, $g_3 = 1.0316$, *and* $g_4 = 1$.

For purely lumped-inductance discontinuities having shunt reactance, $X_{j,j+1}$ is given by

$$\frac{X_{j,j+1}}{Z_0} = \frac{\frac{K_{j,j+1}}{Z_0}}{1 - \left(\frac{K_{j,j+1}}{Z_0}\right)^2} \tag{9}$$

The electrical length is given by

$$\theta_j = \pi - \frac{1}{2}\left[\tan^{-1}\left(2\frac{X_{j-1,j}}{Z_0}\right) + \tan^{-1}\left(2\frac{X_{j,j+1}}{Z_0}\right)\right] \tag{10}$$

The physical distance between centre of iris post to the centre of adjacent iris post is given by

$$l_j = \frac{\lambda_{g0}\theta_j}{2\pi} \tag{11}$$

**Table 1** Dimensions and cavity parameters of SIW filter

| Parameter | Dimension (mm) |
|---|---|
| $a_{SIW}$ | 5.2 |
| $w_{io}$ | 2.18 |
| $w_{12} = w_{23}$ | 1.44 |
| $l_1 = l_3$ | 4.2 |
| $l_2$ | 4.5 |
| h | 0.508 |
| Top/Bottom metal(Cu) layer | 0.017 |

The iris window width, $w_{j,j+1}$, is calculated with help of a plot made by $\frac{X_{j,j+1}}{Z_0}$ $\frac{\lambda_g}{a}$ with $\frac{a}{\lambda_0}$ to calculate $\frac{w_{j,j+1}}{a}$ and finally calculating $w_{j,j+1}$ as discussed in [7].

With the help of $l_j$ (physical distance between the adjacent iris) and $w_{j,j+1}$ (iris window width), the SIW filter cavities and their coupling with other cavities are made.

The SIW filter is designed on a single-layered Rogers RT/Duroid 6002 substrate having $\varepsilon_r = 2.94$ with a height of 0.508 mm. The metallic vias have a diameter of 0.5 mm and periodicity of 0.7 mm. The structure is simulated in an HFSS environment. The 50-Ω microstrip to SIW transition is considered. Due to the symmetry of the Chebyshev parameters, the dimensions of the first and third resonating cavity of the SIW filter are identical. The dimensions of the structure are as shown in Table 1. The structure top view is shown in Fig. 3.

The cavity will have dominant $TE_{101}$ mode having a resonant frequency at $f_{101}$. The higher order mode like $TE_{201}$ mode also exists and might lead to poor stopband performance. But if the excitation to the input cavity is along the adjacent sidewall and output is also taken along adjacent side walls, then a transmission zero will be placed at the upper passband, thereby improving the stopband performance [8]. Other parameter dimensions are not modified. The modified design is as shown in Fig. 4.

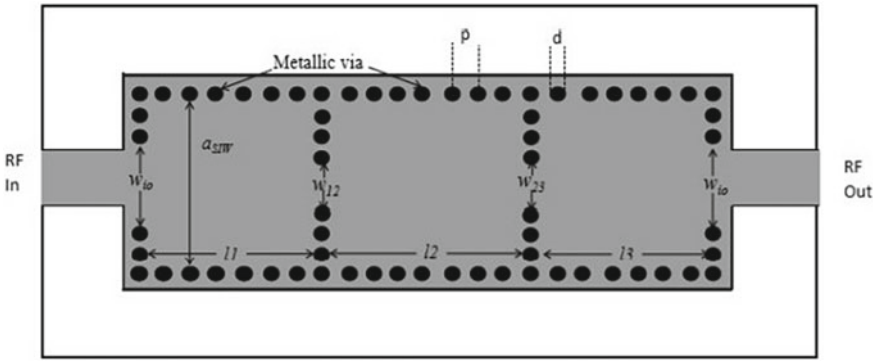


**Fig. 3** Top view of Third-order SIW filter with iris structures

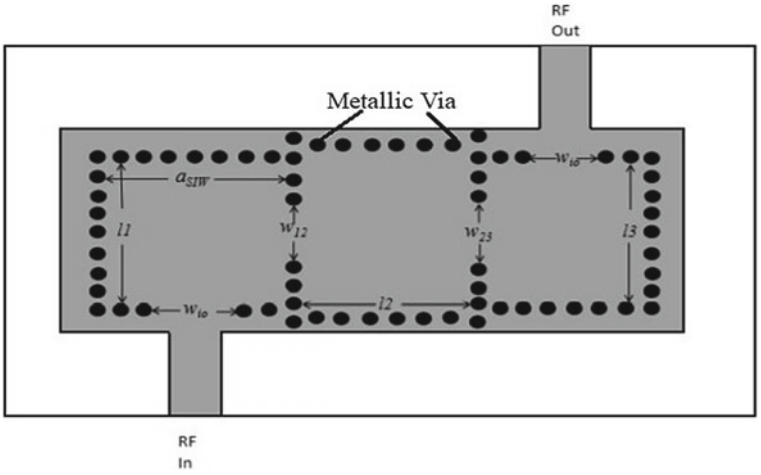


**Fig. 4** Top view of Third-order adjacent side excited SIW filter with iris structures

The external Quality factor of both the designs is calculated using the following expression:

$$Q_e = \frac{f_0}{\Delta f}[9] \tag{12}$$

## 4 Results and Discussions

The response depicting the insertion loss($S_{21}$ in dB) and return loss($S_{11}$ in dB) of the SIW filter design based on front excitation is shown in Fig. 5. From Fig. 5, we find that resonant frequency is at 26.83 GHz and insertion loss is 1.69 dB, and return loss is better than 12 dB throughout the passband. The bandwidth of 820 MHz is obtained to give a fractional bandwidth of 3.05%. The external quality factor $is\ Q_e = 32.71$.

The response for the SIW filter design having adjacent side excitation is shown in Fig. 6. The resonant frequency of this structure is found to be at 26.9 GHz and has a bandwidth of 700 MHz. The insertion loss is 1.71 dB and the return loss better than 20 dB throughout the passband is achieved. The external quality factor is $Q_e = 40.2$.

A transmission zero placed at the upper passband makes the stopband performance improve by a large extent. We can also see that the external Quality factor increases when the excitation is changed to the adjacent side. The higher order modes provide the non-physical cross-coupling in the SIW cavities which help in generating transmission zeros farther from the passband. Thus, improving the stopband performance.

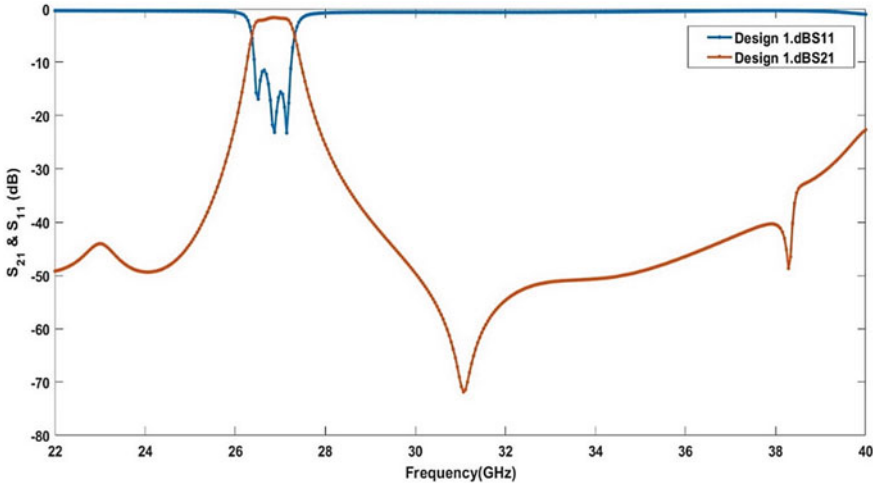


**Fig. 5** Frequency response of the third-order SIW filter

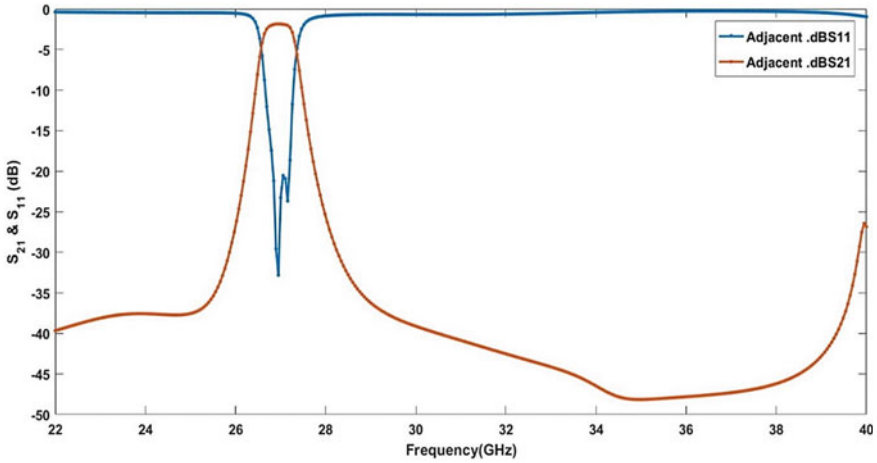


**Fig. 6** Frequency response of the adjacent side excited SIW filter

By increasing the distance of the input/output port to the cavity centre, the location of transmission zero moves farther away from the passband. The response of structure having an adjacently driven and also having an offset with respect to centre of cavity is shown in Fig. 7 showing the improvement in the stopband performance. Thus, by adding an offset with respect to centre of cavity, the orthogonally driven SIW filter structure response has further improved. Table 2. shows a comparison of the different SIW filters along with the adjacently driven proposed design.

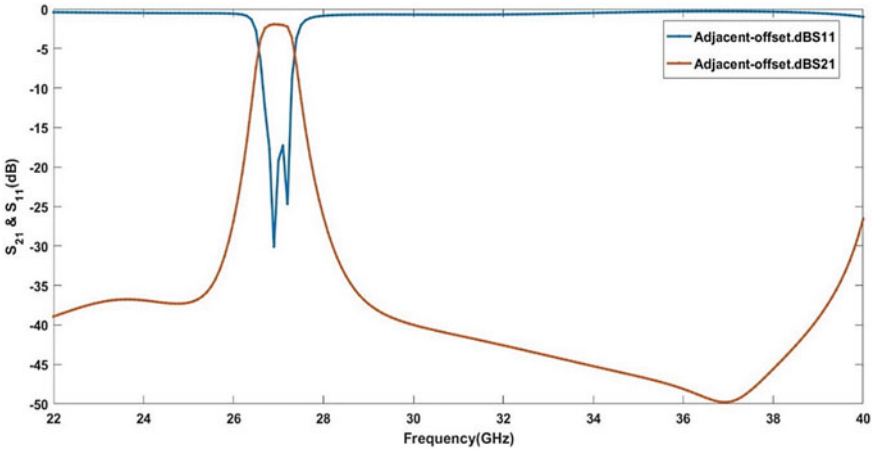


**Fig. 7** Simulated frequency response of SIW filter which is adjacent side excited with offset

**Table 2** Comparison of SIW filters based on insertion loss and return loss

| | Frequency (GHz) | Insertion loss (dB) | Return loss (dB) |
|---|---|---|---|
| [9] | 28 | 2.7 | 15 |
| [10] | 27 | 2.2 | 16 |
| [11] | 28 | 2.2 | 15 |
| Proposed design | 26.5–27.3 | 1.71 | 20 |

The insertion loss has reduced as diameter d is decreased from d = 0.5 mm to d = 0.3 mm keeping the centre of metallic via same for all the d values. There is a shift in the frequency as shown in Fig. 8. This is basically due to the effect of d over the effective width, $a_{eff}$ as in Eq. (1). For the d = 0.3 mm, the metallic vias are very small and hence, laser drilling technology can be used to achieve the aforementioned via dimension. Table 3 shows the insertion loss variation for different values of via diameter.

The group delay simulated responses for the structures having metallic via diameter, d = 0.4 with orthogonal offset excitation and d = 0.5 mm with inline excitation is shown in Fig. 9. From Fig. 9, it is observed that there is a change in the group delay responses of the two structures due to the fact that passband of each structure is different. The simulated group delay for d = 0.5 mm inline excitation structure, at the lower and upper edges, is about 1.32 and 1.12 ns, respectively. The minimum group delay for this structure is 0.85 ns. The simulated group delay for d = 0.4 mm orthogonal offset excitation structure, at the lower and upper edges, is about 1.225 and 1.05 ns, respectively. The minimum group delay for this structure is 0.8 ns.

Further, for improvement in footprint, different topologies of SIW like Half-Mode SIW and air-filled SIW structures [12] can be used. Complementary Split

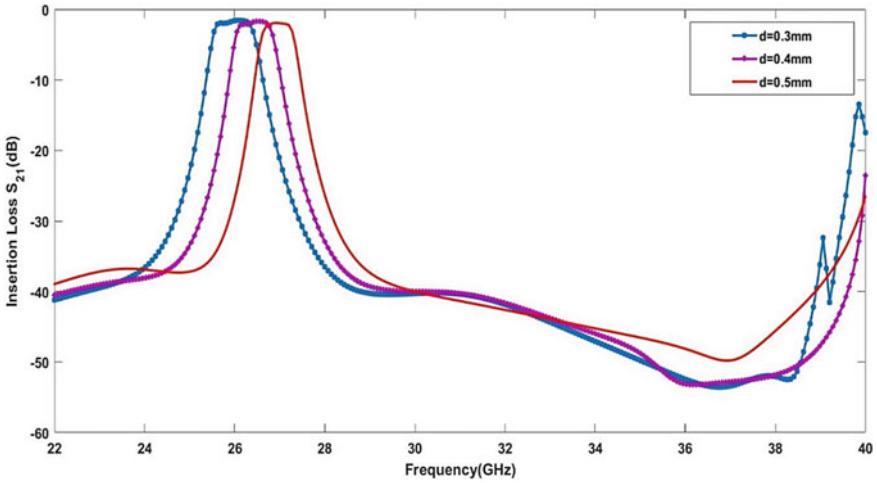


**Fig. 8** Insertion loss variation with respect to changes in via diameter d

**Table 3** Insertion loss variation for various Via diameters

| Via diameter (mm) | 0.5 | 0.4 | 0.3 |
|---|---|---|---|
| Insertion loss (dB) | 1.8 | 1.7 | 1.4 |

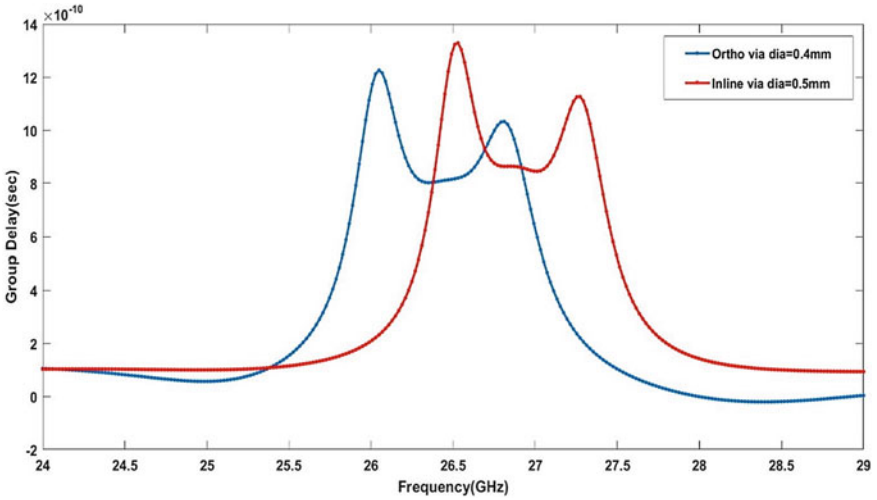


**Fig. 9** Simulated result of group delay for changes in via dimension and excitation type

Ring Resonators (CSRR) loaded SIW filter can be used. The tuning of the filter can be done using the RF MEMS switches and MEMS varactors into the SIW filter structure [13].

## 5 Conclusion

In this chapter, the proposed SIW filter has identical characteristics to the conventional rectangular metallic waveguide filter but has a reduction in size compared to the conventional rectangular waveguide. The analysis of the input strategy and its effect on the stopband performance and external quality factor has been conducted. A study of variation of metallic via diameter effect over the Insertion loss is also made and conclusion can be drawn that insertion loss decreases with decrease in dimension of metallic via. In addition, the study of Group delay with the variation of metallic via diameter is performed. Finally, the third-order adjacent side excited SIW filter has been designed which has the same dimensions as a direct excited SIW filter providing an improved stopband performance and high-quality factor.

**Acknowledgements** This document is prepared in support of the National Institute of Technology, Silchar.

## References

1. D. Peroulis, Tunable filter technologies for 5G communications, in *2018 IEEE International Electron Devices Meeting (IEDM)*, (2018), pp. 14.6.1–14.6.4
2. X.P. Chen, K. Wu, Substrate integrated waveguide (SIW) filter: basic design rules and structure features. IEEE Microw. Mag. **15**(5), 108–116, (2014) A
3. El Mostrah, A. Muller, J.-F. Favennec, B. Potelon, A. Manchec, E. Rius, C. Quendo, Y. Clavet, F. Doukhan, J. Le Nezet, An RF MEMS based digitally tunable SIW filter in X-band for communication satellite applications. Appl. Sci. **9**(9), 1838 (2019)
4. X. Chen, K. Wu, Substrate integrated waveguide filters: design techniques and structure innovations. IEEE Microwave Mag. **15**(6), 121–133 (2014)
5. D. Deslandes, Ke Wu, Accurate modeling, wave mechanisms, and design considerations of a substrate integrated waveguide. IEEE Trans. Microwave Theory Tech. **54**(6), 2516–2526 (2006)
6. G. Matthaei, L. Young, E. Jones, *Microwave Filters, Impedance Matching Networks, and Coupling Structures, Ser* (Artech House Books, Artech House Microwave Library, 1980)
7. N. Marcuvitz, *Waveguide Handbook* (Peter Peregrinus Ltd. on behalf of the Institution of Electrical Engineers, London, 1986)
8. X. Chen, K. Wu, D. Drolet, Substrate integrated waveguide filter with improved stopband performance for satellite ground terminal. IEEE Trans. Microw. Theory Tech. **57**(3), 674–683 (2009). https://doi.org/10.1109/TMTT.2009.2013316
9. L. Ma, J. Zhuang and J. Zhou, A cross-coupled substrate integrated waveguide filter for 28 GHz millimeter wave communications, *2016 IEEE International Symposium on Circuits and Systems (ISCAS)* (Montreal, QC, 2016), pp. 814–817. https://doi.org/10.1109/ISCAS.2016.7527365

10. Z. He, C.J. You, S. Leng et al., Compact inline substrate integrated waveguide filter with enhanced selectivity using new non resonating node. Electron Lett **52**(21), 1778–1780 (2016)
11. K. Gong, W. Hong, Y. Zhang et al., Substrate integrated waveguide quasi-elliptic filters with controllable electric and magnetic mixed coupling. IEEE Trans Microwave Theory Tech. **60**(10), 3071–3078 (2012)
12. F. Parment, A. Ghiotto, T. Vuong, J. Duchamp, K. Wu, Air-filled substrate integrated waveguide for low-loss and high power-handling millimeter wave substrate integrated circuits. IEEE Trans. Microwave Theory Tech **63**(4), 1228–1238
13. V. Sekar, M. Armendariz, K. Entesari, A 1.2–1.6-ghz Substrate Integrated-waveguide RF MEMS tunable filter. IEEE Trans. Microw. Theory Tech. **59**(4), 866–876 (2011)

# Gesture Controlled Robot-Car Using Raspberry PI


**Suman Kumar Pal, Afreen Bano, Ayan Jana, Mitun Kundu, and Arijit Ghosh**

## 1 Introduction

Gestures can originate from different body parts of a human being with the help of which one can interact with any device without having any physical contact with them in reality. Approaches have been made to interface with cameras or application of computer vision techniques for its interpretation on recognition of gesture. In our project, the gestures are read by the accelerometer (MPU6050), which then feeds its data to the Raspberry-Pi microcontroller. In this microcontroller, we use python programming which provides the logic for the motor drivers. The accelerometer is calibrated in different axes (x, y, z). The microcontroller provides logic to the motor driver according to the accelerometer movement (provided by the gestures). The data which is sent to the motor driver is sent wirelessly through encoder-decoder pair. First the parallel data is made serial by the encoder then the data is provided to the transmitter and through the antenna it is sent wirelessly to the receiver end, where the data is provided to the decoder, it then provides the data to the motor driver (L293D) which amplifies the current level and then it provides the current to the two motors which rotates accordingly.

## 2 Literature Review

Navigation of a robot is based on hand-gesture control [1]. The trajectory data obtained by the adopted three-axis accelerometer is transmitted using wireless medium via transmitter–receiver module to a motor driver. The classifier adopts

S. K. Pal (✉) · A. Bano · A. Jana · M. Kundu · A. Ghosh
Department of Applied Electronics and Instrumentation Engineering, RCC Institute of Information Technology, Canal South Road, Kolkata Pin-700 015, India
e-mail: sumanrcc902@gmail.com



C. K. Chanda et al. (eds.), *Advanced Energy and Control Systems*, Lecture Notes in Electrical Engineering 820, https://doi.org/10.1007/978-981-16-7274-3_22

hand trajectories. To improve safety, non-contact and pointing interface is developed. This decreases manufacturing cost and improves the ease of driver movement between different cars [2]. The interface is operated via an onscreen cursor using pointing gestures. This paper illustrates the subsystem responsible for detection and tracking of the driver's hands. The integration of complex functionality into the human–machine interface (HMI) [3] to simplify the interaction with in-car devices for optimal use of human sensor channel is developed. This paper [4] focuses on the recognition of hand gestures automatically by wearing inexpensive motion sensors that shows promising results in practice regarding game appeal. The idea of wearing a sensor in hand is taken from this paper and is implemented here. In this case, a motion sensor is used in hand for the giving the direction, whereas we have used accelerometer sensor instead of a motion sensor. In this paper [5], the preliminary and tertiary driving task are performed together by the human–machine interface, where the directional control is done using the gesture recognition technique. For disabled individuals, hand gesture recognition is an essential and the most intuitive way for communication [6]. According to this paper, both the hand gesture and emotional gestures can be used for recognition of facial expression and social ambience. Hand gesture recognition algorithm combined with two distinct recognizers collectively determine the hand gesture by a process called combinatorial approach recognizer (CAR) equation here. The aim to remove the obstruction between human and machine can be done with the help of glove [7]. The user is enabled to control the hardware by the usage of natural gestures, all these are possible due to presence of many sensors which help in capturing the hand movements and hence control the RC car. The steering, speed, and other parameters can be controlled by the hand gestures using sensors. Effective evaluation during the early prototyping stage is important to ensure the safety in cockpit using in-house solutions, for this reason highly realistic testing environment is needed for valid finding. In case of a real car these studies are time-consuming yet costly, hence, we can study simulator models which will provide a realistic awareness of the above situation [8]. From this research finding, three things are checked, i.e., touch, spin control, and free hand gesture. The development of headsets that has neuro-electric properties can be used to build thought controlled devices which are becoming extremely popular for games, robot-cars, etc. Here [9], the usage of low cost EEG amplifier having limited number of electrodes to develop a motor-controlled brain–computer system is studied. The objective is to extract brain signals to provide direction to the motor are discussed in [10, 11].

## 3 Architecture Diagram

The architecture diagram of our designed system is depicted in Fig. 1 which is divided into two parts: Transmitter Block and Receiver Block.

The transmitter block includes

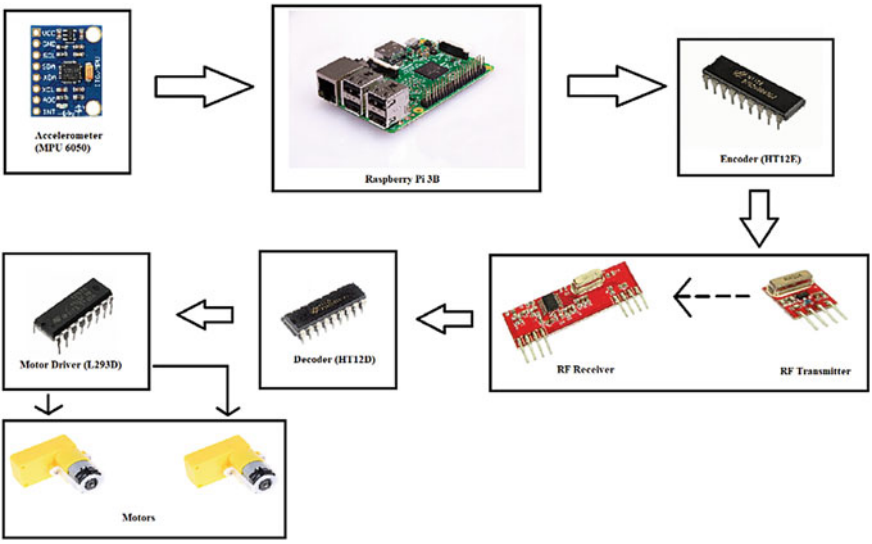


**Fig. 1** Architecture diagram of the designed system

a. MPU6050 accelerometer.
b. Raspberry Pi model 3B
c. Encoder HT 12E
c. RF Transmitter Tx 434

The receiver block includes

a. RF Transmitter Rx 434
b. Encoder HT 12D
c. Motor driver L293D
d. Two motors of robot-car

## *3.1 Accelerometer (MPU 6050)*

An accelerometer has a piezoelectric sensor, so upon movement there will be a change in resistance, which eventually creates a change in output voltage level to measure acceleration, vibration, or any kind of force. MPU6050 is a complete 6-axis Motion Tracking Device consisting of Gyroscope along 3-axis, Accelerometer also along 3-axis, and Digital Motion Processor. To communicate with the microcontrollers, it uses 12C bus interface.

### 3.2 Raspberry PI

The microprocessor that has been used is Raspberry Pi 3 Model B. It can process data ten times faster than the first generation Raspberry Pi and comprises wireless LAN and Bluetooth connectivity for intelligent designs.

### 3.3 Encoder (Ht 12e)

Encoder (HT 12E) is used to encode the 12-bit parallel data into serial data so that the motor rotates through RF transmitter.

### 3.4 RF Module (TX 434/RX 434)

The RF module is used to transmit the serial data from the encoder to receiver terminal at 434 MHz at a rate of 1–10Kbps.

### 3.5 Decoder (Ht 12D)

HT12D is a decoder that converts the serial data from the receiver to parallel form, which is then fed to the motor driver for remote operated system applications. They are paired with equivalent series of encoders having same addresses and data format.

### 3.6 Motor Driver (L293D)

L293D motor driver functions as a current amplifier; it receives a low-current signal from the decoder and provides a high-current signal to drive the motors. We have used this in common mode to drive two DC motors simultaneously in both directions. Enable pins 1 and 9 (used for two motors) are made high to start the motor operation and are controlled by input logic 00 and 11 at pins 2 and 7 and 10 and 15, to stop and start the motor, respectively.

**Table 1** Directional movement from accelerometer data

| Sl. No | Direction | Accelerometer orientation |
|---|---|---|
| 1 | Forward | +y |
| 2 | Reverse | −y |
| 3 | Left | −x |
| 4 | Right | +x |
| 5 | Stop | Rest |

## *3.7 Dc Motor*

The DC motor converts DC power into mechanical energy. It has a revolving armature winding and non-revolving armature magnetic field and permanent magnet and is based on the principle that when current-carrying conductor is placed in a magnetic field, it experiences a mechanical force. The speed of a DC motor is controlled by changing the voltage applied to armature.

The directional movement of the car from accelerometer data is shown in Table 1, and the system methodology is indicated in Fig. 2.

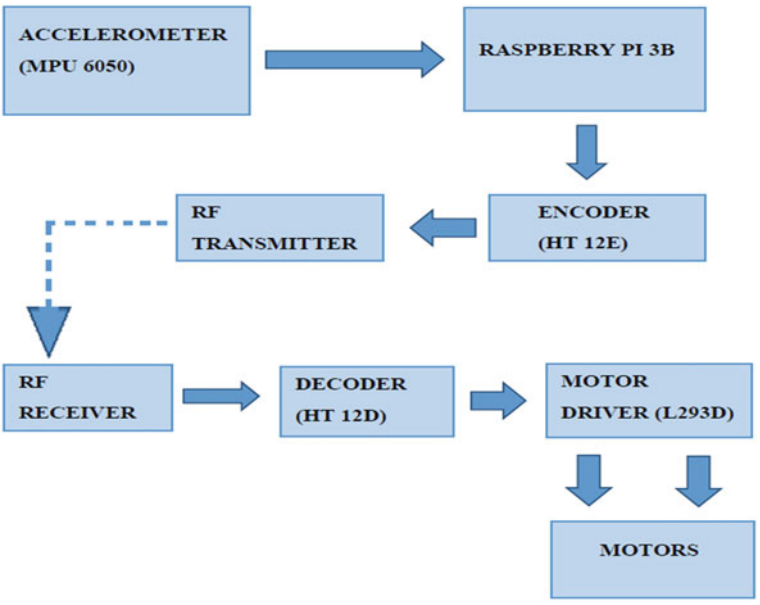


**Fig. 2** Block Diagram of the designed system

## 4 Methodology

The accelerometer MPU6050 obtains the angular wrist rotation in 3-axis, i.e., in x, y, and z directions. The real-time three-dimensional analog data are indicated in the figure below.

The real-time data is fed to the GPIO pins of Raspberry Pi. Any of the GPIO pin can function as input or output pin. Two 5 V pins and two 3 V pins are present on-board, with a number of non-configurable ground pins (0 V). All the remaining pins are general purpose 3 V pins. The python code uploaded in the micro-computer sets or resets the voltage levels of 4 bits using the comparator logics demonstrated in the given table.

From Table 2 we get to see the threshold values of the accelerometer and the logic (the movement in a particular direction) is fed to the microcomputer. According to the direction inferred from Table 2, the 4-bit logic is set or reset following Table 3 as indicated below.

Table 3 provides the movement of the robot-car from the receiver end. The data pins are pins of the L293D motor driver, they are provided with the above logic, hence the motors rotate according to the logic of the data pin, and finally we can observe the movement of the robot-car.

**Table 2** Decision from 3-axis data

| Sl. No | Conditions | Comments |
|---|---|---|
| 1 | $Z > 8$ | Stop |
| 2 | | Check for direction wrt movement |
| 3 | $X < -2$ | Forward direction |
| 4 | $X > 3$ | Backward direction |
| 5 | $Y > 0$ | Right Direction |
| 6 | $Y < 0$ | Left Direction |

**Table 3** Data pins logic

| Data pin | | | | Motor 1 | | Motor 2 | | Comments |
|---|---|---|---|---|---|---|---|---|
| D1 | D2 | D3 | D4 | D1 | D2 | D3 | D4 | |
| 1 | 0 | 1 | 0 | 1 | 0 | 1 | 0 | Forward |
| 0 | 1 | 0 | 1 | 0 | 1 | 0 | 1 | Reverse |
| 1 | 0 | 0 | 1 | 1 | 0 | 0 | 1 | Left |
| 0 | 1 | 1 | 0 | 0 | 1 | 1 | 0 | Right |

## 5 Results

The coordinates after the movement of the accelerometer are provided to the microcomputer, which is eventually sent to the motor driver through the transmitter–receiver section. The values which the data pin of the motor driver gets is equivalent to 9 V and 0 V according to the accelerometer movement (in 1 and 0) is shown in Table 4. The car movement and the orientation of the wheels along with the data in the data pin of the motor controller are shown Table 5 (Fig. 3).

**Table 4** Motion induced by accelerometer orientation

| Accelerometer orientation | Data pin | | | | Motor 1 | | Motor2 | | Comments |
|---|---|---|---|---|---|---|---|---|---|
| | D1 | D2 | D3 | D4 | D1 | D2 | D3 | D4 | |
| +y | 1 | 0 | 1 | 0 | 1 | 0 | 1 | 0 | Forward |
| −y | 0 | 1 | 0 | 1 | 0 | 1 | 1 | 1 | Reverse |
| −x | 1 | 0 | 0 | 1 | 1 | 0 | 0 | 1 | Left |
| +x | 0 | 1 | 1 | 0 | 0 | 1 | 1 | 0 | Right |

**Table 5** Direction of motion induced by accelerometer orientation

| Car movements | Data pins | | Left wheel movement | Data pins | | Right wheel movement |
|---|---|---|---|---|---|---|
| Forward | High | Low | Clockwise | High | Low | Clockwise |
| Backward | Low | High | Anticlockwise | Low | High | Anticlockwise |
| Left | High | Low | Clockwise | Low | high | Anticlockwise |
| Right | Low | High | Anticlockwise | High | low | Clockwise |

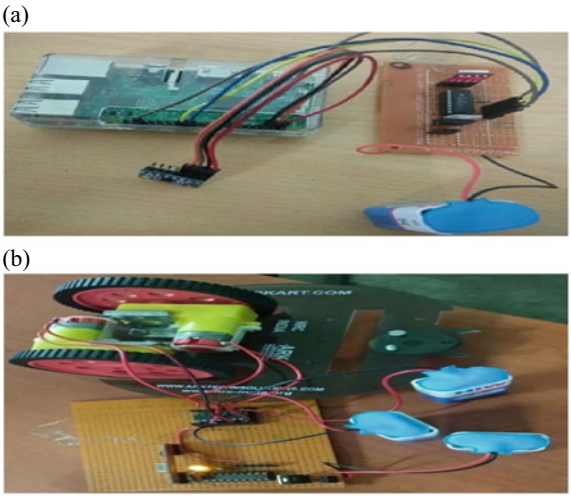


**Fig. 3** **a** Practical hardware set up of Transmitter End, **b** Practical hardware set up of Receiver End

## 6 Conclusion

The objective is to build a robot-car that would run with the help of hand gestures obtained from the Accelerometer MPU 6050 using wireless RF communication. A Raspberry Pi model 3B is used as the controller. On practical testing, the car shows proper movements for the predetermined and calibrated hand gestures. The data from the hand movements with the help of the accelerometer are fed to the Encoder HT 12E through the Raspberry Pi. Then the values are transmitted with the help of Tx 434 (transmitter) and are received by Rx 434 (receiver), where it is decoded by a Decoder HT12D and sent to the motor driver L293D. Thus, the motors are controlled with the data obtained from the motor driver. The car moves only when the accelerometer moves in a specific direction as per the given calibrated values of the accelerometer.

## References

1. W. Xing-Han, S. Mu-Chun, W. Pa-Chun, A hand-gesture-based control interface for a car-robot, in *Proceedings of IEEE/RSJ International Conference on Intelligent Robots and Systems*, Taipei, Taiwan (2010)
2. S. Gordon McAllistel, J. McKenna, W.I. Ricketts, Towards a non-contact driver-vehicle interface, in *Proceedings of IEEE Intelligent Transportation Systems Conference Proceedings.* Dearborn (MI), USA (2000)
3. M. Zobl, M. Geigel, B. Schullec, M. Lang, G. Rigoll, A real-time system for hand gesture controlled operation of in-car devices, in *Proceedings of IEEE*, ICME (2003)
4. D. Bannach, O. Amft, S.K. Kunze, A.E. Heinz, G. Troster, P. Lukowicz, waving real hand gestures recorded by wearable motion sensors to a virtual car and driver in a mixed-reality parking game, in *Proceedings of IEEE Symposium on Computational Intelligence and Games* (2007)
5. A. Pickering C., K.J. Burnhamt, M. Richardson, A research study of hand gesture recognition technologies and applications for human vehicle interaction, in *Proceedings of 3rd Institution of Engineering and Technology Conference on Automotive Electronics* (2007)
6. C. Luo R., Confidence fusion based human-robot interaction with hand gesture and emotion recognition for service robotics, in *Proceedings of 13th IEEE International Symposium on Computational Intelligence and Informatics*, Budapest, Hungary (2012)
7. A. Dekate, A. Kamal, K.S. Surekha, Magic glove- wireless hand gesture hardware controller, in *Proceedings of International Conference on Electronics and Communication Systems (ICECS 2014)*
8. D. Reich, R. Stark, The influence of immersive driving environments on human-cockpit evaluations, in *Proceedings of 48th Hawaii International Conference on System Sciences*, Kauai (2015)
9. R.S. Rupanagudi, G. Varsha, Bha, V.T., R. Supriya, R. Dubey, S. Sukumar, S. Karmarkar, K. Amulya, A. Raman, D. Indrani, A. Srisai, M. Rajagopalan, V. Venkatesh, Nupur Jain, in A novel and secure methodology for keyless ignition and controlling an automobile using air gestures. *Proceedings of International Conference on Advances in Computing, Communications and Informatics (ICACCI)* Jaipur, India (2016)

10. M. Becker, C. KefaleMalsburg, M. Pagel, J. Triesch, J.C. Vorbrüggen, R.P. Würtz, S. Zadel, A gesture-controlled robot for object perception and manipulation. Proc. Auton. Robots **6**(2):203–221 (1999)
11. S. Akyol, U. Canzler, K. Bengler, Wolfgang Hahn. Gesture control for use in automobiles. *Proceedings of MVA2000, IAPR Workshop on Machine Vision Applications*. The University of Tokyo, Japan (Nov. 28–30, 2000)

# Engineering Computing

# An Efficient ZF CSI Technique for Optimal Tradeoffs Between Spectral and Energy Efficiency in Massive MIMO Technology Using Nonconvex Optimization


**N. Satyanarayana Murthy**

## 1 Introduction

The primary motivation behind Area spectral efficiency estimated in bits/Hz/km$^2$ was up so far in [1], with indicator up against the organization in an exceedingly defined geographic territory that may be all the while strengthened by a cell's base station (BS). In spite of the techniques that track regular cell innovation that works in an informed manner, monstrous that MIMO idea is acclimated by preparing BSs with hundreds or thousands of antenna components. Eventually, the specialists of MIMO use their endeavours to putting up together the essential physical layer properties. This specifically indicates the way how channel rationality restricts the procurement of channel state information (CSI), how SEs get influenced and also calculates the capacity to induce lessen between cell impedance. It is seen that the equipment obstruction on reasonable handsets has an occasional impact leading to ghastly productivity [2]. On the off chance that if sending antennas at the transmitter are more in number, the impact of quick blurring may be exhausted. Massive scale blurring additionally goes under the record of by and substantial blurring. Contingent upon its property, it gave the impression to be the foremost awesome antenna element in huge MIMO system [3], yet it's likely to be exposed in [4]. The structure parameters set of Massive MIMO are extraordinarily responsible for SE [5, 6].

N. S. Murthy (✉)
ECE Department, Velagapudi Ramakrishna Siddhartha Engineering College, Vijayawada 520007, India



C. K. Chanda et al. (eds.), *Advanced Energy and Control Systems*, Lecture Notes in Electrical Engineering 820, https://doi.org/10.1007/978-981-16-7274-3_23

## 2 Related Work

In multi-user multi–input–multi–output (MU-MIMO) systems, BS is maintained to help various users with different antennas. Such complex networks are pulled into much consideration for quite a while [7, 8]. Unexpectedly, information associated with BS and customers occur through a symmetrical channel, so BS division transacts with each client in time–frequency assets. It is not ideal from statistical perspective, moreover better caliber is achieved if BS interacts with tiny low number of users at the identical time–frequency property [9, 10]. Be that because it may, complex strategies to alleviate within users obstructions should then be utilized, for instance, maximum-probability multi-user detection on the uplink [11], or on the downlink [12, 13]. As of late, there is a lot of interest for MU-MIMO with massive antenna arrays at the BS. Massive arrays can considerably decrease ICI with suitable preparation [14, 27–41]. Here, such frameworks like "massive MU-MIMO frameworks", moreover as clusters, including many hundreds or more antennas, providing services to several customers are suggested. The MU-MIMO systems plan is honestly the first concern, leading to a heavy conspiracy [15].

Each individual reception tool is targeted on small physical size, and to figure out from reasonable equipment. With a broader radio wire cluster, things begin to determine the determinist, before things that are random. Therefore, the littlest fading is meant to help to endure the stamp. Additionally, when BS antennas are all widespread, users can find the odd channel vectors and BS strategies [16]. The number of antennas that are of unlimited numbers, the essential coordinated channel prepared at BS, the irrelevant disturbance and also the ICI, completely disappear. SE-SE tradeoff problems are usually designed as compulsory optimization models, which are internally compressed [17–19]. Specifically, in ICIs, the mix of consumer energy allocation algorithm makes a considerable challenge to the model. In [20–26] proposed a modified algorithm that enhances the Energy efficiency and capacity of Massive MIMO systems.

## 3 Problem Formulation

An existing RSM (as in [5, 6]) with M distinctive correspondence joins is evaluated. Each connection fixes the transmitter and the receiver system. Let $P = (P_1, P_2, \ldots, \ldots, P_M)$, where $P_j$ signifies the channel control transmitter of connection j. $g_{ij}$ is the channel attained from the transmitter of connection j to the beneficiary of connection I. The obtained SINR at the connection I collector is 53

$$Y_i(P) = \frac{P_i g_{ii}}{\sum_{j=1, j\neq i}^{M} P_j g_{jj} + n_i} \tag{1}$$

where $n_i$ is the noise power at the receiver of link *i*.

Reckoning that, the framework receives a consistent rate plot [5, 6], at that point the information rate of connection I is

$$R_i(P) = \log_2(1 + Y_i(P)) \tag{2}$$

The net power utilized by the system is given by

$$P_{tot}(P) = \sum_{i=1}^{M} (€\ P_i + P_i^C) \tag{3}$$

where ξi is consistent power-enhance insufficient factor of the transmitter of connection I, and $P_iC$ is the circuit control utilization [8]. Correspondingly, the aggregate information rate is equivalent to

$$R_{tot}(P) = \sum_{i=1}^{M} R_i(P) \tag{4}$$

At that point, the EE-SE tradeoff can be assessed by translating the accompanying advancement issue

$$\eta_{EE} = \frac{R_{tot}(P)}{P_{tot}(P)} \text{ s.t.} \quad \text{C1:} \quad R_i(P) \geq r_i^{req}, ¥_i,: \quad 0 \leq P_i \leq P_i^{\max}, ¥_i \tag{5}$$

## 4 System Model

### *4.1 MU-MIMO System Architecture*

The uplink of a MU-MIMO network is inspected. On observing, it can be defined that this frame associates a BS with the diversity of M aerials to attain knowledge from a single radio user. The good thing about single-aerials concluding clientele is that they are uncomplicated, economical, and competence system, and each user still gets high throughput. Apart from this, additional radio antenna has mutual aerials for consumers, as they anticipate that aerials may be considered as antiviral antennas as an additional independent user. The client transmits their data with amount time-recurrence techniques. The M × 1 obtain bearer at the BS is

$$y = 2\sqrt{P_\mu}\,\mathbf{Gx}+\mathbf{n} \tag{6}$$

where G comprises the M × K channel network inside the BS and K clients.

The channel G speaks to geometric fading, quick fading and log-typical fading. The coordinated $g_{mk}$ can be composed as

$$g_{mk} = h_{mk}\sqrt{\beta_k},\ \mathrm{m} = 1, 2 \ldots \mathrm{M} \tag{7}$$

where $h_{mk}$ is the fast fading combined by the $k$th user to the $m$th antenna of the BS. $\sqrt{\beta k}$ models the geometric fading and log fading which is acknowledged to act, naturally supporting over m and to be continuous, much consistent time interim, and known from the before. This presumption is sensible since the separations within the BS and the users are appreciably massive than the separation within the aerials, and the value of $\beta k$ alters at a leisurely pace with respect to time. Then, we have

$$G = HD^{1/2} \tag{8}$$

## *4.2 Perfect Channel-State Information*

The circumstance where the BS has perfect CSI is considered, i.e. it knows G. Let A be a M × K straight locator network which over-rely upon the channel G. By utilizing the added substance straight indicator, the flag got is characterized into flood by expanding it with AH as seeks after

$$r = A^H y. \tag{9}$$

The three standard straight indicators CSI, MRC, ZF are corresponded.

### 4.2.1 Maximum Ratio Combining

For MRC, from (9), by determination of $\log_2(1 + 1/\mathrm{x})$ and utilizing unfairness, we advance the progressive lower restrains on the achieve rate:

$$R\frac{mrc}{p,\ K} \geq R'\frac{mrc}{p,\ K} \tag{10}$$

### 4.2.2 Zero-Forcing Receiver

With ZF, $A^H = (\ G^{\mathrm{H}}G)^{-1}G^H$, or $A^HG = I_K$. Therefore, $\mathrm{a_k}^{\mathrm{H}}\mathrm{g_i} = \delta_{\mathrm{ki}}$, where $\delta k_i = 1$ when $k = \mathrm{i}$ and is equal to 0 elsewhere. From (7), the uplink rate for the $k$th user is

$$R_{p,k}^{zf} = \{\log_2(\frac{p_u}{[(G^HG)^{-1}]_{kk}})\} \tag{11}$$

### 4.2.3 Channel-State Information

With quintessential CSI, Rayleigh fading and $M \geq 2$, the uplink sizable rate with the $k_{\mathrm{th}}$ user for MRC can be lower bounded as follows:

$$\begin{aligned} A^H &= (G^HG + \frac{1}{p_u}I_k)^{-1}G^H \\ &= G^H(G^HG\frac{1}{p_u}I_M)^{-1} \end{aligned} \tag{12}$$

## 5 EE-SE Tradeoff Algorithm

In this sector, a general RSM is adapted to handle the EE-SE tradeoff accumulation complication in the form of (5), acquiesced by representing an ICI to answer the nonconvex optimization.

1: **Initialization**

- Put $\eta_{\ EE}^{\ \mathrm{min}}$ and $\eta_{\ EE}^{\ \mathrm{max}}$, in such a way that $\eta_{\ EE}^{\ \mathrm{min}} \leq \eta_{\ EE}^{\ \mathrm{opt}} \leq \eta_{\ EE}^{\ \mathrm{min}}$.
- Place $n = 0$ and the possible tolerance $\varepsilon > 0$.

2: **while** 1 **do.**

3: $\eta^{\mathrm{n}}{}_{\mathrm{EE}} = (\eta_{\ EE}^{\ \mathrm{max}} + \eta_{\ EE}^{\ \mathrm{min}})/2$.

4: solve the identical problem for a stated $\eta^n{}_{EE}$ and acquire the power allocation program $\{\mathbf{P}^{\mathrm{n}}\}$.

5: **if** $|m(\eta^{\mathrm{n}}{}_{EE}) | = |R_{\mathrm{tot}}(\mathbf{P}^{\mathrm{n}} - \eta^n{}_{EE}P_{tot}(\mathbf{P}^{\mathrm{n}}) | \leq \varepsilon$ **then.**

6: $\{\boldsymbol{P}^*\} = \{\boldsymbol{P}^n\}$ and $\eta^*_{EE} = R_{tot}(\boldsymbol{P}^n)P_{tot}(\boldsymbol{P}^n)$.

7: break.

8: **else.**

9: **if** $m(\eta^n{}_{EE}) < 0$ **then.**

10: $\eta^{\max}{}_{EE} = \eta^n{}_{EE}$.

11: **else**

12: $\eta^{\min}{}_{EE} = \eta^n{}_{EE}$.

13: **end if**

14: **end if**

15: $n = n + 1$.

16: **end while.**

## 6 Experimental Results

### Simulation Parameters

| Technique | ZF with CSI |
|---|---|
| Modulation | Receive space modulation algorithm |
| Network layout | Circle |
| Cell area | 0.25 km × 0.25 km |
| Number of antennas | 100 |
| Number of users | 100 |
| Fading | Small scale fading |
| Software | MATLAB |

From Fig. 1, it is clear that ZF with CSI spectral efficiency is increasing exponentially as number of base stations or antennas increases. With 2 BS, SE is 4 and at BS = 6 it's corresponding SE is 100. We chose 1bit/channel/user. From Fig. 2, it is clear that ZF with perfect CSI spectral efficiency is good when compared with other existing techniques. When 2bit/channel/user is selected, from Fig. 3, it is clear that ZF spectral efficiency is good when compared to other existing techniques. Figure 4 shows spectral efficiency counter to the number of BS antennas for MRC, ZF processing at the receiver, with perfect and with CSI analysis. In this example $K$ = 100 users are served simultaneously, the reference transmit power is $E_{\mathrm{u}} = 5$ dB.

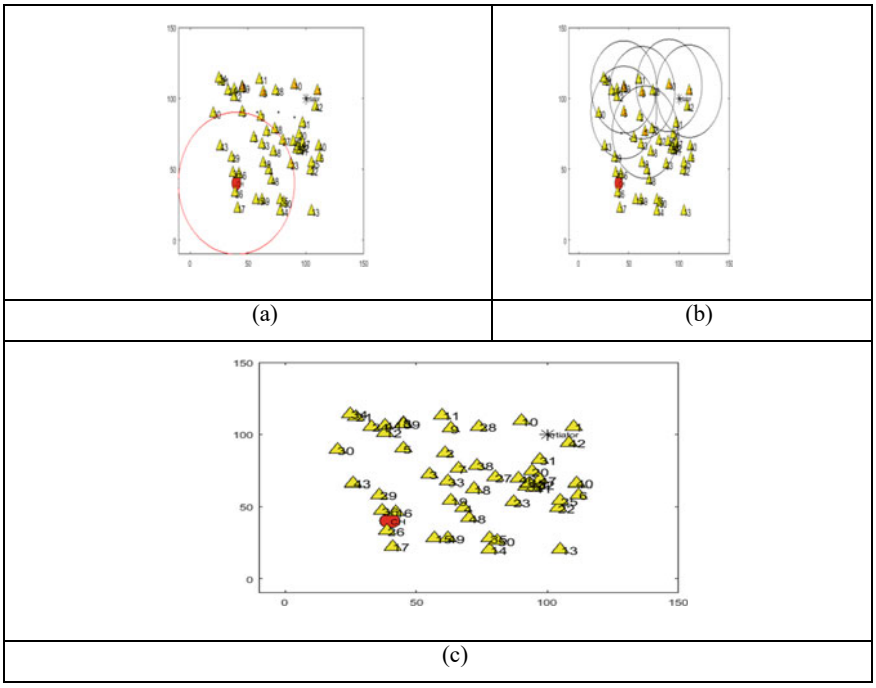


**Fig. 1** Simulation environment for 50 No of users versus No of node antennas

From Figs. 5 and 6, the required power for perfect CSI is less when compared with other existing techniques.

From Fig.7, it clearly depicts, the trade off between Energy efficiency and Spectral efficiency is well balanced for perfect CSI when compared with rest of the techniques. With good spectral efficiency the data rate increases and with good energy efficiency the power consumption or transmit power reduces. For massive mimo systems, we need optimum EE and SE is required so that hardware implementation cost reduces.

## 7 Conclusion

Massive MIMO systems offer the chance of multiplying the SE by two or three orders and also enhancing the (EE) energy efficiency by two orders in magnitude. This is feasible with basic linear processing, for example, MRC or ZF at the BS, and utilizing channel estimates acquired from uplink pilots even in a high mobility environment where half of the channel consistent interval is utilized for training. We simulated for 100 users and antennas more than 100 in number, ZF with perfect CSI

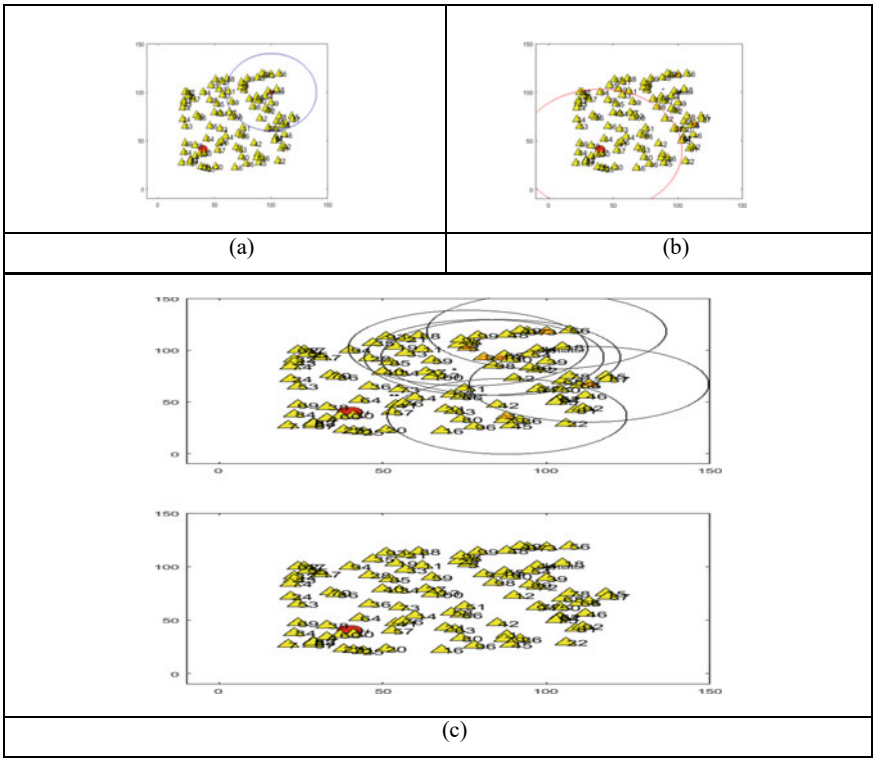


**Fig. 2** Simulation environment for 1000 No of users versus No of node antennas

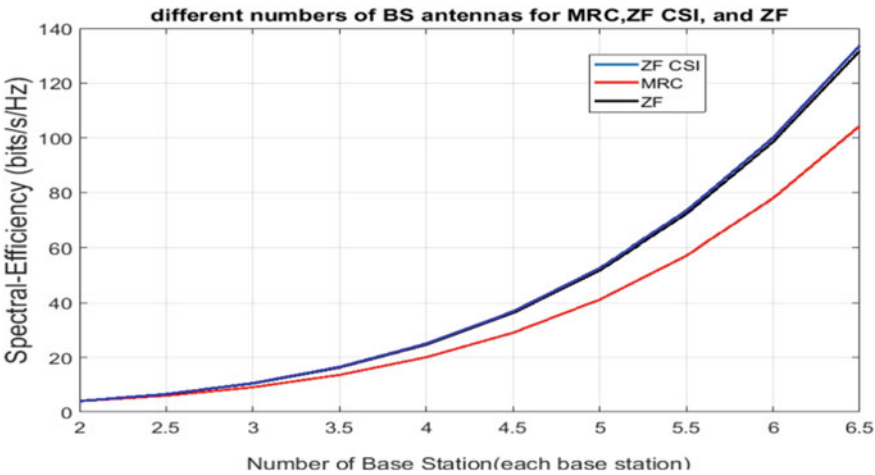


**Fig. 3** SE for distinct numbers of BS radio antennas for MRC, ZF with CSI, and ZF. In this sample there are $K = 100$ users

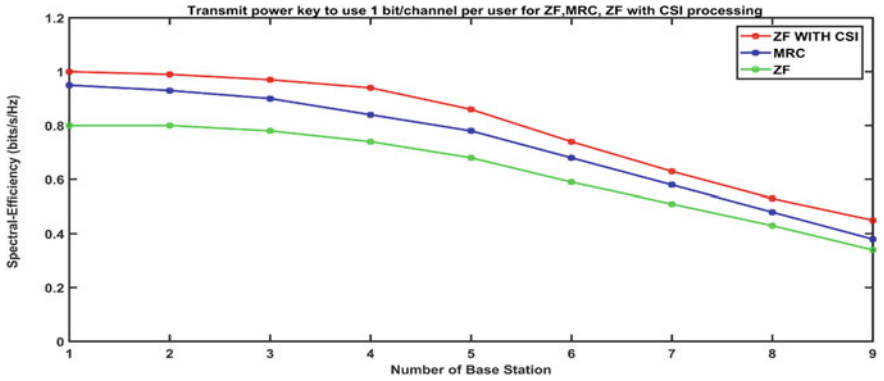


**Fig. 4** 1 bit/channel per user for ZF,MRC, ZF with CSI processing

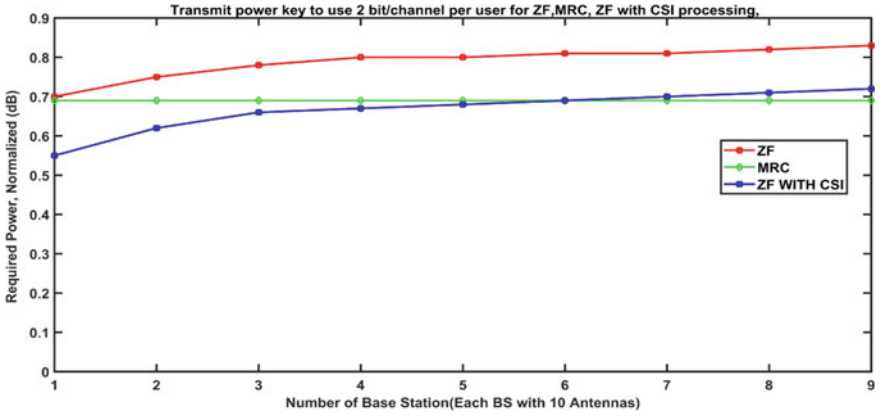


**Fig. 5** SE use 2 bits/channel per each user for MRC, ZF with CSI

is providing good tradeoffs between EE and SE when compared with other linear precoding techniques. Throughput is also increased exponentially with the proposed technique. All these conclusions are validated in small-scale fading environment.

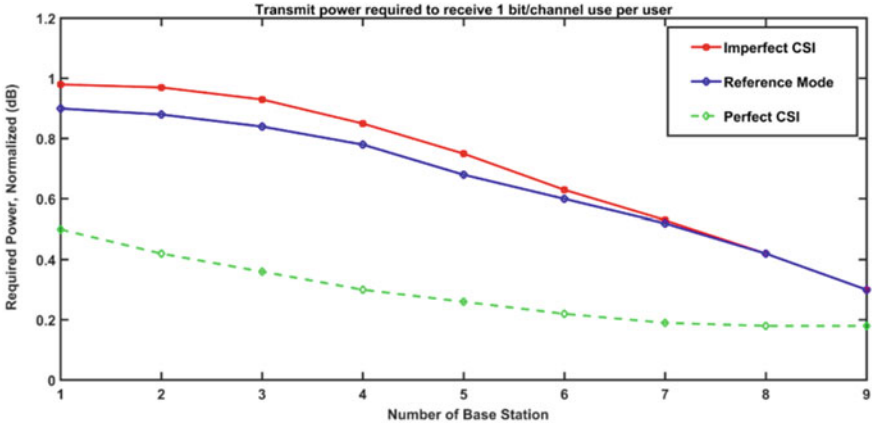


**Fig. 6** Spectral efficiency counter to the number of BS $M$ for MRC, ZF processing at the receiver, with perfect and with CSI analysis. In this example $K = 100$ users are served simultaneously, the reference transmit power is $E_u = 5$ dB

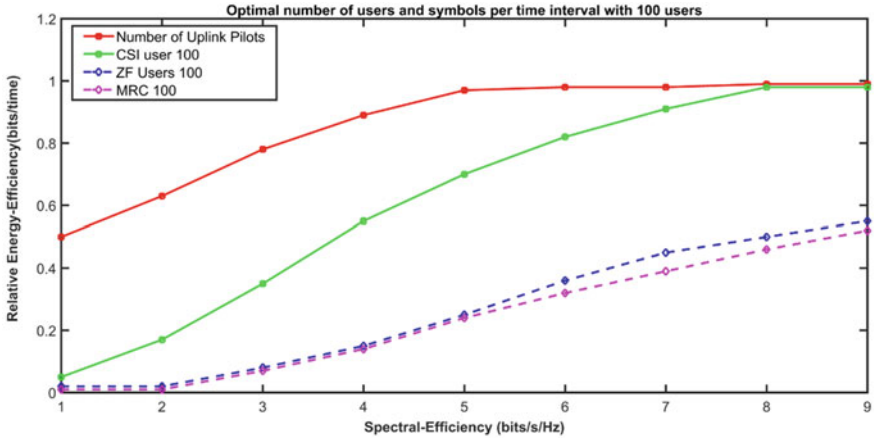


**Fig. 7** Spectral efficiency counter to the number of BS radio antennas $M$ for MRC, ZF managing at the receiver, with CSI (acheived from uplink pilots)

## References

1. J. Hoydis, S. ten Brink, M. Debbah, Massive MIMO in the UL/DL of cellular networks: how many antennas do we need? IEEE Sel Areas Commun **31**(2), 160–171 (2013)
2. E. Björnson, E.G. Larsson, M. Debbah, Optimizing multi-cell massive MIMO for spectral efficiency: How Many users should be scheduled?, 2014 IEEE Global Conference on Signal and Information Processing (GlobalSIP), Atlanta, GA, 2014, pp. 612–616
3. H.Q. Ngo, E.G. Larsson, T.L. Marzetta, Energy and spectral efficiency of very large multiuser MIMO systems[J]. IEEE Trans. Commun. **61**(4), 1436–1449 (2013)

4. Y. Lin, X. Li, W. Fu, Y. Hei, Spectral efficiency analysis for downlink massive MIMO systems with MRT precoding. China Commun. **12**(Supplement), 67–73 (2015)
5. W. Liu, S. Jin, C.K. Wen, M. Matthaiou, X. You, A tractable approach to uplink spectral efficiency of two-tier massive MIMO cellular HetNets. IEEE Commun. Lett. **20**(2), 348–351 (2016)
6. J. Zhang, L. Dai, S. Sun, Z. Wang, On the Spectral efficiency of massive MIMO systems with low-resolution ADCs. IEEE Commun. Lett. **20**(5), 842–845 (2016)
7. W. Tan, S. Jin, C.K. Wen, Y. Jing, Spectral Efficiency of mixed-ADC receivers for massive MIMO systems. IEEE Access **4**, 7841–7846 (2016)
8. A. Sabharwal, P. Schniter, D. Guo, D.W. Bliss, S. Rangarajan, R. Wichman, In-band full-dulex wireless: challenges and opportunities. IEEE J. Sel. Areas Commun. **32**(9), 1637–1652 (2014)
9. S. Hong, J. Brand, J.I. Choi, M. Jain, J. Mehlman, S. Katti, andP. Levis, Applications of self-interference cancellation in 5G and beyond. IEEE Commun. Mag. **52**(2), 114–121 (2014)
10. P. Xing, J. Liu, C. Zhai, Spectral efficiency of the uplink channel in the shared-antenna full-duplex massive MU-MIMO system. , IEEE 83rd Vehicular Technology Conference (VTC Spring). Nanjing **2016**, 1–5 (2016)
11. N.N. Alotaibi, K.A. Hamdi, A direct-code to increase the spectral efficiency of generalized space shift keying modulation, in *2016 IEEE Wireless Communications and Networking Conference, Doha*, 2016, pp. 1–5.
12. H.Q. Ngo, E.G. Larsson, T.L. Marzetta, Uplink power efficiency of multiuser MIMO with very large antenna arrays, in *Proceedings 2011 Allerton Conference Communication, Control, Computer*
13. D. Gesbert, M. Kountouris, R.W. Heath Jr., C.-B. Chae, T. Sälzer, Shifting the MIMO paradigm. IEEE Signal Process. Mag. **24**(5), 36–46 (2007)
14. G. Caire, N. Jindal, M. Kobayashi, N. Ravindran, Multiuser MIMO achievable rates with downlink training and channel state feedback. IEEE Trans. Inf. Theory **56**(6), 2845–2866 (2010)
15. J. Jose, A. Ashikhmin, T.L. Marzetta, S. Vishwanath, Pilot contamination and precoding in multi-cell TDD systems. IEEE Trans. Wireless Commun. **10**(8), 2640–2651 (2011)
16. S. Verdú, *Multiuser Detection*. Cambridge University Press (1998)
17. P. Viswanath, D.N.C. Tse, Sum capacity of the vector Gaussian broadcast channel and uplink-downlink duality. IEEE Trans. Inf. Theory **49**(8), 1912–1921 (2003)
18. H. Weingarten, Y. Steinberg, S. Shamai, The capacity region of the Gaussian multiple-input multiple-output broadcast channel. IEEE Trans. Inf. Theory **52**(9), 3936–3964 (2006)
19. T.L. Marzetta, Noncooperative cellular wireless with unlimited numbers of BS antennas. IEEE Trans. Wirel. Commun. **9**(11), 3590–3600 (2010)
20. J. Fan, Y. Zhang, Energy efficiency of massive MU-MIMO with limited antennas in downlink cellular networks. Digital Signal Process. **86**, 1–10 (2019)
21. Z. Zhang, Z. Chen, M. Shen, B. Xia, Spectral and energy efficiency of multipair two-way full-duplex relay systems with massive MIMO. IEEE J. Sel. Areas Commun. **34**(4), 848–863 (2016)
22. P. Patcharamaneepakorn, S. Wu, C.-X. Wang, el-Hadi M. Aggoune, M.M. Alwakeel, X. Ge, M. Di Renzo, Spectral, energy, and economic efficiency of 5G multicell massive mimo systems with generalized spatial modulation. IEEE Trans. Veh. Technol. **65**(12), 9715–9731 (2016)
23. W. Tan, D. Xie, J. Xia, W. Tan, L. Fan, S. Jin, Spectral and energy efficiency of massive mimo for hybrid architectures based on phase shifters. IEEE Access **6**, 11751–11759 (2018)
24. M.K. Noor Shahida, R. Nordin, M. Ismail, Improved water-filling power allocation for energy-efficient Massive MIMO downlink transmissions. Int. J. Electron. Telecopp. **63,** 79–84 (2017)
25. S.M. Nimmagadda, Enhancement of efficiency and performance gain of massive MIMO system using trial-based rider optimization algorithm. Wirel. Pers Commun (2020). https://doi.org/10.1007/s11277-020-07921-y
26. S.M. Nimmagadda, Optimal spectral and energy efficiency trade-off for massive MIMO technology: analysis on modified lion and grey wolf optimization. Soft Comput. **24**, 12523–12539 (2020). https://doi.org/10.1007/s00500-020-04690-5

27. N.S. Murthy, S..Sri Gowri, B. Prabhakara Rao, Space time block codes using multiple transmitting antennas. J. Wirel. Networking Commun. **5**(1), 9–18 (2015). https://doi.org/10.5923/j.jwnc.20150501.02
28. N.S. Murthy, S. Sri Gowri, B. Prabhakara Rao, Orthogonal Stbcs for five, six and seven transmit antennas. Recent Adv. Commun. Network. Technol. **3**(2), 93–96 2014. ISSN: 2215–082X (Online), ISSN: 2215–0811 (Print) (free journal)
29. N.S. Murthy, S. Sri Gowri, B. Prabhakara Rao, Non orthogonal quasi-orthogonal space-time block codes based on circulant matrix for eight transmit antennas. Int. J. Appl. Eng. Res. **9**, 9341–9351 (2014). ISSN 0973–4562 (Scopus index)
30. N.S. Murthy, S. Sri Gowri, B. Prabhakara Rao, Low delay general complex orthogonal space-time block code for seven and eight transmit antenna. Int. J. Eng. Res. Technol. (IJERT) **2**(6) (2013). ISSN: 2278–0181
31. N.S. Murthy, S. Sri Gowri, B. Prabhakara Rao, Orthogonal space-time block codes for four, five and transmit antennas with 4/7 and 5/11 code rates. Int. J. Eng. Res. Appl. (IJERA) **3**(3), 1380–1382 (2013). ISSN: 2248–9622
32. N.S. Murthy, S. Sri Gowri, B. Prabhakara Rao, Orthogonal space-time block codes for 6 transmit antennas. Int. J. Eng. Res. Appl. (IJERA) **2**(4), 362–364 (2012). ISSN: 2248-9622
33. N.S. Murthy, S. Sri Gowri, B. Prabhakara Rao, Two new general complex orthogonal space-time block codes for 6 and 16 transmit antenna. Int. J. Electron. Commun. Eng. Technol. **3**(2) (2012). ISSN 0976-6464
34. N.S. Murthy, S. Sri Gowri, Full rate general complex orthogonal space-time block code for 8-transmit antenna. ELSEVIER*, SCIVERSE Science Direct Procedia Engineering* in IWIEE 2012, China, Jan. 9–10, 2012. *H Index: 11, IF: 0.61 (Scopus index),* ISSN: 1877–7058
35. N.S. Murthy, S. Sri Gowri, B. Prabhakara Rao, New high rates non-orthogonal stbcs for seven and eight transmit antennas. IETE National J. Innov. Res. II(II), 9–12 (2014). ISSN2320–8961
36. N.S. Murthy, S. Sri Gowri, B. Prabhakara Rao, Quasi-orthogonal space-time block codes based on circulant matrix for eight transmit antennas. *IEEE International Conference on Communication and Signal Processing—ICCSP 14 at Melmaruvathur, on 3rd-5th April 2014*
37. N.S. Murthy, S. Sri Gowri, B. Prabhakara Rao, New orthogonal space-time block code for eight transmit antenna. *Third International Conference on Recent Trends in Engineering & Technology (ICRTET'2014), 28th–30th March 2014,ELSEVIER Publications, Chandwad, Nasik*
38. N.S. Murthy, S. Sri Gowri, B. Prabhakara Rao, Orthogonal space-time block code for six transmit antenna. *International Conference on Communications, Networking and Signal Processing 19–21 September 2013, School of Electronics Engineering, VIT University, Vellore, Tamilnadu, India*
39. N.S. Murthy, S. Sri Gowri, B. Prabhakara Rao, Orthogonal space-time block code for maximal rate Nine Transmit antenna. *Second International Conference on Communication and Signal Processing on April 2013 , QIS engineering college, Ongole*
40. N.S. Murthy, S. Sri Gowri, Complex orthogonal space-time block codes rates 3/7 ,4/8 and 6/8for 3 ,4 and 4 transmit antennas in space time coding. *International Conference on Devices, Circuits and Systems—ICDCS 2012, Mar 15–16, 2012, Karunya University, Coimbatore, IEEE Explore*
41. N.S. Murthy, S. Sri Gowri, P. Satyanarayana, Complex orthogonal space-time block codes rates 5/13 and 6/14 for 5 and 6 transmit antennas. *Wireless Communications, Networking and Mobile Computing (WiCOM), 2011 7th International conference Sept 23–25 at Wuhan, China, IEEE Explore Digital Object Identifier*. https://doi.org/10.1109/wicom.2011.6040107

# Improving the Prediction of Traffic Flow in the Airport System Using Machine Learning


**Esha Agrawal and Chandrakant Navdeti**

## 1 Introduction

The variation in between requirement and airport acceptance capacity is a crucial problem within the national and international air transportation system, because of passengers travel by air increases and inadequate airport acceptance capacity. According to the U.S. transportation system more than 719 million people, around 26,000 flights travel per day in the year 2016 and this becomes more increasing in recent years. It is an ambition of the National Airspace System (NAS) to manage the air traffic flow at the national/international level to fulfill the demand with available capacity at the airport. As an increasing air traffic business, as sudden change in weather condition demand is also increasing [1]. There is some tool available that directly predicts the airport capacity. Overestimation and underestimation [1] of airport capacity are the two major issues in the decision-making process which affects the traffic management system. This paper uses historical air traffic data.

A machine learning framework approach is used to predict the capacity at the terminals area which is shown in Fig. 1. Multi-layer clustering is used on data to find out the clusters. It is an unsupervised learning method.

On some attributes of the database, here we apply the features extraction model which is not previously done. Based on this extracted output classification model is to develop. The classification model predicts the terminal capacity. According to terminal availability, it is easier in an emergency to allocate terminal and runway to that flight. Paper is organized into five parts which are as follows: Part II describes a survey of related work on airport acceptance capability and flight course which more primarily based on clustering and machine learning model. Part III is for problem definition. Part IV gives details about an overview of the framework, data set and details of methods used for airport capacity prediction. Part V shows a result of clustering, classification.

E. Agrawal (✉) · C. Navdeti
Department of Information Technology, SGGSIE & T, Nanded, Maharashtra, India



C. K. Chanda et al. (eds.), *Advanced Energy and Control Systems*, Lecture Notes in Electrical Engineering 820, https://doi.org/10.1007/978-981-16-7274-3_24

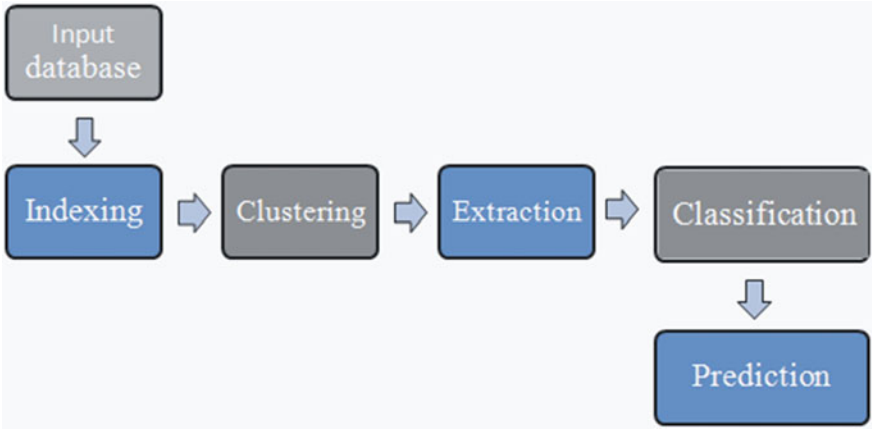


**Fig. 1** Block diagram for airport acceptance capacity

## 2 Previous Work

As a body of literature, a vast amount of data generated and documented periodically by the air traffic control system and advances in computer technology have arisen to investigate how artificial intelligence and research methods are applied to identify and predict air traffic management-related information to enable improved traffic flow management decision-making. Airport efficiency is determined by a variety of economic, organizational and technical factors. Usually, runway configuration is the main structural/operational component that affects an airport's efficiency throughput. The new empirical framework [1] was developed for the estimation of the arrival potential of metroplex which is based on output curves obtained from historical flow patterns. The model for the New York metroplex is illustrated in terms of its scope and significance in the national airport system. Deterministic aircraft movement framework [2] in airspace, regulated air traffic that encircling the airfield. The method performs practical paths, makes detailed forecasts and extracts the mathematical distribution of aircraft trajectory.

In aircraft operations, clustering techniques are more frequently used to estimate airflow patterns for effective design of airport and airspace, airport capacity planning, air traffic flow management. In defining a cluster of arbitrary shapes and good efficiency on a large, DBSCAN is considerably more efficient and simple. Evaluating the algorithm on real-time data. HCA [6] groups taxi paths in space, and in time. Uses recorded data of Charlotte Douglas International Airport. This algorithm shows the typical taxi paths in the form of the clusters, and then these clusters are used to classify unusual airflow patterns.

The airport acceptance rate prediction protocol [5] for forecasting ranges across possible AARs. Actual AAR, climate and prediction observations from San Francisco airport had been used to execute the assessments. Financial, management and

policy frameworks [8] are necessary for handling the requirement and capability of the airports, also measures for evaluating the fundamental judgments and the consequences for the production and management of terminals. It focuses more on travel plans, terminal operation, and smart guide.

The discrete choice model [3, 4] illustrates the value of a utility function in terms of specific variables. The model offers a probabilistic runway configuration estimation for the next 15-min span, provided the temperature, traffic demand, and actual runway configuration [4]. The maximum likelihood discrete choice model [3] explains the influence of various decision-making factors, which makes marginally better predictions of changes in runway layout than a regression model based on different configurations. This approach uses data from the Newark, LaGuardia airports. The system is guided as well as tested in European airspace [7] using empirical scheduled flight details. It uses a specialized reshuffle technique. In this paper, we calculate airport acceptance capacity through a mixed machine learning approach.

## 3 Problem Definition

Due to lack of capacity, there may be a problem of overestimation and underestimation has occurred. In case of any emergency landing, to avoid flight accident as crashing 2 need of traffic management. Overestimation includes holding and divergent situations [1] as shown in Fig. 2. A circle shows holding a flight in the air up to get a free runway. In such a situation, it may suffer because of wind or rain direction.

D indicates diversions flight to another terminal in any unpleasant condition and it may cause flight crashes as c1. Capacity underestimation can lead to an effective sub-use of resources and unnecessary delay in flooring.

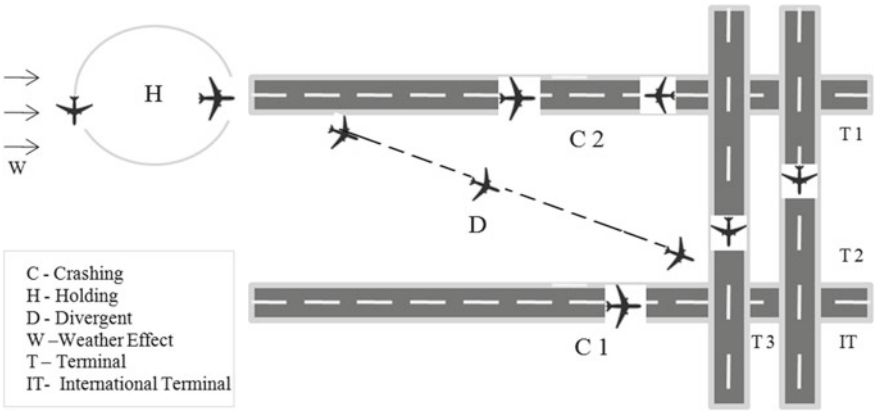


**Fig. 2** Problem in any emergency situation

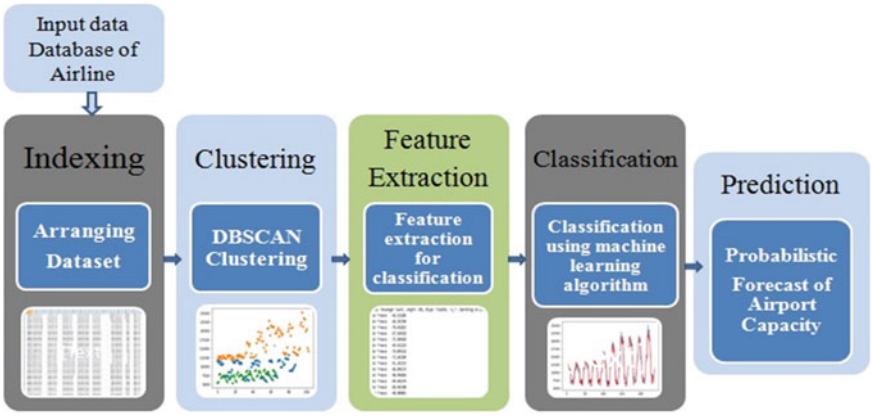


**Fig. 3** Machine Learning framework

## 4 Proposed Methodology

### *4.1 Internal Working of Machine Learning Model and Sub-model for the Prediction of Air Traffic*

The sequential machine learning model is used for identification; prediction of air traffic flow depends on a modular framework which is shown in Fig. 3. After indexing of the data set a multi-layer clustering [1] is used for identifying groups of air traffic patterns. Once air traffic is classified features are extracted by using some attribute as passenger count. Finally, classification is performed on extracted features. Depending on the information produced by the classification process, it will predict traffic flow from historical data. Each module of the frame and data set is described in the following section.

### *4.2 Data Set*

For the prediction of airport acceptance rate informative historical data set retrieved from European union open data set portal. Attribute including Activity Period, Operating Airline, Published Airline, Terminal, Passenger Count, Adjusted Activity Type Code, Adjusted Passenger Count from the year 2005–2016 is used. Data set contains more than 15,000 records.

### 4.3 Clustering-DBSCAN

There is one basic rule that applies to every clustering method to determine similar values and in the cluster the records into groups. Density-Based Spatial Clustering of Application with Noise (DBSCAN) [5] uses to make a group of air traffic within a given timestamp. It is an unsupervised learning method. DBSCAN is mostly widely used in dense regions, separate more dense clusters, and lower dense clusters. Here, we use this clustering algorithm for finding out the density of air traffic flow within a year of an airline and terminal area. Another advantage of this method has the ability to finding out non-convex clusters. DBSCAN focused on the two main input parameters as follows.

Two main parameters are the following.

1. **MinPts**: esp radius contains less number of data points is called as MinPts. On the off chance that a dataset is an enormous pick the bigger estimation of MinPts. As per rule, the MinPts base can be extracted from the number of factors D in the database as, MinPts more than or equivalent to D + 1. The base estimation of MinPts ought not to be under 3.
2. **esp (Ɛ)**: It characterizes the point around an information point, for example, if the separation between any two points is less or equivalent to eps then they are considered as neighbour's point. If the value of eps is too small then a significant proportion of the data would be considered as outliers. If esp value is too larger then the clusters will merge and lots of the data points will be in the same clusters hence less number of clusters will form.
3. Here, we divide the data set into the three clusters high density-based cluster, medium density-based cluster and low density-based cluster as shown in Fig. 4. Airline data are a group in different colour clusters, blue colour which shows high density-based cluster. The X-axis indicates the number of samples, and the Y-axis indicates the number of flights. Blue colour indicates the highest dense region.

### 4.4 Features Extraction

Several features are extracted from airline data for analysing more correctly.

Features are extracted on attribute activity period, passenger count and adjusted passenger count. We calculate features as ema, sma, etc.

1. **Simple Moving Average (SMA)**: It is calculated as the summation of all records $x_i$ divisible by the number of records N. A simple moving average smooths out volatility and makes it easier to predict passenger count within a particular duration. SMA calculated as

$$sma = \frac{\sum_{(i=1)}^{N} x_i}{N} \tag{1}$$

**Fig. 4** Clustering-DBSACN

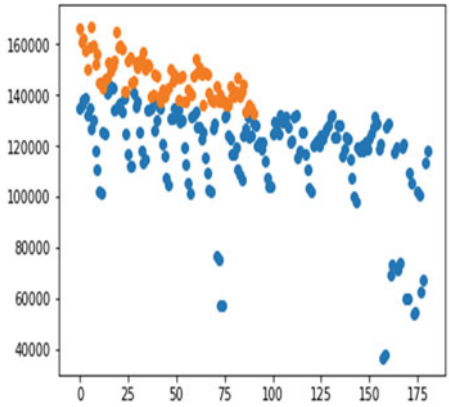


(a) American Airline

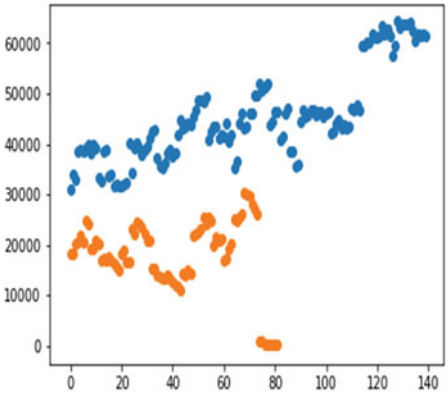


(b) JetBlue Airline

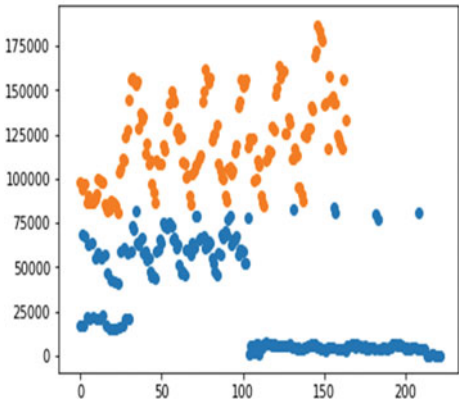


(c) Delta Airline

2. **Expositional Moving Average (EMA)**: It adds more weight in data which is more current data points due to its distinctive calculation, and EMA can follow data points closely than a corresponding SMA. Calculated as

$$ema = endvalue_t \times K + ema_y \times (1 - K) \tag{2}$$

3. **Double Expositional Moving Average (DEMA)**: This average helps to confirm uptrend when the passenger is above the average and helps confirm downtrends when the passenger is below the average. Calculated as

$$dema = 2 \times ema - ema(ema) \tag{3}$$

4. **Triple exponential moving average (TEMA)**: For calculating the TEMA, calculate the first EMA and second EMA. TEMA is calculated by the following formula:

$$tema = 3 \times ema - 3 \times (ema)^2 + (ema)^3 \tag{4}$$

5. **Moving Average of Convergence Divergence (MACD)**: This measure is a set of three time interval, very often calculated using historic data. Focus on more recent passenger records. It is the difference of EMAs with a given period a, b. Here, it is the difference between $EMA_{12}$ and $EMA_{26}$.

$$macd = ema_{12} - ema_{26} \tag{5}$$

6. **Relative Strength Index (RSI)**: The RSI measures the magnitude of data points. The relative strength index is computed in two parts, i.e. RSI for passenger count and adjusted passenger count starts with the following formula. It is also a momentum indicator. Calculated as

$$rsi = 100 - \left[\frac{100}{1 - rs}\right] \tag{6}$$

7. **Stochastic Rsi**: It is a measure of RSI relative to its own high or low range that varies over a given time. This indicator is primarily used for identifying more than average traffic capacity. Calculated as:

$$rsi = \frac{(rsi - minrsi)}{(maxrsi - minrsi + 1)} \tag{7}$$

8. **Average True Range (ATR)**: This predictor is evaluated as follows. In very first step difference of Adjusted passenger and passenger count; in a second step difference of the absolute value of the Adjusted passenger and passenger count close; and the absolute small current value less than the previous close. Therefore, the total real range is a weighted average of the actual ranges.

$$atr = \left(\frac{1}{n}\right) \sum_{(i-1)}^{(n)} tr_i \tag{8}$$

9. **Volatility Ratio (VR)**: It is the technical analysis indicator used to identify passenger count ranges and breakouts. VR is ration of average true range and expositional moving average. VR is calculated by the following formula:

$$vr = \frac{atr}{ema} \tag{9}$$

10. **Williams%Range**: WR is known as the Williams Percent Range. It is a form of momentum indicator. Williams percent R sensor is somewhat similar to and is used in the same manner as the Stochastic oscillator. Where $highest_{high}$ is the highest number of passenger count, $val_{close}$ is the most recent value and $lowest_{low}$ is the lowest number of passenger count.

$$wr = -100 \times \left[\frac{highest_{high} - val_{close}}{highest_{high} - lowest_{low} + 1}\right] \tag{10}$$

11. **Commodity Channel Index (CCI)**: It is a momentum-based oscillator also an unbounded predictor. It is calculated by the difference between present demand and average historical demand as follows:

$$cci = \frac{val_{close} - sma}{0.015 \times val_{deviation}} \tag{11}$$

Table 1 shows sample values of extracted features as sma, ema, dema, tema, macd, cci, wr contain multiple values where RSI and stochastic Rsi, atr contain a single value.

## *4.5 Prediction Using a Machine Learning Algorithm*

The Random Forest is a Machine Learning algorithm, not only used for supervised classification but also used for regression. As the name suggests it is the same as the relationship between forest and ample of different trees. The Random Forest Algorithm combines various decision trees that are having a similar node but utilizes various information that prompts various leaves. The prediction of the random forest is more stable than a decision tree. Here, we use the values of features extraction as input which are shown in Table 1. Every time consider 10 samples values for construction of decision tree. Data is classified in 1 and 0 accordingly that it shows the airport capacity. An algorithm is based on the following steps.

**Table 1** Features values

| F | A | American | Jetblue | Delta |
|---|---|---|---|---|
| SMA | | −4666.7 | −23.45 | 65.35 |
| EMA | | −56.786 | −3533.56 | −243.67 |
| DEMA | | 4.546 | −6333.65 | −46.35 |
| TEMA | | −45.67 | −385.6 | −84.40 |
| MACD | | −251.45 | −407.516 | 17.16 |
| RSI | | 52.398 | 41.96 | 49.0 |
| SRSI | | 0 | −112.289 | 2160.0184 |
| ATR | | 0 | 0 | 487.720 |
| VR | | 0 | 0 | 0.006799 |
| WR | | −0.49,4.8 | 0 | −99.6338 |
| CCI | | −16.4 | 0 | −316.34 |

1. Select in random values features extraction as SMA, EMA, TEMA, DEMA, MACD having many values, bootstrapping of data
2. Construct a decision tree for every for 10 sample each feature
3. Vote the result of a decision tree
4. Prediction according to it.

## 5 Results

In this section, we explain the accuracy, predicted results. Accuracy calculated by the use of accuracy measurement formula is as follows: $v_o$ indicate the observed value, and $v_a$ indicate accepted value. Accuracy depends on the predicted duration. As we use the DBSCAN method get the clusters for the airline which is as shown in Fig. 4.

$$accuracy = \frac{(v_o - v_a)}{v_a} \times 100 \tag{12}$$

As a novelty of our work determining the data analysis features. Table 1 indicates the values of sma, ema, dema, tema, macd, etc. of different airlines. Figure 5 shows the graph of extracted data analysis features. A number of the curve in the graph depending on the count of flights as any airline contains more number of an airline than the graph is denser as shown in Fig. 5c. After using Random Forest machine learning algorithm, we predicted the terminal capacity of the near future.

Table 2 shows the prediction of the next 2 days capacity of terminals. As we see on day 1 capacity of terminal 1 is 68.3% this indicates if any emergency landing is needed on day 1 then terminal 1 is free for that situation.

Figure 6. shows same as in Table 2 in graph. Terminal T3 on day 1 shown by bar with line indicates that only terminal T3 is free on day 1 for any emergency landing.

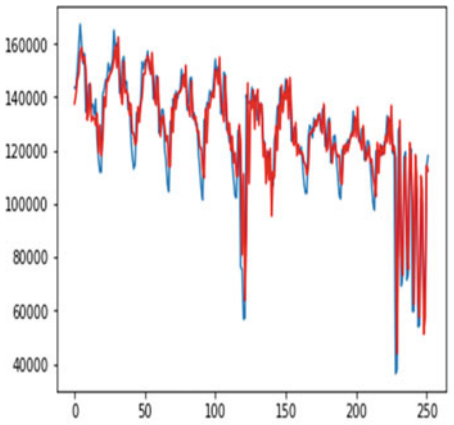


(a) American Airline

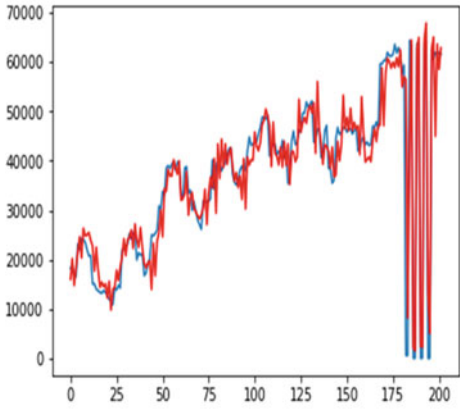


(b) JetBlue Airline

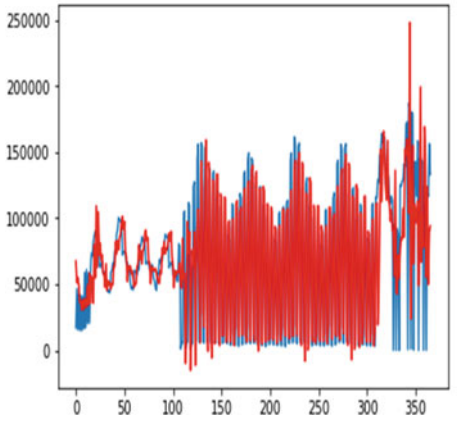


(c) Delta Airline

**Fig. 5** Graph for feature extraction

**Table 2** Two day terminal capacity estimate

| Airline | Day | TC | Incoming | Outgoing |
|---|---|---|---|---|
| American | 1 | T3—68.3% | 2049 | 2049 |
| | 2 | T3—100% | 86,429 | 86,429 |
| JetBlue | 1 | IT—100% | 5880 | 5880 |
| | 2 | IT—100% | 6365 | 6365 |
| Delta | 1 | T1—100% | 6183 | 6183 |
| | 2 | T1—100% | 48,563 | 48,563 |

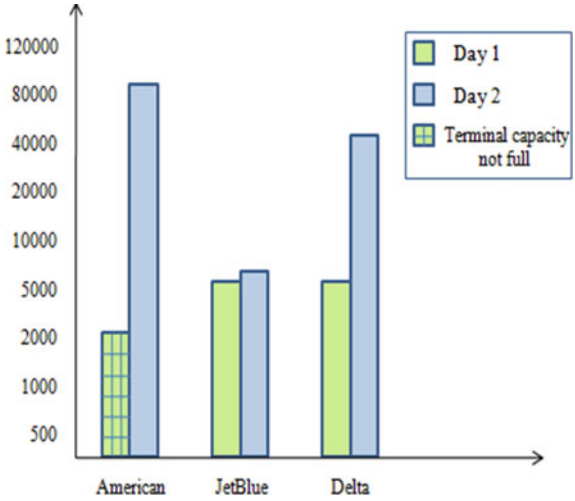


**Fig. 6** Graph for two-day prediction

## 6 Conclusion

Planning of airport acceptance capacity is a complex problem that is faced by air traffic managers every day. This paper presents the machine learning model for the prediction of future airport acceptance capacity towards improved capacity and air traffic flow management. The technique can be extended on any airline network worldwide. A multi-layer clustering is used to make a group of high, low, medium density-based air traffic in the terminal area. Further extracting the functionality of data processing is used as input for Random Forest machine learning. Capability of airports is ultimately predicated on the use of Random Forests. Final result predicts the occupied terminal capacity, accordingly that air traffic managers can manage the air traffic even in any emergency condition it also shows a count of incoming and outgoing passengers and a count of incoming and outgoing flights.

This system works on different airline data of a specific airport. American Airlines shows 83.3% accuracy for the next 2-day prediction. While on the prediction of the

next 72-h, its shows 72.4% accuracy. Prediction accuracy is calculated in the 24-h format; this means that as the duration of prediction decreases accuracy increases. Same as above Delta Airlines shows 82.2% accuracy for the next 48-h prediction and 70% for next 3-day prediction. However, we assume that this approach to machine learning can be very beneficial in informing other ongoing analysis and simulation projects to help other automation systems to enhance safety and operational efficiency at airports.

## References

1. F. Author, Article title. Journal **2**(5), 99–110 (2016); M.M.C. Rocha, R.J. Hansman, Identification, characterization, and prediction of traffic flow patterns in multi-airport systems. IEEE Trans. Intell. Transp. Syst. **20**(5), 1683–1696 (2018)
2. S.T. Barratt, M.J. Kochenderfer, S.P. Boyd, Learning probabilistic trajectory models of aircraft in terminal airspace from position data. IEEE Trans. Intell. Transp. Syst. **20**(9), 3536–3545 (2018)
3. V. Ramanujam, H. Balakrishnan. Estimation of maximum-likelihood discrete-choice models of the runway configuration selection process, in *Proceedings of the 2011 American Control Conference*, pp. 2160–2167. IEEE, 2011
4. A. Jacob, H. Balakrishnan, Predicting airport runway configuration: a discrete-choice modeling approach, in *Proceedings 11th USA/Eur. Air Traffic Manage*. Res. Develop. Seminar, Lisbon, Portugal, pp. 1–11 (2015)
5. C. Jonathan, M.J. Kochenderfer, Probabilistic airport acceptance rate prediction. *AIAA Modeling and Simulation Technologies Conference* (2016)
6. A.M. Churchill, M. Bloem, Clustering aircraft trajectories on the airport surface, in *Proceedings of the 13th USA/Europe Air Traffic Management Research and Development Seminar*, Chicago, IL, USA, pp. 10–13 (2019)
7. M. Bernardo, V.D.P. Servedio, V. Loreto, Congestion transition in air traffic networks. PloS One **10**(5), e0125546 (2015)
8. A. Jacquillat, A.R. Odoni, A roadmap toward airport demand and capacity management. Transp. Res. Part A: Policy Pract. **114**, 168–185 (2018)

# Invasive Weed Optimization Based Reduced Order Modelling


**Rajul Goyal, Girish Parmar, and Afzal Sikander**

## 1 Introduction

Nowadays, in control engineering, it is an emerging field for research to reduce the original systems with high order to models with low order. Generally, if a differential equation is of higher order in the frequency domain, then its transfer function is also of higher order. It is very difficult and tedious to analyze a system with higher order. So, it becomes necessary to minimize the order of transfer function for designing the systems.

Various reduction methods are used on the basis of stability which minimizes the stability problem also. To achieve this, stability criterions are used. "Evolutionary Techniques" are the most prominent algorithms used in the field of reduced order modelling.

Methods are also available for approaching at stable reduced-order approximants using evolutionary techniques [1, 2]. Using the stability equation method an improved method for Pade approximants was proposed in [3].

To enhance capabilities of tuning for conventional PID controller's parameters, several intelligent approaches have been suggested to improve the tuning of PID controller [4–7].

Being inspired from colonizing weeds a novel numerical stochastic optimization algorithm has been proposed in [8]. The properties of weeds may give rise to a powerful optimization algorithm. A method based on IWO technique is used to study the electricity market dynamics [9]. A printed Yagi antenna has been designed and optimized using this IWO technique [10].

Except the methods discussed above, some more references can also be seen for model reduction & control using evolutionary techniques [11–13].

R. Goyal (✉) · G. Parmar
Rajasthan Technical University, Kota, Rajasthan 324010, India

A. Sikander
Dr. B. R. Ambedkar, National Institute of Technology, Jalandhar, Punjab 144011, India



C. K. Chanda et al. (eds.), *Advanced Energy and Control Systems*, Lecture Notes in Electrical Engineering 820, https://doi.org/10.1007/978-981-16-7274-3_25

## 2 Overview of IWO

The IWO has been described in Fig. 1 while the properties, features, advantages, disadvantages, mathematical modelling, pseudo codes for implementing the IWO and comparison with GA and PSO have been given in [8–10, 14–16].

On studying the behaviour of weed plants a biologically inspired innovative algorithm is developed called Invasive Weed Optimization (IWO). Growth of seeds and reproduction concept in a weed colony is used in this algorithm. In the environment weeds grow in a random manner. The robust and adaptive properties of weeds are being used as a mathematical tool for optimization adaptive and robust properties of weeds are being applied [8].

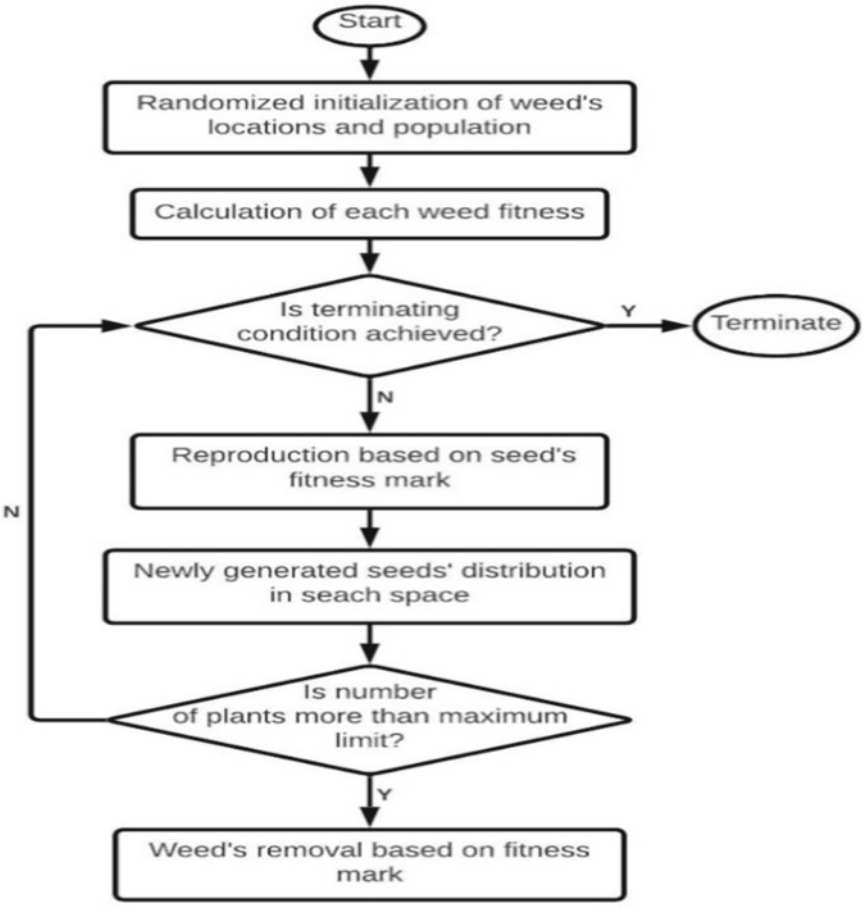


**Fig. 1** Flow chart of IWO

PID controllers have very simple structure and easy tuning. These properties of PID controllers have made them very useful in different process, chemical or paper and pulp industries. As per the requirement of industries finding of suitable measures of PID controller is known as tuning of PID controller. Therefore, in this study an innovative concept for system simplification and its control is proposed. To optimize a pre-specified fitness function with IWO is the basic concept applied in this present work.

## 3 IWO Based Reduced Order Modelling

Usually, physical systems are transformed into mathematical model in the form of differential equations which yields complex high order models which are difficult to understand. The exact analysis of these systems is monotonous, expensive and complicated. So, it is useful to obtain simple model of high order systems. By order reduction the computation and hardware complexity of particular systems can be made easy. The LOS provides an adequate approximation of the original system's response to particular inputs and preserves the stability of the higher order model.

In present work, reduced order modelling of single input single output linear time invariant systems has been done by employing IWO. To minimize the objective function the program with IWO algorithm has been run for 100 iterations. Also, the applied algorithm has been compared with other available researched methods.

### *3.1 Problem Statement*

PID controller is very popular because of the reasons.

Suppose the $r$th order LOS is defined as:

$$R_r(s) = \frac{\alpha_0 + \alpha_1 s + \alpha_2 s^2 + \cdots + \alpha_{n-1} s^{n-1}}{\beta_0 + \beta_1 s + \beta_2 s^2 + \cdots + \beta_n s^n} \tag{1}$$

Now, the objective function; ISE for the same is defined as:

$$ISE = \int_0^\infty [y(t) - y_r(t)]^2 dt \tag{2}$$

where, $y(t)$ & $y_r(t)$ are the step responses of HOS and LOS, respectively.

The MATLAB-SIMULINK model of the above Integrated Square Error with unit step input is shown in Fig. 2.

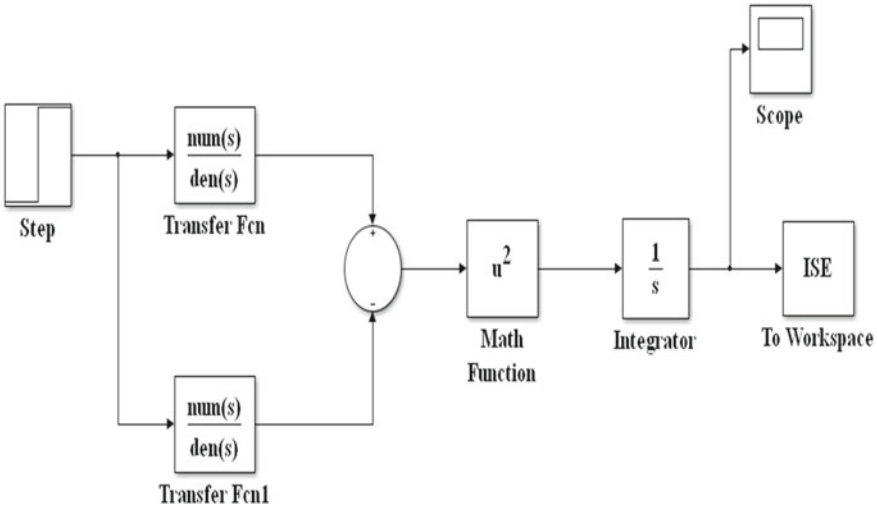


**Fig. 2** SIMULINK model of system with objective function ISE

$$G_n(s) = \frac{a_0 + a_1 s + a_2 s^2 + \cdots + a_{n-1} s^{n-1}}{b_0 + b_1 s + b_2 s^2 + \cdots + b_n s^n} \tag{3}$$

In weed colonies weeds grow severely in a random manner giving a threat to useful plants. Highly adaptiveness in environment, compatibility and stability are the important characteristics of weeds. The optimization of IWO algorithm is based on these useful characteristics of weeds. By this mathematical function is globally optimized. IWO is a powerful and innovative technique.

## 4 Results and Discussions

The present work is elaborated and analyzed using the following numerical/simulation example.

### *4.1 Example: 8th Order SISO-LTI-HOS*

The same example given in [17–19] has been taken for the present work:

$$G_8(s) = \frac{18s^7 + 514s^6 + 5982s^5 + 36380s^4 + 122664s^3 + 222088s^2 + 185760s + 40320}{s^8 + 36s^7 + 546s^6 + 4536s^5 + 22449s^4 + 67284s^3 + 118124s^2 + 109584s + 40320} \tag{4}$$

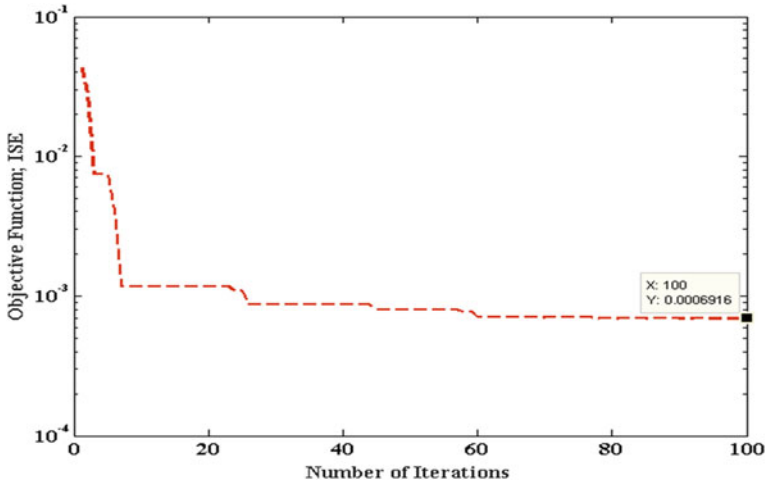


**Fig. 3** Convergence of ISE versus iterations

Now, ISE obtained by IWO with 100 iterations is $6.9165 \times 10^{-4}$ and the convergence diagram for the same is shown in Fig. 3. The polynomials of reduced order system are obtained as.

Denominator polynomial:

$$D_2(s) = 1.0166s^2 + 6.9831s + 5.3466 \tag{5}$$

Numerator polynomial:

$$N_2(s) = 17.1965s + 5.3466 \tag{6}$$

Hence, the 2nd order LOS is given by:

$$R_2(s) = \frac{17.1965s + 5.3466}{1.0166s^2 + 6.9831s + 5.3466} \tag{7}$$

Step and frequency responses of HOS and LOS have been shown in Figs. 4, 5, 6 and 7.

Step responses of HOS and IWO optimized LOS have also been compared as shown in Figs. 8, 9, 10 and 11, for different available techniques.

The comparison of obtained ISE using IWO with other previously researched techniques is also given in Table 1 in which IWO is being proved superior since value of ISE is less as compared to others.

Bar chart comparison for the ISE has also been shown in Fig. 12 from which it can be seen that the ISE value obtained by IWO algorithm is less in comparison to other available techniques in literature.

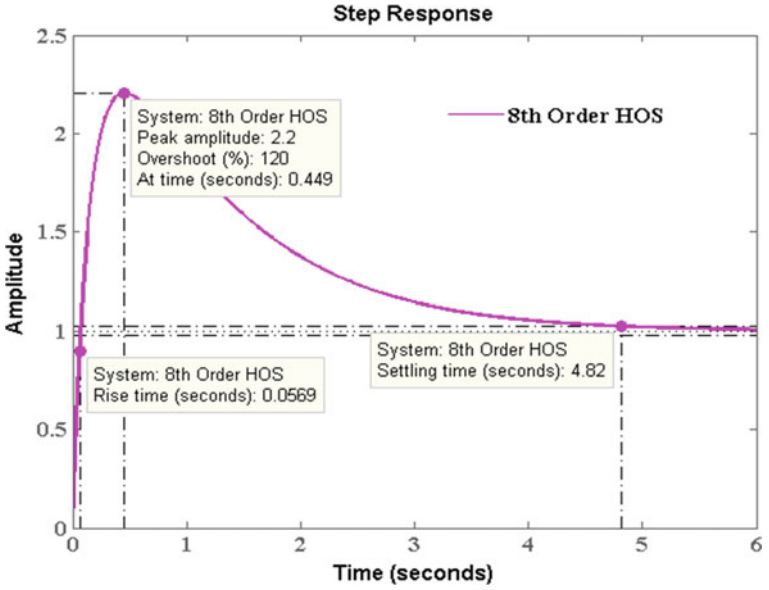


**Fig. 4** Step response of 8th order HOS

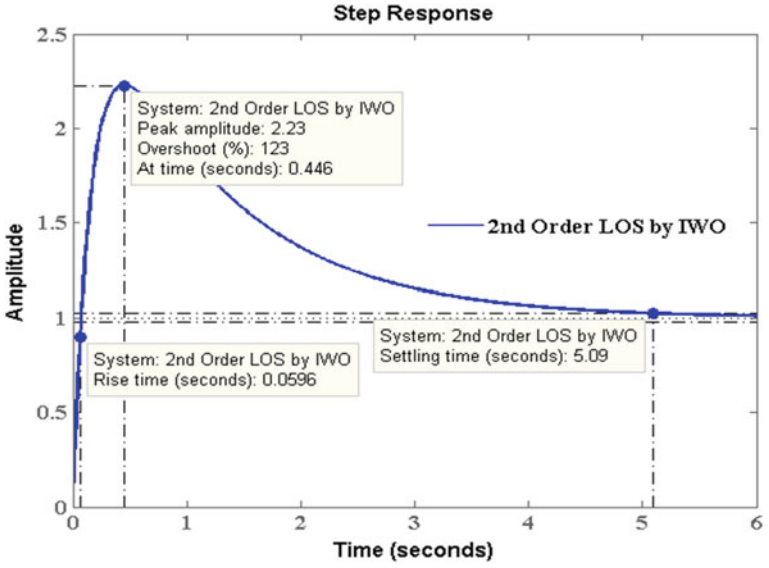


**Fig. 5** Step response of 2nd order LOS

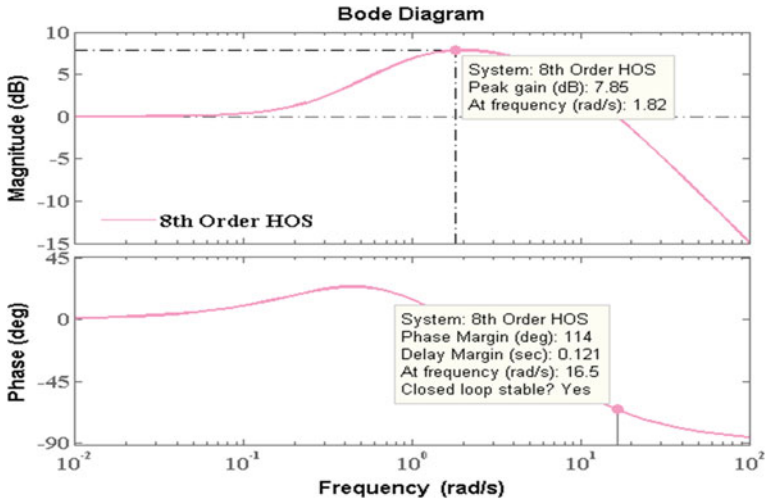


**Fig. 6** Frequency response of 8th order HOS

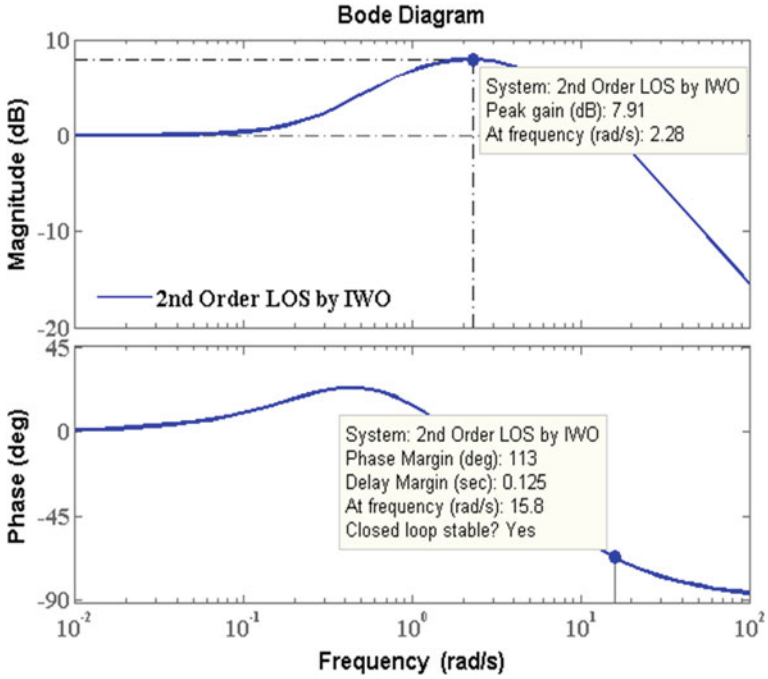


**Fig. 7** Frequency response of 2nd order LOS

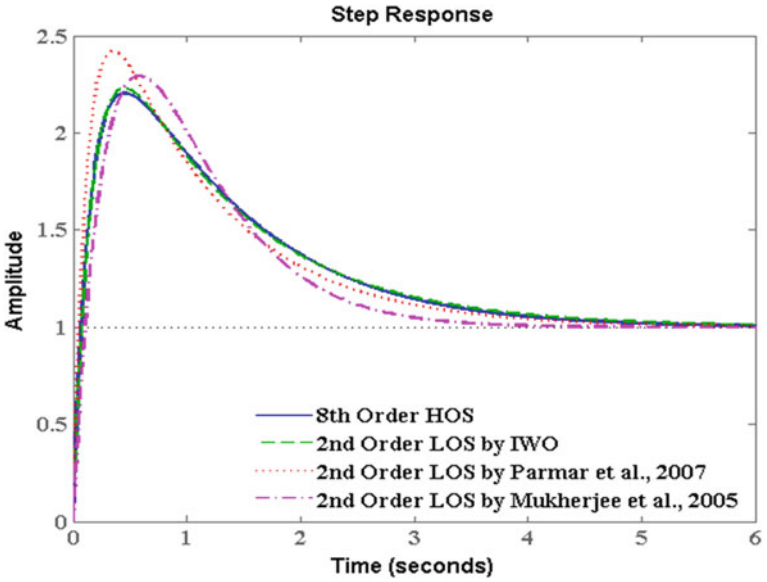


**Fig. 8** Step responses compared with existing techniques

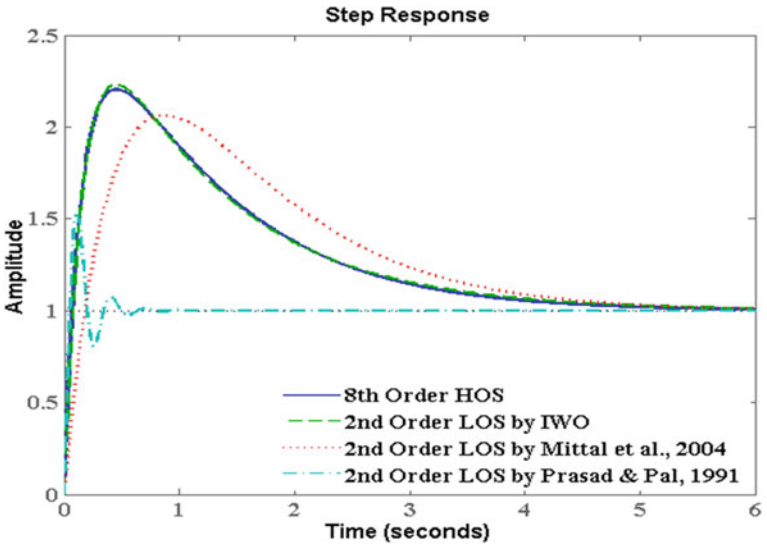


**Fig. 9** Step responses compared with existing techniques

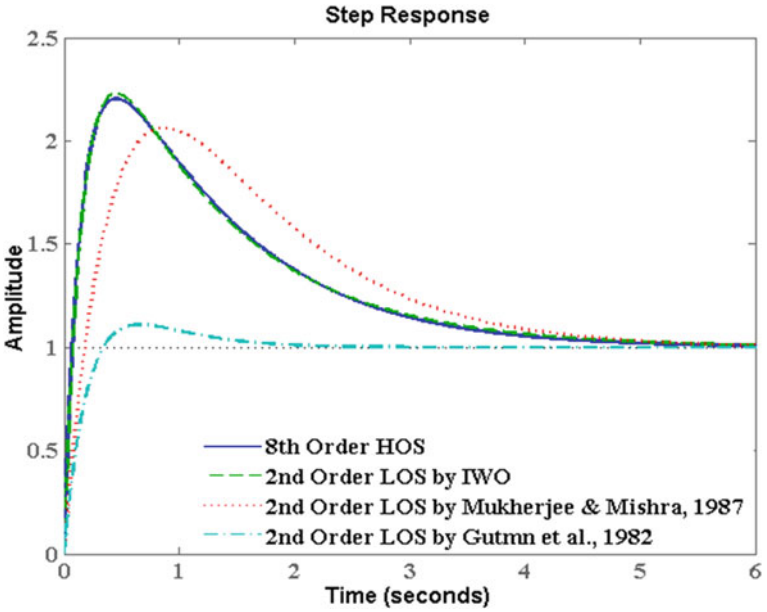


**Fig. 10** Step responses compared with existing techniques

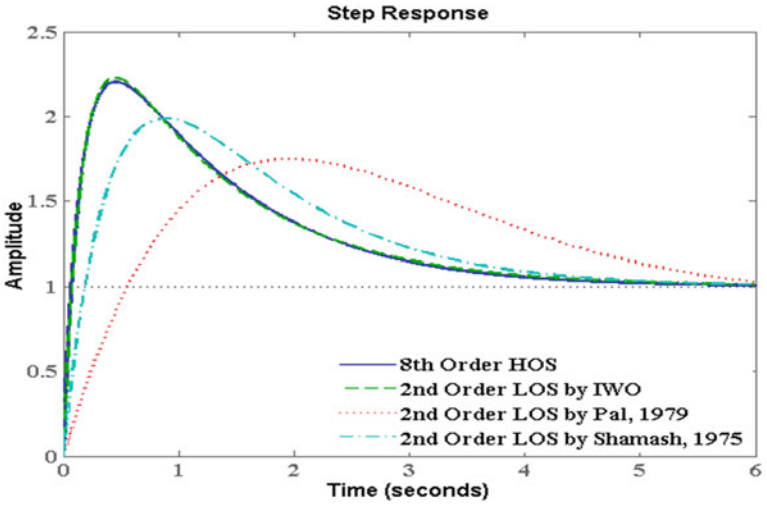


**Fig. 11** Step responses compared with existing techniques

**Table 1** ISE compared with other techniques

| Method | Reduced models | ISE |
|---|---|---|
| IWO algorithm | $\frac{17.1956s + 5.3466}{1.0166s^2 + 6.9831s + 5.3466}$ | $6.9165 \times 10^{-4}$ |
| Mukherjee and Mishra [20] | $\frac{7.0903s + 1.9907}{s^2 + 3s + 2}$ | 6.9165 |
| Hutton and Friedland [21] | $\frac{1.98955s + 0.43184}{s^2 + 1.17368s + 0.43184}$ | 18.3848 |
| Gutman et al. [17] | $\frac{4\ [133747200s + 203212800]}{85049280\ s^2 + 552303360s + 812851200}$ | 8.816 |
| Krishnamurthy and Seshadri [18] | $\frac{155658.6152s + 40320}{65520s^2 + 75600s + 40320}$ | 17.5345 |
| Pal [22] | $\frac{151776.576\,s + 40320}{65520\,s^2 + 75600\,s + 40320}$ | 17.6566 |
| Mukherjee et al. [16] | $\frac{11.3909s + 4.4357}{s^2 + 4.2122s + 4.4357}$ | 2.1629 |
| Parmar et al. [23] | $\frac{24.1144s + 8}{s^2+9s + 8}$ | 1.7924 |
| Mittal et al. [19] | $\frac{7.0908s+1.9906}{s^2 + 3s + 2}$ | 6.9159 |
| Prasad and Pal [24] | $\frac{17.98561s + 500}{s^2 + 13.24571\,s + 500}$ | 18.4299 |
| Shamash [25] | $\frac{6.7786s + 2}{s^2 + 3s + 2}$ | 7.3183 |

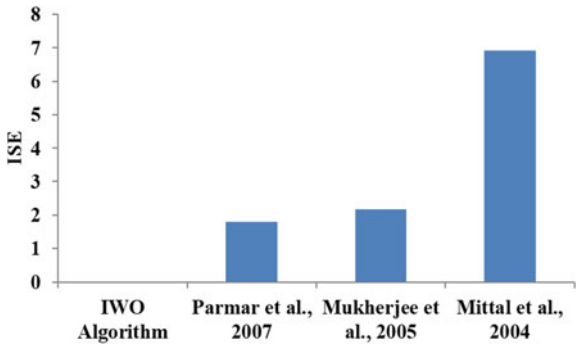


**Fig. 12** Bar chart comparison

## 5 Conclusions

In the present work, IWO has been employed for reducing order of SISO-LTI systems. Objective function used is to minimize the ISE. Unknown parameters of all polynomials of LOS are evaluated effectively using the IWO algorithm. For the sake of fair comparison and analysis an example has been simulated. The step responses of HOS and obtained LOS using IWO have been also been compared with available techniques. Simulation results show that the response of IW optimized LOS is closely approaching to the HOS. To show the effectiveness of IWO algorithm, bar chart comparison has also been shown.

## References


1. S. Panda, S. K.Tomar, R. Prasad, C. Ardil, Model reduction of linear systems by conventional and evolutionary techniques. Int. J. Electr. Comput. Energet. Electron. Commun. Eng. **3**(11) (2009)
2. S. Panda, J.S. Yadav, N.P. Patidar, C. Ardil, Evolutionary techniques for model order reduction of large scale linear systems. Int. J. Electr. Comput. Energet. Electron. Commun. Eng. **6**(9) (2012)
3. J. Pal, Improved pade approximants using stability equation method. Electron. Lett. **19**(11), 426–427 (1983)
4. Y. Yan, W.A. Klop, M. Molenaa, P. Nijdam, Tuning a pid controller: practicle swarm optimization versus genetic algorithms (2010)
5. K.J. Astrom, T. Hagglund, *PID Controllers: Theory, Design and Tunning*, 2nd ed. International Society of Automation (1995). ISBN 978-1–55617-516-9
6. P.V. Overschee, B.D. Moor, *RAPID: The End of Heuristic Tuning*. IFAC Proceeding (Elsevier, 2000)
7. K.H. Ang, G. Chong, Y. Li, PID control system: analysis, design and technology. IEEE Trans. Control Syst. (2005)
8. A.R. Mehrabian, C. Lucas, A novel numerical optimization algorithm inspired from weed colonization. Ecol. Inform. 355–366 (2006)
9. M. Sahraei-Ardakani, M. Roshanaei, A. Rahimi-Kian, C. Lucas, A study of electricity market dynamics using invasive weed colonization optimization, in *Proceedings of IEEE Symposium Computational Intelligenes Games (CIG '08)*, December 2008, pp. 276–282
10. S.H. Sedighy, A.R. Mallahzadeh, M. Soleimani, J. Rashed-Mohassel, Optimization of printed Yagi antenna using invasive weed optimization (IWO). IEEE Antennas Wirel. Propag. Lett. **9**, 1275–1278 (2010)
11. R. Goyal, G. Parmar, A. Sikander, A new approach for simplification and control of linear time invariant systems. Microsyst. Technol. Springer **25**, 599–607 (2019)
12. H.R. Sepehri, C. Lucas, A recommender system based on invasive weed optimization algorithm, in *Proceedings of IEEE Congress on Evolutionary Computation (CEC '07)*, September 2007, pp. 4297–4304
13. A.R. Mallahzadeh, H. Oraizi, Z. Davoodi-Rad, Application of the invasive weed optimization technique for antenna configurations. Prog. Electromag. Res. **79**, 137–150 (2008)
14. D.I. Abu, M.K. Oth, M.K. Zaer, S. Abo, F. Mohd, Invasive weed optimization for model order reduction of linear MIMO systems. Appl. Math. Modell. **37**, 4570–4577 (2013)
15. S. Saxena, Y.V. Hote, Advances in internal model control technique: a review and future prospects. IETE Tech. Rev. **29**, 461–472 (2012)
16. S. Mukherjee, M. Satakshi, R.C. Mittal, Model order reduction using response matching technique. J. Franklin Inst. **342**, 503–519 (2005)
17. P.O. Gutman, C.F. Mannerfelt, P. Molander, Contributions to the model reduction problem. IEEE Trans. Automat. Control **AC-27**(2), 454–455 (1982)
18. V. Krishnamurthy, V. Seshadri, Model reduction using the Routh stability criterion. IEEE Trans. Autom. Control **AC-23**(4), 729–731 (1978)
19. A.K. Mittal, R. Prasad, S.P. Sharma, Reduction of linear dynamic systems using an error minimization technique. J. Inst. Eng. India, IE (I) J. EL **84**, 201–206 (2004)
20. S. Mukherjee, R.N. Mishra, Order reduction of linear systems using an error minimization technique. J. Franklin Inst. **323**(1), 23–32 (1987). K.J. Astrom, PID controllers: theory, design and tuning. InstrtSoc Am. (1995)
21. M.F. Hutton, B. Friedland, Routh approximations for reducing order of linear time invariant systems. IEEE Trans. Automat. Control **AC-20**(3), 329–337 (1975)
22. J. Pal, Stable reduced order Pade approximants using the Routh Hurwitz array. Electron. Lett. **15**(8), 225–226 (1979)
23. G. Parmar, R. Prasad, S. Mukherjee, Order reduction of linear dynamic systems using stability equation method and GA. Int. J. Electr. Comput. Electron. Commun. Eng. **1**(2) (2007)

24. R. Prasad, J. Pal, Stable reduction of linear systems by continued fractions. J. Inst. Engrs. India, IE (I) J. EL **72**, pp. 113–116 (1991)
25. Y. Shamash, Linear system reduction using Pade approximation to allow retention of dominant modes. Int. J. Control **21**(2), 257–272 (1975)

# A Novel Model-Order Diminution Algorithm for LTIC System Using Whale Optimization


**Jay Kumar, Girish Parmar, and Afzal Sikander**

## 1 Introduction

In engineering system design, most of the problems are complex and complicated. The mathematical modeling of such a system generally results in a higher-order system (HOS). The analysis of such a higher-order model consumes a lot of simulation time and requires a large amount of storage and integrated circuits. Therefore, the model-order reduction (MOR) technique is used to approximate higher-order system (HOS) into lower-order system (LOS) which retains the fundamental properties of the original system [1]. MOR techniques were introduced many decades ago; still, a generalization algorithm is required to keep the dynamic characteristics of HOS intact with that of LOS.

Presently, order reduction has been used in various research fields such as chemical plants, aircraft, fluid dynamics digital communication network, economic system control system and electrical power system [2–4].

The rest of the paper is organized as follows: Sect. 2 briefly discusses the literature review; Sect. 3 describes the whale optimization algorithm; Sect. 4 describes the stated problem; Sect. 5 gives the simulation results of the selected numerical problem. The concluding remarks are given in Sect. 6.

J. Kumar (✉) · G. Parmar
Rajasthan Technical University, Kota, Rajasthan 324010, India

A. Sikander
Dr. B. R. Ambedkar, National Institute of Technology, Jalandhar, Punjab 144011, India



C. K. Chanda et al. (eds.), *Advanced Energy and Control Systems*, Lecture Notes in Electrical Engineering 820, https://doi.org/10.1007/978-981-16-7274-3_26

## 2 Literature Review

Order diminution is an important research area of control system since the inception of model-order diminution around the early 1960s when Davison presented "The Modal Analysis" by state space techniques. Later on, many researchers started to exploit this new area: Davidson [23], Chen and Shieh [24] used frequency-domain expansions; Gibilaro and Lees [25] matched the moments of the impulse response; Hutton and Friedland [26] used the Routh approach [5] for high-frequency approximation.

Various methods are available in the literature. Based on the embedding domain, these techniques can be categorized into two groups [6, 7], conventional time, frequency-domain techniques and evolutionary technique-based order diminution technique. The choice of order diminution method is dependent on the closeness of lower-order system's (LOS) response to the higher-order system (HOS). The time-domain-order diminution techniques require extensive knowledge of the eigen values and eigen vectors of higher-order systems, whereas frequency-domain techniques are algebraic in nature and in certain cases can reduce stable system to unstable system, and vice versa. Frequency-domain methods start from classical techniques such as eigen spectrum analysis [6], pade approximation [8] etc. It suffers from instability, non-minimum phase behavior, non-uniqueness and accuracy. Later on, mixed methods [9–11] were discovered which give more stability and avoid non-minimum phase condition but suffers in flexibility.

Due to certain drawbacks in conventional techniques, there is a space for the search engine optimization methods in the order diminution field to improve the performance by optimally choosing the value of lower-order system's coefficients. Wilson [12, 13] discussed the problem of optimality in model-order reduction (MOR) and recommended an optimization technique based on error minimization. In recent times, many evolutionary algorithms are used for the reduction of HOS, like Cuckoo search optimization [14], particle swarm optimization [15], Big Bang–Big Crunch algorithm [11, 16, 17], invasive weed optimization [18] and modified Cuckoo search [19]. These algorithms determine the numerator and denominator coefficient of the LOS by minimizing an objective function. Apart from these optimization methods, researchers are still searching for a universal optimization algorithm that can be implemented to all types of problems with full effectiveness.

In this paper, whale optimization has been utilized for order reduction of the LTIC system by minimizing the ISE as an objective function. The simulation results obtained from the WOA method are compared with the other techniques.

## 3 Background Concept

### *3.1 Time-Domain and Frequency-Domain Analysis*

Time-domain response is evaluated in terms of peak time, rise time, maximum overshoot, settling time etc. To make the design procedure simple logical and straightforward, there is a need for simple or fewer indices to evaluate the performance of the system. Various indices like integral square error (ISE), integral absolute error (IAE) and impulse response energy (IRE) are used in control theory. In the frequency-domain bode plot, the Nyquist plot is used for stability analysis.

### *3.2 Whale Optimization Algorithm (WOA)*

Whale optimization is a meta-heuristic algorithm proposed by Mirjalili and Lewis [20]. It is based on the swarm humpback behavior of whales. The interesting fact about the humpback whales is their devour technique called bubble-net feeding. During devour, whales create the special bubbles along a circular path surrounding their feed animal by spiraling up and bubbling up as they dive around 12 m below the surface and then swim upward the surface following the bubbles. The basic flowchart of the WOA algorithm is shown in Fig. 1.

## 4 Statement of Problem

The transfer function (TF) for *n*th-order SISO-LTI-HOS has been defined as

$$G_n(s) = \frac{\sum_{i=0}^{n-1} x_i s}{\sum_{i=0}^{n} y_i s} \tag{1}$$

where $x_i$ and $y_i$ are constants.

The *m*th-order reduced model of Eq. (1) is given as

$$R_m(s) = \frac{N_m(s)}{D_m(s)} = \frac{\sum_{i=0}^{m-1} c_i s^i}{\sum_{i=0}^{m} d_i s^i} \tag{2}$$

where $m < n$ *and* $c_i$ and $d_i$ are unknown constants.

ISE is considered an objective function, defined as [11, 12, 21, 22]

**Fig. 1** Flowchart of WOA

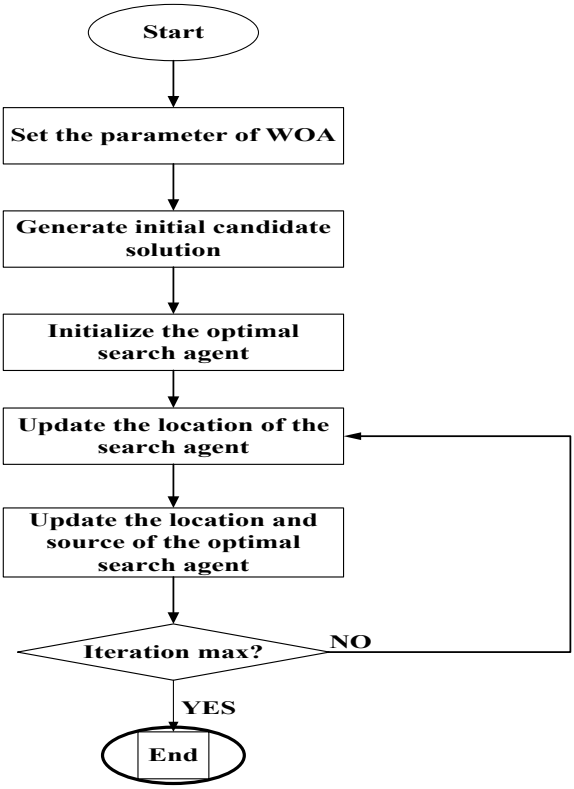


$$\text{ISE} = \int_0^\infty [y(t) - y_r(t)]^2 \text{dt} \tag{3}$$

The other performance indices used in the present paper are given as [12, 22]

$$\text{IAE} = \int_0^\infty |e(t)| \text{dt} \tag{4}$$

$$\text{IRE} = \int_0^\infty g^2(t) \text{dt} \tag{5}$$

where $e(t)$ is the error signal between step response of $y(t)$ (HOS) and $y_r(t)$ (LOS) as given in Eq. (4), and $g(t)$ is the impulse response of the system as given in Eq. (5).

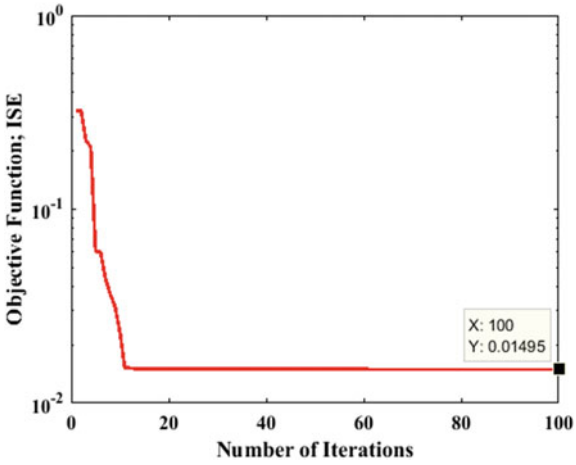


**Fig. 2** Convergence of objective function for example

## 5 Numerical Example and Simulation Results

Example: Let us consider a fourth-order system with repeated poles in s-plane defined as [19]

$$G_4(s) = \frac{1}{s^4 + 4s^3 + 6s^2 + 4s + 1} \tag{6}$$

After WOA being applied, the second-order LOS is obtained with ISE as 1.495 $\times$ $10^{-2}$, given by

$$R_2(s) = \frac{0.001s + 1.6771}{9.9984s^2 + 6.3484s + 1.6771} \tag{7}$$

Figure 2 shows the convergence of ISE by WOA. Figures 3 and 4 and Tables 1 and 2 present the comparison between time-domain response and frequency-domain response of fourth-order HOS with second-order LOS along with its parameters and performance indices obtained by the WOA and some recent algorithms.

The simulation results show the supremacy of WOA over the other algorithms. Further, the performance of the proposed algorithm is also shown in Fig. 5.

## 6 Conclusions

In the present work, it is observed from the obtained result that (i) WOA has better matching capability during the transient response of reduce-order model; (ii) The time-domain parameters of reduced second order obtained by WOA and original

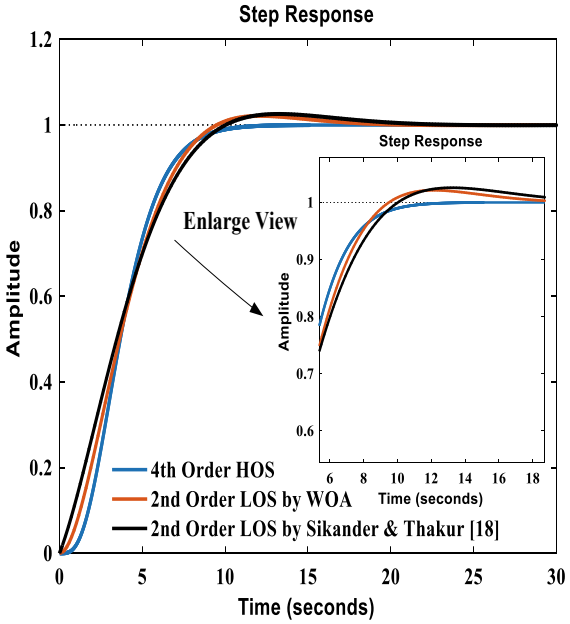


**Fig. 3** Step response of HOS and LOS for example

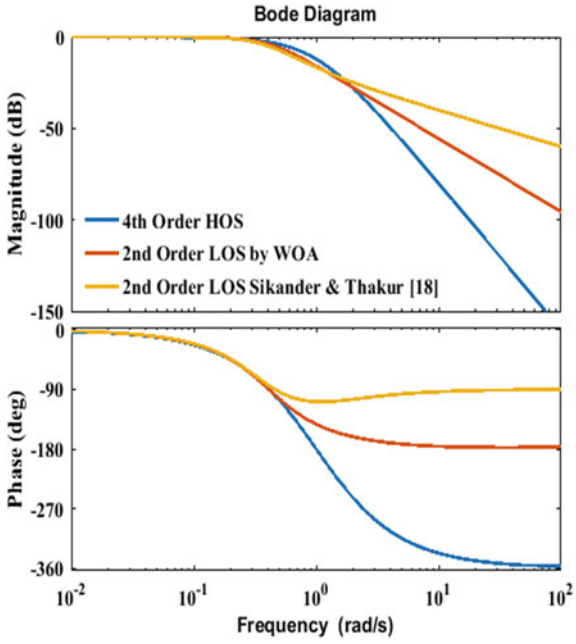


**Fig. 4** Bode plots of HOS and LOS for example

**Table 1** Comparison for the performance indices obtained by WOA and some recent algorithms for example

| Performance parameters | Reduced models | IRE | ISE | IAE |
|---|---|---|---|---|
| Original model | – | 0.1562 | – | – |
| WOA (proposed) | $\frac{0.001s + 1.6771}{9.9984s^2 + 6.3484s + 1.6771}$ | 0.1319 | $1.495 \times 10^{-2}$ | 0.4133 |
| Sikander and Thakur [19] | $\frac{0.1s + 0.1158}{s^2 + 0.5202s + 0.1158}$ | 0.1219 | $4.58 \times 10^{-2}$ | 0.6764 |

**Table 2** Comparison for the transient response parameters obtained by proposed WOA and some recent algorithms for example

| Performance parameters | Rise time (s) | Settling time (s) | Over shoot (%) |
|---|---|---|---|
| Original model | 4.94 | 9.08 | 0 |
| WOA (proposed) | 5.8 | 13 | 2.12 |
| Sikander and Thakur [19] | 6.56 | 15.63 | 2.56 |

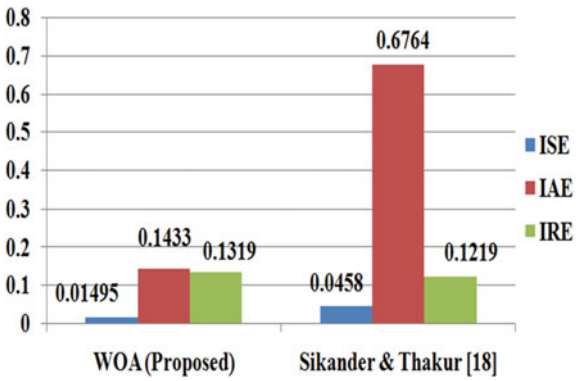


**Fig. 5** Bar chart comparison for example

fourth-order HOS are fairly similar; (iii) The reduced-order model obtained by WOA reveals the lowest value of ISE when compared.

## References

1. A. Sikander, R. Prasad, A new technique for reduced-order modelling of linear time-invariant system. IETE J. Res. 1–9 (2017)
2. J. Singh, K. Chatterjee, C.B. Vishwakarma, System reduction by eigen permutation algorithm and improved padé approximations. IJMCPECE, World Acad. Sci. Eng. Technol. **8**, 180–184 (2014)
3. C.B. Vishwakarma, Model order reduction of linear dynamic systems for control system design. Ph.D. Thesis, IIT Roorkee, Roorkee India (2009)

4. P. Saraswat, G. Parmar, A comparative study of differential evolution and simulation annealing for order reduction of large scale systems, in *IEEE Conf. on Communication, Control and Intelligent Systems (CCIS-2015)*, GLA University, Mathura (UP), India (2015)
5. D.K. Sambariya, O. Sharma, Routh approximation: an approach of model order reduction in SISO and MIMO systems. Indonesian J. Electr. Eng. Comput. Sci. **2**, 486–500 (2016)
6. G. Parmar, S. Mukherjee, R. Prasad, System reduction using eigen spectrum analysis and pade approximation technique. Int. J. Comput. Math. Taylor & Francis **84**, 1871–1880 (2007)
7. G. Parmar, S. Mukherjee, R. Prasad, System reduction using factor division algorithm and eigen spectrum analysis. Appl. Math. Model. **31**, 2542–2552 (2007)
8. S. Ghosh, N. Senroy, Balanced truncation approach to power system model order reduction. Electr. Power Compon. Syst. **41**, 747–764 (2013)
9. L.S. Shieh, Y.J. Wei, A mixed method for multivariable system reduction. IEEE Trans. Automat. Control **AC-20**, 429–432 (1975)
10. A. Narwal, R. Prasad, A novel order reduction approach for LTI systems using cuckoo search optimization and stability equation. IETE J. Res. **62**, 154–163 (2016)
11. S.R. Desai, R. Prasad, A new approach to order reduction using stability equation and big bang big crunch optimization. Syst. Sci. Control Eng. **1**, 20–27 (2013)
12. A. Sikander, R. Prasad, A novel order reduction method using cuckoo search algorithm. IETE J. Res. **61**, 83–90 (2015)
13. A. Sikander, R. Prasad, New technique for system simplification using cuckoo search and ESA. Indian Acad. Sci. 1–6 (2017)
14. J. Kumar, A. Sikander, M. Mehrotra, G. Parmar, A new soft computing approach for order diminution of interval system. Int. J Syst. Assur. Eng. Manage. **11**, 366–373 (2020). https://doi.org/10.1007/s13198-019-00865-y
15. A. Nadi, O. Alsmadi, Z. Hammour, Reduced order modeling of linear MIMO systems using particle swarm optimization, in *7th International Conference on Autonomic and Autonomous Systems (ICAS)*, Venice, Italy (2011), pp. 62–66
16. P. Boby, J. Pal, An evolutionary computation-based approach for reduced order modeling of linear systems, in *IEEE International Conference on Computational Intelligence and Computing Research, ICCIC* (2010), pp. 28–29
17. S.R. Desai, R. Prasad, A novel order diminution of LTI systems using big bang big crunch optimization and routh approximation. Appl. Math. Model. **37**, 8016–8028 (2013)
18. A. Nadi, O. Alsmadi, Invasive weed optimization for model order reduction of linear MIMO systems. Appl. Math. Model. **37**, 4570–4577 (2013)
19. A. Sikander, P. Thakur, Reduced order modelling of linear time invariant system using modified cuckoo search algorithm. Soft Comput. Springer, Berlin, Heidelberg, 1–11 (2017)
20. S. Mirjalili, A. Lewis, The whale optimization algorithm. Adv. Eng. Softw. **95**, 51–67 (2016)
21. I. Khanam, G. Parmar, Application of stochastic fractal search in order reduction of large scale LTI systems, in *IEEE International Conference on Computer, Communications and Electronics (Comptelix 2017)*, Manipal University, Jaipur (2017), pp. 190–194
22. D.K. Sambariya, G. Arvind, High order diminution of LTI system using stability equation method. Br. J. Math. Comput. Sci. **13**, 1–15 (2016)
23. J.E. Davison, A method for simplifying linear dynamic systems, IEEE Trans. Autom. Control. **11**, 93–101 (1966)
24. C.F. Chen, L.S. Shieh, A novel approach to linear model simplification, Int. J. Control. **8**, 561–570 (1968)
25. L.G. Gibilaro, F.P. Lees, The reduction of complex transfer function models to simple models using the method of moments. Chem.Eng. Sci. **24**(1), 85-93 (1969). ISSN 0009-2509, https://doi.org/10.1016/0009-2509(69)80011-4
26. M.F. Hutton, B. Freidland, Routh approximation for Reducing order of LTI systems. IEEE Trans. Autom. Control. **20**, 329–337 (1975)